Numerical Methods for Fluid-Solid Coupled Simulations: Robin Interface Conditions and Shock-Dominated Applications

Shunxiang Cao

Dissertation submitted to the Faculty of the

Virginia Polytechnic Institute and State University

in partial fulfillment of the requirements for the degree of

Doctor of Philosophy

in

Aerospace Engineering

Kevin G. Wang, Chair

Robert A. Canfield

Seongim S. Choi

Wayne L. Neu

Christopher J. Roy

July 23, 2019

Blacksburg, Virginia

Keywords: Fluid-structure interaction, Robin-Neumann interface conditions, Embedded boundary method, Shock wave, Damage and fracture, Cavitation

Numerical Methods for Fluid-Solid Coupled Simulations: Robin Interface Conditions and Shock-Dominated Applications

Shunxiang Cao

ABSTRACT

This dissertation investigates the development of numerical algorithms for coupling computational fluid dynamics (CFD) and computational solid dynamics (CSD) solvers, and the use of these solvers for simulating fluid-solid interaction (FSI) problems involving large deformation, shock waves, and multiphase flow. The dissertation consists of two parts. The first part investigates the use of Robin interface conditions to resolve the well-known numerical added-mass instability, which affects partitioned coupling procedures for solving problems with incompressible flow and strong added-mass effect. First, a one-parameter Robin interface condition is developed by linearly combining the conventional Dirichlet and Neumann interface conditions. Next, a numerical algorithm is developed to implement the Robin interface condition in an embedded boundary method for coupling a parallel, projection-based incompressible viscous flow solver with a nonlinear finite element solid solver. Both an analytical study and a numerical study reveal that the new algorithm can clearly outperform conventional Dirichlet-Neumann procedures in terms of both stability and accuracy, when

the parameter value is carefully selected. Moreover, the studies also indicate that the optimal parameter value depends on the materials and geometry of the problem. Therefore, to efficiently solve FSI problems involving non-uniform structures, a generalized Robin interface condition is presented, in which the constant parameter is replaced by a spatially varying function that depends on the local material and geometric properties of the structure. Numerical experiments using two benchmark problems show that the spatially varying Robin interface condition can clearly improve numerical accuracy compared to the constant-parameter version with the same computational cost.

The second part of this dissertation focuses on simulating complex FSI problems featuring shock waves, multiphase flow (e.g., bubbles), and shock-induced material damage and fracture. A recently developed three-dimensional computational framework is employed, which couples a multiphase, compressible CFD solver and a nonlinear finite element CSD solver using an embedded boundary method and a partitioned procedure. In particular, the CFD solver applies a level-set method to capture the evolution of the bubble surface, and the CSD solver utilizes a continuum damage mechanics model and an element erosion method to simulate the dynamic fracture of the material. Two computational studies are presented. The first one investigates the dynamic response and failure of a brittle material exposed to a prescribed shock wave. The predictive capability of the computational framework is first demonstrated by simulating a series of laboratory experiments in the context of shock wave lithotripsy. Then, a parametric study is conducted to elucidate the significant effects of the shock wave's profile on material damage. In the second study, the computational framework

is applied to simulate shock-induced bubble collapse near various solid and soft materials. The reciprocal effect of the material's properties (e.g., acoustic impedance, Young's modulus) on bubble dynamics is discussed in detail.

Numerical Methods for Fluid-Solid Coupled Simulations: Robin Interface Conditions and Shock-Dominated Applications

Shunxiang Cao

GENERAL AUDIENCE ABSTRACT

Numerical simulations that couple computational fluid dynamics (CFD) solvers and computational solid dynamics (CSD) solvers have been widely used in the solution of nonlinear fluid-solid interaction (FSI) problems underlying many engineering applications. This is primarily because they are based on partitioned solutions of fluid and solid subsystems, which facilitates the use of existing numerical methods and computational codes developed for each subsystem. The first part of this dissertation focuses on developing advanced numerical algorithms for coupling the two subsystems. The aim is to resolve a major numerical instability issue that occurs when solving problems involving incompressible, heavy fluids and thin, lightweight structures. Specifically, this work first presents a new coupling algorithm based on a one-parameter Robin interface condition. An embedded boundary method is developed to enforce the Robin interface condition, which can be advantageous in solving problems involving complex geometry and large deformation. The new coupling algorithm has been shown to significantly improve numerical stability when the constant parameter is carefully

selected. Next, the constant parameter is generalized into a spatially varying function whose local value is determined by the local material and geometric properties of the structure. Numerical studies show that when solving FSI problems involving non-uniform structures, using this spatially varying Robin interface condition can outperform the constant-parameter version in both stability and accuracy under the same computational cost.

In the second part of this dissertation, a recently developed three-dimensional multiphase CFD - CSD coupled solver is extended to simulate complex FSI problems featuring shock wave, bubbles, and material damage and fracture. The aim is to understand the material's response to loading induced by a shock wave and the collapse of nearby bubbles, which is important for advancing the beneficial use of shock wave and bubble collapse for material modification. Two computational studies are presented. The first one investigates the dynamic response and failure of a brittle material exposed to a prescribed shock wave. The causal relationship between shock loading and material failure, and the effects of the shock wave's profile on material damage are discussed. The second study investigates the shock-induced bubble collapse near various solid and soft materials. The two-way interaction between bubble dynamics and materials response, and the reciprocal effects of the material's properties are discussed in detail.

Acknowledgments

First, I would like to thank my advisor, Dr. Kevin G. Wang for his advice and mentorship during this 5-year-long journey. On top of providing the financial support to make my graduate research successful, he also encouraged me when I struggled with difficulties in research and provided me great opportunities to build up my academic career. Working as the first graduate assistant in Multiphysics Modeling and Computational Lab under his guidance will be an unforgettable experience in my life.

Second, I would like to gratefully acknowledge my coauthors for their contributions to the work presented in this dissertation. I want to thank Dr. Alex Main for his help in the development of the imcompressible CFD solver, Dr. Ying Zhang, Mr. Defei Liao and Dr. Pei Zhong for the experimental work on Shockwave Lithotripsy project, and my lab mate Dr. Guangyao Wang for his contributions to the two projects of this dissertation. I also want to thank all other members of my dissertation committee, Dr. Robert A. Canfield, Dr. Seongim Choi, Dr. Wayne Neu and Dr. Christopher Roy, for giving me professional and helpful suggestions, and reviewing this dissertation.

Also, I would like to thank my partners, office mates and friends who encouraged and supported me during these five years. Particularly, I want to thank Mr. Howard Chung, Dr. Jianxun Wang, Dr. Xingsheng Sun, Mr. Yang Song and Mr. Robert Masti for their companionship during the long-hours research life in the office, as well as the wonderful fishing life on the New River. I also want to express my sincere gratitude to my best friends, Ms. Yingying Xie and Ms. Yilin Ji, and an important person, Ms. Yiyun Luo, for their support, encouragement and friendship from the first day I met them.

Lastly, but most importantly, I would like to thank my grandmother, Shizhi Sun, and my parents, Xiangle Cao and Jing wei, for their education, support and encouragement. This dissertation is also dedicated in loving memory to my grandfather, Yongyun Wei.

Contents

List of Figures

List of Tables

Chapter 1

Introduction

Fluid-solid interaction (FSI) plays an important role in various science and engineering fields such as aerospace, marine, civil and biomedical engineering. One well-known example in aerospace engineering is aeroelasticity, which concerns the interaction between the deformable body of an aerial vehicle and the aerodynamic forces of the surrounding airstream [1]. Aeroelastic phenomena such as wing torsional divergence and flutter can cause catastrophic failure of flexible structures, and hence, the study of aeroelasticity is an important aspect of aircraft design. In marine and civil engineering, typical FSI problems include, but not limited to, the interaction of marine propeller with cavitating flows [2], the implosion of underwater structures [3], the interaction between offshore structures (e.g., offshore platforms, wind turbines) and environmental loadings (e.g., ocean wave, wind) [4, 5], and the wind-induced vibration of long bridges and tall buildings [6]. FSI is also the primary mechanism underlying many biomechanical applications such as hemodynamics in human

circulation system [7], vocal-fold oscillation during phonation [8] and some noninvasive therapies such as shock wave lithotripsy [9] — just to name a few examples. In many of the applications mentioned above, the interactions between fluid and structures are commonly characterized by the following features:

- the fluid flow has a strong impact on the structure (in terms of hydrodynamic loadings, can be cyclic), leading to large structural deformations and possibly material failures;
- the structure also has significant reciprocal effects on the fluid dynamics (e.g., rapidly accelerating or decelerating the surrounding flow), and features complex geometries and/or various material properties (e.g., can be metal, rock, soft tissue);
- discontinuous phenomena, such as shock wave, multiphase flow, fatigue and fracture, are often involved.

These give rise to a highly nonlinear system in which the fluid and structural governing equations are strongly coupled through the interface/transmission conditions i.e., the kinematic and dynamic conditions at the fluid-solid interface. In this regard, it is of great importance to take into account the two-way coupling between the fluid and solid subsystems in the analysis of this kind of FSI problems. Otherwise, significant error can be introduced if the problem is solved as a fluid-only or a solid-only problem [10].

However, the solution of this highly nonlinear, strongly coupled system is challenging. For most of the FSI problems, it is nearly impossible to obtain the analytical solution of the coupled system because of the complexity. At the same time, the experimental studies

are often found to have limited scopes [11] (e.g., with low spatial resolution and/or lack of capability in capturing transient phenomena [12]). Thanks to the rapid advance of computer techniques in the past few decades, especially the development of high-performance computer (HPC), numerical simulation has become an effective and efficient alternative approach for solving these fluid-solid coupled problems.

Existing numerical methods for solving FSI problems can be broadly divided into two categories: *monolithic procedures* and *partitioned procedures*. In a monolithic procedure, the fluid and solid governing equations are time-integrated simultaneously as one system. This approach accounts for the strong coupling between the fluid and solid but requires a fully-integrated fluid-solid solver. The partitioned procedure, on the other hand, solves the fluid and solid governing equations separately, for example, by using a computational fluid dynamics (CFD) and a computational solid dynamics (CSD) solver. The interface conditions at the fluid-solid interface are enforced through data exchange between two solvers. Therefore, partitioned procedures can be advantageous in terms of maintaining software modularity and leveraging well-developed algorithms and solvers, which is intrinsically well-suited to the multi-physics nature of the problem. Also, recent developments in CFD and CSD have largely improved the predictive capability of fluid and solid solvers, and thus, expanding the boundary of CFD-CSD coupled simulation to cover more real-world FSI applications.

In this regard, this dissertation focuses on the CFD-CSD coupled simulation based on partitioned procedures for the solution of nonlinear FSI problems. Depending on the compressibility of the fluid flow involved therein, FSI problems can be categorized as either incom-

pressible FSI problems or compressible FSI problems. Since the physics of incompressible and compressible fluid, as well as the mathematical properties of their governing equations, are dramatically different, the numerical challenges encountered in the simulations of these two categories of problems are also different. To motivate the current work, Section 1.1 introduces several specific engineering applications from each category, and describes the numerical challenges involved in their simulations. The objective and accomplishments of this dissertation are then presented in Section 1.2 and Section 1.3, respectively.

1.1 Motivations

1.1.1 Incompressible FSI applications

Aquatic propulsion

Unmanned underwater vehicles(UUV) has become a powerful and ubiquitous tool for science, commercial, and military missions such as graphic data collection [13], fisheries research [14] and anti-submarine warfare [15]. To achieve optimal functions in various operation environments, the vehicles need to be versatile, capable of performing multiple tasks with different locomotion gaits. These versatility requirements are often beyond the capability of conventional propulsors, such as marine propellers and underwater gliders. In this regard, there has been increasing interest in designing unconventional, flexible propulsors that are inspired by the superior locomotion abilities of some aquatic animals such as fish and water

snake [16]. These bio-inspired propulsors are often designed to mimic the appendages of those animals (e.g., fin, tail) such that similar kinematic performance can be achieved. However, the underlying mechanisms of fish locomotion, such as the causal relationship between solid motions and propulsive force generation, have not been fully understood, which hinders the design process. In this regard, CFD-CSD coupled simulation can be a powerful tool as it is capable to characterize the dynamic interaction between flexible, reconfigurable, fin-like structures and the surrounding fluid medium.

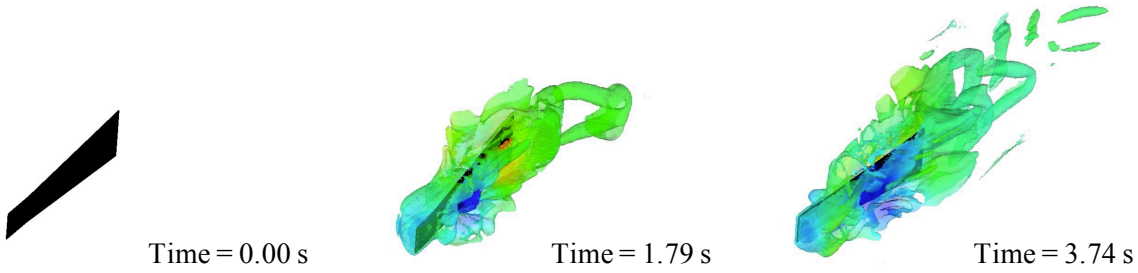

Figure 1.1: Snapshots of a three dimensional CFD-CSD coupled simulation of a flapping fin (with a thickness of 1.6 mm) in water. Black panel is the fin structure and the colored contour visualizes the fluid vorticity. In the simulation, the motion of the leading edge of fin and the inflow velocity are prescribed.

However, when the above coupled simulation is applied to a fin with a relatively small thickness (e.g., < 1 mm), numerical instability occurs (see Figure 1.2). This instability issue is associated with partitioned procedures and it is often referred to as artificial or numerical added-mass effect. It has been found that when the problem involves a heavy, incompressible fluid and/or a slender domain — a common scenario in applications involving liquid and/or lightweight thin structures, the partitioned procedure can be unconditionally unstable [17, 18]. A common practice to mitigate this instability is to perform multiple

subiterations between the fluid and solid solvers in the fashion of fixed-point iteration. In this way, however, the computational cost increases dramatically. Thus, developing more efficient methods to mitigate this numerical instability is currently an active research topic.

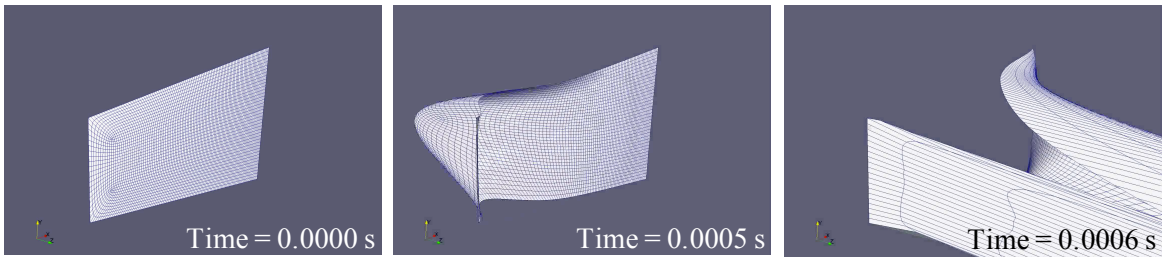

Figure 1.2: Numerical instability occurs when the fin has a relatively small thickness. Solution becomes unstable within a few time steps.

Hemodynamics

The strong interaction between blood flow and structures in the circulatory system (e.g., vascular wall, heart valves) has been found closely related to the progression, prediction, and treatment of many cardiovascular diseases (e.g., cerebral aneurysm, aortic stenosis) [19]. Previous numerical studies on hemodynamics primarily focus on the fluid dynamics of the blood flow without considering the motion of the blood vessel. However, recent research has found that the vessel deformation significantly affects the hemodynamic factors that play determinant roles in cardiovascular diseases, such as the wall shear stress [20]. In this regard, applying CFD-CSD coupled simulation to take vessel deformation into account is important for avoiding misleading results. Nevertheless, several numerical challenges associated with CFD-CSD coupled simulations remain unsolved. For example, since the density of blood

flow and tissue are comparable, the numerical added-mass effect described in Section 1.1.1 is a major issue. A relatively large number of fluid-solid subiterations are required to mitigate the instability (often > 10), leading to extremely high computational cost. Also, the complex geometries and large deformation of the blood vessels have posed substantial difficulties in mesh generation and the coupling of fluid and solid computational domains. These challenges have motivated the development of an efficient, robust and numerically stable CFD-CSD coupled computational framework.

1.1.2 Compressible FSI applications

Shock wave lithotripsy

Shock wave lithotripsy (SWL) is a first-line, non-invasive therapy of urinary stone disease. The basic process is to focus extracorporeally generated, high-intensity acoustic pulses (shock waves) onto kidney stones and progressively break the stones into small pieces (< 5 millimeters in diameter, Figure 1.3) such that they can be excreted along with urine. Despite the widespread use of SWL since its inception in the early 1980s [21], clinical practices show that this therapy has relatively low success rate and high retreatment rate [22], as well as high risk of complications ($\sim 40\%$ as reported in [23]). The primary reason hindering the development of more efficient and safer lithotripter is that the fundamental physical principles, including the mechanisms of stone fragmentation and side effects (e.g., tissue injury), have not been fully understood. In the past two decades, extensive research has been devoted to develop-

ing numerical models that are capable to capture the detailed dynamics of this shock-stone interaction problem [24, 25, 26, 27, 28, 29]. However, the multi-physics nature of this problem has posed significant challenges to numerical simulation. For example, SWL involves dynamic interaction of four materials, including liquid, solid, tissue and gas. Also, the stone fragmentation is a progressive process under multiple cyclic loading, and thus, modeling the progression of fracture is important. In this regard, a high-fidelity fluid-solid coupled model with the capabilities to simulate the dynamic fracture of the stone can be a powerful tool to elucidate the causal relationship between shock loading and stone fragmentation.

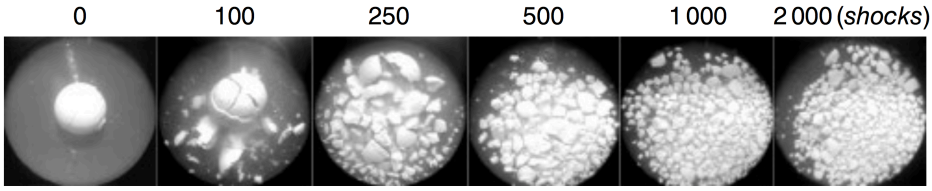

Figure 1.3: Stone comminution under cyclic shock loadings (adopted from Figure 58.1 in [21])

Cavitation-induced material modification

The formation and collapse of cavitation bubble under large pressure variation have previously been considered as a destructive phenomenon associated with, for example, the marine propeller erosion and noise generation. This is because the rapid compression of internal gases during the bubble collapse can form a high-speed micro-jet (up to around 1000 m/s [30]) and emit strong shock waves (up to several hundred MPa), which induce damage to the nearby materials (see Figure 1.4). Recently, however, there is a growing interest in utilizing cavitation for high-precision material modification as it allows energy to be focused safely

and released rapidly within a small target region. For example, high pressure generated by the micro-jet and the emitted shock wave can be used in the comminution of kidney stone [31], the non-invasive removal of human tissue (*histotripsy*) [32] and increasing the permeability of biologic tissues for drug delivery (*sonoporation*) [33]. In these applications, the boundaries between the meritorious effects of cavitation (e.g., stone fragmentation) and its deleterious effects (e.g., rupture of blood vessels in kidney) are often very narrow. Thus, to achieve delicate controls of the cavitation process, it is important to fully understand the dynamics of bubble collapse near different types of materials and the resulting material failures. The accurate solution of this cavitation-material interaction problems requires a high-fidelity CFD-CSD coupled computational framework that is capable to capture shock wave, multiphase flow, and the complex, nonlinear material behaviors such as dynamic fracture.

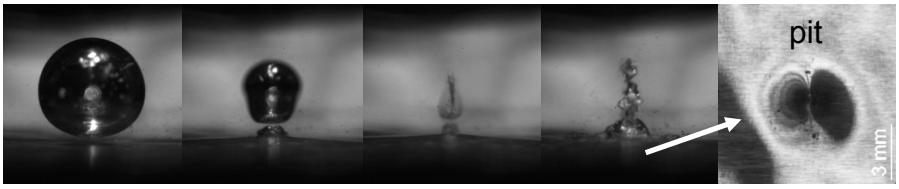

Figure 1.4: Collapse of a cavitation bubble near aluminum foil. A pit is formed on the material surface (last figure) after the collapse. Photograph used with permission of B. Zhao & O. Coutier-Delgosha (Virginia Tech).

1.2 Objectives

The current work aims at addressing those numerical challenges highlighted in Section 1.1. Specifically, the first part of this dissertation aims at developing a numerically stable partitioned procedure for CFD-CSD coupling, targeting at incompressible FSI problems that involves strong added-mass effect and complex, large-deformed structures. The new coupling algorithm should:

- be able to mitigate the numerical added-mass effect efficiently;
- be able to handle the large deformation of fluid-solid interface;
- be effective and robust when the structures have spatially varying material properties and complex geometries.

The proposed method should be verified and demonstrated using academic examples.

The second part of this dissertation aims at developing a multiphase fluid-solid coupled computational model to accurately predict the two-way interaction between fluid and material involved in Shock Wave Lithotripsy (SWL) and cavitation-induced material modification. For SWL, particular focus will be placed on:

- modeling and simulating material damage and fracture;
- characterizing the causal relationship between the prescribed shock load, the elastic waves in the solid material, and the resulting material damage and fracture

For cavitation-induced material modification, particular focus will be placed on:

- modeling non-spherical collapse of a single bubble with different materials in its vicinity;
- characterizing the reciprocal effect of material properties on the collapse dynamics of the bubble.

1.3 Dissertation accomplishments and outline

1.3.1 Dissertation accomplishments

The major accomplishments of this dissertation are summarized as follows.

- Development of a novel CFD-CSD coupled computational framework for solving incompressible FSI problems involving strong added-mass effect, non-uniform flexible structure, and large structural deformation. Key components include:
  (a) a parallel, projection-based, incompressible CFD solver and a finite element CSD solver;
  (a) the use of Robin-Neumann interface conditions in fluid-solid coupling to mitigate the numerical added-mass effect;
  (a) an Embedded Robin Boundary Method featuring the use of operator splitting and a modified ghost fluid method to enforce the Robin interface condition on

fluid-solid interfaces embedded in structured non-body-conforming CFD grids;

(a) generalization of the Robin parameter as a spatially varying function whose local value is chosen based on the local material and geometric properties of the structure.

- Characterization of the effects of Robin parameter on numerical stability and solution accuracy using a numerical study based on the new computational framework and a mathematical analysis based on a simplified 2D FSI model problem.

- Development of a three-dimensional (3D) fluid-solid coupled model for simulating shock-induced damage and fracture in a brittle material submerged in liquid. In particular, a continuum damage mechanics model and an element erosion method are applied to model and simulate the material damage and fracture. After model calibration and validation using a laboratory experiment, a computational study is carried out to investigate the causal relationship among shock load, elastic wave, and crack formation, as well as the effects of shock waveform, magnitude and the size of the target material on the material damage.

- Extension of the above 3D computational model to simulate the shock-induced collapse of an air bubble in water, with various elastic and viscoelastic materials in its vicinity. After model verification, a computational study is carried out to characterize the fluid-material interaction and investigate the reciprocal effects of material's properties, including acoustic impedance and Young's modulus, on the collapse dynamics of the

bubble.

1.3.2 Outline

This dissertation is organized in the manuscript (multi-paper) format, in which each of the main chapters is in the format of a peer-reviewed article. The remainder of this dissertation is organized as follows.

Chapter 2 and 3 are two articles about the use of Robin-Neumann partitioned procedure for solving incompressible FSI problems with strong added-mass effect. Specifically, Chapter 2 presents the development of a novel CFD-CSD coupled computational framework based on an Embedded Robin Boundary Method, as well as a study of the effects of the Robin parameter on numerical stability and solution accuracy. In Chapter 3, the Robin parameter is generalized as a spatially varying function, and two models to determine its local value based on local structural properties are proposed and compared. A modified Turek-Hron benchmark problem and a simplified FSI model problem are used to demonstrate the new Robin interface condition.

Chapter 4 and 5 are two articles about the use of a high-fidelity fluid-solid coupled solver to explore the mechanism underlying Shock Wave Lithotripsy and cavitation-induced material modification. Specifically, Chapter 4 presents the CFD-CSD coupled analysis of shock-induced damage and dynamic fracture in a cylindrical body submerged in liquid. In Chapter 5, the above CFD-CSD coupled analysis is extended to analyze the shock-induced bubble

collapse near various elastic and viscoelastic materials.

Finally, a conclusion and a summary of future work are consigned to Chapter 6.

Bibliography

[1] R. Kamakoti and W. Shyy, "Fluid–structure interaction for aeroelastic applications," *Progress in Aerospace Sciences*, vol. 40, no. 8, pp. 535–558, 2004.

[2] Y. L. Young, "Fluid–structure interaction analysis of flexible composite marine propellers," *Journal of Fluids and Structures*, vol. 24, no. 6, pp. 799–818, 2008.

[3] C. Farhat, K. Wang, A. Main, S. Kyriakides, L.-H. Lee, K. Ravi-Chandar, and T. Belytschko, "Dynamic implosion of underwater cylindrical shells: experiments and computations," *International Journal of Solids and Structures*, vol. 50, no. 19, pp. 2943–2961, 2013.

[4] Y. Bazilevs, M.-C. Hsu, J. Kiendl, R. Wüchner, and K.-U. Bletzinger, "3d simulation of wind turbine rotors at full scale. part ii: Fluid–structure interaction modeling with composite blades," *International Journal for numerical methods in fluids*, vol. 65, no. 1-3, pp. 236–253, 2011.

[5] J. Yan, A. Korobenko, X. Deng, and Y. Bazilevs, "Computational free-surface fluid–

structure interaction with application to floating offshore wind turbines," *Computers & Fluids*, vol. 141, pp. 155–174, 2016.

[6] M. P. Païdoussis, S. J. Price, and E. De Langre, *Fluid-structure interactions: cross-flow-induced instabilities*. Cambridge University Press, 2010.

[7] C. A. Taylor and C. Figueroa, "Patient-specific modeling of cardiovascular mechanics," *Annual review of biomedical engineering*, vol. 11, pp. 109–134, 2009.

[8] M. Feistauer, P. Sváček, and J. Horáček, "Numerical simulation of fluid–structure interaction problems with applications to flow in vocal folds," in *Fluid-structure interaction and biomedical applications*, pp. 321–393, Springer, 2014.

[9] J. J. Rassweiler, T. Knoll, K.-U. Köhrmann, J. A. McAteer, J. E. Lingeman, R. O. Cleveland, M. R. Bailey, and C. Chaussy, "Shock wave technology and application: an update," *European urology*, vol. 59, no. 5, pp. 784–796, 2011.

[10] F.-K. Benra, H. J. Dohmen, J. Pei, S. Schuster, and B. Wan, "A comparison of one-way and two-way coupling methods for numerical analysis of fluid-structure interactions," *Journal of applied mathematics*, vol. 2011, 2011.

[11] G. Hou, J. Wang, and A. Layton, "Numerical methods for fluid-structure interactiona review," *Communications in Computational Physics*, vol. 12, no. 2, pp. 337–377, 2012.

[12] M. Krafczyk, M. Cerrolaza, M. Schulz, and E. . Rank, "Analysis of 3d transient blood

flow passing through an artificial aortic valve by lattice–boltzmann methods," *Journal of Biomechanics*, vol. 31, no. 5, pp. 453–462, 1998.

[13] C. C. Eriksen, T. J. Osse, R. D. Light, T. Wen, T. W. Lehman, P. L. Sabin, J. W. Ballard, and A. M. Chiodi, "Seaglider: A long-range autonomous underwater vehicle for oceanographic research," *IEEE Journal of oceanic Engineering*, vol. 26, no. 4, pp. 424–436, 2001.

[14] P. G. Fernandes, P. Stevenson, A. S. Brierley, F. Armstrong, and E. J. Simmonds, "Autonomous underwater vehicles: future platforms for fisheries acoustics," *ICES Journal of Marine Science*, vol. 60, no. 3, pp. 684–691, 2003.

[15] R. L. Wernli, "Auvs-a technology whose time has come," in *Proceedings of the 2002 Interntional Symposium on Underwater Technology (Cat. No. 02EX556)*, pp. 309–314, IEEE, 2002.

[16] A. J. Ijspeert, "Biorobotics: Using robots to emulate and investigate agile locomotion," *science*, vol. 346, no. 6206, pp. 196–203, 2014.

[17] P. Causin, J.-F. Gerbeau, and F. Nobile, "Added-mass effect in the design of partitioned algorithms for fluid–structure problems," *Computer methods in applied mechanics and engineering*, vol. 194, no. 42-44, pp. 4506–4527, 2005.

[18] C. Förster, W. A. Wall, and E. Ramm, "Artificial added mass instabilities in sequential staggered coupling of nonlinear structures and incompressible viscous flows," *Computer methods in applied mechanics and engineering*, vol. 196, no. 7, pp. 1278–1293, 2007.

[19] Y. Bazilevs, M.-C. Hsu, Y. Zhang, W. Wang, T. Kvamsdal, S. Hentschel, and J. Isaksen, "Computational vascular fluid–structure interaction: methodology and application to cerebral aneurysms," *Biomechanics and modeling in mechanobiology*, vol. 9, no. 4, pp. 481–498, 2010.

[20] R. Torii, M. Oshima, T. Kobayashi, K. Takagi, and T. E. Tezduyar, "Influence of wall elasticity in patient-specific hemodynamic simulations," *Computers & Fluids*, vol. 36, no. 1, pp. 160–168, 2007.

[21] A. Neisius and P. Zhong, "Physics of shock-wave lithotripsy," *Smith's Textbook of Endourology*, pp. 689–712, 2019.

[22] N. L. Miller and J. E. Lingeman, "Treatment of kidney stones: current lithotripsy devices are proving less effective in some cases," *Nature Reviews Urology*, vol. 3, no. 5, p. 236, 2006.

[23] M. S. Al-Marhoon, O. Shareef, I. S. Al-Habsi, A. S. Al Balushi, J. Mathew, and K. P. Venkiteswaran, "Extracorporeal shock-wave lithotripsy success rate and complications: initial experience at sultan qaboos university hospital," *Oman medical journal*, vol. 28, no. 4, p. 255, 2013.

[24] R. O. Cleveland and O. A. Sapozhnikov, "Modeling elastic wave propagation in kidney stones with application to shock wave lithotripsy," *The Journal of the Acoustical Society of America*, vol. 118, no. 4, pp. 2667–2676, 2005.

[25] O. A. Sapozhnikov, A. D. Maxwell, B. MacConaghy, and M. R. Bailey, "A mechanistic analysis of stone fracture in lithotripsy," *The Journal of the Acoustical Society of America*, vol. 121, no. 2, pp. 1190–1202, 2007.

[26] M. Wijerathne, M. Hori, H. Sakaguchi, and K. Oguni, "3d dynamic simulation of crack propagation in extracorporeal shock wave lithotripsy," in *IOP Conference Series: Materials Science and Engineering*, vol. 10, p. 012120, IOP Publishing, 2010.

[27] D. Fovargue, *Multiscale and multiphysics computational models of processes in shock wave lithotripsy*. PhD thesis, The University of North Carolina at Chapel Hill, 2013.

[28] K. G. Wang, "Multiphase fluid-solid coupled analysis of shock-bubble-stone interaction in shockwave lithotripsy," *International journal for numerical methods in biomedical engineering*, vol. 33, no. 10, p. e2855, 2017.

[29] Y. Zhang, I. Nault, S. Mitran, E. S. Iversen, and P. Zhong, "Effects of stone size on the comminution process and efficiency in shock wave lithotripsy," *Ultrasound in medicine & biology*, vol. 42, no. 11, pp. 2662–2675, 2016.

[30] E. Johnsen and T. Colonius, "Numerical simulations of non-spherical bubble collapse," *Journal of fluid mechanics*, vol. 629, pp. 231–262, 2009.

[31] Y. A. Pishchalnikov, O. A. Sapozhnikov, M. R. Bailey, J. C. Williams Jr, R. O. Cleveland, T. Colonius, L. A. Crum, A. P. Evan, and J. A. McAteer, "Cavitation bubble cluster activity in the breakage of kidney stones by lithotripter shockwaves," *Journal of endourology*, vol. 17, no. 7, pp. 435–446, 2003.

[32] A. D. Maxwell, T.-Y. Wang, C. A. Cain, J. B. Fowlkes, O. A. Sapozhnikov, M. R. Bailey, and Z. Xu, "Cavitation clouds created by shock scattering from bubbles during histotripsy," *The Journal of the Acoustical Society of America*, vol. 130, no. 4, pp. 1888–1898, 2011.

[33] C. E. Brennen, "Cavitation in medicine," *Interface focus*, vol. 5, no. 5, p. 20150022, 2015.

Chapter 2

Robin-Neumann Transmission Conditions for Fluid-Structure Coupling: Embedded Boundary Implementation and Parameter Analysis

(Published in *International Journal for Numerical Methods in Engineering*, 115, 578-603, 2018.)

S. Cao [a], A. Main [b], K. G. Wang [a]

[a] Department of Aerospace and Ocean Engineering, Virginia Polytechnic Institute and State

University, Blacksburg, VA 24061, United States

[b] Department of Civil and Environmental Engineering, Duke University, Durham, NC 27708, United States

Abstract

Partitioned procedures are appealing for solving complex fluid-structure interaction (FSI) problems, as they allow existing computational fluid dynamics (CFD) and computational structural dynamics (CSD) algorithms and solvers to be combined and re-used. However, for problems involving incompressible flow and strong added-mass effect (e.g., heavy fluid, slender structure), partitioned procedures suffer from numerical instability, which typically requires additional sub-iterations between the fluid and structural solvers, hence significantly increasing the computational cost. This paper investigates the use of Robin-Neumann transmission conditions to mitigate the above instability issue. Firstly, an embedded Robin boundary method is presented in the context of projection-based incompressible CFD and finite-element-based CSD. The method utilizes operator splitting and a modified ghost fluid method to enforce the Robin transmission condition on fluid-structure interfaces embedded in structured, non-body-conforming CFD grids. The method is demonstrated and verified using the Turek and Hron benchmark problem, which involves a slender beam undergoing large, transient deformation in an unsteady, vortex-dominated channel flow. Secondly, this paper investigates the effect of the combination parameter in the Robin transmission condi-

tion, α_f, on numerical stability and solution accuracy. The paper presents a numerical study using the Turek and Hron benchmark problem, and an analytical study using a simplified FSI model featuring an Euler-Bernoulli beam interacting with a two-dimensional incompressible, inviscid flow. Both studies reveal a trade-off between stability and accuracy: smaller values of α_f tend to improve numerical stability, yet deteriorates the accuracy of the partitioned solution. Using the simplified FSI model, the critical value of α_f that optimizes this trade-off is derived and discussed.

Keywords

Fluid-structure interaction, Partitioned procedure, Robin-Neumann transmission conditions, Embedded boundary method, Numerical added-mass effect

2.1 Introduction

Within the past few decades, extensive research has been devoted to the development of numerical methods for simulating dynamic fluid-structure interaction (FSI) problems in various science, engineering, and biomedical applications. Existing methods can be broadly divided into two categories: monolithic procedures and partitioned procedures (e.g., [1, 2, 3, 4, 5, 6]). In a monolithic procedure (e.g., [1, 2]), the fluid and structural governing equations are combined and time-integrated simultaneously as one system. The partitioned procedures, on

the other hand, solve the fluid and structural governing equations separately, therefore can be advantageous in terms of maintaining software modularity and leveraging existing CFD (computational fluid dynamics) and CSD (computational structural dynamics) solvers (e.g., [3, 4, 5, 6]). Specifically, in partitioned procedures, the kinematic and dynamic interface conditions, also referred to as transmission conditions, are enforced through data exchange between the two solvers. The most common strategy is to prescribe the velocity of the fluid at the fluid-structure interface to be the velocity of the structure computed by the CSD solver, while the traction on the wetted surface of the structure is computed using the fluid pressure and viscous stress. In other words, the kinematic and dynamic interface conditions are enforced by applying a Dirichlet boundary condition in the fluid sub-system and a Neumann boundary condition in the structural sub-system.

In the category of partitioned procedures, explicit (or "loose") coupling schemes solve the fluid and the structural governing equations once per time step, without additional sub-iteration. Despite successful applications for solving FSI problems with compressible flows (e.g., [7, 8, 9, 10, 11, 12, 13, 14]), explicit coupling schemes have been found to be unconditionally unstable when the fluid is incompressible, and has high mass density compared to that of the structure — a common scenario in applications involving liquids and/or lightweight structures (e.g., [5, 6]). This stability issue, referred to as the numerical added mass effect, can be mitigated by performing multiple (often more than 10) sub-iterations between the fluid and structural solvers in the fashion of fixed-point iteration. However, this approach — referred to as implicit (or "strong") coupling — significantly increases the

computational cost [5].

To mitigate the numerical added-mass effect more efficiently, a few ideas have been proposed and explored in the past decade, including the kinematically coupled schemes (e.g., [15, 16, 17]), semi-implicit coupling (e.g., [18]), and the Robin-Neumann transmission conditions (e.g., [19]). In particular, Badia *et al.* [19] proposed to replace the Dirichlet boundary condition for the fluid solver by a Robin boundary condition, that is, a linear combination of the kinematic and dynamic interface conditions. The Robin-Neumann transmission conditions is mathematically equivalent with the conventional Dirichlet-Neumann transmission conditions. Nonetheless, it is found that when employed in a partitioned procedure, it can reduce the number of sub-iterations required to achieve stability, when the linear combination parameter is carefully selected. Moreover, since it only requires modifying the boundary condition of the fluid sub-system, the Robin-Neumann transmission conditions is also appealing from the software development standpoint.

A few authors have applied the Robin-Neumann transmission conditions in the arbitrary Lagrangian-Eulerian (ALE) framework for solving two-way coupled FSI problems [19, 20, 21]. Recently, Li *et al.* [22] has also applied it in a mixed Eulerian-Lagrangian framework featuring moving overlapping grids. However, for FSI problems involving complex geometry, large structural deformation, and possibly topological change (e.g., fracture), immersed/embedded boundary methods may be appealing because of its simplification of mesh generation and robustness [7, 8, 9, 10, 11, 12]. In practice, these types of FSI problems also tend to involve strong added-mass effect — for example, large structural deformation is often associated

with heavy fluid and/or lightweight structures. Therefore, introducing the Robin-Neumann transmission conditions to immersed/embedded boundary methods is valuable. In this work, we present an embedded Robin boundary method for the partitioned solution of FSI problems involving incompressible fluid flow and strong added-mass effect. The method is built on top of a six-step projection-based incompressible flow solver [23]. It features the use of an operator-splitting scheme to enforce the Robin boundary condition in different steps of the flow solver. In addition, the method uses a modified ghost fluid method in which the ghost cells are populated using an asymmetric finite difference scheme, in order to enforce the Robin boundary condition.

An issue associated with the Robin-Neumann transmission conditions is the introduction of a numerical parameter — denoted as α_f in this work as well as some previous papers — which arises from the linear combination of the kinematic and dynamic interface conditions. The value of α_f has no impact to the mathematical model, as long as it is nonzero. However, its impact to the numerical properties of partitioned solution procedures requires attention and investigation. Previous studies have revealed, primarily through numerical experiments, that different values of α_f may either improve or deteriorate numerical stability. Nonetheless, how to choose an appropriate value for a specific problem is still an open question (cf. [19, 24, 25]). On the other hand, the effect of α_f on numerical accuracy is largely unknown in the literature. It is reasonable to speculate that this effect may be significant, given that when α_f approaches zero, the kinematic interface condition is simply lost. Therefore, in this work we analyze both the stability and the accuracy properties of a partitioned procedure with Robin-

Neumann transmission conditions. Specifically, we do this in two ways: both numerically using the developed embedded Robin boundary method and the well-known Turek and Hron benchmark problem, and analytically by considering a simplified two-dimensional model problem.

The remainder of this paper is organized as follows. Section 2.2 specifies the context and governing equations of the FSI problem and Robin-Neumann based partitioned procedures, referred to as Robin-Neumann schemes hereafter. Section 2.3 presents the aforementioned embedded Robin boundary method and numerical experiments. Section 2.4 presents a mathematical analysis of the stability and accuracy properties of the Robin transmission condition, independent of specific spatial discretization schemes (e.g., finite element, finite difference, etc.) and time integrators (explicit, implicit), using a 2D model problem involving incompressible, inviscid flow and an Euler-Bernoulli beam. Finally, a few concluding remarks are given in Section 2.5.

2.2 Mathematical model

2.2.1 Fluid and structural governing equations

We consider the interaction of a two-dimensional (2-D) incompressible viscous fluid flow with a deformable structure. A typical mathematical model for the coupled system involves fluid governing equations defined in $\Omega_f^* \subset \mathbb{R}^2$ and structural governing equations defined

in $\Omega_s \subset \mathbb{R}^2$ (Figure 2.1). In the setting of an Eulerian embedded boundary method, the subspace covered by the structure is regarded as a fictitious fluid domain region. Therefore, an extended, time-invariant fluid domain can be defined as $\Omega_f = \Omega_f^* \cup \Omega_s$. The fluid-structure interface Σ (also referred to as the embedded interface) is the wetted surface of the structure, which is defined by $\Sigma = \partial\Omega_f^* \cap \partial\Omega_s$. Here, ∂ denotes domain boundary. We further assume that the fluid is Newtonian and laminar, hence its dynamics is governed by the following incompressible Navier-Stokes (N-S) equations.

$$\mathscr{F}(\mathbf{U}, P) = 0 := \begin{cases} \nabla \cdot \mathbf{U} = 0 & \text{in } \Omega_f \qquad (2.1a) \\ \dfrac{\partial \mathbf{U}}{\partial t} + \mathbf{U} \cdot \nabla \mathbf{U} - \nu \Delta \mathbf{U} + \dfrac{1}{\rho_f} \nabla P = 0 & \text{in } \Omega_f \qquad (2.1b) \end{cases}$$

with intrinsic boundary conditions on the outer boundaries of the fluid domain, i.e. $\partial\Omega_f = \partial\Omega_f^* \setminus \Sigma$

$$\mathscr{B}(\mathbf{U}, P) = 0 \qquad \text{on } \partial\Omega_f \qquad (2.2)$$

where $t \in [0, \infty)$ denotes time, ρ_f is the fluid density, $\mathbf{U} = (u, v)^T$ is fluid velocity vector, P denotes the fluid pressure and ν the kinematic viscosity. For problems of our interest, several types of Dirichlet and/or Neumann boundary conditions may be applied on $\partial\Omega_f^* \setminus \Sigma$, including non-slip wall, velocity inlet, and the "*do nothing*" outflow boundary conditions.

The structure is considered to be elastic, and subjected to large deformation. Its equation

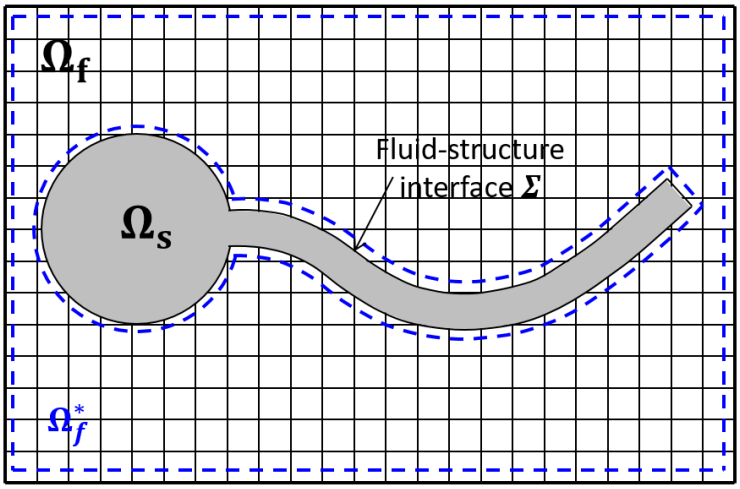

Figure 2.1: Configuration of fluid-structure coupled problem

of dynamic equilibrium is given by

$$\mathscr{S}(\mathbf{d}(\mathbf{X},t)) = 0 := \rho_s(\mathbf{X},t)\frac{\partial^2 \mathbf{d}(\mathbf{X},t)}{\partial t^2} - \nabla\cdot\left(J^{-1}\mathbf{F}\cdot\mathbf{S}\cdot\mathbf{F}^T\right) - \rho_s(\mathbf{X},t)\,\mathbf{b}(\mathbf{X},t) = 0 \qquad \text{in}\,\Omega_s, \tag{2.3}$$

where $\mathbf{X}$ denotes the material coordinate, $\mathbf{d}$ denotes the displacement vector of the structure, ρ_s is the structure density, $\mathbf{S}$ is the second Piola-Kirchhoff (PK2) stress tensor, $\mathbf{F}$ is the deformation gradient, $\mathbf{b}$ denotes the body force per unit mass, $J = \det\mathbf{F}$. In this work, we consider a Saint Venant-Kirchhoff constitutive law characterized by two independent Lamé constants λ_s, μ_s and the Green-Lagrange strain $\mathbf{E}$, which is given by

$$\mathbf{S} = \lambda_s tr(\mathbf{E})\mathbf{I} + 2\mu_s\mathbf{E}. \tag{2.4}$$

where $\mathbf{I}$ is the identity matrix and $\mathbf{E} = \frac{1}{2}(\mathbf{F}^T\cdot\mathbf{F} - \mathbf{I})$.

The interaction between the fluid and the structure is governed by the interface conditions. We assume the fluid-structure interface to be impermeable, and thus, the fluid and structural governing equations are coupled by a kinematic interface condition, i.e. the continuity of velocity (Eq. (2.5a)), and a dynamic interface condition, i.e. the continuity of normal stress (Eq. (2.5b))

$$\mathbf{U} = \frac{\partial \mathbf{d}}{\partial t} \qquad \text{on } \Sigma \tag{2.5a}$$

$$\sigma_f \mathbf{n} = \sigma_s \mathbf{n} \qquad \text{on } \Sigma \tag{2.5b}$$

where $\mathbf{n}$ denotes the unit normal pointing towards the structure. σ_f denotes the fluid stress tensor, and is defined as $\sigma_f = -P\mathbf{I} + 2\mu_f \epsilon$, where ϵ denotes the strain rate tensor, and μ_f is the dynamic viscosity. σ_s is Cauchy stress tensor of the structure, which can be related to PK2 stress by

$$\sigma_s = J^{-1}\mathbf{F} \cdot \mathbf{S} \cdot \mathbf{F}^T.$$

Combining the governing equations and the transmission conditions, the 2-D fluid-structure coupled problem can be stated as follows.

Find $\mathbf{d} = \mathbf{d}(x, y, t)$, $\mathbf{U} = \mathbf{U}(x, y, t)$, $P = P(x, y, t)$ *such that*

$$
\begin{cases}
\nabla \cdot \mathbf{U} = 0 & \text{in } \Omega_f \quad (2.6a) \\
\dfrac{\partial \mathbf{U}}{\partial t} + \mathbf{U} \cdot \nabla \mathbf{U} - \nu \Delta \mathbf{U} + \dfrac{1}{\rho_f} \nabla P = 0 & \text{in } \Omega_f \quad (2.6b) \\
\mathscr{B}(\mathbf{U}, P) = 0 & \text{on } \partial\Omega_f^* \setminus \partial\Sigma \quad (2.6c) \\
\rho_s \dfrac{\partial^2 \mathbf{d}}{\partial t^2} - \nabla \cdot \left(J^{-1} \mathbf{F} \cdot \mathbf{S} \cdot \mathbf{F}^T \right) - \rho_s \mathbf{b} = 0 & \text{in } \Omega_s \quad (2.6d) \\
\mathbf{U} = \dfrac{\partial \mathbf{d}}{\partial t} & \text{on } \Sigma \quad (2.6e) \\
\sigma_f \mathbf{n} = \sigma_s \mathbf{n} & \text{on } \Sigma \quad (2.6f)
\end{cases}
$$

Equations (2.6) can be used to model FSI problems involving low speed flow and flexible, reconfigurable and/or morphing structures subjected to large deformation, where fluid compressibility is negligible and geometric nonlinearity of the structure needs to be accounted for. Examples include, but are not limited to, flapping wing miniature air vehicle, underwater flexible-fin propulsion, and blood flow in arteries.

2.2.2 Robin-Neumann transmission conditions

In this work, the numerical solution of Eqs. (2.6) is based on the partitioned procedure, in which existing CFD and CSD solvers are employed for the separate evolution of the two subsystems in a staggered manner. The conventional Dirichlet-Neumann partitioned procedure

splits the coupled system into a fluid sub-system with the kinematic transmission condition (i.e. Eq. (2.6e)) and a structural sub-system with the dynamic transmission condition (i.e. Eq. (2.6f)). Nonetheless, we re-write Eqs. (2.6e) and (2.6f) as a pair of Robin-Neumann transmission conditions, i.e.

$$\alpha_f \rho_s \tau_s \frac{D\mathbf{U}}{Dt} + \sigma_f \mathbf{n} = \alpha_f \rho_s \tau_s \frac{\partial^2 \mathbf{d}}{\partial t^2} + \sigma_s \mathbf{n} \qquad \text{on } \Sigma \tag{2.7a}$$

$$\sigma_f \mathbf{n} = \sigma_s \mathbf{n} \qquad \text{on } \Sigma \tag{2.7b}$$

where $D/Dt = \partial/\partial t + \mathbf{U}\cdot\nabla$ is the total derivative, $\alpha_f > 0$ is a non-dimensional coefficient, and τ_s denotes the thickness of the structure. We note that in this work, as well as some previous studies (e.g., [22, 21]), the Robin condition combines the time derivative of Eq. (2.6e) with Eq. (2.6f), whereas in some other studies (e.g., [19]), the Robin condition directly combines the two equations.

Equipped with the Robin-Neumann transmission conditions, the fluid and structural sub-systems can be formulated by

$$\text{Fluid:} \begin{cases} \mathscr{F}(\mathbf{U}, P) = 0 & \text{in } \Omega_f \quad (2.8a) \\ \mathscr{B}(\mathbf{U}, P) = 0 & \text{on } \partial\Omega_f^* \setminus \Sigma \quad (2.8b) \\ \alpha_f \rho_s \tau_s \dfrac{D\mathbf{U}}{Dt} + \sigma_f \mathbf{n} = \alpha_f \rho_s \tau_s \dfrac{\partial^2 \mathbf{d}}{\partial t^2} + \sigma_s \mathbf{n} & \text{on } \Sigma \quad (2.8c) \end{cases}$$

$$\text{Structure:} \begin{cases} \mathscr{S}(\mathbf{d}) = 0 & \text{in } \Omega_s \quad (2.8d) \\ \sigma_s \mathbf{n} = \sigma_f \mathbf{n} & \text{on } \Sigma \quad (2.8e) \end{cases}$$

2.3 Computational framework

2.3.1 Partitioned solution procedure

To couple the fluid and structural sub-systems in Eqs.(2.8), two strategies are considered in this work. One is explicit coupling, which solves the two sub-systems once per time step. The other one is implicit coupling, which solves the two sub-systems iteratively in the fashion of fixed-point iteration. Both schemes require solving the following equations to advance the system from time t^n to t^{n+1}.

$$\text{Fluid:}\begin{cases} \mathscr{F}(\mathbf{U}_{k+1}^{n+1}, P_{k+1}^{n+1}) = 0 & \text{in } \Omega_f \quad (2.9a) \\ \mathscr{B}(\mathbf{U}_{k+1}^{n+1}, P_{k+1}^{n+1}) = 0 & \text{on } \partial\Omega_f^* \setminus \Sigma \quad (2.9b) \\ \alpha_f \rho_s \tau_s \dfrac{D\mathbf{U}_{k+1}^{n+1}}{Dt} + \sigma_{f,k+1}^{n+1}\mathbf{n} = \alpha_f \rho_s \tau_s \left(\dfrac{\partial^2 \mathbf{d}}{\partial t^2}\right)_k^{n^\bullet} + \sigma_{s,k}^{n^\bullet}\mathbf{n} & \text{on } \Sigma \quad (2.9c) \end{cases}$$

$$\text{Structure:}\begin{cases} \mathscr{S}(\mathbf{d}_{k+1}^{n+1}) = 0 & \text{in } \Omega_s \quad (2.9d) \\ \sigma_{s,k+1}^{n+1}\mathbf{n} = \sigma_{f,k}^{n^\bullet}\mathbf{n} & \text{on } \Sigma \quad (2.9e) \end{cases}$$

where k is the index of sub-iteration in the case of implicit coupling. Also,

$$n^\bullet = \begin{cases} n, & \text{if } k = 0, \\ n+1, & \text{otherwise.} \end{cases}$$

In other words, when $k = 0$, the transmission conditions are enforced using the solutions from the previous time step. Specifically, the fluid sub-system is advanced to t^{n+1} using the structural acceleration and normal stress on Σ at t^n, and the structure is subjected to fluid traction computed at t^n. In the case of implicit coupling, additional sub-iterations are conducted, with $k = 1,\ 2,\ .\ .\ .$ When $k > 0$, the latest solutions from sub-iteration k, which are evaluated at t^{n+1}, are exchanged between the fluid and structural solvers, leading to a Gauss-Seidel type iteration.

2.3.2 Numerical methods for solving the fluid sub-system

A finite-difference project method

In the fluid sub-system, the incompressible N-S equations are solved using a finite-difference projection method on a cell-centered, collocated Cartesian grid. This method can be summarized in six steps.

- **Step 1**: The momentum equation (Eq.(2.1b)) is discretized by

$$(\mathbf{I} - \eta_2 \nu \mathbf{L})(\mathbf{I} - \eta_1 \nu \mathbf{L})\mathbf{U}_{k+1}^{*,n+1} = (\mathbf{I} + \eta_3 \nu \mathbf{L})\mathbf{U}^n - \Delta t(\mathbf{I} + \eta_4 \nu \mathbf{L}) \left(\mathbf{N}^{n+\frac{1}{2}} + \frac{1}{\rho_f} \mathbf{G} P^{n-\frac{1}{2}} \right), \tag{2.10}$$

  where $\mathbf{U}_{k+1}^{*,n+1}$ denotes the unknown intermediate velocity[1], defined in the extended CFD domain Ω_f. Δt is the time step size, $\mathbf{L}$ and $\mathbf{G}$ denote the discrete Laplace operator

[1]Hereafter, $\mathbf{U}$ and $\mathbf{P}$ are used to denote the spatially discretized velocity and pressure fields.

and the discrete gradient operator, respectively. $\mathbf{I}$ denotes the identity operator. $\mathbf{N}^{n+\frac{1}{2}}$ represents the explicit, second-order Godunov approximation of the nonlinear advection term $[(\mathbf{U}\cdot\nabla)\mathbf{U}]^{n+\frac{1}{2}}$ [26]. η_i, $i = 1, 2, 3, 4$, are numerical parameters introduced by Twizell *et al.* [27] to improve numerical stability.

- **Step 2**: The intermediate velocity $\mathbf{U}_{k+1}^{*,n+1}$ is projected onto a space that satisfies the divergence-free constraint (i.e. Eq. (2.1a)), by solving a pressure-Poisson equation, which, in discrete form, reads

$$\mathbf{L}(\phi_{k+1}^{n+1}) = \mathbf{D}\mathbf{U}_{k+1}^{*,n+1}, \tag{2.11}$$

where ϕ_{k+1}^{n+1} is the scalar potential in Helmholtz decomposition, and $\mathbf{D}$ denotes the discrete divergence operator. Along the boundaries of the fluid domain other than the fluid-structure interface, $\mathbf{n}\cdot\nabla\phi = 0$ is specified in the regions where $\mathbf{U}^*$ is subjected to a Dirichlet boundary condition, while $\phi = 0$ is specified where $\mathbf{U}^*$ is subjected to a "*do nothing*" boundary condition.

- **Step 3**: The velocity at time t^{n+1} is obtained by

$$\mathbf{U}_{k+1}^{n+1} = \mathbf{U}_{k+1}^{*,n+1} - \mathbf{G}\phi_{k+1}^{n+1}. \tag{2.12}$$

- **Step 4**: Following Griffith *et al.* [23], the momentum equation is solved again without the pressure gradient term, i.e.

$$(\mathbf{I} - \eta_2 \nu \mathbf{L})(\mathbf{I} - \eta_1 \nu \mathbf{L})\widetilde{\mathbf{U}}_{k+1}^{*,n+1} = (\mathbf{I} + \eta_3 \nu \mathbf{L})\mathbf{U}^n - \Delta t(\mathbf{I} + \eta_4 \nu \mathbf{L})\mathbf{N}^{n+\frac{1}{2}}. \tag{2.13}$$

- **Step 5**: Similar to Step 2, the intermediate velocity $\widetilde{\mathbf{U}}_{k+1}^{*,n+1}$ is projected, i.e.

$$\mathbf{L}(\widetilde{\phi}_{k+1}^{n+1}) = \mathbf{D}\widetilde{\mathbf{U}}_{k+1}^{*,n+1}. \tag{2.14}$$

- **Step 6**: Finally, the pressure at time $t^{n+\frac{1}{2}}$ is obtained as

$$P_{k+1}^{n+\frac{1}{2}} = \frac{\rho_f}{\Delta t}(\mathbf{I} + \eta_4 \nu \mathbf{L})^{-1}(\mathbf{I} - \eta_2 \nu \mathbf{L})(\mathbf{I} - \eta_1 \nu \mathbf{L})\widetilde{\phi}_{k+1}^{n+1}. \tag{2.15}$$

In this work, the discrete operators $\mathbf{G}$ and $\mathbf{D}$ are constructed using a second-order central difference scheme. The Laplace operator is constructed using a five-point central difference scheme [26]. Steps 4 to 6 are based on the work by Griffith *et al.* [23], for suppressing spurious oscillations associated with embedded/immersed boundary methods.

An embedded Robin boundary method

Embedded/immersed boundary methods simplify a number of issues associated with the geometry and motion of the fluid-structure interface. Nonetheless, the fact that the CFD

grid does not conform to the wetted surface of the structure complicates the treatment of interface conditions. In order to enforce the Robin transmission condition (Eq. (2.9c)), the proper boundary conditions for the auxiliary variables — i.e. $\mathbf{U}^*$, ϕ, $\widetilde{\mathbf{U}}^*$, and $\widetilde{\phi}$ — need to be specified. To this end, we first discretize Eq. (2.9c) in time by

$$\alpha_f \rho_s \tau_s \left[\frac{\mathbf{U}_{k+1}^{n+1} - \mathbf{U}^n}{\Delta t} + (\mathbf{U} \cdot \nabla \mathbf{U})_k^{n^\bullet} \right] + \sigma_{f,k+1}^{n+1} \mathbf{n} = \alpha_f \rho_s \tau_s \left(\frac{\partial^2 \mathbf{d}}{\partial t^2} \right)_k^{n^\bullet} + \sigma_{s,k}^{n^\bullet} \mathbf{n} \qquad \text{on } \Sigma, \quad (2.16)$$

where the structural acceleration $\left(\partial^2 \mathbf{d}/\partial t^2\right)$ is computed by the structural solver, then transferred to the fluid solver. Then, we propose to enforce Eq. (2.16) using an operator splitting method, in the same fashion as the projection method. Specifically,

$$\mathbf{U}_{k+1}^{*,n+1} = \mathbf{U}^n + \frac{\Delta t}{\alpha_f \rho_s \tau_s} \left\{ -\sigma_{f,k+1}^{*,n+1} \mathbf{n} + \alpha_f \rho_s \tau_s \left(\frac{\partial^2 \mathbf{d}}{\partial t^2} \right)_k^{n^\bullet} + \sigma_{s,k}^{n^\bullet} \mathbf{n} - \alpha_f \rho_s \tau_s \left(\mathbf{U} \cdot \nabla \mathbf{U} \right)_k^{n^\bullet} \right\}, \quad (2.17a)$$

$$- \frac{\alpha_f \rho_s \tau_s}{\Delta t} \left(\frac{\partial \phi}{\partial \mathbf{n}} \right)_{k+1}^{n+1} + \hat{\sigma}_{f,k+1}^{n+1} \mathbf{n} \cdot \mathbf{n} = 0. \quad (2.17b)$$

In this work, we enforce Eq. (2.17a) in Steps 1 and 4, and Eq. (2.17b) in Steps 2 and 5. It is notable that in Eqs (2.17a) and (2.17b), the fluid stress tensors $\sigma_{f,k+1}^{*,n+1}$ and $\hat{\sigma}_{f,k+1}^{n+1}$ are unknown. We approximate their values by

$$(\sigma_{f,k+1}^{*,n+1})_{i,j} \approx -\theta P^{n-\frac{1}{2}} \delta_{i,j} + \mu \left(\frac{\partial \mathbf{U}_{k,i}^{*,n^\bullet}}{\partial x_j} + \frac{\partial \mathbf{U}_{k,j}^{*,n^\bullet}}{\partial x_i} \right) \qquad i,j = 1,2$$

$$(\hat{\sigma}_{f,k+1}^{n+1})_{i,j} \approx -\frac{\rho_f}{\Delta t} \phi_{k+1}^{n+1} \delta_{i,j} - \mu \left[\frac{\partial \left(\partial \phi_k^{n^\bullet} / \partial x_i \right)}{\partial x_j} + \frac{\partial \left(\partial \phi_k^{n^\bullet} / \partial x_j \right)}{\partial x_i} \right] \qquad i,j = 1,2$$

where θ is 1 for Step 1, and 0 for Step 4. With this approximation, Eq. (2.17a) becomes a

Dirichlet boundary condition, whereas Eq. (2.17b) remains a Robin boundary condition.

To enforce Eq. (2.17a) in Steps 1 and 4 of the projection method, we apply the ghost-cell method proposed by Tseng *et al.* [28], despite that their work focused on fluid flows with fixed boundaries. Specifically, the ghost cells are defined to be the cells in the CFD mesh that are covered by the structure and adjacent to the interface — neighboring at least one cell on the fluid side. By specifying a *fictitious* fluid state in each ghost cell, we can implicitly impose the interface condition. The procedure can be summarized in three steps.

(1) Given the position of the wetted surface of the structure, identify the ghost cells. Then, Eq. (2.10) in Step 1 (similarly, Eq. (2.13) in Step 4) can be re-written in the following compact form

$$\begin{bmatrix} \mathbf{A}_{11} & \mathbf{A}_{12} \\ \mathbf{A}_{21} & \mathbf{A}_{22} \end{bmatrix} \begin{bmatrix} \mathbf{U}^*_{real} \\ \mathbf{U}^*_{ghost} \end{bmatrix} = \begin{bmatrix} \mathbf{b}_{real} \\ \mathbf{b}_{ghost} \end{bmatrix}, \tag{2.18}$$

where the subscripts *real* and *ghost* denote the real and ghost cells in the extended CFD domain.

(2) Specify the intermediate velocity at each ghost cell with a value determined by the local reconstruction scheme proposed in [28], which can be written in a compact form as

$$\mathbf{U}^*_{ghost} = \mathbf{f}\Big(\mathbf{U}^*_{real,k}, \Big(\frac{\partial^2 \mathbf{d}}{\partial t^2}\Big)_k, \sigma_{s,k}, \mathbf{U}_k, \mathbf{U}^n, P^{n-\frac{1}{2}}\Big). \tag{2.19}$$

(3) Solve

$$\mathbf{A}_{11}\mathbf{U}^*_{real} = \mathbf{b}_{real} - \mathbf{A}_{12}\mathbf{f}\Big(\mathbf{U}^*_{real,k}, \Big(\frac{\partial^2 \mathbf{d}}{\partial t^2}\Big)_k, \sigma_{s,k}, \mathbf{U}_k, \mathbf{U}^n, P^{n-\frac{1}{2}}\Big), \tag{2.20}$$

and obtain the intermediate velocity $\mathbf{U}^*_{k+1}$ in Step 1 (similarly, $\widetilde{\mathbf{U}}^*_{k+1}$ in Step 4).

To enforce the Robin boundary condition, i.e. Eq. (2.17b), in Steps 2 and 5 of the projection method, we employ an asymmetric finite difference scheme, which can be considered as an application of the general Poisson equation solver proposed by Jomaa *et al.* [29, 30] to the context of CFD and FSI. The procedure can be summerized in three steps.

(1) Given the position of the wetted surface of the structure, identify the fluid cells adjacent to the embedded boundary (marked with "●" in Figure 2.2).

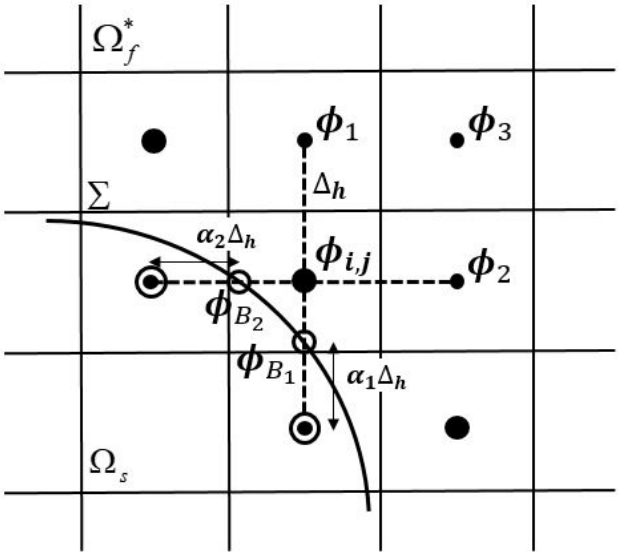

Figure 2.2: An illustration of the asymmetric finite different stencil for discretizing the Poisson equation on fluid cells adjacent to the embedded boundary.

(2) For the *boundary cells* identified in (1), modify the discrete Laplace operator in Steps 2 and 5 of the projection method by applying an asymmetric finite difference scheme.

For example, for cell (i,j) in Figure 2.2,

$$\begin{aligned}\mathbf{L}\left(\phi_{k+1}^{n+1}\right)_{i,j} = \frac{2}{\Delta_h^2}\Bigg[&\frac{\phi_1}{2-\alpha_1}+\frac{\phi_2}{2-\alpha_2}+\frac{\phi_{B_1}}{(1-\alpha_1)(2-\alpha_1)}\\ &+\frac{\phi_{B_2}}{(1-\alpha_2)(2-\alpha_2)}-\frac{2-\alpha_1-\alpha_2}{(1-a_1)(1-a_2)}\phi_{i,j}\Bigg]_{k+1}^{n+1},\end{aligned} \tag{2.21}$$

where Δ_h denotes the Cartesian grid size. α_1 and α_2 are non-dimensional geometric parameters, providing the distance from (i,j) to two points on the interface, B_1 and B_2.

ϕ_{B_1} and ϕ_{B_2} denote the values of ϕ at B_1 and B_2, which need to be determined using the Robin boundary condition. Specifically, at B_1 and B_2, Eq. (2.17b) becomes

$$\begin{cases}\left(\dfrac{\partial\phi_{B_1}}{\partial\mathbf{n}}\right)_{k+1}^{n+1}+\dfrac{\rho_f}{\alpha_f\rho_s\tau_s}\phi_{B_1,k+1}^{n+1}=D_{B_1}, & \text{(2.22a)}\\ \left(\dfrac{\partial\phi_{B_2}}{\partial\mathbf{n}}\right)_{k+1}^{n+1}+\dfrac{\rho_f}{\alpha_f\rho_s\tau_s}\phi_{B_2,k+1}^{n+1}=D_{B_2}, & \text{(2.22b)}\end{cases}$$

where D_{B_1} and D_{B_2} are given by

$$D_{B_1} = -\frac{\Delta t}{\alpha_f\rho_s\tau_s}\left[2\mu\frac{\partial^2\phi_k^{n^\bullet}}{\partial x^2}n_x^2+4\mu\frac{\partial^2\phi_k^{n^\bullet}}{\partial x\partial y}n_xn_y+2\mu\frac{\partial^2\phi_k^{n^\bullet}}{\partial y^2}n_y^2\right]\Bigg|_{B_1}, \tag{2.23}$$

$$D_{B_2} = -\frac{\Delta t}{\alpha_f\rho_s\tau_s}\left[2\mu\frac{\partial^2\phi_k^{n^\bullet}}{\partial x^2}n_x^2+4\mu\frac{\partial^2\phi_k^{n^\bullet}}{\partial x\partial y}n_xn_y+2\mu\frac{\partial^2\phi_k^{n^\bullet}}{\partial y^2}n_y^2\right]\Bigg|_{B_2}. \tag{2.24}$$

We discretize $\partial\phi_{B_1}/\partial\mathbf{n}$ and $\partial\phi_{B_2}$ in Eq. (2.22) again using an asymmetric finite difference scheme, i.e.

$$\begin{aligned}\frac{\partial \phi_{B_1}}{\partial \mathbf{n}} =& \frac{n_{y1}}{\Delta_h}\Bigg\{ \left[\left(\frac{1}{1-\alpha_1}+\frac{2-\alpha_2}{1-\alpha_2}\right)-\left(2-\alpha_1-\frac{n_{x1}}{n_{y1}}\right)\frac{2-\alpha_1}{1-\alpha_1}\right]\phi_{i,j} \\ &- \left[\frac{n_{x1}}{n_{y1}}\frac{3-2\alpha_1}{(1-\alpha_1)(2-\alpha_1)}\right]\phi_{B_1} - \frac{1}{(1-\alpha_2)(2-\alpha_2)}\phi_{B_2} \\ &+ \left(\frac{3-2\alpha_2}{2-\alpha_2}-\alpha_1\right)\phi_1 + \left[\left(2-\alpha_1-\frac{n_{x1}}{n_{y1}}\right)\frac{1-\alpha_1}{2-\alpha_1}\right]\phi_2 - (1-\alpha_1)\phi_3\Bigg\} \\ \equiv& C_{11}\phi_{i,j} + C_{12}\phi_{B_1} + C_{13}\phi_{B_2} + C_{14}\phi_1 + C_{15}\phi_2 + C_{16}\phi_3,\end{aligned} \tag{2.25}$$

$$\begin{aligned}\frac{\partial \phi_{B_2}}{\partial \mathbf{n}} =& \frac{n_{x2}}{\Delta_h}\Bigg\{ \left[\left(\frac{1}{1-\alpha_2}+\frac{2-\alpha_1}{1-\alpha_1}\right)-\left(2-\alpha_2-\frac{n_{y2}}{n_{x2}}\right)\frac{2-\alpha_2}{1-\alpha_2}\right]\phi_{i,j} \\ &- \left[\frac{n_{y2}}{n_{x2}}\frac{3-2\alpha_2}{(1-\alpha_2)(2-\alpha_2)}\right]\phi_{B_2} - \frac{1}{(1-\alpha_1)(2-\alpha_1)}\phi_{B_1} \\ &+ \left[\left(2-\alpha_2-\frac{n_{y2}}{n_{x2}}\right)\frac{1-\alpha_2}{2-\alpha_2}\right]\phi_1 + \left(\frac{3-2\alpha_1}{2-\alpha_1}-\alpha_2\right)\phi_2 - (1-\alpha_2)\phi_3\Bigg\} \\ \equiv& C_{21}\phi_{i,j} + C_{22}\phi_{B_1} + C_{23}\phi_{B_2} + C_{24}\phi_1 + C_{25}\phi_2 + C_{26}\phi_3.\end{aligned} \tag{2.26}$$

Substituting Eqs. (2.25) and (2.26) into Eq. (2.22) yields a 2×2 linear system for ϕ_{B_1} and ϕ_{B_2}, i.e.

$$\begin{bmatrix} C_{12}+\dfrac{\rho_f}{\alpha_f\rho_s\tau_s} & C_{13} \\ C_{22} & C_{23}+\dfrac{\rho_f}{\alpha_f\rho_s\tau_s}\end{bmatrix}\begin{bmatrix}\phi_{B_1}\\ \phi_{B_2}\end{bmatrix} = \begin{bmatrix} D_{B_1}-C_{11}\phi_{i,j}-C_{14}\phi_1-C_{15}\phi_2-C_{16}\phi_3 \\ D_{B_2}-C_{21}\phi_{i,j}-C_{24}\phi_1-C_{25}\phi_2-C_{26}\phi_3\end{bmatrix}. \tag{2.27}$$

By solving this linear system, ϕ_{B_1} and ϕ_{B_2} can be expressed as linear functions of ϕ_1,

ϕ_2, ϕ_3 and $\phi_{i,j}$, i.e.

$$\phi^{n+1}_{B_1,k+1} = M_{10} + M_{11}\phi_1 + M_{12}\phi_2 + M_{13}\phi_3 + M_{14}\phi_{i,j}, \tag{2.28}$$

$$\phi^{n+1}_{B_2,k+1} = M_{20} + M_{21}\phi_1 + M_{22}\phi_2 + M_{23}\phi_3 + M_{24}\phi_{i,j}, \tag{2.29}$$

where

$$\begin{aligned}
M_{10} &= \left[(C_{23} + \frac{\rho_f}{\alpha_f\rho_s\tau_s})D_{B_1} - C_{13}D_{B_2}\right] \Big/ G_1,\\
M_{20} &= \left[C_{22}D_{B_1} - \left(C_{12} + \frac{\rho_f}{\alpha_f\rho_s\tau_s}\right)D_{B_2}\right] \Big/ G_2,\\
M_{11} &= \left[C_{13}C_{24} - \left(C_{23} + \frac{\rho_f}{\alpha_f\rho_s\tau_s}\right)C_{14}\right] \Big/ G_1,\\
M_{21} &= \left[-C_{22}C_{14} + \left(C_{12} + \frac{\rho_f}{\alpha_f\rho_s\tau_s}\right)C_{24}\right] \Big/ G_2,\\
M_{12} &= \left[C_{13}C_{25} - \left(C_{23} + \frac{\rho_f}{\alpha_f\rho_s\tau_s}\right)C_{15}\right] \Big/ G_1,\\
M_{22} &= \left[-C_{22}C_{15} + \left(C_{12} + \frac{\rho_f}{\alpha_f\rho_s\tau_s}\right)C_{25}\right] \Big/ G_2,\\
M_{13} &= \left[C_{13}C_{26} - \left(C_{23} + \frac{\rho_f}{\alpha_f\rho_s\tau_s}\right)C_{16}\right] \Big/ G_1,\\
M_{23} &= \left[-C_{22}C_{16} + \left(C_{12} + \frac{\rho_f}{\alpha_f\rho_s\tau_s}\right)C_{26}\right] \Big/ G_2,\\
M_{14} &= \left[C_{13}C_{21} - \left(C_{23} + \frac{\rho_f}{\alpha_f\rho_s\tau_s}\right)C_{11}\right] \Big/ G_1,\\
M_{24} &= \left[-C_{22}C_{11} + \left(C_{12} + \frac{\rho_f}{\alpha_f\rho_s\tau_s}\right)C_{21}\right] \Big/ G_2,\\
G_1 &= \frac{(C_{12}\alpha_f\rho_s\tau_s + \rho_f)(C_{23}\alpha_f\rho_s\tau_s + \rho_f)}{(\alpha_f\rho_s\tau_s)^2} - C_{13}C_{22},\\
G_2 &= C_{13}C_{22} - \frac{(C_{12}\alpha_f\rho_s\tau_s + \rho_f)(C_{23}\alpha_f\rho_s\tau_s + \rho_f)}{(\alpha_f\rho_s\tau_s)^2}.
\end{aligned} \tag{2.30}$$

Substituting Eqs. (2.28) and (2.29) into Eq. (2.21) yields

$$\begin{aligned}
\mathbf{L}\left(\phi_{k+1}^{n+1}\right)_{i,j} = \Bigg\{ & \left[\frac{M_{10}}{(1-\alpha_1)(2-\alpha_1)} + \frac{M_{20}}{(1-\alpha_2)(2-\alpha_2)}\right] \\
& + \left[\frac{1}{2-\alpha_1} + \frac{M_{11}}{(1-\alpha_1)(2-\alpha_1)} + \frac{M_{21}}{(1-\alpha_2)(2-\alpha_2)}\right]\phi_1 \\
& + \left[\frac{1}{2-\alpha_2} + \frac{M_{12}}{(1-\alpha_1)(2-\alpha_1)} + \frac{M_{22}}{(1-\alpha_2)(2-\alpha_2)}\right]\phi_2 \\
& + \left[\frac{M_{13}}{(1-\alpha_1)(2-\alpha_1)} + \frac{M_{23}}{(1-\alpha_2)(2-\alpha_2)}\right]\phi_3 \\
& + \left[\frac{M_{14}}{(1-\alpha_1)(2-\alpha_1)} + \frac{M_{24}}{(1-\alpha_2)(2-\alpha_2)} - \frac{2-\alpha_1-\alpha_2}{(1-\alpha_1)(1-\alpha_2)}\right]\phi_{i,j} \Bigg\}_{k+1}^{n+1} \frac{2}{\Delta_h^2}
\end{aligned} \tag{2.31}$$

(3) Solve the resulting linear system in Step 2 (similarly, Step 5) of the projection method for ϕ_{k+1}^{n+1} (similarly, $\widetilde{\phi}_{k+1}^{n+1}$).

2.3.3 Numerical methods for the structural sub-system

In this work, we consider the representative case of a geometrically nonlinear beam in 2-D, and semi-discretize the governing equation Eq. (2.9d) using the continuum-based (CB) beam element [31]. Specifically, the beam is modeled as a set of adjoining quadrilateral beam elements (Figure 2.3). The intersection of each two adjacent elements is called a *fiber*, whose midpoint is defined as a master node. The motion of the beam is described by the motion of master nodes characterized by the location $\mathbf{x}$ and the rotation θ. A pair of slave nodes are defined at the top and bottom end of a fiber, identified by superscript "+" and "−", respectively. The CB beam element relies on two assumptions: (1) the fibers are straight and inextensible; and (2) the beam is in a state of plane stress.

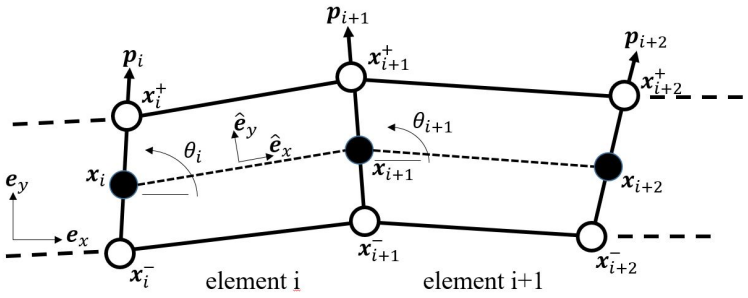

Figure 2.3: A schematic drawing of two adjoining CB beam element.

According to the first assumption, the positions of two slave nodes associated with master node i are given by

$$\mathbf{x}_i^+ = \mathbf{x}_i + \frac{h_i}{2}\mathbf{p}_i, \qquad \mathbf{x}_i^- = \mathbf{x}_i - \frac{h_i}{2}\mathbf{p}_i, \tag{2.32}$$

where h_i denotes the thickness of the beam at node i and $\mathbf{p}_i = \cos\theta_i \mathbf{e}_x + \sin\theta_i \mathbf{e}_y$ is the unit vector along the fiber. Eq. (2.32) enables the transformation of nodal forces and element matrices evaluated at the slave nodes to that at the master nodes. The plane stress assumption can be imposed while computing the internal force by setting the normal stress perpendicular to the axis of the beam to be zero and modifying the Green-Lagrange strain. In summary, the equation of motion for one element can be written as

$$\mathbf{M}_e \ddot{\mathbf{u}}_e^m + \mathbf{T}_e^T \mathbf{M}_e^s \dot{\mathbf{T}}_e \dot{\mathbf{u}}_e^m + \mathbf{f}^{int} = \mathbf{f}^{ext}, \tag{2.33}$$

where $\mathbf{u}_e^m = [\mathbf{x}_i, \theta_i, \mathbf{x}_{i+1}, \theta_{i+1}]^T$ denotes the motion of master nodes in element i, M_e is the mass matrix, $\mathbf{T}_e$ is the transformation matrix, $\mathbf{M}_e^s$ is the mass matrix for the quadrilaterial continuum element. $\mathbf{f}^{int}$ and $\mathbf{f}^{ext}$ denote the internal and external nodal forces, respectively.

The time integration of Eq. (2.33) is done using the Newmark-β algorithm. We refer the readers to [32] for additional details.

2.3.4 Numerical experiment: Flow past a cylinder

The fluid solver is first applied to simulate a laminar channel flow over a circular cylinder [33]. The geometry of this benchmark problem is shown in Figure 2.4. A uniform grid with 500×100 cells is used to discretize the spatial domain, including the region occupied by the cylinder. The velocity at the inlet is specified as

$$u(0, y, t) = \frac{6y(H - y)}{H^2}\,\mathrm{m/s}, \qquad v(0, y, t) = 0\,\mathrm{m/s}, \tag{2.34}$$

which yields a Reynolds number of 100.

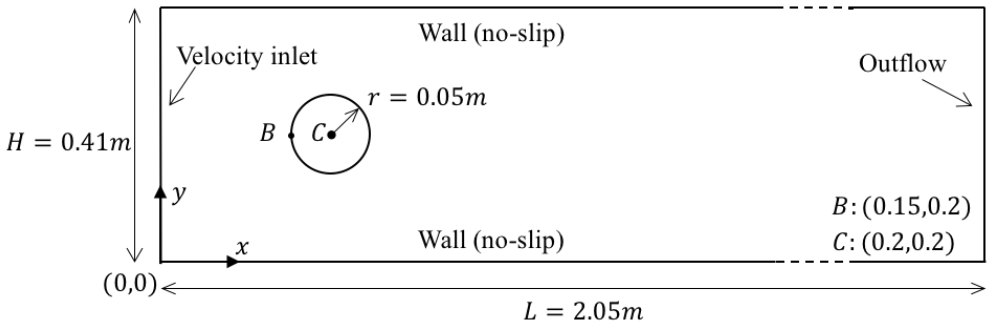

Figure 2.4: Flow geometry with boundary conditions.

Figures 2.5 and 2.6 present the vorticity and pressure fields at one time instant ($t = 11.38s$). The vortices shed by the cylinder are clearly evident. These results are in close agreement with those presented in [34].

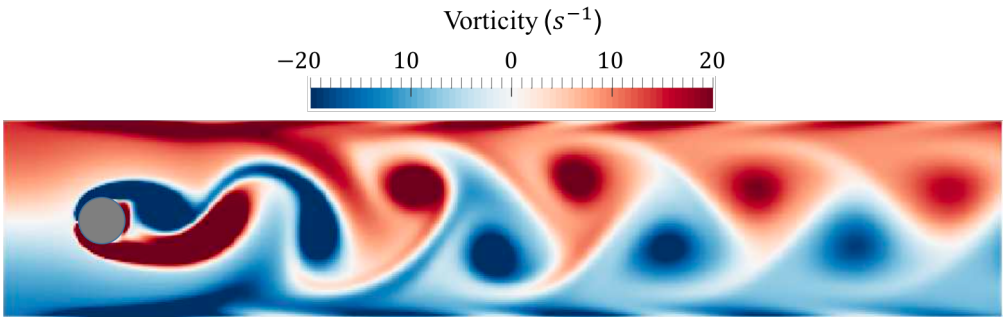

Figure 2.5: Vorticity of laminar flow over a fixed cylinder at time $t = 11.38$ s

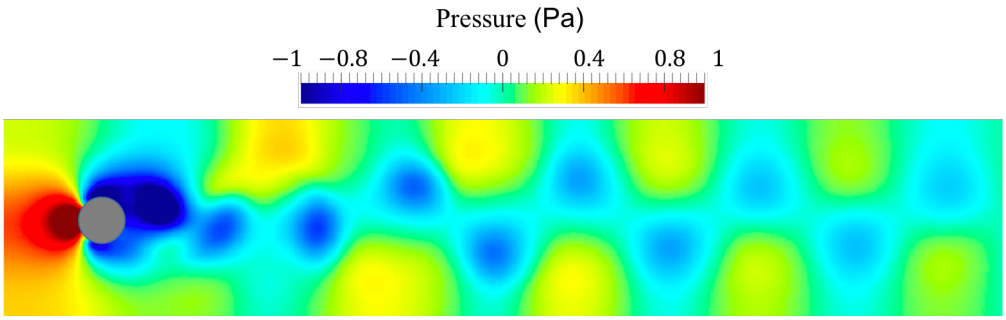

Figure 2.6: Pressure of laminar flow over a fixed cylinder at time $t = 11.38$ s.

Further, Table 2.1 presents three characteristics, namely the Strouhal number (f^*), the maximum drag coeffcient ($C_{d,\max}$), and the maximum lift coefficient ($C_{l,\max}$), in comparison with references in the literature. For all the three quantities, the discrepancy is less than 4%.

	f^*	$C_{d,max}$	$C_{l,max}$
Schafer and Turek [33]	$0.295 - 0.305$	$3.22 - 3.24$	$0.99 - 1.01$
Current work	0.295	3.16	1.05

Table 2.1: Predicted flow characteristics, in comparison with reference results in the literature.

2.3.5 Numerical experiment: The Turek and Hron benchmark problem

Problem description

The Robin-Neumann partitioned scheme is applied to solve the well-known Turek and Hron benchmark problem [35]. This problem involves a two-dimensional laminar incompressible channel flow around a flexible beam which is mounted on the back of a fixed cylinder. The geometry of this problem is shown in Figure 2.7.

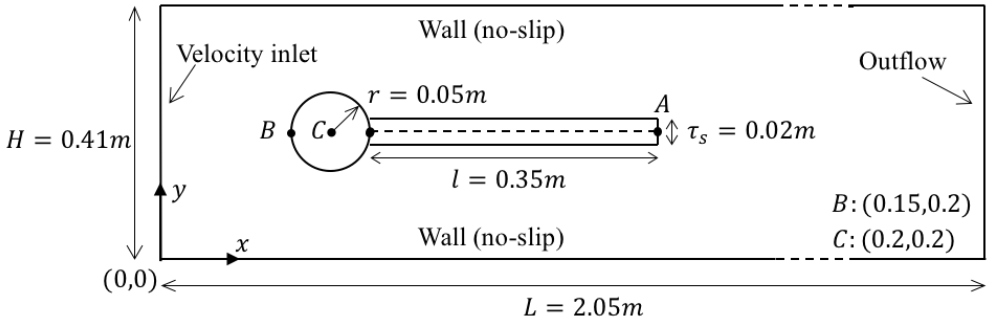

Figure 2.7: Geometry of the Turek and Hron FSI benchmark problem.

In the fluid domain, no-slip boundary condition is enforced on the top and bottom walls. A parabolic velocity profile is prescribed at the inflow boundary,

$$u\left(0,y,t\right) = 1.5\bar{U}\frac{y\left(H-y\right)}{\left(H/2\right)^2}, \qquad v\left(0,y,t\right) = 0 \tag{2.35}$$

where H is the height of the fluid domain and $\bar{U}$ is the average inflow velocity. At the channel outlet (i.e. the right boundary of the fluid domain), a "*do nothing*" boundary condition is

applied. Two test cases presented in Turek and Hron's paper, namely FSI2 and FSI3, are investigated here. The values of model parameters are given in Table 2.2.

parameter	FSI2	FSI3
$\rho_s[\frac{kg}{m^3}]$	1.0×10^4	1.0×10^3
ν_s	0.4	0.4
$\mu_s[\frac{kg}{ms^2}]$	5.0×10^5	2.0×10^6
$\rho_f[\frac{kg}{m^3}]$	1×10^3	1×10^3
$\nu_f[\frac{m^2}{s}]$	1×10^{-3}	1×10^{-3}
$U[\frac{m}{s}]$	1	2
Re	100	200

Table 2.2: Parameter settings for test case FSI2 and FSI3 in [35] (structural density ρ_s, fluid density ρ_f, Poisson ratio ν_s, shear modulus μ_s, and kinematic viscosity ν_f)

Verification of the embedded Robin boundary method

The proposed embedded Robin boundary method is first verified using test case FSI2, with $\alpha_f = 5.0 \times 10^6$. Specifically, a mesh convergence analysis has been conducted on Cartesian grids with resolutions of 125×25, 250×50, 500×100, and 1000×200. The solutions obtained using the last two meshes differ by less than 1%, in terms of the maximum beam tip vertical displacement. A temporal convergence analysis has been conducted for 4.1×10^{-4} s $\leq \Delta t \leq 3.28 \times 10^{-3}$ s, using the 500×100 fluid mesh and a structural mesh with 80 beam elements (Figure 2.8). The solutions given by $\Delta t = 8.2 \times 10^{-4}$ s and $\Delta t = 4.1 \times 10^{-4}$ s differ by less than 1% (also in terms of beam tip vertical displacement).

Therefore, a reference solution is obtained with the 500×100 fluid mesh, 80 beam elements, and a time step size of 8.2×10^{-4} s. In each time step, fluid-structure sub-iterations are

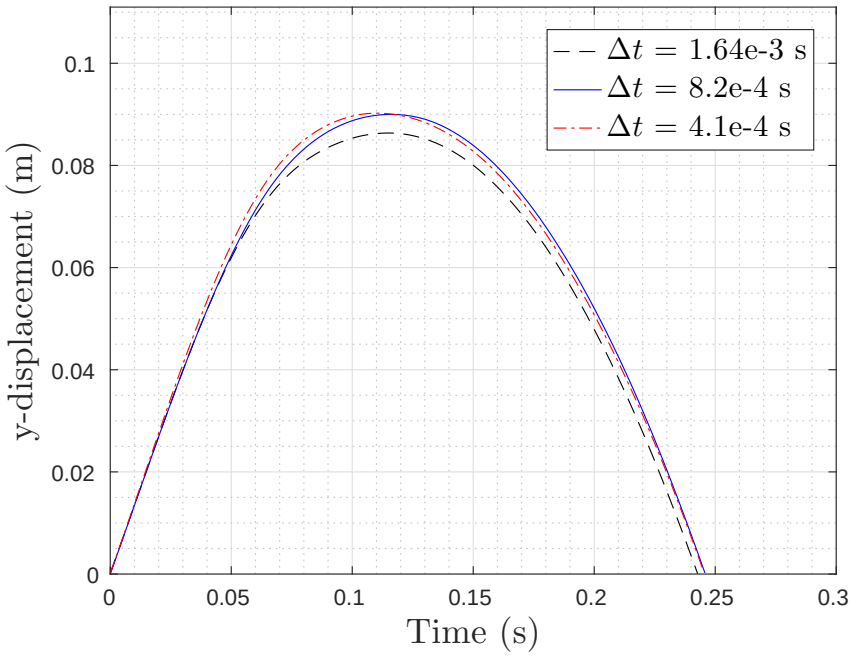

Figure 2.8: Comparison of the beam tip displacement predicted with different time step sizes over half of a vibration cycle (synchronized at the beginning of the cycle).

performed until convergence. Specifically, the convergence criterion is based on the relative residual in the Robin boundary condition Eq.(2.17a), i.e.

$$\frac{\|\mathbf{R}_k^{n+1}\|_2}{\|\mathbf{R}_0^{n+1}\|_2} < \varepsilon_{FS}, \tag{2.36}$$

where

$$\mathbf{R}_k^{n+1} = \mathbf{U}_k^{*,n+1} - \mathbf{U}^n - \frac{\Delta t}{\alpha_f \rho_s \tau_s} \left\{ -\sigma_{f,k}^{*,n+1}\mathbf{n} + \alpha_f \rho_s \tau_s \left(\frac{\partial^2 \mathbf{d}}{\partial t^2} \right)_k^{n+1} + \sigma_{s,k}^{n+1}\mathbf{n} - \alpha_f \rho_s \tau_s \left(\mathbf{U} \cdot \nabla \mathbf{U} \right)_k^{n+1} \right\}. \tag{2.37}$$

The reference solution is obtained with $\varepsilon_{FS} = 5.0 \times 10^{-3}$, which requires around 10 sub-

Authors	$Y_{A,max}$ ($\times 10^{-3}$ m)	T_y (s)	f^*
Turek & Hron [35]	81.8	0.52	0.192
Tian *et al.*[36]	78.0	0.53	0.189
Bhardwaj & Mittal [37]	92.0	0.52	0.192
Current work	89.9	0.5	0.2

Table 2.3: Comparison of the current result with results from three previous studies.

iterations per time step. We have also tested smaller tolerances, but the effect on the solution is negligible.

Figures 2.9, 2.10 present the converged reference solution, including fluid pressure, vorticity, and beam deformation, at four time instants during one period of beam vibration. It is clear that, for this example problem, fluid-structure interaction is dominated by vortex shedding and vortex-induced structural vibration, which is consistent with previous studies (e.g., [35, 36, 37]). In addition, Figure 2.11 presents the vertical displacement at the beam tip (i.e. point A in Figure 2.7). After the beam reaches a periodic steady state, the tip displacement varies within $\delta y \in [-87.8, 89.9] \times 10^{-3}$ m, with a period of 0.5 s.

Table 2.3 compares the current numerical solution with previous results from [35, 36, 37], in terms of the maximum vertical displacement at the beam tip ($Y_{A,max}$), the period of oscillation (T_y), and the Strouhal number (f^*). For $Y_{A,max}$, the current result is within the interval given by the three references. For T_y and f^*, the current results differ from those of Turek & Hron [35] by approximately 4%.

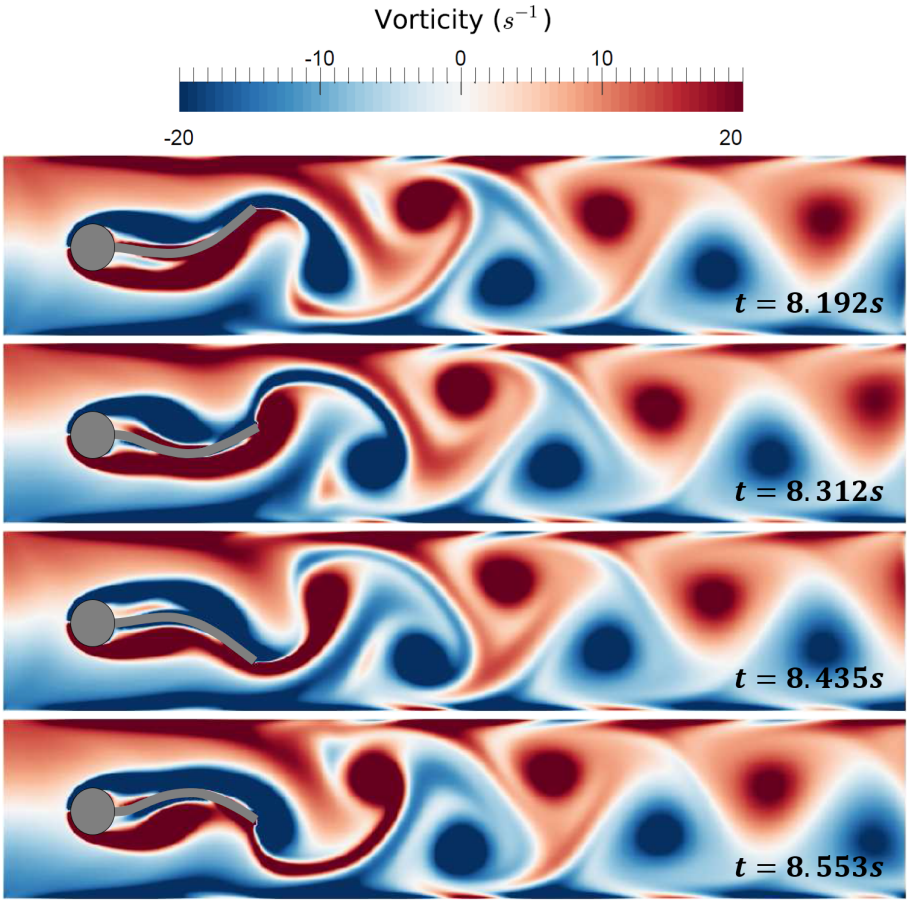

Figure 2.9: Vorticity at four time instances during one period of beam vibration.

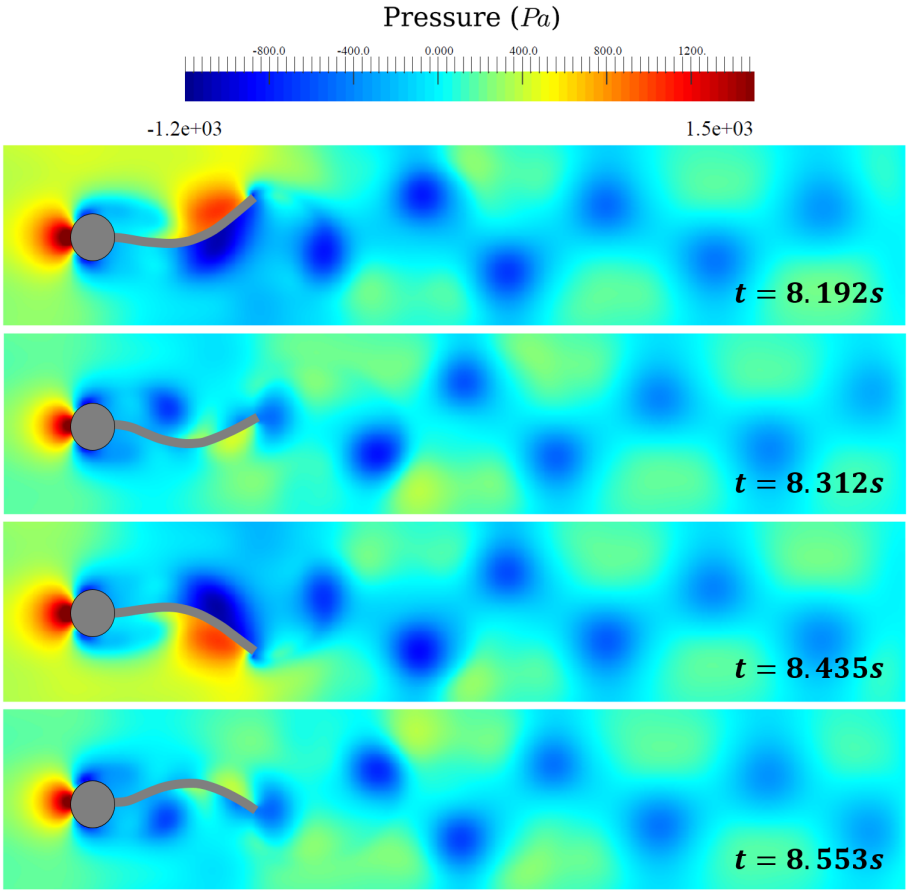

Figure 2.10: Fluid pressure at four time instances during one period of beam vibration.

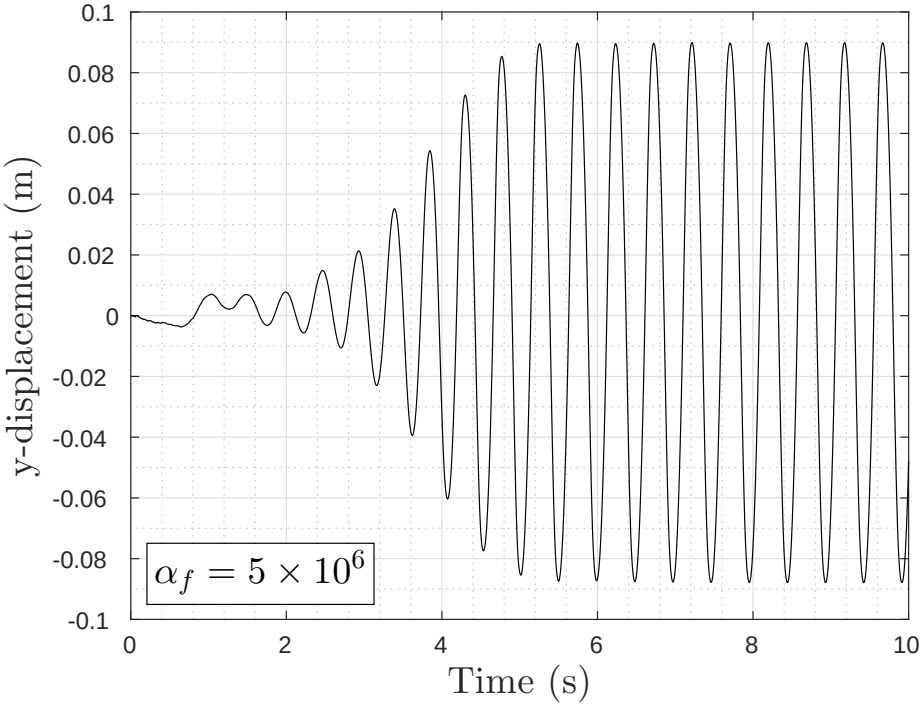

Figure 2.11: Time-history of beam tip displacement (for FSI2).

Effect of α_f on numerical stability and accuracy

We investigate the effect of the new parameter introduced with the Robin transmission condition, α_f, on numerical stability and accuracy. Specifically, we consider two test cases described in Turek and Hron [35], namely FSI2 and FSI3, and vary the value of α_f over a broad range, from 0.025 to 5.0×10^6. The two test cases differ in that FSI3 has a structure-fluid density ratio (i.e. ρ_s/ρ_f) that is 10 times lower, which leads to significantly stronger added-mass effect.

Tables 2.4 and 2.5 show the effect of α_f on numerical stability, for test cases FSI2 and FSI3, respectively. For each sample value of α_f, we vary the number of fluid-structure sub-iterations between 1 and 5, and record the outcome of the simulation in terms of the number of time steps before the solution blows up. Here, the solution is considered to have blown up if any structural node has moved out of the CFD domain. In all the simulations, the time step size is fixed at $\Delta t = 8.2 \times 10^{-4}$ s.

Number of F-S sub-iterations	$\alpha_f = 5.0 \times 10^{6\dagger}$	$\alpha_f = 0.5$	$\alpha_f = 0.05$	$\alpha_f = 0.025$
1	58	2475	3067	3335
2	104	stable	stable	stable
3	stable‡	stable	stable	stable

† In this case, the Robin transmission condition is close to the conventional Dirichlet condition.
‡ "stable" represents that the simulation time has exceeded 14 s ($>$ 17073 time steps) and no numerical instability is observed.

Table 2.4: The number of time steps the simulation can reach before instability occurs (FSI2)

Number of F-S sub-iterations	$\alpha_f = 5.0 \times 10^6$	$\alpha_f = 0.5$	$\alpha_f = 0.05$	$\alpha_f = 0.025$
1	10	13	104	124
2	6	8	stable	stable
3	4	6	stable	stable
5	3	4	stable	stable

Table 2.5: The number of time steps the simulation can reach before instability occurs (FSI3)

Overall, the data presented in the two tables indicate that as α_f decreases, the partitioned numerical solution procedure becomes more stable. A few specific observations are noteworthy.

- In the scenario of explicit coupling (i.e. 1 sub-iteration per time step), smaller α_f allows the simulation to run longer, before the solution blows up.
- In the scenario of implicit coupling, for any prescribed number of sub-iterations, there exists a threshold α_f^* such that the numerical solution procedure is stable for all $\alpha_f < \alpha_f^*$.
- As the prescribed number of sub-iterations increases, the stability threshold α_f^* increases. Also, as the added-mass effect becomes weaker (e.g., FSI2 vs. FSI3), the stability threshold α_f^* increases.

In addition, Tables 2.4 and 2.5 indicate that both increasing the number of sub-iterations and decreasing α_f can effectively stabilize a partitioned solution procedure. Nonetheless, it is notable that the former approach significantly increases the computational cost, whereas the latter does not.

To examine the effect of α_f on numerical accuracy, we simulate test case FSI2 with implicit coupling. Two groups of simulations are performed. In the first group, we fix the number of sub-iterations to three (3) per time step. In the second group, we continue the sub-iterations until the convergence criterion Eq. (2.36) is met. Specifically, we set $\varepsilon_{FS} = 5.0 \times 10^{-3}$, which leads to around 10 sub-iterations per time step. For both cases, we vary α_f between 0.025 and 0.5, while keeping other parameters unchanged. For comparison, the converged solution obtained with $\alpha_f = 5 \times 10^6$ (showed in Figure 2.11) is used as a reference.

Figure 2.12 compares, in two separate sub-figures, the beam tip displacement obtained from the two groups of simulations. In both cases, the solution obtained with $\alpha_f = 0.5$ is in close agreement with the reference solution. However, with smaller values of α_f, the solution becomes less accurate. The loss of accuracy is likely due to the fact that, as α_f is reduced, the influence of the kinematic transmission condition (i.e. Eq. (2.6e) is suppressed — in the extreme case, when $\alpha_f = 0$, this transmission condition is completely dropped.

In summary, despite the fact that the Robin-Neumann transmission conditions (in the continuous form, Eqs. (2.7)) is mathematically equivalent for all $\alpha_f \in (0, \infty)$, the above numerical analysis shows that when a partitioned numerical solution procedure is employed, the value of α_f has clear impacts on both numerical stability and solution accuracy. More importantly, the analysis reveals a trade-off between stability and accuracy, when setting the value of α_f: smaller values of α_f tend to improve numerical stability, yet lower the accuracy of the numerical solution. Furthermore, the different results from two test cases (Tables 2.4 and 2.5) indicate that the optimal value of α_f, if exists, is likely to be problem dependent.

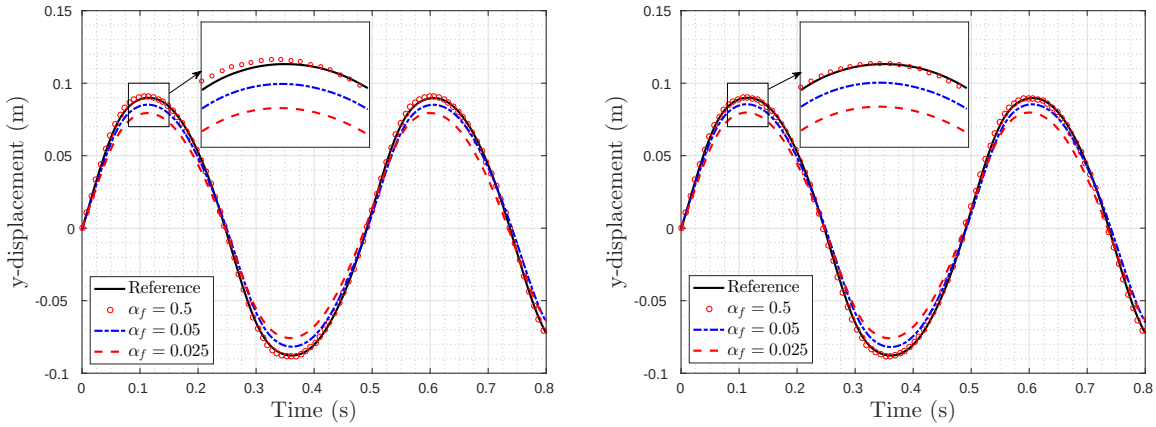

Figure 2.12: Comparison of tip displacement predicted with different value of α_f (for FSI2, synchronized at the beginning of one cycle): (a) with a fixed number of sub-iterations (3 per time step); (b) with a fixed residual tolerance ($\varepsilon_{FS} = 5.0 \times 10^{-3}$).

2.4 Further investigation on the Robin combination parameter

We analyze a simplified two-dimensional (2D) FSI model problem, for which the exact solution can be derived in closed form. The objective is to investigate the stability and accuracy properties of the Robin-Neumann scheme, including the effects of the linear combination parameter α_f, independently of specific spatial discretization schemes and numerical time-integrators.

2.4.1 A model problem

We consider the interaction of a flexible linear beam with a linear, inviscid, incompressible flow (Figure 2.13). Let Ω_s be the structural domain, occupied by a simply-supported Euler-

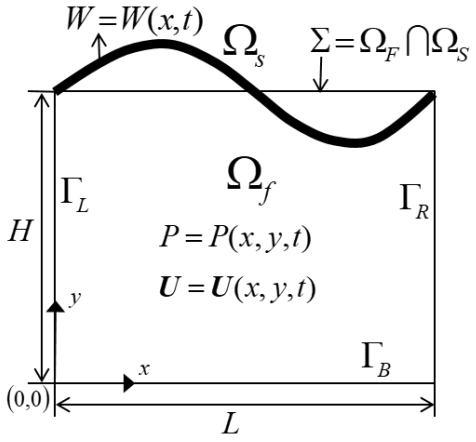

Figure 2.13: A model FSI problem.

Bernoulli beam. The fluid occupies a 2D rectangular domain $\Omega_f = (0, L) \times (0, H)$ with length L and height H. Ω_f has a common boundary with Ω_s at its top boundary, which is the fluid-structure interface, i.e. $\Sigma = \partial\Omega_f \cap \partial\Omega_s$. We assume that the left and right boundaries of Ω_f are periodic. Moreover, because the structural deformation is small, we neglect the variation of Ω_f in time. For simplicity, we only consider transverse displacements of the beam. With these assumptions, the model problem reads:

Find $W = W(x,t)$, $\mathbf{U} = \mathbf{U}(x,y,t)$, $P = P(x,y,t)$ *such that*

$$
\begin{cases}
EI\dfrac{\partial^4 W}{\partial x^4} + \rho_s bh\dfrac{\partial^2 W}{\partial t^2} = f & \text{in } (0,T)\times\Omega_s \quad (2.38a)\\
\rho_f\dfrac{\partial \mathbf{U}}{\partial t} + \nabla P = 0 & \text{in } (0,T)\times\Omega_f \quad (2.38b)\\
\nabla\cdot\mathbf{U} = 0 & \text{in } (0,T)\times\Omega_f \quad (2.38c)\\
\mathbf{U}\cdot\mathbf{n} = 0 & \text{on } \Gamma_B \quad (2.38d)\\
\dfrac{\partial P}{\partial n}|_{\Gamma_L} = \dfrac{\partial P}{\partial n}|_{\Gamma_R},\ P|_{\Gamma_L} = P|_{\Gamma_R} & (2.38e)
\end{cases}
$$

where ρ_f, $\mathbf{U}$, and P denote the fluid density, velocity, and pressure, respectively. W denotes the transverse displacement of the beam. Γ_L, Γ_R, and Γ_B denote the left, right and bottom boundary of Ω_f, respectively. E denotes the Young's modulus of the beam material and I the second moment of the area of the beam's cross-section. ρ_s is the density of the beam material. h and b denote the height and width of the beam, respectively. f denotes the flow-induced force on the beam. The beam is pinned on both ends, which gives $W|_{\partial\Omega_s} = 0$ and $\partial^2 W/\partial x^2|_{\partial\Omega_s} = 0$. On Σ, the kinematic and dynamic interface conditions are given by

$$\begin{cases} \mathbf{U} \cdot \mathbf{n} = \dfrac{\partial W}{\partial t}(x,t) & \text{on } \Sigma \quad (2.39a) \\ f = Pb & \text{on } \Sigma \quad (2.39b) \end{cases}$$

where $\mathbf{n}$ is the outward unit normal from the fluid domain.

Exploiting the property of divergence-free, the fluid velocity $\mathbf{U}$ can be eliminated from the coupled system. Also, with a linear combination parameter $\alpha_f \in (0, \infty)$, the Dirichlet-Neumann transmission conditions (i.e. Eq. (2.39)) can be converted into mathematically equivalent Robin-Neumann transmission conditions. With these modifications, the coupled system of equations reads:

$$
\begin{cases}
EI\dfrac{\partial^4 W}{\partial x^4} + \rho_s bh\dfrac{\partial^2 W}{\partial t^2} = f & \text{in } (0,T)\times\Omega_s & \text{(2.40a)}\\
W|_{\partial\Omega_s} = \dfrac{\partial^2 W}{\partial x^2}|_{\partial\Omega_s} = 0 & & \text{(2.40b)}\\
\nabla^2 P = 0 & \text{in } (0,T)\times\Omega_f & \text{(2.40c)}\\
\dfrac{\partial P}{\partial y} = 0 & \text{on } \Gamma_B & \text{(2.40d)}\\
\dfrac{\partial P}{\partial y}|_{\Gamma_L} = \dfrac{\partial P}{\partial y}|_{\Gamma_R},\ P|_{\Gamma_L} = P|_{\Gamma_R} & & \text{(2.40e)}\\
\alpha_f\dfrac{\partial P}{\partial y} + Pb = -\alpha_f\rho_f\dfrac{\partial^2 W}{\partial t^2} + f & \text{on } \Sigma & \text{(2.40f)}\\
f = Pb & \text{on } \Sigma & \text{(2.40g)}
\end{cases}
$$

The exact solution of the above system of equations, which is independent of α_f, can be derived analytically, and expressed in closed-form. In this regard, we refer the reader to Banks *et al.*[38].

2.4.2 Semi-analytical solution using a Robin-Neumann partitioned procedure

We employ a partitioned procedure to separate the fluid and structural sub-systems, then solve each sub-system analytically within every time step. Specifically, the Z-shaped partitioned procedure shown in Figure 2.14 is taken as an example. Within the time step from

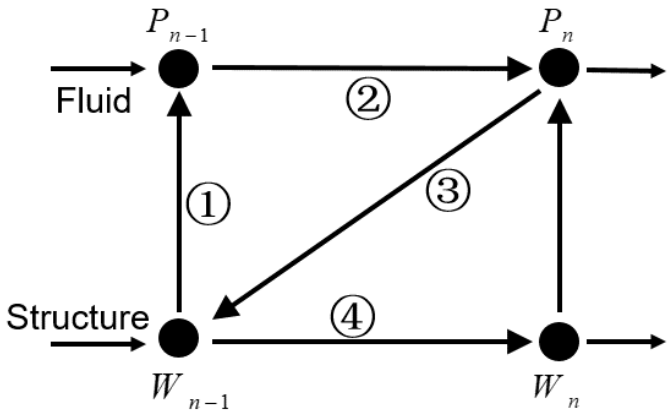

Figure 2.14: A Z-shaped partitioned procedure.

t_{n-1} to t_n, the fluid sub-system is governed by

$$\begin{cases} \nabla^2 P_n = 0 & \text{in } \Omega_f \quad (2.41a) \\ \alpha_f \dfrac{\partial P_n}{\partial y} + P_n b = P_{n-1} b - \alpha_f \rho_f \dfrac{\partial^2 W_{n-1}(x, t_{n-1})}{\partial t^2} & \text{on } \Sigma \quad (2.41b) \\ \dfrac{\partial P_n}{\partial y}\Big|_{\Gamma_B} = 0, \ \dfrac{\partial P_n}{\partial y}\Big|_{\Gamma_L} = \dfrac{\partial P_n}{\partial y}\Big|_{\Gamma_R}, \ P_n\Big|_{\Gamma_L} = P_n\Big|_{\Gamma_R} & \quad (2.41c) \end{cases}$$

In particular, Eq. (2.41b) is a Robin boundary condition. This boundary value problem can be solved using the method of separation of variables and Fourier series. The result is

$$P_n(x, y) = \sum_{i=1}^{\infty} \hat{P}_{n,i}(y) \sin(kx), \quad (2.42)$$

where $k = \dfrac{2\pi i}{L}$, and

$$\hat{P}_{n,i}(y) = \frac{\cosh(kH)b}{\alpha_f k \sinh(kH) + b\cosh(kH)}\hat{P}_{n-1,i}(y) - \frac{\alpha_f \rho_f \cosh(ky)}{\alpha_f k \sinh(kH) + b\cosh(kH)}\frac{d^2\hat{W}_{n-1,i}}{dt^2}\Big|_{t=t_{n-1}}, \tag{2.43}$$

where $\hat{W}_{n-1,i}$ denotes the beam displacement of mode i.

Then, the pressure load on Σ at t_n is applied to the structural sub-system, which gives

$$\begin{cases} EI\dfrac{\partial^4 W_n}{\partial x^4} + \rho_s bh\dfrac{\partial^2 W_n}{\partial t^2} = P_n(x,H)b \qquad \text{in } (t_{n-1},t_n)\times\Omega_s & \text{(2.44a)} \\ W_n(x,t_{n-1}) = W_{n-1}(x,t_{n-1}) & \text{(2.44b)} \\ W_n|_{\partial\Omega_s} = 0,\ \dfrac{\partial^2 W_n}{\partial x^2}\Big|_{\partial\Omega_s} = 0. & \text{(2.44c)} \end{cases}$$

This initial boundary value problem can also be solved analytically through separation of variables and Fourier series, which gives

$$W_n(x,t) = \sum_{i=1}^{\infty} \hat{W}_{n,i}(t)\sin(kx). \tag{2.45}$$

Again, $k = \dfrac{2\pi i}{L}$. $\hat{W}_{n,i}(t)$ is given by

$$\hat{W}_{n,i}(t) = G_1\cos(\omega_{0,i}t) + G_2\sin(\omega_{0,i}t) + \frac{\hat{P}_{n,i}(H)b}{EIk^4}, \tag{2.46}$$

where $\omega_{0,i}$ is the natural frequency of the beam associated with mode i, i.e.

$$\omega_{0,i} = \sqrt{\frac{EIk^4}{\rho_s bh}}. \tag{2.47}$$

and

$$G_1 = \cos(\omega_{0,i}t_{n-1})\hat{W}_{n-1,i}(t_{n-1}) - \frac{\cos(\omega_{0,i}t_{n-1})b}{EIk^4}\hat{P}_{n,i}(H) - \frac{\sin(\omega_{0,i}t_{n-1})}{\omega_{0,i}}\frac{d\hat{W}_{n-1,i}}{dt}\Big|_{t=t_{n-1}} \tag{2.48}$$

$$G_2 = \sin(\omega_{0,i}t_{n-1})\hat{W}_{n-1,i}(t_{n-1}) - \frac{\sin(\omega_{0,i}t_{n-1})b}{EIk^4}\hat{P}_{n,i}(H) + \frac{\cos(\omega_{0,i}t_{n-1})}{\omega_{0,i}}\frac{d\hat{W}_{n-1,i}}{dt}\Big|_{t=t_{n-1}} \tag{2.49}$$

2.4.3 Effect of α_f on numerical stability

Combining Eqs. (2.43) and (2.46), we can derive a recursive formula for each Fourier mode of the structural solution. Specifically, let

$$\hat{\mathbf{K}}_n = \begin{bmatrix} \hat{W}_n \\ \dfrac{d\hat{W}_n}{dt} \\ \dfrac{d^2\hat{W}_n}{dt^2} \end{bmatrix}_{t=t_n}. \tag{2.50}$$

Then, we can derive

$$\hat{\mathbf{K}}_n = \mathbf{C}_{RN}\hat{\mathbf{K}}_{n-1}, \tag{2.51}$$

where

$$\mathbf{C}_{RN} = \begin{bmatrix} (1-M_1)\cos(\omega_0\Delta t) + M_1 & \frac{\sin(\omega_0\Delta t)}{\omega_0} & M_2(1-\cos(\omega_0\Delta t)) \\ -\omega_0(1-M_1)\sin(\omega_0\Delta t) & \cos(\omega_0\Delta t) & M_2\omega_0\sin(\omega_0\Delta t) \\ -\omega_0^2(1-M_1)\cos(\omega_0\Delta t) & -\omega_0\sin(\omega_0\Delta t) & M_2\omega_0^2\cos(\omega_0\Delta t) \end{bmatrix}. \tag{2.52}$$

To simplify the notation, we have dropped the mode number i in the above expressions. Δt denotes the time step size. M_1 and M_2 are given by

$$M_1 = \frac{1}{\alpha_f k \tanh(kH)/b + 1}, \qquad M_2 = \frac{\rho_s bh - \alpha_f \rho_f}{EIk^4[\alpha_f k \tanh(kH)/b + 1]}. \tag{2.53}$$

The stability property of the Robin-Neumann partitioned procedure is thus determined by that of Eq. (2.51). Let $\rho(\mathbf{C}_{RN})$ denote the spectral radius of matrix $\mathbf{C}_{RN}$. Apparently, $\rho(\mathbf{C}_{RN})$ is a continuous function of Δt. A straightforward derivation gives

$$\lim_{\Delta t \to 0} |\rho(\mathbf{C}_{RN})| = \left| \frac{1 - \alpha_f \rho_f/(\rho_s bh)}{\alpha_f k \tanh(kH)/b + 1} \right| \equiv \Phi_{RN}. \tag{2.54}$$

Eq. (2.54) reveals that the stability of the Robin-Neumann partitioned procedure depends on the physical parameters of the FSI problem, including the structure-fluid density ratio ρ_s/ρ_f, the thickness of the beam h, the height of the fluid domain H and the wave number k. In particular, the procedure becomes unstable if the added-mass effect is significant, for example, if the problem involves a heavy fluid and/or a slender domain. This is consistent

with previous findings on Dirichlet-Neumann partitioned procedures (e.g., Causin *et al.*[5]). More importantly, Eq. (2.54) indicates that, in addition to the physical parameters, the numerical stability of the Robin-Neumann partitioned procedure also depends on the value of α_f.

We introduce non-dimensional parameters $\eta = \rho_s/\rho_f$, $\alpha = \alpha_f k/b$, $C_h = kh$, and $C_H = kH$. Substituting these parameters into Eq. (2.54) gives a stability criterion for the Robin-Neumann partitioned procedure,

$$\Phi_{RN}(\eta, C_h, C_H, \alpha) = \left| \frac{\eta - \alpha/C_h}{\eta + \alpha\eta \tanh(C_H)} \right| \leq 1. \tag{2.55}$$

Figure 2.15 shows the dependence of Φ_{RN} on η, C_H, and the non-dimensional Robin combination parameter α. Now, it is clear that for any given set of physical parameters, there exists a *critical* value $\alpha_{f,c}$, such that for any $\alpha_f < \alpha_{f,c}$, the Robin-Neumann partitioned procedure is stable when Δt is sufficiently small. On the other hand, if $\alpha_f > \alpha_{f,c}$, the Robin-Neumann partitioned procedure may be unconditionally unstable. In particular, this indicates that for problems for which the conventional Dirichlet-Neumann partitioned procedure is unconditionally unstable, the Robin-Neumann partitioned procedure can be conditionally stable when an appropriate value of α_f is specified.

The critical value $\alpha_{f,c}$ can be obtained by setting $\Phi_{RN} = 1$, which gives

$$\alpha_{f,c} = \frac{2\rho_s bh}{\rho_f - \rho_s hk \tanh(kH)}. \tag{2.56}$$

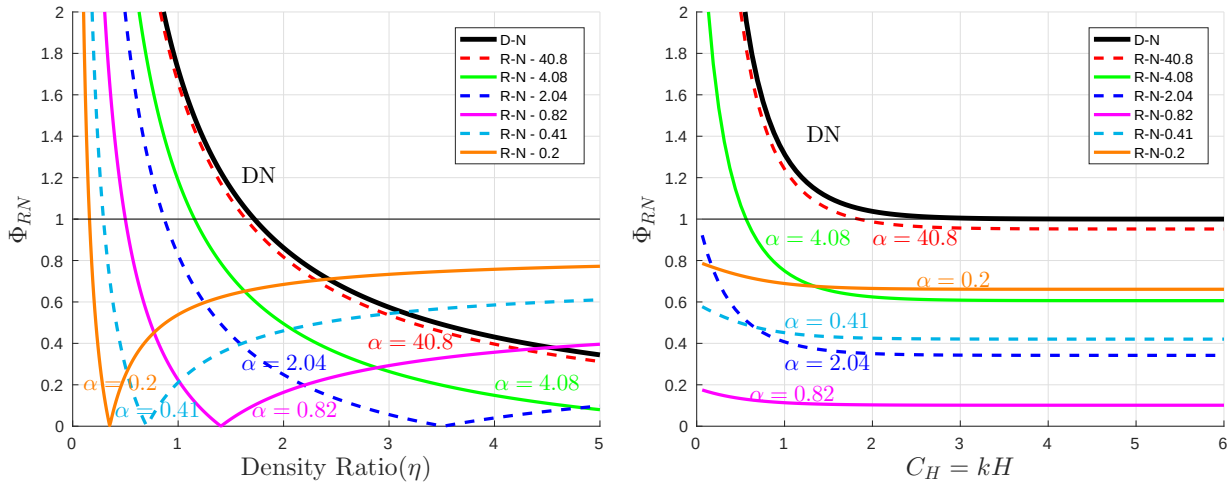

Figure 2.15: (a) Dependence of Φ_{RN} on density ratio η (with $C_h = 0.5806$, $C_H = 2\pi$). (b) Dependence of Φ_{RN} on non-dimensional parameter C_H (with $C_h = 0.5806$, $\eta = 1.7225$).

It is not surprising that $\alpha_{f,c}$ is smaller — in other words, the interval of feasible values of α_f is narrower — for FSI problems involving stronger added-mass effect (e.g., small structure-fluid density ratio, slender structure, etc.). More specifically, $\alpha_{f,c}$ can be rewritten as

$$\alpha_{f,c} = \frac{2}{\rho_f \left(\frac{1}{m_s} - \frac{1}{m_a} \right)}, \tag{2.57}$$

where $m_s = \rho_s bh$ is the structural mass per unit length of beam, and

$$m_a = \frac{\rho_f b}{k \tanh(kH)} \tag{2.58}$$

is the added mass (due to fluid) per unit length of beam. Equation (2.57) explicitly shows that $\alpha_{f,c}$ depends on the difference between the actual structural mass and the added mass.

Further, we introduce *added cross-sectional area* as

$$A_a = \frac{b}{k \tanh(kH)}, \tag{2.59}$$

which is comparable to the actual cross-sectional area $A_s = bh$. Then,

$$\alpha_{f,c} = \frac{2}{\dfrac{1}{\eta A_s} - \dfrac{1}{A_a}}, \tag{2.60}$$

which shows that $\alpha_{f,c}$ depends on the ratio between the densities of the fluid and the structure, but not the value of each of them.

Remark: When $\alpha_f \to \infty$, the Robin transmission condition Eq. (2.41b) reduces to the conventional Dirichlet transmission condition. Thus, from Eq. (2.54) we can derive a stability criterion for Dirichlet-Neumann explicit coupling partitioned procedure, i.e.

$$\lim_{\Delta t \to 0} |\rho(\mathbf{C}_{DN})| = \frac{\rho_f \cosh(kH)}{\rho_s h k \sinh(kH)} \equiv \Phi_{DN} \leq 1. \tag{2.61}$$

This criterion is similar to those derived by Causin *et al.*[5], Förster [6] *et al.*, Banks *et al.*[38]. Nonetheless, unlike the previous works, here Eq. (2.61) is derived directly from a partitioned procedure, without using any specific spatial discretization scheme or numerical time-integrator.

2.4.4 Effect of α_f on solution accuracy

To examine the effect of α_f on the accuracy of the Robin-Neumann partitioned procedure, we formulate the cumulative error of the scheme. To simplify the derivation, we replace the beam acceleration in Eq. (2.50) by a new variable $\hat{D}$, defined by

$$\hat{D}_n = \frac{\omega_0^2(1-M_1)}{1-M_2\omega_0^2}\hat{W}_n + \frac{d^2\hat{W}_n}{dt^2}. \tag{2.62}$$

Then, the recursive formula Eq. (2.51) becomes

$$\widetilde{\mathbf{K}}_n = \widetilde{\mathbf{C}}_{RN}\widetilde{\mathbf{K}}_{n-1}, \tag{2.63}$$

where $\widetilde{\mathbf{K}}_n = \left[\hat{W}_n, \frac{d\hat{W}_n}{dt}, \hat{D}_n\right]^T_{t=t_n}$, and

$$\widetilde{\mathbf{C}}_{RN} = \begin{bmatrix} \frac{M_1-M_2\omega_0^2+(1-M_1)\cos(\omega_0\Delta t)}{1-M_2\omega_0^2} & \frac{\sin(\omega_0\Delta t)}{\omega_0} & M_2\left(1-\cos(\omega_0\Delta t)\right) \\ -\frac{(1-M_1)\omega_0\sin(\omega_0\Delta t)}{1-M_2\omega_0^2} & \cos(\omega_0\Delta t) & M_2\omega_0\sin(\omega_0\Delta t) \\ \frac{2(1-M_1)\omega_0^2\left(M_1-M_2\omega_0^2\right)\sin\left(\frac{\omega_0\Delta t}{2}\right)^2}{\left(1-M_2\omega_0^2\right)^2} & \frac{\omega_0\left(-M_1+M_2\omega_0^2\right)\sin(\omega_0\Delta t)}{1-M_2\omega_0^2} & \frac{M_2\omega_0^2\left[1-M_1+\left(M_1-M_2\omega_0^2\right)\cos(\omega_0\Delta t)\right]}{1-M_2\omega_0^2} \end{bmatrix}. \tag{2.64}$$

Clearly, Eq. (2.63) can also be re-written as

$$\widetilde{\mathbf{K}}_n = \widetilde{\mathbf{K}}_{n-1} + \Delta t \mathbf{A}(t_{n-1}, \widetilde{\mathbf{K}}_{n-1}, \Delta t), \tag{2.65}$$

while the incremental function $\mathbf{A}(\cdot)$ can be easily derived. The local truncation error τ for time step $[t_{n-1}, t_n]$ and the cumulative error ε at the final time t_{final} are given by

$$\begin{aligned} \tau_n &= \widetilde{\mathbf{K}}_e(t_n) - \widetilde{\mathbf{K}}_e(t_{n-1}) - \Delta t \mathbf{A}(t_{n-1}, \widetilde{\mathbf{K}}_e(t_{n-1}), \Delta t), & (2.66) \\ \varepsilon_{final} &= \widetilde{\mathbf{K}}_e(t_{final}) - \widetilde{\mathbf{K}}_{final}, & (2.67) \end{aligned}$$

where $\widetilde{\mathbf{K}}_e(t_n)$ denotes the exact solution at $t = t_n$.

Assuming the Robin-Neumann partitioned procedure — with a prescribed α_f — is conditionally stable for $\Delta t \in (0, \Delta t_{max})$, then the following lemma holds.

Lemma 1. ***Lemma 1.*** *Let*

$$D = \Big\{ (t, \widetilde{\mathbf{K}}, \Delta t) : 0 \leq t \leq t_{final},\ 0 < \Delta t < \Delta t_{max},\ mod(t_{final}, \Delta t) = 0 \Big\}.$$

If there exists a constant $Q \in \mathcal{R}^+$, such that for all $(t, \widetilde{\mathbf{K}}_1, \Delta t)$, $(t, \widetilde{\mathbf{K}}_2, \Delta t) \in D$,

$$|\mathbf{A}(t, \widetilde{\mathbf{K}}_1, \Delta t) - \mathbf{A}(t, \widetilde{\mathbf{K}}_2, \Delta t)| \leq Q |\widetilde{\mathbf{K}}_1 - \widetilde{\mathbf{K}}_2|; \tag{2.68}$$

then,

$$|\varepsilon_{final}| \equiv |\widetilde{\mathbf{K}}_e(t_{final}) - \widetilde{\mathbf{K}}_{final}| \leq \frac{|\tau_{max}|}{Q\Delta t}\left(e^{Qt_{final}} - 1\right), \tag{2.69}$$

where

$$\tau_{max} = \max_{1\leq n\leq N} |\tau_n|$$

denotes the maximum local truncation error, and N is the total number of time step.

Proof. From Eqs. (2.65) and (2.66), the cumulative error at $t_{final} = t_N$ satisfies

$$\varepsilon_{final} = \varepsilon_{N-1} + \Delta t\left[\mathbf{A}(t_{N-1}, \widetilde{\mathbf{K}}_e(t_{N-1}), \Delta t) - \mathbf{A}(t_{N-1}, \widetilde{\mathbf{K}}_{N-1}, \Delta t)\right] + \tau_N. \tag{2.70}$$

Since $\left(t_{N-1}, \widetilde{\mathbf{K}}_e(t_{N-1}), \Delta t\right) \in D$, $\left(t_{N-1}, \widetilde{\mathbf{K}}_{N-1}, \Delta t\right) \in D$, Eq. (2.68) implies that

$$|\varepsilon_{final}| \leq (1 + Q\Delta t)|\varepsilon_{N-1}| + |\tau_N|. \tag{2.71}$$

With $\varepsilon_0 = 0$, it follows by induction that

$$|\varepsilon_{final}| \leq \frac{|\tau_{max}|}{Q\Delta t}\left[(1 + Q\Delta t)^N - 1\right] \leq \frac{|\tau_{max}|}{Q\Delta t}\left(e^{Qt_N} - 1\right) = \frac{|\tau_{max}|}{Q\Delta t}\left(e^{Qt_{final}} - 1\right) \tag{2.72}$$

□

With Lemma 1, we can prove the following theorem on the cumulative error in beam displacement.

Theorem 1. *For the Z-shaped partitioned procedure described in Figure 2.14, when* $\alpha_f = \alpha_{f,c}$*, the cumulative error in beam displacement at* t_{final} *is proportional to* Δt^2*.*

Proof. For simplification of derivation, we consider the two-step recursive formula of the Robin-Neumann scheme,

$$\widetilde{\mathbf{K}}_{n+1} = \widetilde{\mathbf{K}}_{n-1} + 2\Delta t \mathbf{A}(t_{n-1}, \widetilde{\mathbf{K}}_{n-1}, \Delta t) \tag{2.73}$$

where

$$\mathbf{A}(t_{n-1}, \widetilde{\mathbf{K}}_{n-1}, \Delta t) = \frac{1}{2\Delta t}\left(\widetilde{\mathbf{C}}_{RN}^2 - \mathbf{I}\right)\widetilde{K}_{n-1} \equiv \widetilde{\mathbf{C}}_p \widetilde{\mathbf{K}}_{n-1}. \tag{2.74}$$

The explicit expression of $\widetilde{\mathbf{C}}_p$ can be derived from Eqs. (2.64) and (2.74), i.e.

$$\widetilde{\mathbf{C}}_p = \begin{bmatrix} \frac{(M_1-1)\left[-2+M_2\omega_0^2+M_3\right]\sin^2\left(\frac{\omega_0\Delta t}{2}\right)}{\Delta t\left(M_2\omega_0^2-1\right)} & \frac{\left(-M_3-M_2\omega_0^2\right)\sin\left(\omega_0\Delta t\right)}{2\Delta t\omega_0} & \frac{M_2(1-M_3)\sin^2\left(\frac{\omega_0\Delta t}{2}\right)}{\Delta t} \\ \frac{(M_1-1)\omega_0(M_3+M_2\omega_0^2)\sin\left(\omega_0\Delta t\right)}{2\Delta t(M_2\omega_0^2-1)} & \frac{(-2+M_1-M_2\omega_0^2)\sin^2\left(\omega_0\Delta t\right)}{2\Delta t} & \frac{M_2\omega_0(-1-M_3)\sin\left(\omega_0\Delta t\right)}{2\Delta t} \\ \frac{(M_1-1)\omega_0^2(M_1-M_2\omega_0^2)(-1+M_3)\sin^2\left(\frac{\omega_0\Delta t}{2}\right)}{\Delta t(M_2\omega_0^2-1)^2} & \frac{\omega_0(-M_1+M_2\omega_0^2)(1+M_3)\sin\left(\omega_0\Delta t\right)}{2\Delta t(M_2\omega_0^2-1)} & \frac{-M_4}{2\Delta t(M_2\omega_0^2-1)^2} \end{bmatrix}, \tag{2.75}$$

where M_3 and M_4 are given by

$$\begin{aligned}
M_3 =&(-2 + M_1 - M_2\omega_0^2)\cos(\omega_0\Delta t) - M_1,\\
M_4 =&(-1 + M_2\omega_0^2)^2 - M_2^2\omega_0^4\left[1 - M_1 + (M_1 - M_2\omega_0^2)\cos(\omega_0\Delta t)\right]^2\\
&+ 4(M_1 - 1)M_2\omega_0^2(M_1 - M_2\omega_0^2)\sin^4\left(\frac{\omega_0\Delta t}{2}\right) + M_2\omega_0^2(-1 + M_2\omega_0^2)(-M_1 + M_2\omega_0^2)\sin^2(\omega_0\Delta t).
\end{aligned}$$

It is notable that as $\Delta t \to 0$, the asymptotic behavior of $\widetilde{\mathbf{C}}_p$ is dramatically different for different values of α_f. Specifically,

when $\alpha_f = \alpha_{f,c}$,

$$\widetilde{\mathbf{C}}_p = \begin{bmatrix} \mathcal{O}(\Delta t) & \mathcal{O}(1) & \mathcal{O}(\Delta t) \\ \mathcal{O}(1) & \mathcal{O}(\Delta t) & \mathcal{O}(1) \\ \mathcal{O}(\Delta t) & \mathcal{O}(1) & \mathcal{O}(1) \end{bmatrix}, \tag{2.76}$$

when $\alpha_f < \alpha_{f,c}$,

$$\widetilde{\mathbf{C}}_p = \begin{bmatrix} \mathcal{O}(\Delta t) & \mathcal{O}(1) & \mathcal{O}(\Delta t) \\ \mathcal{O}(1) & \mathcal{O}(\Delta t) & \mathcal{O}(1) \\ \mathcal{O}(\Delta t) & \mathcal{O}(1) & \mathcal{O}(\frac{1}{\Delta t}) \end{bmatrix}. \tag{2.77}$$

The above two equations suggest that, if and only if $\alpha_f = \alpha_{f,c}$, $\widetilde{\mathbf{C}}_p$ is bounded as Δt approaches zero. By Lemma 1, there exists $Q^* \in \mathcal{R}^+$ such that

$$\varepsilon_{W,final} \leq \frac{\tau_{W,max}}{Q^*\Delta t}\left(e^{Q^* t_{final}} - 1\right). \tag{2.78}$$

For the Z-shaped partitioned procedure described in Figure 2.14, the local truncation error is

$$\tau_{W,n} = \frac{\omega\tilde{w}\left(\omega_0^2 - \omega^2\right)\cos\left(\omega t_n\right)\left[5hk\alpha_f\rho_s + \left(-3\alpha_f\rho_f + 8bh\rho_s\right)\coth\left(kH\right)\right]}{3h\rho_s\left[k\alpha_f + b\coth\left(kH\right)\right]}\Delta t^3 + \mathcal{O}(\Delta t^4), \tag{2.79}$$

where ω is the frequency of the beam associated with mode i, i.e.

$$\omega = \sqrt{\frac{EIk^4}{\rho_s bh + \dfrac{\rho_f b}{k\tanh\left(kH\right)}}}. \tag{2.80}$$

Therefore, $\tau_{W,max} = \mathcal{O}(\Delta t^3)$, and

$$\varepsilon_{W,final} \leq \frac{\mathcal{O}\left(\Delta t^3\right)}{Q^*\Delta t}\left(e^{Q^* t_{final}} - 1\right) = \mathcal{O}\left(\Delta t^2\right). \tag{2.81}$$

□

Remark:

- It can be shown that, when paired with the conventional Dirichlet-Neumann transmission conditions, the Z-shaped partitioned procedure is (globally) only first-order accurate in beam displacement. The fact that when $\alpha_f = \alpha_{f,c}$, the Robin-Neumann transmission conditions gives second-order accuracy is remarkable.

- The above proof cannot be extended to $\alpha_f < \alpha_{f,c}$. This is because Eq. (2.77) shows

that $\widetilde{C}_p$ is unbounded as $\Delta t \to 0$. Moreover, our numerical experiments — to be shown in Section 2.4.5 — reveal that when $\alpha_f < \alpha_{f,c}$, the Robin-Neumann scheme is (globally) only first-order accurate.

2.4.5 Numerical experiments

We consider a representative example of the model problem, with geometric properties $H = 1$ m, $b = 0.01540$ m, $h = 0.0924$ m, $L = 1$ m. The initial condition of beam's kinematics is given by

$$W(x, t_0) = 0, \qquad \frac{\partial W}{\partial t}|_{t_0} = 2\tilde{w}\omega \sin(kx), \qquad \frac{\partial^2 W}{\partial t^2}|_{t_0} = 0,$$

where $\tilde{w}$ denotes the vibration amplitude. Here, we set $k = 2\pi$, $E = 70$ GPa, $I = 1 \times 10^{-6}$ m^4, $\rho_s = 1000$ kg/m^3, $\rho_f = 876$ kg/m^3, $\tilde{w} = 0.01$ m.

Substituting the above geometric and material properties into Eq. (2.56), we obtain

$$\alpha_{f,c} \simeq 0.0096328 \text{ m}^2.$$

To demonstrate the stability properties of the Robin-Neumann partitioned procedure (discussed in Section 2.4.3), we evaluate the semi-analytical, partitioned solution with $\alpha_f = \alpha_{f,c}$ and $1.05\alpha_{f,c}$. Figure 2.16 shows the predicted time-history of beam displacement at $x = 0.25$ m. As expected, the scheme is stable with $\alpha_f = \alpha_{f,c}$, yet the solution blows up with $\alpha_f > \alpha_{f,c}$.

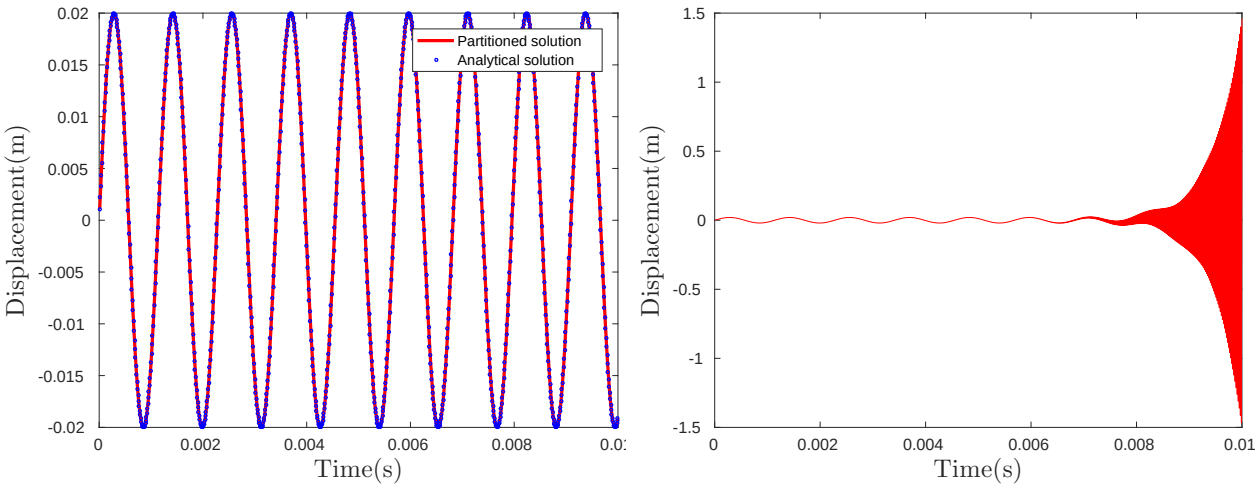

(a) (b)

Figure 2.16: Partitioned solution of beam displacement at $x = 0.25$ using a Robin-Neumann partitioned procedure with two different combination parameters: (a) $\alpha_f = \alpha_{f,c}$ and (b) $\alpha_f = 1.05\alpha_{f,c}$.

To demonstrate the accuracy properties of the Robin-Neumann partitioned procedure (discussed in Section 2.4.4), we evaluate the semi-analytical, partitioned solution with $\alpha_f = 1.62 \times 10^{-3}, 4.29 \times 10^{-3}, 6.96 \times 10^{-3}$ m^2, and $\alpha_{f,c}$. In particular, $\alpha_f = 1.62 \times 10^{-3}$ m^2 is obtained by imposing

$$\Phi_{RN}(\alpha_f) = 0,$$

which gives

$$\alpha_f = \eta A_s. \tag{2.82}$$

This is consistent with the approach presented in several previous studies (e.g., [19, 21, 20, 38]), that is, determining α_f by "embedding" a simplified structural governing equation into the fluid equations. Here, we denote it by $\alpha_{f,0}$. Figure 2.17 compares the time-history of error in beam displacement at $x = 0.25$. It is clear that as α_f decreases, the magnitude of

numerical error increases. This is consistent with the finding obtained from the Turek and Hron benchmark problem (Section 2.3.5).

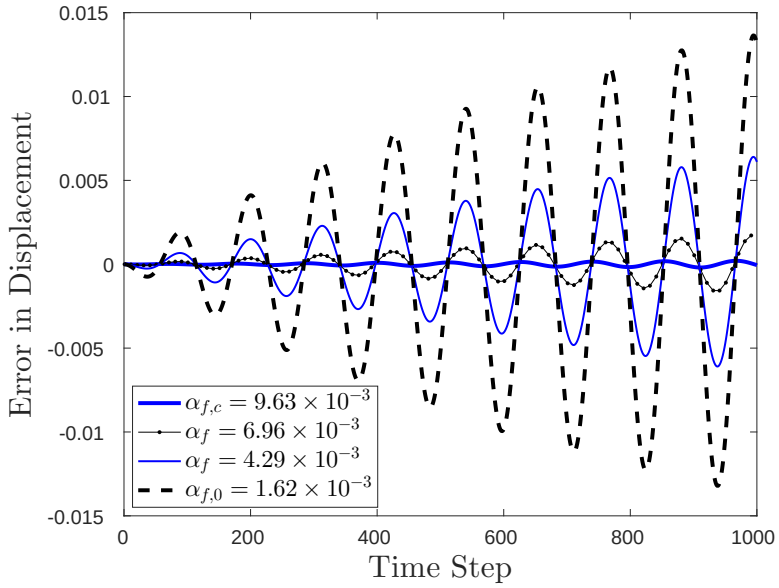

Figure 2.17: Comparison of error magnitude

Finally, Figure 2.18 shows that, using the Z-shaped partitioned procedure, the Robin-Neumann transmission conditions with $\alpha_{f,c}$ gives second-order accuracy in time, which verifies Theorem 1. Nonetheless, the scheme is only first-order accurate for $\alpha_f < \alpha_{f,c}$ (including $\alpha_f = \alpha_{f,0}$).

2.5 Conclusions

Partitioned procedures can be appealing for solving complex fluid-structure interaction problems, as they allow existing CFD and CSD algorithms and solvers to be combined and reused. However, for problems involving incompressible flow and strong added-mass effect (e.g.,

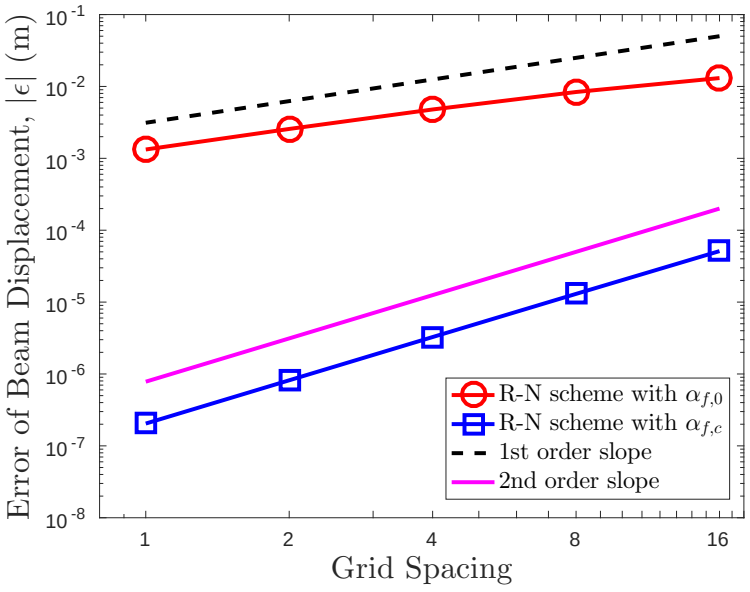

Figure 2.18: Comparison of the order of accuracy

heavy fluid, slender structure), partitioned procedures have been found to suffer from numerical instability, which requires sub-iterations between the fluid and structural solvers, hence significantly increasing the computational cost. This paper presents a fundamental research on the use of Robin-Neumann transmission conditions to mitigate this instability issue. In this regard, a few recent studies have applied Robin-Neumann transmission conditions in the arbitrary Lagrangian-Eulerian (ALE) framework and in a mixed Eulerian-Lagrangian framework featuring moving overlapping grid. In this paper, we have presented a so-called embedded Robin boundary method, thereby introducing the Robin-Neumann transmission conditions to immersed/embedded boundary methods. This method utilizes operating splitting and a modified ghost fluid method to enforce the Robin transmission condition on an embedded fluid-structure interface, in the context of a projection-based incompressible flow solver and a finite element structural solver. The method is demonstrated and verified using

the well-known Turek and Hron benchmark problem, which features a slender beam undergoing large, nonlinear deformation in an unsteady, vortex-dominated channel flow. As expected, the enforcement of Robin-Neumann transmission conditions reduces the number of sub-iterations required for achieving numerical stability.

The Robin transmission condition involves a numerical parameter, α_f, which comes from the linear combination of the kinematic and dynamic interface conditions. In this paper, we have analyzed the effects of α_f on numerical stability and solution accuracy. Specifically, we have presented a numerical study using the embedded Robin boundary method and two test cases from the Turek and Hron benchmark problem, as well as an analytical study using a simplified 2-D model problem featuring an Euler-Bernoulli beam interacting with a 2-D incompressible, inviscid flow. Overall, we found that the value of α_f has clear impact on both stability and accuracy. More specifically, our study reveals a trade-off: smaller values of α_f tend to improve numerical stability, yet deteriorates the accuracy of the numerical solution. In addition, using the simplified model problem, we have derived, in closed-form expression, the critical value of α_f for each mode of structural deformation that optimizes accuracy while ensuring stability. Potentially, this closed-form expression may be utilized to develop formulas and algorithms for setting the value of α_f in more complex FSI simulations.

The work presented in this paper has a number of limitations. The development and demonstration of the embedded Robin boundary method are presented for two-dimensional fluid flows and beam structures. Extension to three-dimension and more complex structures is conceptually straightforward, yet may require substantial effort on code development. Also,

the numerical properties of Robin-Neumann transmission conditions are analyzed for one partitioned procedure, i.e. the Z-shaped partitioned procedure. Extension to other partitioned procedures (e.g., those discussed in [39, 40]) is straightforward, and will be investigated in our future work.

Acknowledgments

The authors gratefully acknowledge the support of the National Science Foundation (NSF) under Award Number CBET-1706003 (S.C. and K.G.W.), the support of the Office of Naval Research (ONR) under Award Number N00014-17-1-2831 (K.G.W.), and the faculty start-up support from Virginia Tech (K.G.W.).

Bibliography

[1] B. Hübner, E. Walhorn, and D. Dinkler, "A monolithic approach to fluid–structure interaction using space–time finite elements," *Computer methods in applied mechanics and engineering*, vol. 193, no. 23, pp. 2087–2104, 2004.

[2] C. Michler, S. Hulshoff, E. Van Brummelen, and R. De Borst, "A monolithic approach to fluid–structure interaction," *Computers & fluids*, vol. 33, no. 5, pp. 839–848, 2004.

[3] C. A. Felippa, K. Park, and C. Farhat, "Partitioned analysis of coupled mechanical systems," *Computer methods in applied mechanics and engineering*, vol. 190, no. 24, pp. 3247–3270, 2001.

[4] H. G. Matthies and J. Steindorf, "Partitioned strong coupling algorithms for fluid–structure interaction," *Computers & Structures*, vol. 81, no. 8, pp. 805–812, 2003.

[5] P. Causin, J.-F. Gerbeau, and F. Nobile, "Added-mass effect in the design of partitioned algorithms for fluid–structure problems," *Computer methods in applied mechanics and engineering*, vol. 194, no. 42, pp. 4506–4527, 2005.

[6] C. Förster, W. A. Wall, and E. Ramm, "Artificial added mass instabilities in sequential staggered coupling of nonlinear structures and incompressible viscous flows," *Computer methods in applied mechanics and engineering*, vol. 196, no. 7, pp. 1278–1293, 2007.

[7] K. Wang, P. Lea, and C. Farhat, "A computational framework for the simulation of high-speed multi-material fluid–structure interaction problems with dynamic fracture," *International Journal for Numerical Methods in Engineering*, vol. 104, no. 7, pp. 585–623, 2015.

[8] V. Lakshminarayan, C. Farhat, and A. Main, "An embedded boundary framework for compressible turbulent flow and fluid–structure computations on structured and unstructured grids," *International Journal for Numerical Methods in Fluids*, vol. 76, no. 6, pp. 366–395, 2014.

[9] C. Farhat, K. Wang, A. Main, S. Kyriakides, L.-H. Lee, K. Ravi-Chandar, and T. Belytschko, "Dynamic implosion of underwater cylindrical shells: experiments and computations," *International Journal of Solids and Structures*, vol. 50, no. 19, pp. 2943–2961, 2013.

[10] C. Farhat and V. K. Lakshminarayan, "An ale formulation of embedded boundary methods for tracking boundary layers in turbulent fluid–structure interaction problems," *Journal of Computational Physics*, vol. 263, pp. 53–70, 2014.

[11] P. D. Lea, C. Farhat, and K. G. Wang, "A fluid-structure coupled computational framework for fluid-induced failure and fracture," in *ASME 2015 34th International Conference on Ocean, Offshore and Arctic Engineering*, pp. V05BT04A014–V05BT04A014, American Society of Mechanical Engineers, 2015.

[12] K. G. Wang, P. Lea, A. Main, O. McGarity, and C. Farhat, "Predictive simulation of underwater implosion: Coupling multi-material compressible fluids with cracking structures," in *ASME 2014 33rd International Conference on Ocean, Offshore and Arctic Engineering*, pp. V08AT06A028–V08AT06A028, American Society of Mechanical Engineers, 2014.

[13] S. E. Turner and J. M. Ambrico, "Underwater implosion of cylindrical metal tubes," *Journal of Applied Mechanics*, vol. 80, no. 1, p. 011013, 2013.

[14] T. Moyer, J. Stergiou, G. Reese, J. Luton, and N. Abboud, "Navy enhanced sierra

mechanics (nesm): Toolbox for predicting navy shock and damage," *Computing in Science & Engineering*, vol. 18, no. 6, pp. 10–18, 2016.

[15] G. Guidoboni, R. Glowinski, N. Cavallini, and S. Canic, "Stable loosely-coupled-type algorithm for fluid–structure interaction in blood flow," *Journal of Computational Physics*, vol. 228, no. 18, pp. 6916–6937, 2009.

[16] M. Bukač, S. Čanić, R. Glowinski, J. Tambača, and A. Quaini, "Fluid–structure interaction in blood flow capturing non-zero longitudinal structure displacement," *Journal of Computational Physics*, vol. 235, pp. 515–541, 2013.

[17] S. Canic, B. Muha, and M. Bukac, "Stability of the kinematically coupled β-scheme for fluid-structure interaction problems in hemodynamics," *International journal of numerical analysis and modeling*, vol. 12, no. 1, pp. 54–80, 2015.

[18] M. A. Fernández, J.-F. Gerbeau, and C. Grandmont, "A projection algorithm for fluid–structure interaction problems with strong added-mass effect," *Comptes Rendus Mathematique*, vol. 342, no. 4, pp. 279–284, 2006.

[19] S. Badia, F. Nobile, and C. Vergara, "Fluid–structure partitioned procedures based on robin transmission conditions," *Journal of Computational Physics*, vol. 227, no. 14, pp. 7027–7051, 2008.

[20] M. A. Fernández, J. Mullaert, and M. Vidrascu, "Explicit robin–neumann schemes for the coupling of incompressible fluids with thin-walled structures," *Computer Methods in Applied Mechanics and Engineering*, vol. 267, pp. 566–593, 2013.

[21] M. A. Fernández, M. Landajuela, and M. Vidrascu, "Fully decoupled time-marching schemes for incompressible fluid/thin-walled structure interaction," *Journal of Computational Physics*, vol. 297, pp. 156–181, 2015.

[22] L. Li, W. Henshaw, J. Banks, D. Schwendeman, and A. Main, "A stable partitioned fsi algorithm for incompressible flow and deforming beams," *Journal of Computational Physics*, vol. 312, pp. 272–306, 2016.

[23] B. E. Griffith and C. S. Peskin, "On the order of accuracy of the immersed boundary method: Higher order convergence rates for sufficiently smooth problems," *Journal of Computational Physics*, vol. 208, no. 1, pp. 75–105, 2005.

[24] J. Degroote, "On the similarity between dirichlet–neumann with interface artificial compressibility and robin–neumann schemes for the solution of fluid-structure interaction problems," *Journal of computational physics*, vol. 230, no. 17, pp. 6399–6403, 2011.

[25] F. Nobile and C. Vergara, "Partitioned algorithms for fluid-structure interaction problems in haemodynamics," *Milan journal of mathematics*, vol. 80, no. 2, pp. 443–467, 2012.

[26] D. Drikakis and W. Rider, *High-resolution methods for incompressible and low-speed flows*. Springer Science & Business Media, 2006.

[27] E. H. Twizell, A. B. Gumel, and M. Arigu, "Second-order, l 0-stable methods for the heat equation with time-dependent boundary conditions," *Advances in Computational Mathematics*, vol. 6, no. 1, pp. 333–352, 1996.

[28] Y.-H. Tseng and J. H. Ferziger, "A ghost-cell immersed boundary method for flow in complex geometry," *Journal of computational physics*, vol. 192, no. 2, pp. 593–623, 2003.

[29] Z. Jomaa and C. Macaskill, "Numerical solution of the 2d poisson equation on an irregular domain with robin boundary conditions," *ANZIAM Journal*, vol. 50, pp. 413–428, 2008.

[30] Z. Jomaa and C. Macaskill, "The shortley–weller embedded finite-difference method for the 3d poisson equation with mixed boundary conditions," *Journal of Computational Physics*, vol. 229, no. 10, pp. 3675–3690, 2010.

[31] T. Belytschko, W. K. Liu, B. Moran, and K. Elkhodary, *Nonlinear finite elements for continua and structures*. John wiley & sons, 2013.

[32] A. Main, "A study of fluid-structure interaction on overlapping grids with a focus on flexible beams," tech. rep., Technical Report LLNL-TR-643858, Lawrence Livermore National Laboratory, 2013.

[33] M. Schäfer, S. Turek, F. Durst, E. Krause, and R. Rannacher, "Benchmark computations of laminar flow around a cylinder," in *Flow simulation with high-performance computers II*, pp. 547–566, Springer, 1996.

[34] C.-C. Liao, Y.-W. Chang, C.-A. Lin, and J. McDonough, "Simulating flows with moving rigid boundary using immersed-boundary method," *Computers & Fluids*, vol. 39, no. 1, pp. 152–167, 2010.

[35] S. Turek and J. Hron, "Proposal for numerical benchmarking of fluid-structure interaction between an elastic object and laminar incompressible flow," in *Fluid-structure interaction*, pp. 371–385, Springer, 2006.

[36] F.-B. Tian, H. Dai, H. Luo, J. F. Doyle, and B. Rousseau, "Fluid–structure interaction involving large deformations: 3d simulations and applications to biological systems," *Journal of computational physics*, vol. 258, pp. 451–469, 2014.

[37] R. Bhardwaj and R. Mittal, "Benchmarking a coupled immersed-boundary-finite-element solver for large-scale flow-induced deformation," *AIAA journal*, vol. 50, no. 7, pp. 1638–1642, 2012.

[38] J. W. Banks, W. D. Henshaw, and D. W. Schwendeman, "An analysis of a new stable partitioned algorithm for fsi problems. part ii: Incompressible flow and structural shells," *Journal of Computational Physics*, vol. 268, pp. 399–416, 2014.

[39] C. Farhat, K. G. Van der Zee, and P. Geuzaine, "Provably second-order time-accurate loosely-coupled solution algorithms for transient nonlinear computational aeroelasticity," *Computer methods in applied mechanics and engineering*, vol. 195, no. 17, pp. 1973–2001, 2006.

[40] C. Farhat, A. Rallu, K. Wang, and T. Belytschko, "Robust and provably second-order explicit–explicit and implicit–explicit staggered time-integrators for highly non-linear compressible fluid–structure interaction problems," *International Journal for Numerical Methods in Engineering*, vol. 84, no. 1, pp. 73–107, 2010.

Chapter 3

A Spatially Varying Robin Interface Condition for Fluid-Structure Coupled Simulations

(Submitted to *International Journal for Numerical Methods in Engineering*, under review)

S. Cao [a], G. Wang [a], K. G. Wang [a]

[a] Department of Aerospace and Ocean Engineering, Virginia Polytechnic Institute and State University, Blacksburg, VA 24061, United States

My coauthor Dr. Guangyao Wang contributed Section 3.1, 3.3, 3.6 in this chapter.

Abstract

We present a spatially varying Robin interface condition for solving fluid-structure interaction problems involving incompressible fluid flows and non-uniform flexible structures. Recent studies have shown that for uniform structures with constant material and geometric properties, a constant one-parameter Robin interface condition can improve the stability and accuracy of partitioned numerical solution procedures. In this work, we generalize the parameter to a spatially varying function that depends on the structure's local material and geometric properties, without varying the exact solution of the coupled fluid-structure system. We present an algorithm to implement the Robin interface condition in an embedded boundary method for coupling a projection-based incompressible viscous flow solver with a nonlinear finite element structural solver. We demonstrate the numerical effects of the spatially varying Robin interface condition using two example problems: a simplified model problem featuring a non-uniform Euler-Bernoulli beam interacting with an inviscid flow, and a generalized Turek-Hron problem featuring a non-uniform, highly flexible beam interacting with a viscous laminar flow. Both cases show that a spatially varying Robin interface condition can clearly improve numerical accuracy (by up to 2 orders of magnitude in one instance) for the same computational cost. Using the second example problem, we also demonstrate and compare two models for determining the local value of the combination function in the Robin interface condition.

Keywords

fluid-structure interaction, partitioned procedure, Robin interface condition, embedded boundary method, incompressible flow, added mass effect

3.1 Introduction

Extensive research has been devoted to developing partitioned procedures to couple computational fluid and structural dynamics solvers for simulating fluid-structure interaction (FSI) problems [1, 2, 3, 4, 5]. A common approach is to enforce the kinematic interface condition, i.e. the continuity of velocity across the fluid-structure interface, as a Dirichlet boundary condition in the fluid solver, and to enforce the dynamic interface condition, i.e. the continuity of stress, as a Neumann boundary condition in the structural solver. This type of Dirichlet-Neumann partitioned procedures have been used to simulate a broad range of FSI problems, including problems with large structural deformation, compressible flow, shock waves, and fluid-induced instabilities and failures (e.g., [6, 7, 8, 9, 10, 11])

Nonetheless, a well-known issue of Dirichlet-Neumann partitioned procedures is that for problems involving incompressible flow and strong added mass effect (e.g., heavy fluid, thin/slender structure), the scheme becomes unstable, regardless of the spatial and temporal discretization schemes used in the fluid and structural solvers. This issue, often referred to as the numerical (or artificial) added mass effect, has been formulated using simplified

model problems [12, 13]. Specifically, Causin *et al.* [12] showed that a partitioned procedure becomes unconditionally unstable when the structure-to-fluid density ratio is below a threshold or the structure has a slender shape. Förster *et al.* [13] also investigated the stability criterion for several different temporal discretization schemes, and showed that they all become unconditionally unstable under strong added mass effect. A widely used approach to mitigate the numerical added mass effect is to perform subiterations between the fluid and structural solvers in the fashion of the Gauss-Seidel method [14, 15, 16, 17]. The drawback of this approach is obvious: it multiplies the computational cost by the number of subiterations. For example, Badia *et al.* [16] showed that to simulate a pressure wave propagating in a deformable pipe, a Dirichlet-Neumann partitioned procedure requires more than 100 subiterations per time step when the structure-to-fluid density ratio is equal to one.

Over the past decade, several research teams have investigated the use of Robin interface condition to mitigate the numerical added mass effect [18, 19, 5, 20, 21, 22, 23, 24, 25, 26, 27]. The basic idea is to substitute the kinematic interface condition by its linear combination with the dynamic interface condition. The resulting Robin-Neumann interface conditions are mathematically equivalent to the original Dirichlet-Neumann conditions, as long as the combination factor — denoted by α_f in this paper and several others — is nonzero. It has been shown that when α_f is carefully chosen, a Robin-Neumann partitioned procedure can eliminate the requirement of subiteration or reduce the number needed to achieve stability. For example, Badia *et al.* [18] proposed to design α_f based on simplified model equations (e.g., a linear piston), and have shown that for an example problem with a uniform mem-

brane, a speed-up of up to one order of magnitude can be achieved. Nobile *et al.* [19, 5, 20] and Fernandez *et al.* [21, 22] have introduced the Robin interface condition to different types of partitioned procedures and fluid/structural governing equations, and demonstrated their performance in the context of blood flow - vessel wall interaction. To solve FSI problems involving complex geometry and large deformation, Cao *et al.* [23] have developed an algorithm to enforce the Robin interface condition using an embedded boundary method. They have also shown that when choosing the value of α_f, there is a trade-off: smaller values of α_f tend to improve numerical stability, yet deteriorate the accuracy of the numerical solution. Also, Li *et al.* [24] have introduced the Robin interface condition to the overset mesh framework. Basting *et al.* [25] have implemented it in an Arbitrary Lagrangian-Eulerian (ALE) framework with a variational mesh optimization algorithm. More generally, the idea of constructing a Robin interface condition to couple different physical domains has been applied to solve other multiphysics problems, such as fluid-structure-thermal interaction [28] and multiscale fracture mechanics [29].

Notably, previous studies on the use of Robin interface condition for fluid-structure coupling have focused on uniform structures with globally constant material and geometric properties. Examples include uniform beams and thin-walled tubes with constant thickness, density and elastic moduli. Moreover, previous studies have assumed that the Robin combination factor α_f is also a constant; while at the same time, several authors have suggested that in order to mitigate the numerical added mass effect, the value of α_f must be determined based on the material and geometry of the specific problem being solved (e.g., [18, 26, 23]). In this work,

we generalize α_f to a spatially varying function, and investigate its numerical effects for FSI problems involving structures with spatially varying material properties. This study is motivated by three considerations. First, in real-world FSI problems, the structure of interest is often non-uniform, and may have complex geometry. For example, the density and the thickness of a thin-walled structure, either man-made or natural, often takes different values at different locations. Second, the previous findings mentioned above naturally suggest that if the geometric and material properties of the structure vary from one region to another, a globally constant α_f may not be optimal. It may be beneficial to generalize α_f to a variable function. Third, after generalizing α_f to a spatially varying function, the Robin-Neumann interface conditions remain mathematically equivalent to the original Dirichlet-Neumann conditions (as long as $\alpha_f \neq 0$). In other words, the generalization does not change the true solution of the coupled fluid-structure system.

More specifically, in this paper we address the following questions.

- Would a spatially varying combination function, $\alpha_f(\mathbf{X})$, outperform a constant α_f in terms of numerical accuracy and/or stability?
- If the answer to the above question is yes, how to design the function $\alpha_f(\mathbf{X})$ in order to achieve the improvement?

The remainder of this paper is organized as follows. In Section 3.2, we describe the context of this work by specifying the fluid and structural governing equations, constitutive models, and the Robin-Neumann interface conditions. Briefly speaking, we consider incompressible

laminar fluid flows interacting with thin, elastic structures. Next, in Section 3.3 we investigate the effects of spatially varying $\alpha_f(\mathbf{X})$ using a simplified model problem, in which the structure is an Euler-Bernoulli beam and the fluid domain is assumed to be fixed in time. Further, in Section 3.4, we consider a more realistic model problem, that is, a generalized Turek-Hron problem in which the flexible beam consists of multiple segments with different material properties. Using this example, we present the implementation of spatially varying $\alpha_f(\mathbf{X})$ in an embedded boundary framework, and discuss its numerical effects. In Section 3.5, we present and compare two model equations for determining the local value of the spatially varying combination function. Finally, we provide a few concluding remarks in Section 3.6.

3.2 Physical Model

3.2.1 Fluid and structural governing equations

We consider an incompressible viscous fluid flow interacting with a deformable structure, possibly with complex geometry and spatially varying material properties. The physical model couples the fluid governing equations defined in Ω_f and the structural governing equations defined in Ω_s (Figure 3.1). The fluid-structure interface, Σ, is thus defined by $\Sigma = \partial\Omega_f \cap \partial\Omega_s$. In this paper, we further assume that the fluid is Newtonian and the flow is laminar. Hence, its dynamics is governed by the following incompressible Navier-Stokes

(N-S) equations.

$$\mathscr{F}(\mathbf{U}, P) = 0 := \begin{cases} \nabla \cdot \mathbf{U} = 0 & \text{in } \Omega_f, \quad (3.1a) \\ \dfrac{\partial \mathbf{U}}{\partial t} + \mathbf{U} \cdot \nabla \mathbf{U} - \nu \Delta \mathbf{U} + \dfrac{1}{\rho_f} \nabla P = 0 & \text{in } \Omega_f, \quad (3.1b) \end{cases}$$

where t denotes time, ρ_f is the fluid density, $\mathbf{U}$ is the fluid velocity vector, P is the fluid pressure and ν the kinematic viscosity. On the outer boundary of the fluid domain, different types of boundary conditions such as no-slip wall, inlet and outlet conditions may be applied, which can be written collectively as

$$\mathscr{B}(\mathbf{U}, P) = 0 \qquad \text{on } \partial\Omega_f \setminus \Sigma. \tag{3.2}$$

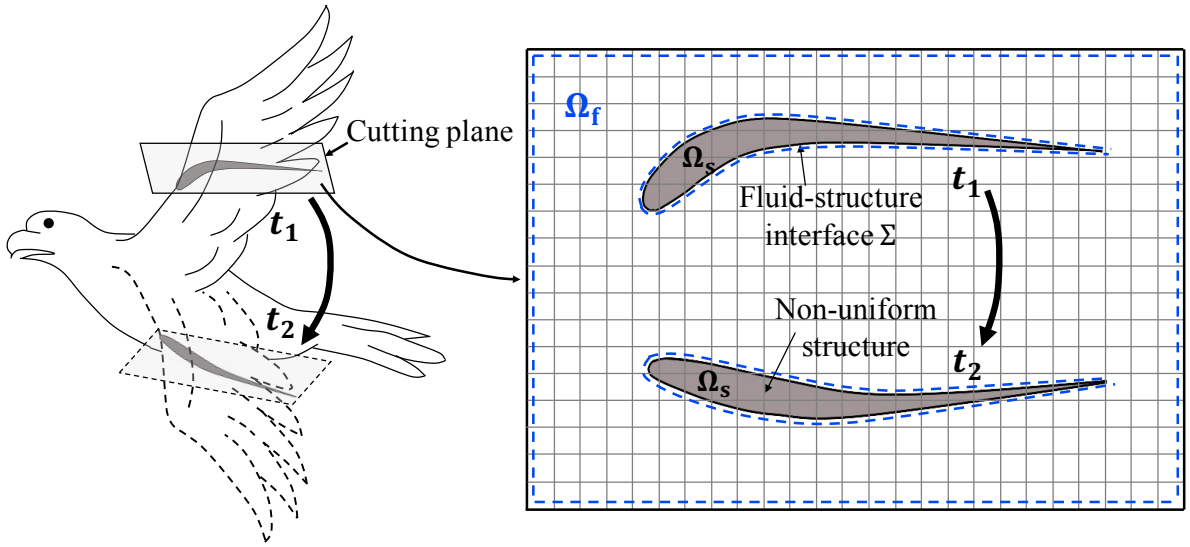

Figure 3.1: A fluid-structure interaction problem.

The structure is assumed to be elastic, and can have spatially varying material properties.

To account for the possibility of large deformation, geometric nonlinearity is considered. Therefore, the dynamic equilibrium of the structure can be formulated as

$$\mathscr{S}(\mathbf{d}(\mathbf{X},t)) = 0 := \rho_s(\mathbf{X})\frac{\partial^2 \mathbf{d}(\mathbf{X},t)}{\partial t^2} - \nabla\cdot\left(J^{-1}\mathbf{F}\mathbf{S}\mathbf{F}^T\right) - \rho_s(\mathbf{X})\,\mathbf{b}(\mathbf{X},t) = 0 \qquad \text{in}\,\Omega_s, \tag{3.3}$$

where $\mathbf{X}$ denotes the material coordinates, $\mathbf{d}$ denotes displacement, ρ_s denotes mass density, $\mathbf{S}$ is the second Piola-Kirchhoff (PK2) stress tensor, $\mathbf{F}$ is the deformation gradient, $J = \det \mathbf{F}$, and $\mathbf{b}$ denotes the body force per unit mass which is assumed to be zero here. In this work, we apply the St. Venant-Kirchhoff constitutive model, given by

$$\mathbf{S} = \lambda_s tr(\mathbf{E})\mathbf{I} + 2\mu_s\mathbf{E}, \tag{3.4}$$

where $\mathbf{I}$ is the identity matrix, and $\mathbf{E} = \frac{1}{2}(\mathbf{F}^T\mathbf{F} - \mathbf{I})$. λ_s and μ_s are the Lamé coefficients.

The fluid-structure interface is assumed to be impermeable. Thus, the fluid and structural governing equations are coupled by a kinematic interface condition, i.e. the continuity of velocity (Eq. (3.5a)), and a dynamic interface condition, i.e. the continuity of stress (Eq. (3.5b))

$$\mathbf{U} = \frac{\partial \mathbf{d}}{\partial t} \qquad \text{on}\,\Sigma, \tag{3.5a}$$

$$\sigma_f\mathbf{n} = \sigma_s\mathbf{n} \qquad \text{on}\,\Sigma, \tag{3.5b}$$

where $\mathbf{n}$ denotes the unit normal pointing towards Ω_s. σ_f denotes the fluid stress tensor, given by $\sigma_f = -P\mathbf{I} + 2\mu_f\mathbf{e}$, where $\mathbf{e}$ is the fluid strain rate tensor, and μ_f denotes the dynamic

viscosity. σ_s denotes the Cauchy stress tensor of the structure, which can be related to PK2 stress by

$$\sigma_s = J^{-1}\mathbf{F}\mathbf{S}\mathbf{F}^T.$$

3.2.2 Spatially varying Robin interface condition

The Dirichlet interface condition, Eq. (3.5a), can be substituted by its linear combination with the Neumann interface condition, Eq. (3.5b), yielding a Robin interface condition. In this way, we obtain a pair of Robin-Neumann interface conditions[1], i.e.

$$\alpha_f(\mathbf{X})\frac{D\mathbf{U}}{Dt} + \sigma_f\mathbf{n} = \alpha_f(\mathbf{X})\frac{\partial^2\mathbf{d}}{\partial t^2} + \sigma_s\mathbf{n} \qquad \text{on } \Sigma, \tag{3.6a}$$

$$\sigma_f\mathbf{n} = \sigma_s\mathbf{n} \qquad \text{on } \Sigma, \tag{3.6b}$$

where $D/Dt = \partial/\partial t + \mathbf{U}\cdot\nabla$, and α_f is the linear combination parameter. As mentioned in Section 3.1, previous studies have assumed α_f to be a constant parameter. Here, we generalize it to be a spatially varying function.

Equipped with this new pair of interface conditions, the fluid and structural sub-systems can

[1]We note that in this work, as well as some previous studies (e.g., [24, 22]), the Robin condition combines the time derivative of Eq. (3.5a) with Eq. (3.5b), whereas in some other studies (e.g., [18]), the Robin condition directly combines Eq. (3.5a) with Eq. (3.5b).

be written as

$$\text{Fluid:}\begin{cases} \mathscr{F}(\mathbf{U},P)=0 & \text{in } \Omega_f & \text{(3.7a)}\\ \mathscr{B}(\mathbf{U},P)=0 & \text{on } \partial\Omega_f \setminus \Sigma & \text{(3.7b)}\\ \alpha_f(\mathbf{X})\dfrac{D\mathbf{U}}{Dt}+\sigma_f\mathbf{n}=\alpha_f(\mathbf{X})\dfrac{\partial^2\mathbf{d}}{\partial t^2}+\sigma_s\mathbf{n} & \text{on } \Sigma & \text{(3.7c)}\end{cases}$$

$$\text{Structure:}\begin{cases} \mathscr{S}(\mathbf{d})=0 & \text{in } \Omega_s & \text{(3.7d)}\\ \sigma_s\mathbf{n}=\sigma_f\mathbf{n} & \text{on } \Sigma & \text{(3.7e)}\end{cases}$$

Next, we investigate the effect of the generalized, spatially varying α_f on the stability and accuracy of partitioned solution procedures, starting with a simplified model problem.

3.3 A simplified model problem

3.3.1 Model setup

We consider a simplified model problem, in which a linear inviscid incompressible flow interacts with a *non-uniform* Euler-Bernoulli beam. Figure 3.2 presents a schematic drawing of the problem setup. The structure is a simply-supported Euler-Bernoulli beam, featuring lengthwise variation of density, $\rho_s(x)$ (Eq. (3.8a)). The other relevant material and geometric parameters — namely Young's modulus (E), and the width (b) and thickness (h) of the beam's cross section — are still assumed to be constant parameters. The fluid domain is a

rectangular box underneath the beam, i.e. $\Omega_f = (0, L) \times (0, H)$. Given the small deformation of the beam, we assume that Ω_f does not change in time. Also, assuming an inviscid flow with a velocity field that has zero mean (in time) and small disturbance, the middle two terms in Eq. (3.1b) can be dropped, which leads to Eq. (3.8b). The left and right boundaries are assumed to be periodic (Eq. (3.8e)), while the bottom boundary is assumed to be a wall (Eq. (3.8d)).

$$\begin{cases} EI\dfrac{\partial^4 W}{\partial x^4} + \rho_s(x) bh \dfrac{\partial^2 W}{\partial t^2} = f(x,t) & \text{in } (0,T) \times \Omega_s \quad (3.8a) \\ \rho_f \dfrac{\partial \mathbf{U}}{\partial t} + \nabla P = 0 & \text{in } (0,T) \times \Omega_f \quad (3.8b) \\ \nabla \cdot \mathbf{U} = 0 & \text{in } (0,T) \times \Omega_f \quad (3.8c) \\ \mathbf{U} \cdot \mathbf{n} = 0 & \text{on } \Gamma_B \quad (3.8d) \\ \dfrac{\partial P}{\partial \mathbf{n}}\big|_{\Gamma_L} = \dfrac{\partial P}{\partial \mathbf{n}}\big|_{\Gamma_R}, P\big|_{\Gamma_L} = P\big|_{\Gamma_R}, & \quad (3.8e) \end{cases}$$

Here, W denotes the transverse displacement of the beam. ρ_f, U, and P denote fluid density, velocity, and pressure, respectively. Γ_L, Γ_R and Γ_B denote the left, right and bottom boundaries of Ω_f, respectively. f denotes the flow-induced force on the beam.

Since the beam is simply supported on both ends, we have

$$W(0,t) = W(L,t) = 0 \qquad \text{and} \qquad \frac{\partial^2 W(0,t)}{\partial x^2} = \frac{\partial^2 W(L,t)}{\partial x^2} = 0, \qquad \forall t > 0. \tag{3.9}$$

On the fluid-structure interface (Σ), the kinematic and dynamic interface conditions are

given by

$$\mathbf{U} \cdot \mathbf{n} = \frac{\partial W}{\partial t} \qquad \text{and} \qquad f = Pb \qquad \text{on } \Sigma, \tag{3.10}$$

where $\mathbf{n}$ is the unit surface normal vector pointing towards the structure.

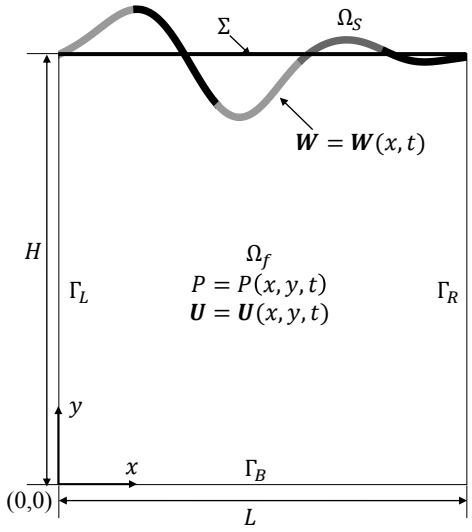

Figure 3.2: A simplified fluid-structure interaction model.

Combining Eqs. (3.8b) and (3.8c), we can eliminate the fluid velocity $\mathbf{U}$ from the system. Also, we combine the kinematic and dynamic interface conditions into a Robin interface condition, with a spatially varying combination factor $\alpha_f(x)$. After these manipulations, we obtain the following system of equations.

$$
\begin{cases}
EI\dfrac{\partial^4 W}{\partial x^4} + \rho_s(x)bh\dfrac{\partial^2 W}{\partial t^2} = f(x,t) & \text{in } (0,T)\times\Omega_s & \text{(3.11a)}\\
W = 0, \dfrac{\partial^2 W}{\partial x^2} = 0, & \text{at } x=0 \text{ and } x=L & \text{(3.11b)}\\
\nabla^2 P = 0 & \text{in } (0,T)\times\Omega_f & \text{(3.11c)}\\
\dfrac{\partial P}{\partial y} = 0 & \text{on } \Sigma_B & \text{(3.11d)}\\
\dfrac{\partial P}{\partial y}\big|_{\Gamma_L} = \dfrac{\partial P}{\partial y}\big|_{\Gamma_R}, P\big|_{\Gamma_L} = P\big|_{\Gamma_R}, & & \text{(3.11e)}\\
\alpha_f(x)\dfrac{\partial P}{\partial y} + Pb = -\alpha_f(x)\rho_f\dfrac{\partial^2 W}{\partial t^2} + f & \text{on } \Sigma & \text{(3.11f)}\\
f = Pb. & \text{on } \Sigma & \text{(3.11g)}
\end{cases}
$$

We consider two representative cases in which the beam's density is defined to be a smoothed step function.

- Case 1 (Figure 3.3(a)): The beam's density, $\rho_s(x)$, features two distinct values with a smooth transition in between. It is defined by

$$\rho_s(x) = \frac{\rho_{s1} + e^{\gamma x - c}\rho_{s2}}{e^{\gamma x - c} + 1}, \tag{3.12}$$

  where $\rho_{s1} = 50$ kg/m^3 and $\rho_{s2} = 4000$ kg/m^3 define the two density values, i.e. the two "steps". c and γ are two parameters that control the location and width of the transition zone. Here, $c = 100$, $\gamma = 200$ m^{-1}.

- Case 2 (Figure 3.3(b)): The beam's density, $\rho_s(x)$, features six steps. It is defined by

$$\rho_s(x) = \frac{\rho_s^{(k)} + e^{\gamma x - c^{(k)}} \rho_s^{(k+1)}}{e^{\gamma x - c^{(k)}} + 1}, \qquad \frac{(k-1)L}{5} \leq x \leq \frac{kL}{5}, \quad k = 1, 2, 3, 4, 5. \tag{3.13}$$

In this case, $\rho_s^{(1)} = 4000\ \text{kg/m}^3$, $\rho_s^{(2)} = 2025\ \text{kg/m}^3$, $\rho_s^{(3)} = 50\ \text{kg/m}^3$, $\rho_s^{(4)} = 1366.67\ \text{kg/m}^3$, $\rho_s^{(5)} = 2683.33\ \text{kg/m}^3$, and $\rho_s^{(6)} = 4000\ \text{kg/m}^3$. Also, $c^{(1)} = 20$, $c^{(2)} = 60$, $c^{(3)} = 100$, $c^{(4)} = 140$, and $c^{(5)} = 180$, $\gamma = 200\ \text{m}^{-1}$.

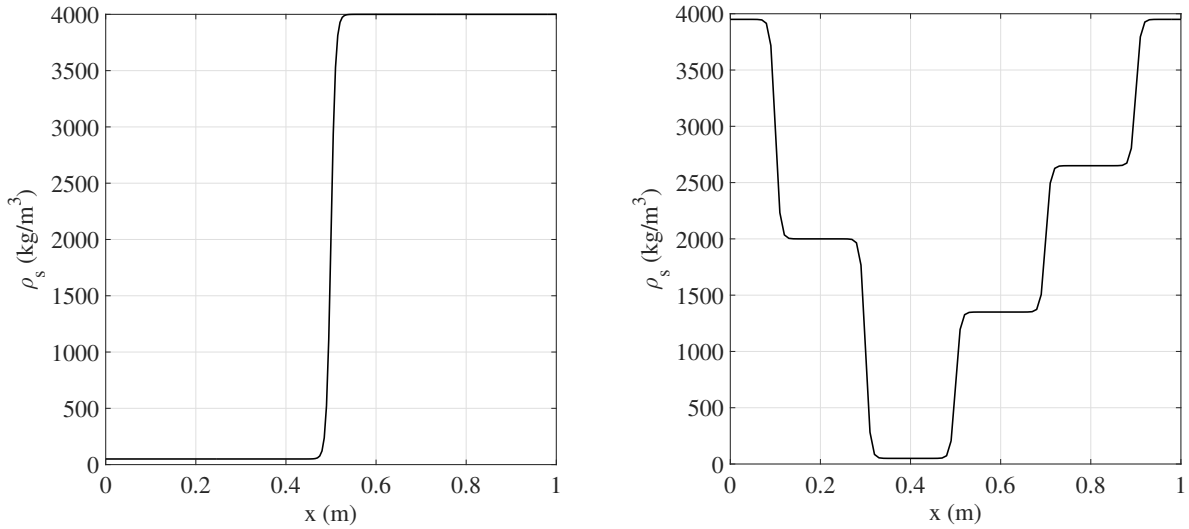

Figure 3.3: Two representative cases of non-uniform Euler-Bernoulli beam with spatially varying density. (a) Case 1. (b) Case 2.

In both cases, $E = 30$ GPa, $b = 0.01$ m, $h = 0.03$ m, $L = 1$ m, $H = 1$ m, and $\rho_f = 876\ \text{kg/m}^3$. The initial displacement and acceleration of the beam are set to zero. The initial value of velocity is defined by

$$v(x, 0) = v_0 \sin\left(\frac{2n\pi x}{L}\right), \tag{3.14}$$

where $v_0 = 17.28$ m/s and $n = 3$. In addition, the initial (dynamic) pressure of the fluid is set to zero.

We solve this model problem using a standard partitioned procedure. The two-dimensional Laplace equation of the fluid sub-system is solved using the five-point finite difference scheme. The structural equation is semi-discretized using a standard Galerkin finite element method, then integrated in time using the Hilbert-Hughes-Taylor α (HHT-α) method. Additional details of the numerical solution procedure are provided in Appendix 3.A.

Remarks:

- A simpler version of this problem, in which the beam has uniform density and α_f is a constant, has been solved both numerically and analytically (e.g., [30, 23]). Cao *et al.* [23] have derived the value of α_f that optimizes the trade-off between numerical stability and accuracy, i.e.

$$\alpha_{f,opt} = \frac{2}{\rho_f \left(\frac{1}{m_s} - \frac{1}{m_a} \right)}, \tag{3.15}$$

  where $m_s = \rho_s bh$ and $m_a = \dfrac{\rho_f b}{k \tanh(kH)}$ represent respectively the structural mass and the added mass of the fluid. The fact that $\alpha_{f,opt}$ depends on the structure's material and geometry (and how they compare with properties of the fluid flow) naturally suggests that for structures with spatially varying material properties or complex geometry, it may be advantageous to generalize α_f to a spatially varying function.

- In addition to the density of the beam, other parameters such as EI, b and h can also be generalized to spatially varying functions. We have tested some of these parameters. The results and findings obtained using a spatially varying density — to be presented in the next subsection — are found to be representative.

3.3.2 Numerical analysis: Constant α_f versus $\alpha_f(x)$

Case 1

Figures 3.4 and 3.5 show the converged numerical solution, which will be used as a reference for analyzing the effect of $\alpha_f(x)$ on accuracy. The accuracy of this reference solution has been verified by mesh convergence analysis and by comparison with the solution of a monolithic procedure, described briefly in Appendix A. Because of the spatial variation of the beam's density, the time history of mid-point deflection is not periodic (Figure 3.4), although the initial condition is a sine function. For the same reason, the magnitude of beam deflection and the fluid pressure are not symmetric with respect to the midline of the computational domain ($x = 0.5$ m).

Figures 3.6 and 3.7 present the solutions obtained using the Robin-Neumann interface conditions with different constant values of α_f, in comparison with the reference solution. Both the fluid and the structural meshes have a resolution of 0.01 m. The time step size is set to be relatively large — specifically, 2×10^{-6} s — such that numerical errors can be easily observed and compared. Three different choices of α_f are presented in the figure, specifically,

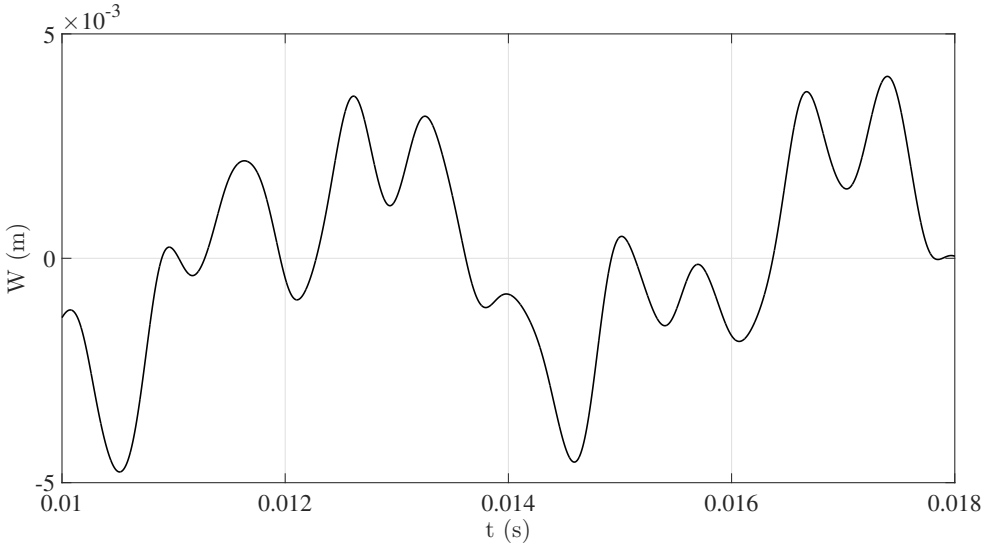

Figure 3.4: Converged solution of Case 1: Time history of beam displacement at the midpoint ($x = 0.50$ m).

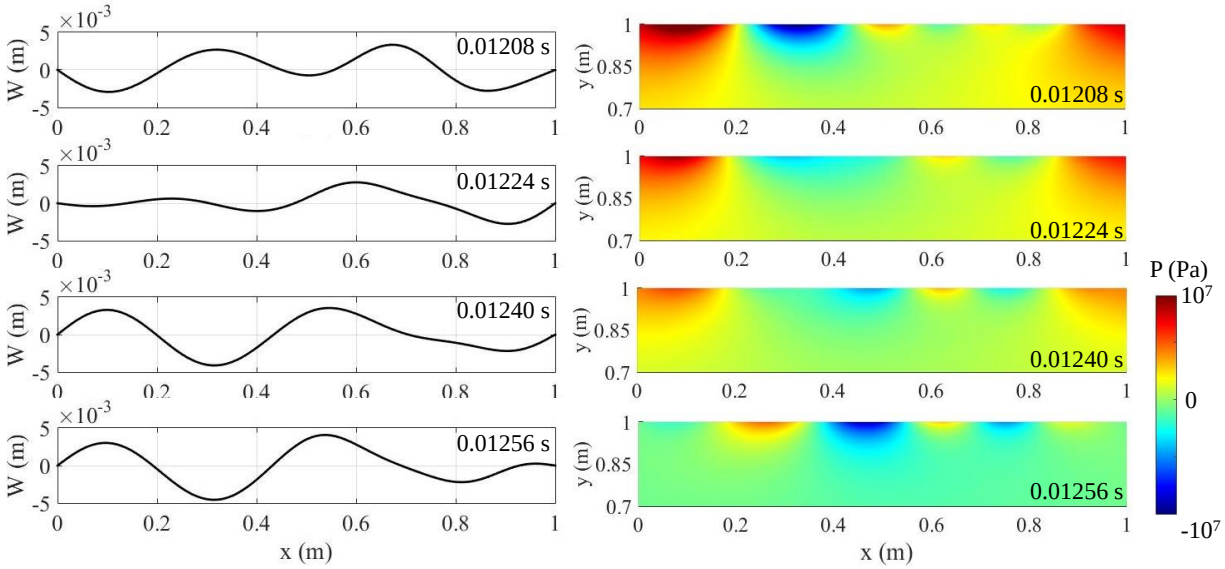

Figure 3.5: Snapshots of the converged solution of Case 1. Left: Beam deflection. Right: Fluid pressure. (Only the region above $y = 0.7$ m, where pressure varies significantly, is shown.)

3.0×10^{-5}, 4.0×10^{-5}, and 5.0×10^{-5} m^2 (for simplicity, we omit the unit m^2 for α_f in the rest of Section 3.3). Evidently, as α_f increases, the solution becomes more accurate. This is consistent with the result by Cao *et al.* [23] for a uniform beam with constant density. It is also notable that when α_f exceeds 5.0×10^{-5}, the numerical scheme becomes unconditionally unstable. For example, Figure 3.8 shows that with $\alpha_f = 5.1 \times 10^{-5}$, the solution blows up in less than 0.2 ms. Therefore, numerically we have found that for a specific pair of mesh resolution and time step size — which indicates a fixed computational cost — the most accurate solution that can be obtained using a constant α_f is given by $\alpha_f = 5.0 \times 10^{-5}$. The observed trade-off between accuracy and stability, when selecting a constant value for α_f, is also consistent with the finding of Cao *et al.* [23].

Next, we investigate the effects of a spatially varying $\alpha_f(x)$. Given that the beam density is a smoothed step function, we consider a simple model for $\alpha_f(x)$ that shares the same shape. Specifically, we define

$$\alpha_f(x) = \alpha_{f0} \frac{\rho_s(x)}{\rho_{s0}}, \tag{3.16}$$

where ρ_{s0} is the minimum value of density along the beam (50 kg/m^3 in this case), and α_{f0} is a constant value estimated based on ρ_{s0}. In this case, we set $\alpha_{f0} = 5 \times 10^{-5}$.

Figure 3.9 presents the relative error of the solution obtained using the above $\alpha_f(x)$, in comparison with the most accurate solution that can be obtained using a constant α_f, i.e. with $\alpha_f = 5.0 \times 10^{-5}$. Evidently, the use of a spatially varying function $\alpha_f(x)$ leads to a reduction of numerical error in both the fluid and the structural solutions. Specifically, the

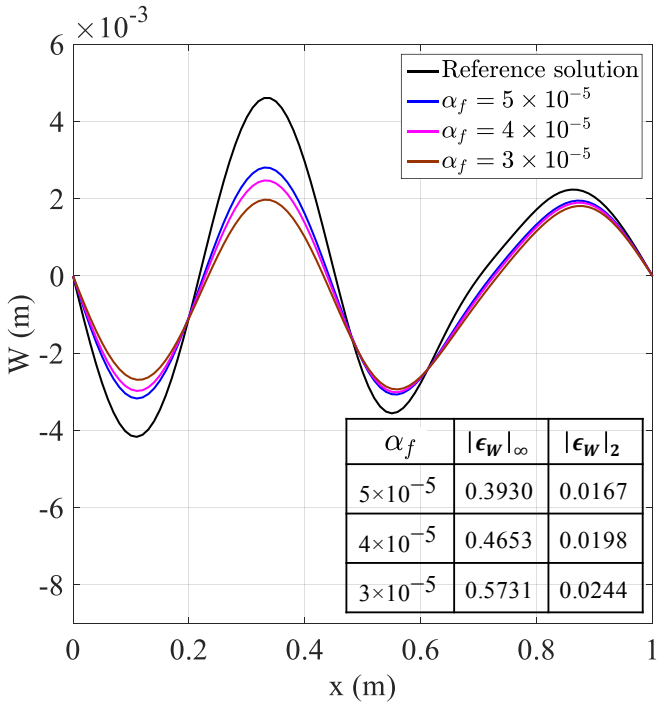

α_f	$\lvert\epsilon_W\rvert_\infty$	$\lvert\epsilon_W\rvert_2$
5×10^{-5}	0.3930	0.0167
4×10^{-5}	0.4653	0.0198
3×10^{-5}	0.5731	0.0244

Figure 3.6: Beam displacement at $t = 0.0015$ s obtained using different constant values of α_f, in comparison with the converged reference solution. ϵ_W denote the relative error in beam displacement normalized using their maximum values.

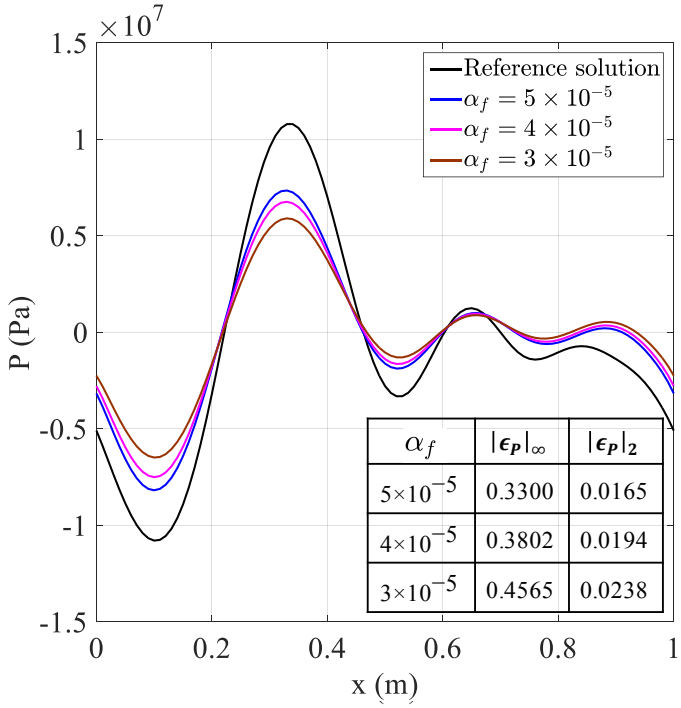

Figure 3.7: Fluid pressure at the fluid-structure interface obtained using different constant values of α_f, in comparison with the converged reference solution. ϵ_P denote the relative error in the fluid pressure at interface, normalized using their maximum values.

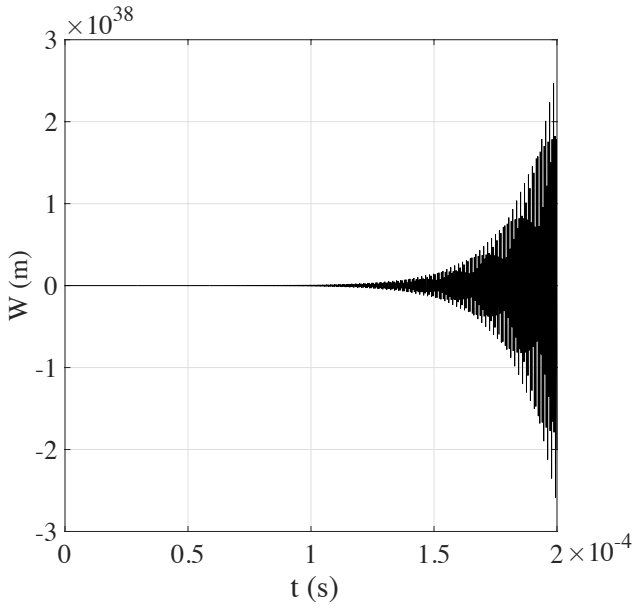

Figure 3.8: Time history of mid-point beam displacement obtained with $\alpha_f = 5.1 \times 10^{-5}$.

maximum relative error in beam deflection decreases by 21.09%, from 0.3930 to 0.3102, while in fluid pressure it decreases by 20.09%, from 0.3300 to 0.2637.

Case 2

For reference, Figure 3.10 shows a few snapshots of the converged fluid and structural solutions, which are independent of the choice of α_f.

When a constant α_f is applied, we find again, for fixed mesh resolution and time step size, the numerical solution becomes more accurate as the value of α_f increases, until α_f reaches a critical value, after which the solution blows up. For a 100-element structural mesh, a 100×100 fluid mesh, and a time step size of 2×10^{-6} s, this critical value is found to be 5.0×10^{-5}, same as in Case 1. This is likely because in both cases, the minimum value of

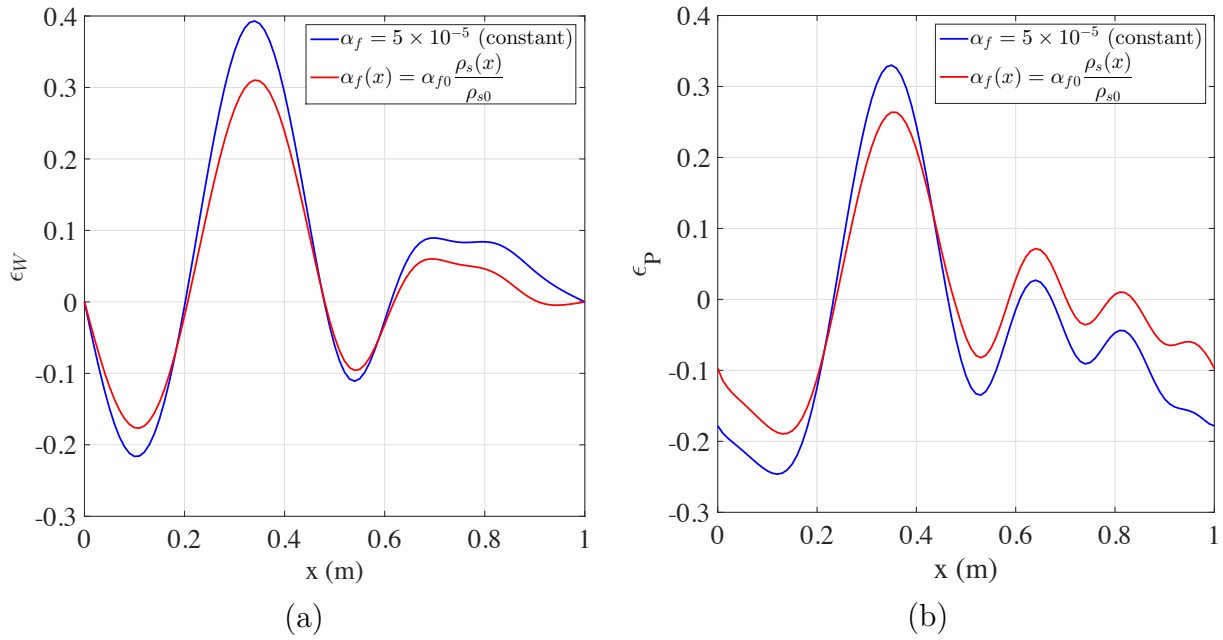

Figure 3.9: Comparison of constant α_f and a spatially varying function $\alpha_f(x)$ for Case 1. (a) Relative error in beam deflection. (b) Relative error in fluid pressure at interface (i.e. $y = 1$ m).

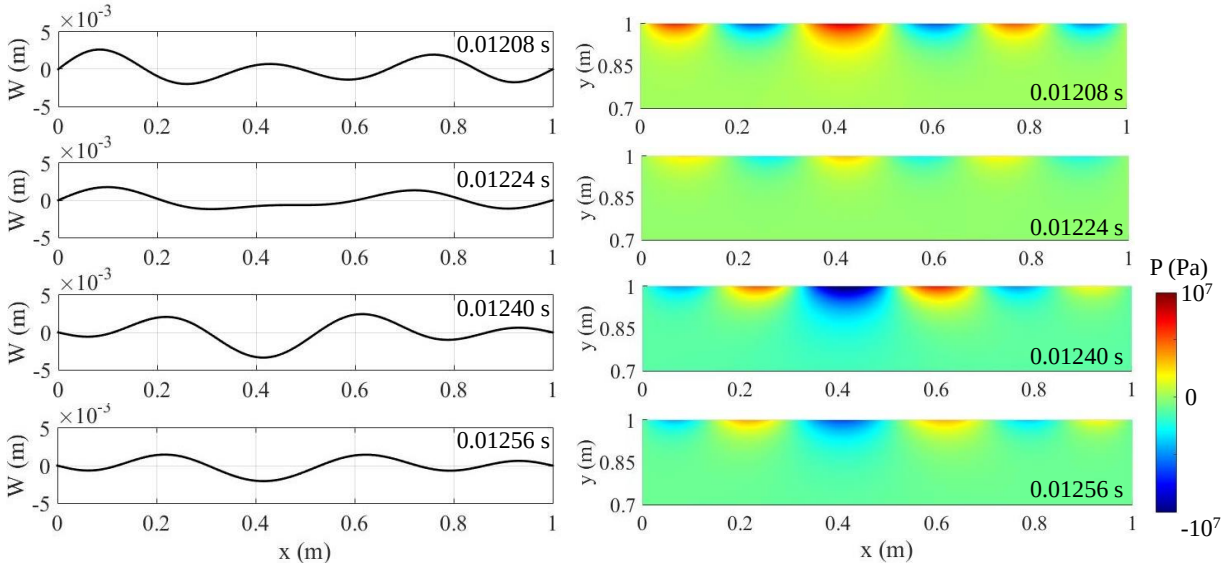

Figure 3.10: Snapshots of the converged solution of Case 2. Left: Beam deflection. Right: Fluid pressure. (Only the region above $y = 0.7$ m, where pressure varies significantly, is shown.)

the density function $\rho_s(x)$ are the same.

To investigate the effect of spatially varying $\alpha_f(x)$, we adopt the same model function introduced in Case 1, i.e. Eq. (3.16). Again, we set $\rho_{s0} = 50$ kg/m^3 and $\alpha_{f0} = 5.0 \times 10^{-5}$, based on the minimum value of the beam's density. Figure 3.11 compares the relative error in the structural and fluid solutions obtained using $\alpha_f(x)$ with the most accurate solution that can be obtained with a constant α_f, i.e., with $\alpha_f = 5.0 \times 10^{-5}$. Comparing with Figure 3.9 (Case 1), we find that the benefit of using a spatially varying $\alpha_f(x)$ is more significant in this case. Specifically, the maximum relative error in beam deflection and fluid pressure is reduced by 47.44% and 42.47%, respectively. Again, we note that this error reduction is achieved by exploiting the spatial variation of the structure's material property, with virtually no increase in computational cost.

3.4 A Modified Turek-Hron Model Problem

Based on the result obtained from the simplified model problem, we now move onto solving Eqs. (3.7) and investigating the effects of spatially varying Robin interface condition in a more realistic setting.

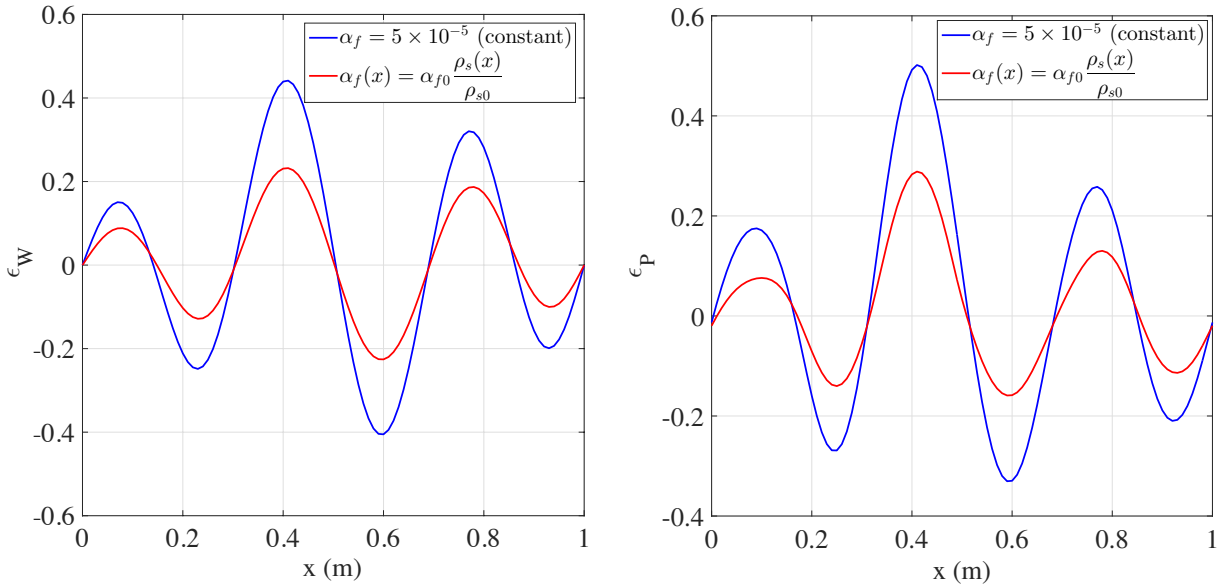

(a) (b)

Figure 3.11: Comparison of constant α_f and a spatially varying function $\alpha_f(x)$ for Case 2. (a) Relative error in beam deflection. (b) Relative error in fluid pressure at the interface (i.e. $y = 1$ m).

3.4.1 Problem description

We consider a two-dimensional laminar incompressible channel flow interacting with a non-uniform, nonlinear beam mounted on the back of a fixed cylinder. Figure 3.12 shows the geometry of the problem. It is similar to the well-known Turek-Hron benchmark problem [31], except that the attached beam considered here consists of two segments, denoted by Γ_A and Γ_B, with significantly different mass densities. Specifically, the structure-to-fluid density ratio, ρ_s/ρ_f, is 0.3 in Γ_A and 10.0 in Γ_B. This indicates that segment Γ_A is subjected to stronger added mass effect. At the inflow boundary of the fluid domain, the following

velocity profile is prescribed.

$$u\left(0,y,t\right)=1.5\bar{U}\frac{y\left(H-y\right)}{\left(H/2\right)^{2}},\qquad v\left(0,y,t\right)=0, \tag{3.17}$$

where u and v denote the velocity components in the x and y directions. H is the height of the fluid domain and $\bar{U}$ is the average inflow velocity. At the channel outlet (i.e. the right boundary of the fluid domain), a "do nothing" boundary condition is applied. The no-slip boundary condition is enforced on the top and bottom walls. At the beginning of the simulation, the beam is at rest and straight as shown in the figure. Specific parameter values involved in this problem are given in Table 3.1.

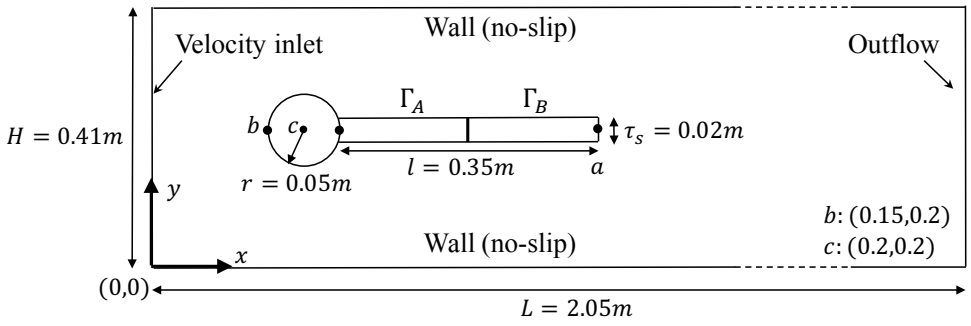

Figure 3.12: Geometry of the modified Turek-Hron benchmark problem.

	Segment Γ_A			Segment Γ_B			Fluid			
parameter	ρ_s $[kg/m^3]$	ν_s	μ_s $[kg/(ms^2)]$	ρ_s $[kg/m^3]$	ν_s	μ_s $[kg/(ms^2)]$	ρ_f $[kg/m^3]$	ν_f $[m^2/s]$	$\bar{U}$ $[m/s]$	Re
value	300	0.4	5.0×10^5	1.0×10^4	0.4	5.0×10^5	1×10^3	1×10^{-3}	1	100

Table 3.1: Parameters of the problem (ρ_s: density of the structure; ν_s: Poisson's ratio; μ_s: shear modulus; ρ_f: density of the fluid; ν_f: kinematic viscosity).

3.4.2 Numerical solution approach

We employ the fluid-structure coupled computational framework recently developed by Cao *et al.* [23]. The main components of this framework include a projection-based incompressible flow solver, a finite element structural dynamics solver, and an embedded boundary method to enforce the Robin transmission condition. The computational framework has been verified using the original Turek-Hron benchmark problem with a uniform beam [31]. In this work, we extend the computational framework to enable the use of spatially varying Robin interface condition, i.e. Eq. (3.7c), and apply it to solve the modified Turek-Hron problem.

Specifically, the coupling between the fluid and structural sub-systems is based on an implicit coupling scheme which solves the two sub-systems iteratively at each time step. The following equations are solved to advance the system from time t^n to t^{n+1}.

$$\text{Fluid:}\begin{cases} \mathscr{F}(\mathbf{U}_{k+1}^{n+1}, P_{k+1}^{n+1}) = 0 & \text{in } \Omega_f \quad (3.18a) \\ \mathscr{B}(\mathbf{U}_{k+1}^{n+1}, P_{k+1}^{n+1}) = 0 & \text{on } \partial\Omega_f \setminus \Sigma \quad (3.18b) \\ \alpha_f(\mathbf{X})\dfrac{D\mathbf{U}_{k+1}^{n+1}}{Dt} + \sigma_{f,k+1}^{n+1}\mathbf{n} = \alpha_f(\mathbf{X})\left(\dfrac{\partial^2 \mathbf{d}}{\partial t^2}\right)_k^{n^\bullet} + \sigma_{s,k}^{n^\bullet}\mathbf{n} & \text{on } \Sigma \quad (3.18c) \end{cases}$$

$$\text{Structure:}\begin{cases} \mathscr{S}(\mathbf{d}_{k+1}^{n+1}) = 0 & \text{in } \Omega_s \quad (3.18d) \\ \sigma_{s,k+1}^{n+1}\mathbf{n} = \sigma_{f,k}^{n^\bullet}\mathbf{n} & \text{on } \Sigma \quad (3.18e) \end{cases}$$

where k is the index of subiteration. Also,

$$n^\bullet = \begin{cases} n, & \text{if } k = 0, \\ n+1, & \text{otherwise.} \end{cases}$$

At the fluid-structure interface (Σ), the latest solution information (i.e. fluid traction, structural acceleration and stress) are exchanged between the fluid and structural solvers, leading to a Gauss-Seidel type iteration.

To advance the fluid sub-system, the incompressible N-S equations are solved using a six-step, finite-difference projection method [32] on a cell-centered, collocated Cartesian grid. The spatially varying Robin interface condition, Eq. (3.18c), is enforced on the fluid-structure interface using an embedded boundary method. Specifically, we first discretize Eq. (3.18c) in time by

$$\alpha_f(\mathbf{X})\left[\frac{\mathbf{U}_{k+1}^{n+1}-\mathbf{U}^n}{\Delta t}+(\mathbf{U}\cdot\nabla\mathbf{U})_k^{n^\bullet}\right]+\sigma_{f,k+1}^{n+1}\mathbf{n}=\alpha_f(\mathbf{X})\left(\frac{\partial^2\mathbf{d}}{\partial t^2}\right)_k^{n^\bullet}+\sigma_{s,k}^{n^\bullet}\mathbf{n} \qquad \text{on } \Sigma, \quad (3.19)$$

where the structural acceleration $\left(\partial^2\mathbf{d}/\partial t^2\right)$ is computed by the structural solver, then transferred to the fluid solver. Then, we apply an operator splitting method to split Eq. (3.19) in the same fashion as the projection method in the incompressible flow solver. This leads to

$$\mathbf{U}_{k+1}^{*,n+1}=\mathbf{U}^n+\frac{\Delta t}{\alpha_f(\mathbf{X})}\left\{-\sigma_{f,k+1}^{*,n+1}\mathbf{n}+\alpha_f(\mathbf{X})\left(\frac{\partial^2\mathbf{d}}{\partial t^2}\right)_k^{n^\bullet}+\sigma_{s,k}^{n^\bullet}\mathbf{n}-\alpha_f(\mathbf{X})\left(\mathbf{U}\cdot\nabla\mathbf{U}\right)_k^{n^\bullet}\right\} \quad (3.20a)$$

$$-\frac{\alpha_f(\mathbf{X})}{\Delta t}\left(\frac{\partial\phi}{\partial\mathbf{n}}\right)_{k+1}^{n+1}+\hat{\sigma}_{f,k+1}^{n+1}\mathbf{n}\cdot\mathbf{n}=0 \quad (3.20b)$$

Here, $\mathbf{U}^*$ denotes the intermediate velocity, i.e. the solution of the fluid momentum equation. ϕ is an auxiliary variable in projection step. σ^* and $\hat{\sigma}$ denote the two components of the decomposed fluid stress tensor. Eq. (3.20a) is enforced on the embedded interface as the boundary condition for $\mathbf{U}^*$, using a ghost-cell method [33]. Eq. (3.20b) is enforced on the embedded interface as the boundary condition for Poisson's equation in projection step, using an asymmetric finite difference scheme [34, 35]. The algorithm for solving the fluid sub-system is summarized in Algorithm 1. For additional details of the projection method and the embedded Robin boundary method, we refer the reader to [23].

Again, we emphasize that in Eq. (3.20), α_f is a spatially varying function. Nonetheless, as long as a closed-form formulation is available, the computational overhead caused by this generalization is negligible.

For the structural sub-system, we consider a geometrically nonlinear beam in 2-D, and semi-discretize the governing equation (Eq. (3.18d)) using the continuum-based beam element [36]. Specifically, the beam is modeled as a set of adjoining quadrilateral beam elements, which relies on two assumptions: (1) the fibers are straight and inextensible; and (2) the beam is in a state of plane stress. The equation of motion for each element can be written as

$$\mathbf{M}_e \ddot{\mathbf{u}}_e^m + \mathbf{T}_e^T \mathbf{M}_e^s \dot{\mathbf{T}}_e \dot{\mathbf{u}}_e^m + \mathbf{f}^{int} = \mathbf{f}^{ext}, \tag{3.31}$$

where $\mathbf{u}_e^m$ denotes the motion of the master nodes, M_e is the mass matrix, $\mathbf{T}_e$ is the transformation matrix, $\mathbf{M}_e^s$ is the mass matrix for the quadrilaterial continuum element. $\mathbf{f}^{int}$

Algorithm 1 Algorithm for the fluid sub-system

1: Solve the momentum equation for intermediate velocity $\mathbf{U}_{k+1}^{*,n+1}$:

$$(\mathbf{I}-\eta_2\nu\mathbf{L})(\mathbf{I}-\eta_1\nu\mathbf{L})\mathbf{U}_{k+1}^{*,n+1} = (\mathbf{I}+\eta_3\nu\mathbf{L})\mathbf{U}^n - \Delta t(\mathbf{I}+\eta_4\nu\mathbf{L})\left(\mathbf{N}^{n+\frac{1}{2}} + \frac{1}{\rho_f}\mathbf{G}P^{n-\frac{1}{2}}\right) \qquad \text{in } \Omega_f, \quad (3.21)$$

$$\mathbf{U}_{k+1}^{*,n+1} = \mathbf{U}^n + \frac{\Delta t}{\alpha_f(\mathbf{X})}\left\{-\sigma_{f,k+1}^{*,n+1}\mathbf{n} + \alpha_f(\mathbf{X})\left(\frac{\partial^2\mathbf{d}}{\partial t^2}\right)_k^{n^\bullet} + \sigma_{s,k}^{n^\bullet}\mathbf{n} - \alpha_f(\mathbf{X})\left(\mathbf{U}\cdot\nabla\mathbf{U}\right)_k^{n^\bullet}\right\} \qquad \text{on } \Sigma. \quad (3.22)$$

where $\mathbf{L}$ and $\mathbf{G}$ denotes the discrete Laplace operator and the discrete gradient operator, $\mathbf{I}$ is the identity operator, and $\mathbf{N}^{n+\frac{1}{2}}$ represents an approximation of the nonlinear advection term.

2: Project $\mathbf{U}_{k+1}^{*,n+1}$ onto a space that satisfies the divergence-free constraint:

$$\mathbf{L}(\phi_{k+1}^{n+1}) = \mathbf{D}\mathbf{U}_{k+1}^{*,n+1} \qquad \text{in } \Omega_f, \quad (3.23)$$

$$-\frac{\alpha_f(\mathbf{X})}{\Delta t}\left(\frac{\partial\phi}{\partial\mathbf{n}}\right)_{k+1}^{n+1} + \hat{\sigma}_{f,k+1}^{n+1}\mathbf{n}\cdot\mathbf{n} = 0 \qquad \text{on } \Sigma. \quad (3.24)$$

where D denotes the discrete divergence operator.

3: Update velocity at time t^{n+1}:

$$\mathbf{U}_{k+1}^{n+1} = \mathbf{U}_{k+1}^{*,n+1} - \mathbf{G}\phi_{k+1}^{n+1}. \quad (3.25)$$

4: Solve the momentum equation again without the pressure gradient term for intermediate velocity $\widetilde{\mathbf{U}}_{k+1}^{*,n+1}$:

$$(\mathbf{I}-\eta_2\nu\mathbf{L})(\mathbf{I}-\eta_1\nu\mathbf{L})\widetilde{\mathbf{U}}_{k+1}^{*,n+1} = (\mathbf{I}+\eta_3\nu\mathbf{L})\mathbf{U}^n - \Delta t(\mathbf{I}+\eta_4\nu\mathbf{L})\mathbf{N}^{n+\frac{1}{2}} \qquad \text{in } \Omega_f, \quad (3.26)$$

$$\widetilde{\mathbf{U}}_{k+1}^{*,n+1} = \mathbf{U}^n + \frac{\Delta t}{\alpha_f(\mathbf{X})}\left\{-\sigma_{f,k+1}^{*,n+1}\mathbf{n} + \alpha_f(\mathbf{X})\left(\frac{\partial^2\mathbf{d}}{\partial t^2}\right)_k^{n^\bullet} + \sigma_{s,k}^{n^\bullet}\mathbf{n} - \alpha_f(\mathbf{X})\left(\mathbf{U}\cdot\nabla\mathbf{U}\right)_k^{n^\bullet}\right\} \qquad \text{on } \Sigma. \quad (3.27)$$

5: Project $\widetilde{\mathbf{U}}_{k+1}^{*,n+1}$ onto a space that satisfies the divergence-free constraint:

$$\mathbf{L}(\widetilde{\phi}_{k+1}^{n+1}) = \mathbf{D}\widetilde{\mathbf{U}}_{k+1}^{*,n+1} \qquad \text{in } \Omega_f, \quad (3.28)$$

$$-\frac{\alpha_f(\mathbf{X})}{\Delta t}\left(\frac{\partial\widetilde{\phi}}{\partial\mathbf{n}}\right)_{k+1}^{n+1} + \hat{\sigma}_{f,k+1}^{n+1}\mathbf{n}\cdot\mathbf{n} = 0 \qquad \text{on } \Sigma. \quad (3.29)$$

6: Update fluid pressure at time t^{n+1}:

$$P_{k+1}^{n+\frac{1}{2}} = \frac{\rho_f}{\Delta t}(\mathbf{I}+\eta_4\nu\mathbf{L})^{-1}(\mathbf{I}-\eta_2\nu\mathbf{L})(\mathbf{I}-\eta_1\nu\mathbf{L})\widetilde{\phi}_{k+1}^{n+1} \qquad \text{in } \Omega_f. \quad (3.30)$$

and $\mathbf{f}^{ext}$ denote the internal and external nodal forces, respectively. The time integration of Eq. (3.31) is done using the Newmark-β algorithm. To avoid redundancy, we refer the reader to Main [37] for additional details of the structural solver.

3.4.3 Result

Figures 3.13 and 3.14 present the converged numerical solution, specifically, the fluid vorticity, pressure and the beam 's deformation at four time instants during one period of beam vibration. It is clear that vortex shedding and vortex-induced structural vibration are the dominating features of this problem. In addition, Figure 3.15(a) presents the time history of the vertical displacement (δy) at the beam tip (i.e. point a in Figure 3.12). After the beam reaches a periodic steady state, the tip displacement varies within $\delta y \in [-0.089, 0.0915]$ m, with a period of 0.48 seconds. It is interesting to compare the solution of the current problem with that of the original Turek-Hron benchmark problem (test case FSI-2), as they only differ in the beam's density within Γ_A. Figure 3.15(b) compares the vertical displacement at the beam tip. Even though the density within Γ_A is more than one order of magnitude smaller in the current problem, the vibration frequency and amplitude only change slightly. This is because the other properties of the beam (e.g., elastic moduli, thickness) and the Reynolds number of the flow remain unchanged. And the Reynolds number is known as the key factor of the vortex shedding of the cylinder that drives the beam's vibration.

To obtain a reference solution for error analysis, a mesh convergence analysis has been

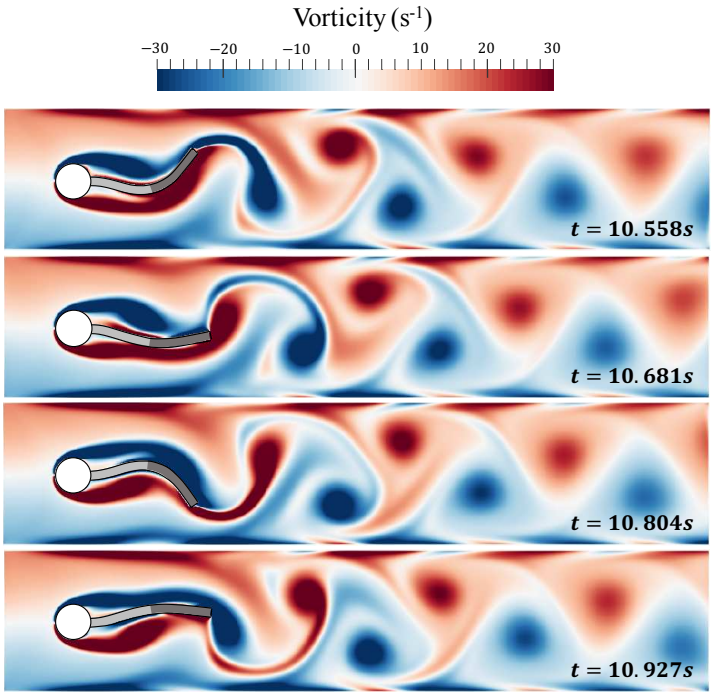

Figure 3.13: Vorticity at four time instances during one period of beam vibration.

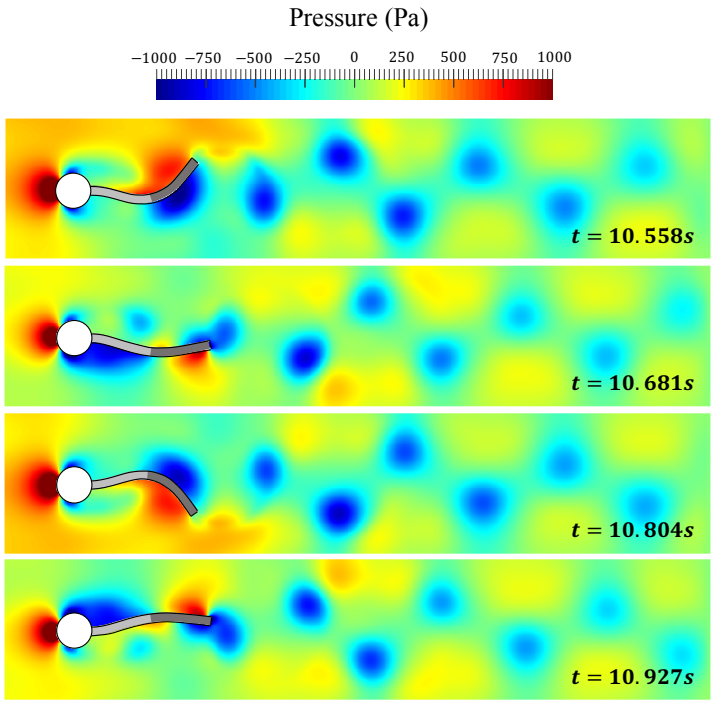

Figure 3.14: Fluid pressure at four time instances during one period of beam vibration.

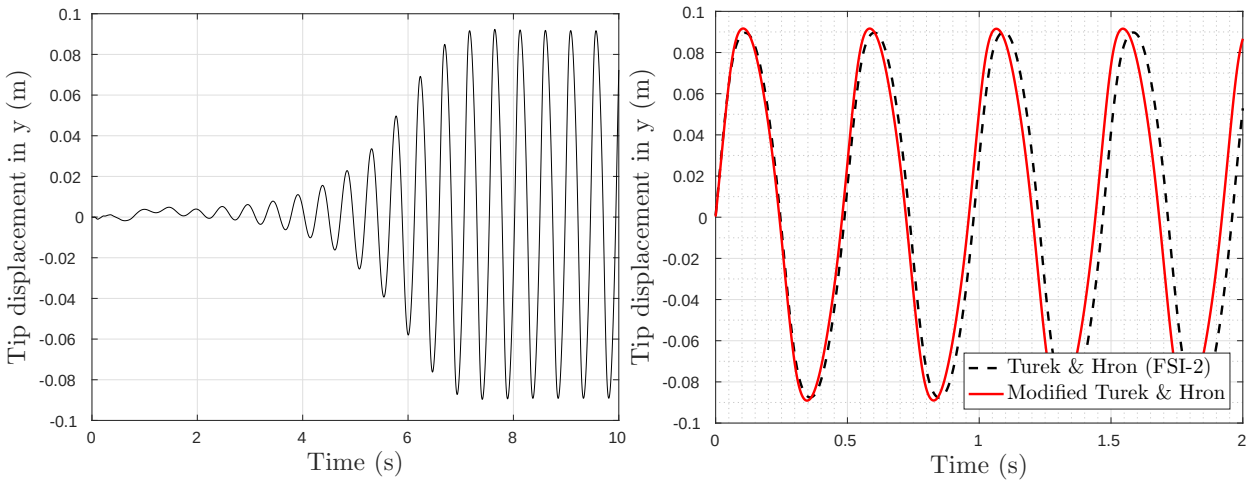

(a) (b)

Figure 3.15: (a) Time history of beam tip displacement in y direction; (b) Comparison with the original Turek-Hron benchmark problem (test case FSI-2) [31]. In Subfigure (b), time is synchronized for the easy of comparison. The synchronized time instance 0 corresponds to 7.591 s in the original Turek-Hron problem, and 7.543 s in the modified one.

conducted using Cartesian fluid meshes with resolution of 250×50, 500×100, and 1000×200. The solutions obtained using the last two meshes differ by less than 2%, in terms of the maximum vertical displacement at the beam tip. A temporal convergence analysis has also been conducted for 3.0×10^{-4} s $\leq \Delta t \leq 1.2 \times 10^{-3}$ s, using the 500×100 fluid mesh and 80 beam elements (Figure 3.16). The solutions given by $\Delta t = 6.0 \times 10^{-4}$ s and $\Delta t = 3.0 \times 10^{-4}$ s differ by 2.1%, also in terms of the maximum vertical displacement at the beam tip. The results presented in Figures 3.13, 3.14, and 3.15 are computed using the 1000×200 fluid mesh, a structural mesh with 160 elements, and a time step size of 4.1×10^{-4} s. Also, six fluid-structure subiterations are performed at each time step.

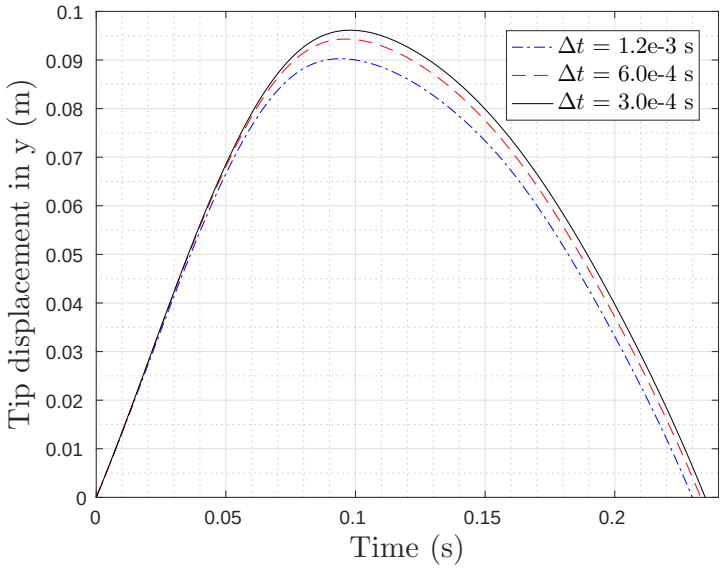

Figure 3.16: Temporal convergence result

3.4.4 Constant α_f versus $\alpha_f(\mathbf{X})$

We design two groups of numerical experiments. In the first group, a constant α_f is specified over the entire beam structure. In the second group, a spatially varying $\alpha_f(\mathbf{X})$ is applied. Specifically, because the beam has two segments, and the density remains constant within each segment, we define $\alpha_f(\mathbf{X})$ to be a piecewise constant function, given by

$$\alpha_f(\mathbf{X}) = \alpha_{f,A}\mathbb{1}_{\Gamma_A} + \alpha_{f,B}\mathbb{1}_{\Gamma_B} = \begin{cases} \alpha_{f,A}, & \text{in } \Gamma_A, \\ \alpha_{f,B}, & \text{in } \Gamma_B. \end{cases} \tag{3.32}$$

All the computations are carried out using a 500×100 fluid mesh, a structural mesh with 80 elements, a time step of 8.2×10^{-4}s, and a fixed number of subiterations (3 per time step). Hence, the results from both groups are obtained with the same computational cost.

In the first group, we vary the value of α_f over a broad range, from 2.0 to 1.0×10^6 kg/m^2, and determine the threshold value for achieving numerical stability. For simplicity, we omit the unit kg/m^2 for α_f in the rest of the paper. The result shows that the solution is stable if and only if $\alpha_f \leq 4.25$. This is demonstrated by Figure 3.17 in which the fluid pressure fields obtained with $\alpha_f = 4.25$ and $\alpha_f = 4.5$ are compared. It is clear that for $\alpha_f = 4.5$ — a value slightly above the limit — the pressure field oscillates, and as time increases, both the structural and the fluid solutions blow up. Notably, the numerical instability initiates around segment Γ_A of the beam, where the structure-to-fluid density ratio is small. This indicates that if a constant α_f is used for solving FSI problems with a non-uniform structure, the largest value of α_f that can be used (to achieve better accuracy without losing stability) is likely determined by the region with strongest added mass effect.

To examine the effect of constant α_f on numerical accuracy, Figure 3.18 presents the solutions obtained with three values, $\alpha_f = 4.25$, 4.0, and 3.0, in comparison with the converged reference solution. It is clear that the solution becomes less accurate as α_f is reduced. The trade-off between stability and accuracy is consistent with the finding shown by Cao *et al.* [23] for the original Turek-Hron problem. Notably, the solution obtained with $\alpha_f = 4.25$ represents the most accurate solution that can be obtained using a constant α_f for the chosen meshes, time step size, and number of subiterations (i.e. a fixed computational cost).

In the second group of experiments, we consider the use of a piecewise constant $\alpha_f(\mathbf{X})$, with $\alpha_{f,A}$ fixed to 3.0, and $\alpha_{f,B}$ varied over a broad range, from 3.0 to 1.0×10^6. For example, Figure 3.18 shows the solutions of two trials, $\alpha_{f,B} = 100.0$ and 1.0×10^6, in comparison

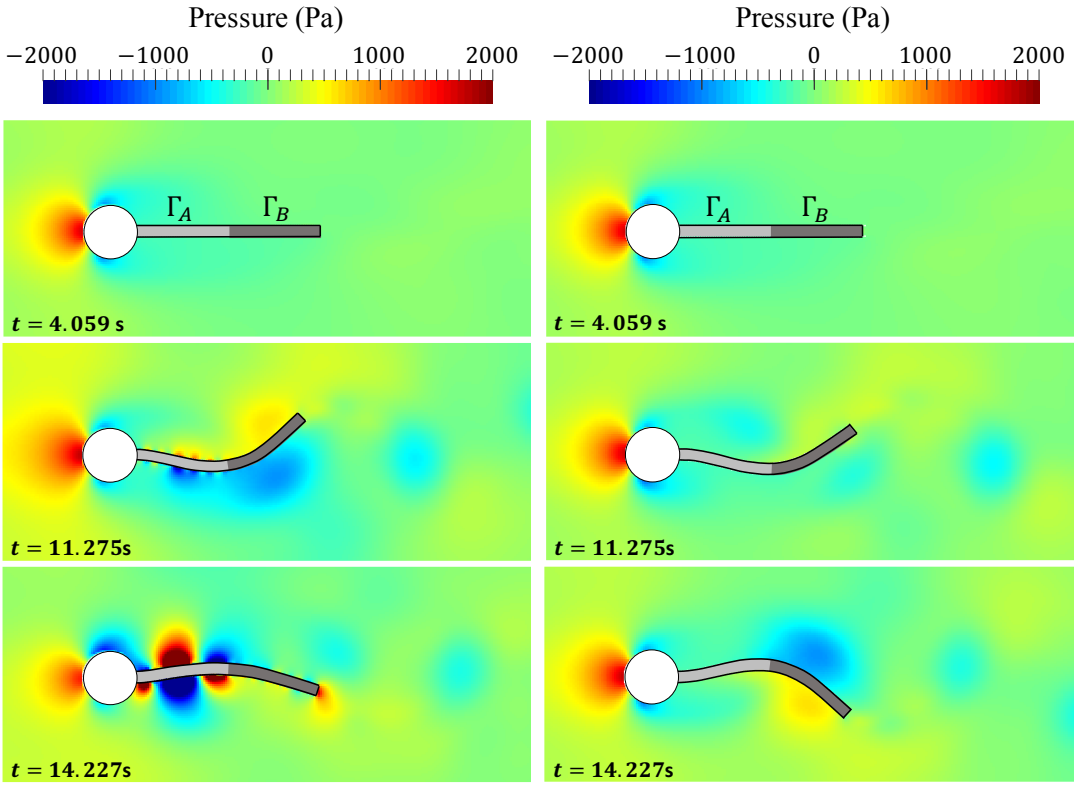

(a) $\alpha_f = 4.5$, unstable (b) $\alpha_f = 4.25$, stable

Figure 3.17: Comparison of fluid pressure obtained using two constant values of α_f across the stability limit.

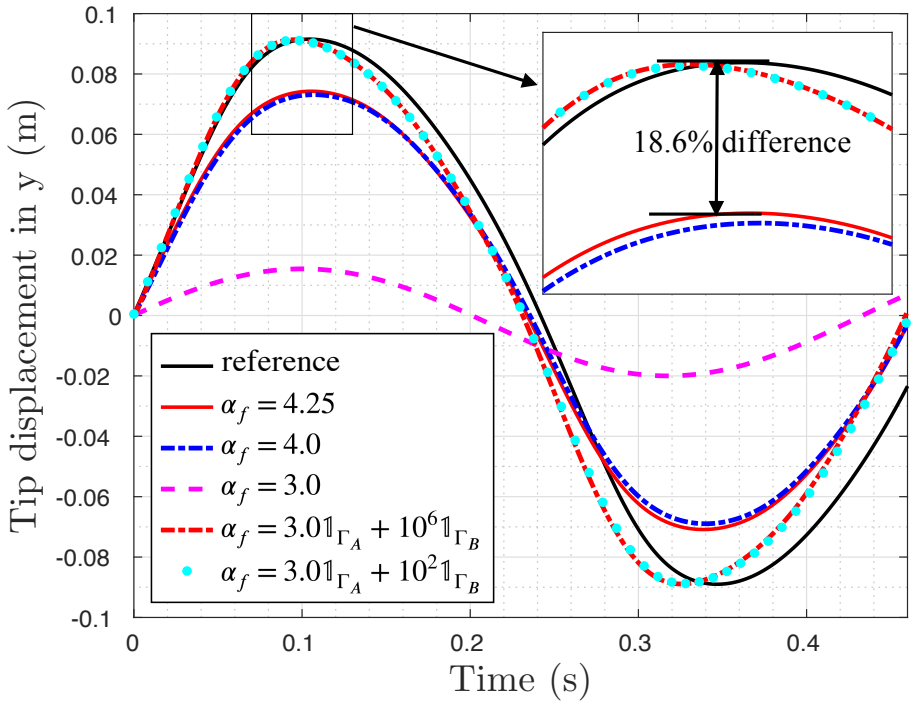

Figure 3.18: Comparison of beam tip displacement obtained with different constant values of α_f and spatially varying $\alpha_f(X)$.

with the reference solution. In both cases, the predicted maximum displacement at beam tip differs from the reference solution by less than 1%. More importantly, for both cases, the solutions are more accurate than the most accurate solution that can be obtained using a constant α_f.

Table 3.2 summarizes the relative error in maximum vertical tip displacement (ϵ_d) obtained using different constant values of α_f and spatially varying $\alpha_f(\mathbf{X})$. Comparing the trials in each group — that is, trials 1 through 4 and 5 through 8 — we find that for both constant and spatially varying α_f, numerical accuracy improves as α_f increases, until exceeding the stability limit. Comparing trial 1 with trial 7, it is evident that increasing the value of α_f in Γ_B from 3.0 to 100.0 leads to dramatic improvement in accuracy. In this case, ϵ_d decreases from 82.9% to 0.2%, by a factor of over 415. Also, comparing trial 3 with trial 7, we see that for this benchmark problem, a spatially varying α_f outperforms the optimal constant value of α_f by a factor of 93, without increasing the computational cost.

	Constant α_f				Spatially varying α_f			
Trial no.	1	2	3	4	5	6	7	8
α_f	3.0	4.0	4.25	4.5	$3.0\mathbb{1}_{\Gamma_A}$ $+5.0\mathbb{1}_{\Gamma_B}$	$3.0\mathbb{1}_{\Gamma_A}$ $+10.0\mathbb{1}_{\Gamma_B}$	$3.0\mathbb{1}_{\Gamma_A}$ $+10^2\mathbb{1}_{\Gamma_B}$	$3.0\mathbb{1}_{\Gamma_A}$ $+10^6\mathbb{1}_{\Gamma_B}$
ϵ_d	82.9%	19.7%	18.6%	N/A*	20.0%	10%	0.2%	0.2%

* unstable.

Table 3.2: Comparison of constant values of α_f with spatially varying α_f: Numerical error in maximum vertical tip displacement (ϵ_d).

3.5 Models for the Spatially Varying Combination Factor

3.5.1 Two models

We present two models for determining the local value of $\alpha_f(\mathbf{X})$ in the spatially varying Robin interface condition (Eq. (3.7c)). Based on the findings shown in the previous sections, we take two factors into account in the design of such models. First, the model should account for the trade-off between stability and accuracy, i.e., one would prefer to increase the value of α_f, but must avoid "falling off the cliff", that is, exceeding the stability limit. Second, a point on the structure subjected to stronger added mass effect requires a smaller value of α_f at that point to maintain stability.

Previous studies have indicated that α_f should depend on the density of the structure and — for thin-walled and slender structures — its thickness (e.g., [18, 23]). Therefore, we first build a model in which the local value of $\alpha_f(\mathbf{X})$ varies linearly with the local structural mass per unit area. Specifically, we propose

$$\text{Model 1:} \quad \alpha_f(\mathbf{X}) = \alpha_{f,0}\frac{\rho_s(\mathbf{X})h(\mathbf{X})}{\rho_{s0}h_0}, \tag{3.33}$$

where $\rho_s(\mathbf{X})$ and $h(\mathbf{X})$ denote the density of the structure and its thickness. $\rho_{s0}h_0$ is a normalization factor, defined here to be the minimum structural mass per unit area on the

structure. $\alpha_{f,0}$ is a constant that should be chosen based on $\rho_{s0}h_0$ (corresponding to the point on the structure with strongest added mass effect) in order to achieve better accuracy without losing stability.

The second model exploits the simplified model problem presented in Section 3.3, but with a uniform beam. For this problem, we have derived an optimal constant value of α_f, i.e. Eq. (3.15). Based on this finding, we propose

$$\text{Model 2:} \quad \alpha_f(\mathbf{X}) = \begin{cases} C\dfrac{M_s(\mathbf{X})M_a}{M_a - M_s(\mathbf{X})}, & \text{if } M_a > (1+\varepsilon)M_s(\mathbf{X}) \\ CM_a\varepsilon^{-1}, & \text{otherwise} \end{cases}, \tag{3.34}$$

where M_s and M_a represent the structural mass and the added mass of the fluid per unit area, respectively. C is a constant parameter that can be either estimated based on the region of the structure with strongest added mass effect, or calibrated to optimize accuracy. ε is a small numerical tolerance to avoid numeric overflow and division by zero. Equation (3.34) states that in regions where the added mass of the fluid is greater than the mass of the structure, the value of α_f reflects the ratio between these two quantities. In other regions, where the added mass effect is not significant, a large constant value of α_f is used to avoid loss of accuracy.

We define

$$M_s = \rho_s(\mathbf{X})h(\mathbf{X}) \quad \text{and} \quad M_a = \frac{\lambda\rho_f}{2\pi}, \tag{3.35}$$

where λ is the wavelength corresponding to the fundamental frequency of the structure (or

the dominant vibration frequency of the problem). Its value can be either computed through a modal analysis or estimated based on knowledge of the problem.

3.5.2 Numerical experiment

To demonstrate and compare the two models introduced above, we consider a modified Turek-Hron problem that is slightly more complex than the one introduced in Section 3.4. The flexible beam is designed to have four segments with various density values, instead of two segments as in Section 3.4. Each segment has a length of 0.0875 m. The density ρ_s is set to 300, 1,000, 2,000, and 10,000 kg/m^3 in the four segments, from left to right. Therefore, the first segment, [0, 0.0875], is the one that has the strongest added mass effect. Other parameter values involved in the problem are set to be the same as in Section 3.4, specifically, in Figure 3.12 and Table 3.1.

Figure 3.19 presents the converged solution, obtained using a 1000×200 fluid mesh, a structural mesh with 160 elements, a time step size of 2.05×10^{-4} s and 6 fluid-structure subiterations per time step. The solution is similar to the previous one in Section 3.4, with some subtle differences. For example, Figure 3.20 compares the structural displacement at three points, marked as P_1, P_2, P_3 in Figure 3.19. It shows that the two beams vibrate at slightly different frequencies, and point P_1 exhibits different modes.

Next, we perform three groups of numerical tests, using a 500×100 fluid mesh, a 80-element structural mesh, and with 3 fluid-structure subiterations per time step. The first group uses

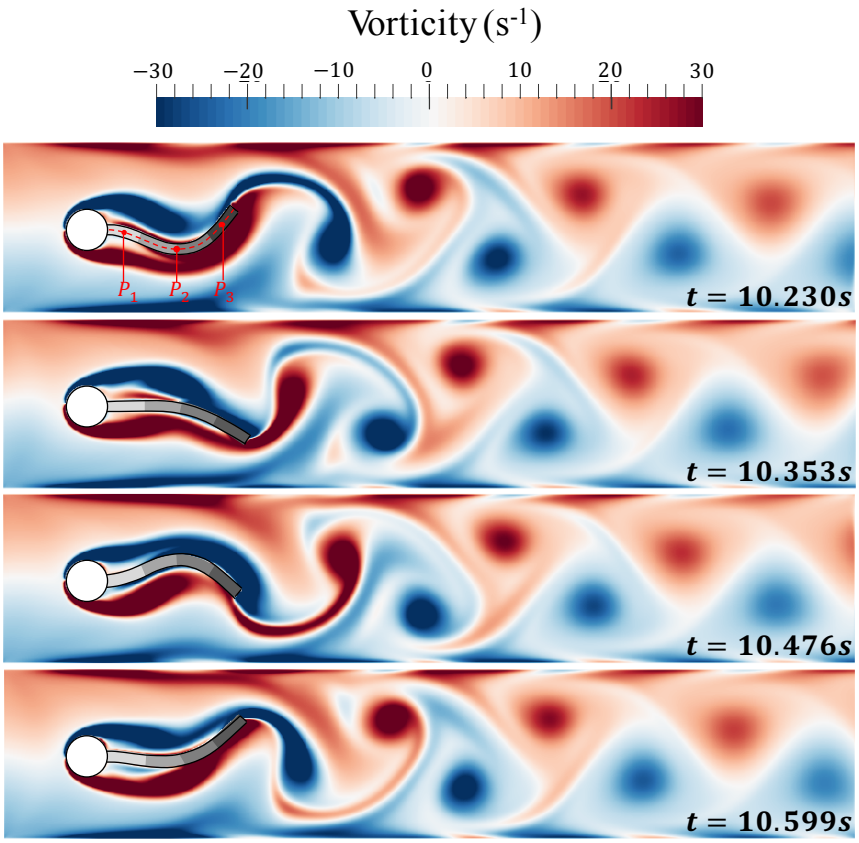

Figure 3.19: Vorticity at four time instances during one period of beam vibration.

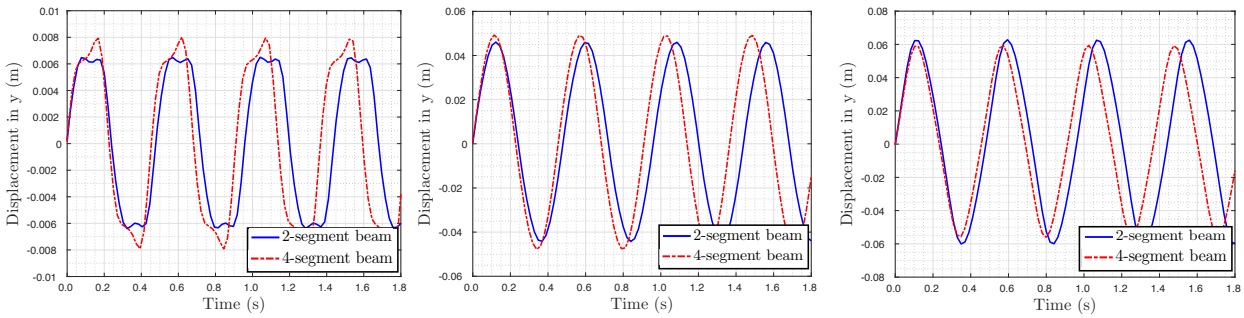

(a) (b) (c)

Figure 3.20: Comparison of the structural displacement in the vertical direction: (a) P_1 ($X = 0.04375$ m); (b) P_2 ($X = 0.175$ m); (c) P_3 ($X = 0.30625$ m). For each plot, time is synchronized for the ease of comparison.

a constant value of α_f. We first perform a series of simulations in which the value of α_f is varied, while the time step size is set to 8.2×10^{-4} s. We found that the optimal value of α_f is 4.25, in the sense that smaller values would give less accurate solutions, while larger values would cause instability. Then, we conduct another series of simulations in which α_f is set to 4.25, while the time step size, Δt, is varied between 4.1×10^{-4} s and 1.64×10^{-3} s. The second group of tests uses a spatially varying Robin interface condition, modeled using Eq. (3.33), i.e. Model 1. We set $\alpha_{f,0}$ to ensure that along the first segment of the beam, $\alpha_f(\mathbf{X}) = 4.25$ (Figure 3.21(b)). We also vary Δt between 4.1×10^{-4} s and 1.64×10^{-3} s. The third group of tests uses a spatially varying Robin interface condition, modeled using Eq. (3.34), i.e. Model 2. Again, we ensure that along the first segment of the beam, $\alpha_f(\mathbf{X}) = 4.25$, and vary the time step size within the same interval.

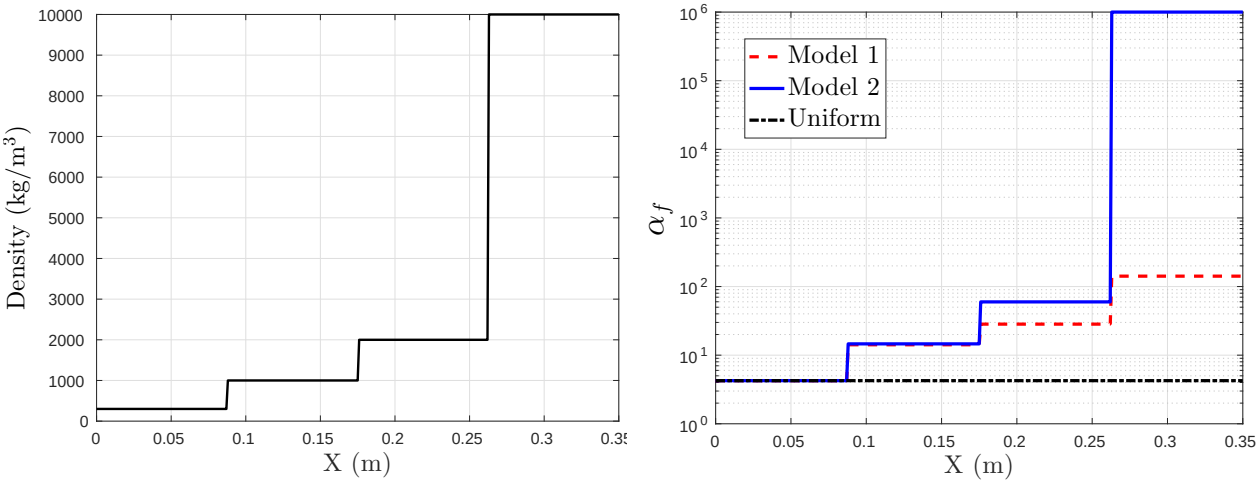

(a) (b)

Figure 3.21: (a) Density distribution along the beam. (b) The local values of three tested α_f.

In the third group of tests, we specify $\lambda = \bar{U}/f_v = D/St$, where $\bar{U}$ and f_v denote the

mean inflow velocity and the frequency of vortex shedding, respectively. D is the diameter of the cylinder, and St is the Strouhal number. In other words, because in this problem the structural deformation is driven by vortex shedding, we use the frequency of vortex shedding to approximate the dominant frequency of the structure. St can be estimated based on standard measurements for flow past a fixed cylinder. For example, Williamson showed that for Reynolds number (Re) around 100, $St(Re) = 0.2175 - 5.1064/Re$ [38].

Figure 3.22 compares the vertical displacement of the beam's tip during one period of vibration. In addition, Table 3.3 presents the numerical error in the maximum vertical tip displacement. Evidently, when the time step size is fixed, both models of $\alpha_f(\mathbf{X})$ provide better accuracy than the optimal constant α_f. For example, in terms of maximum beam tip displacement, when $\Delta t = 8.2 \times 10^{-4}$ s, Model 1 reduces the error by a factor of 8.17 (2.4% vs. 19.6%), while Model 2 reduces the error by a factor of 7.54 (2.6% vs. 19.6%). Moreover, by varying the time step size, we can also observe the advantage of the spatially varying $\alpha_f(\mathbf{X})$. The solution obtained with either model of $\alpha_f(\mathbf{X})$ using $\Delta t = 1.23 \times 10^{-3}$ s is almost as accurate as the solution obtained with the optimal constant α_f, using $\Delta t = 4.10 \times 10^{-4}$ s.

	Numerical error in maximum vertical tip displacement (ϵ_d)		
Time step size	Constant α_f	$\alpha_f(\mathbf{X})$ — Model 1	$\alpha_f(\mathbf{X})$ — Model 2
$\Delta t = 4.10 \times 10^{-4}$s	5.1%	1.7%	0.4%
$\Delta t = 8.20 \times 10^{-4}$s	19.6%	2.4%	2.6%
$\Delta t = 1.23 \times 10^{-3}$s	79.1%	6.2%	5.4%
$\Delta t = 1.64 \times 10^{-3}$s	96.7%	9.9%	8.9%

Table 3.3: Numerical error in the maximum vertical tip displacement obtained with the constant α_f and two modeled $\alpha_f(\mathbf{X})$.

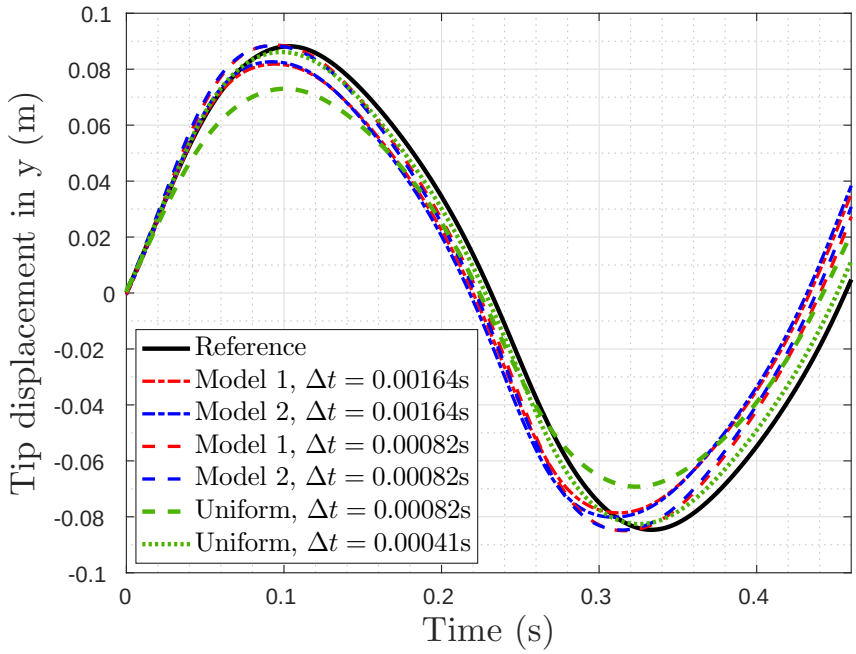

Figure 3.22: Comparison of the vertical displacement of beam tip predicted using the two modeled $\alpha_f(\mathbf{X})$ and the constant α_f. For comparison purposes, the results of one vibration cycle are presented and synchronized at the beginning of the cycle.

3.6 Concluding remarks

We have introduced a spatially varying Robin interface condition for solving fluid-structure interaction problems involving incompressible flow, non-uniform structure, and strong added mass effect. This idea is motivated both by recent findings about applying a constant-parameter Robin interface condition for uniform structures, and by the practical need to efficiently simulate more complex structures with spatially varying material and geometric properties. To assess the spatially varying Robin interface condition, we have constructed and solved two model problems generalized from well-known benchmark problems in the literature, including a generalized Turek-Hron problem that exhibits large, fluid-induced structural deformation. For both model problems, we first find, as a baseline, the most accurate result that can be obtained using a constant Robin parameter for a fixed computational cost. Then, we show that a spatially varying Robin interface condition can clearly improve accuracy (by 93 times in one instance) with the same mesh resolution, time step size, and number of fluid-structure subiterations, i.e. the same computational cost. Moreover, we have presented the implementation of the spatially varying Robin interface condition using an embedded boundary method to couple a projection-based incompressible flow solver with a finite element structural dynamics solver. Furthermore, we have proposed and demonstrated two closed-form formulas to determine the spatially varying function $\alpha_f(\mathbf{X})$ based on the structure's local material and geometric properties. The first one simply conforms to the spatial variation of the structure's properties, while the second one is designed by estimating the local added mass effect and exploiting a simplified model problem. In summary,

this study has provided evidence that for fluid-structure interaction problems involving non-uniform structures with spatially varying material and geometric properties, it is beneficial to apply a spatially varying Robin interface condition, as compared to the constant-parameter version recently discussed in the literature. Future studies may consider exploring additional advantages of a spatially varying Robin interface condition (e.g., reducing the number of fluid-structure subiterations), developing new formulas for the spatially varying α_f, and applying the spatially varying Robin interface condition to large-scale simulations. Also, the parameter α_f in the Robin interface condition can be generalized to temporally varying or solution-adaptive functions, which may be beneficial for certain types of problems.

Acknowledgments

The authors gratefully acknowledge the support of the National Science Foundation (NSF) under awards CBET-1751487 and CBET-1706003, and the support of the Office of Naval Research (ONR) under award N00014-19-1-2102. The authors thank Dr. Alex Main for his advice and assistance on this study.

Appendix

3.A Solution of a simplified model problem

We employ a partitioned procedure to separate the fluid and structural sub-systems in Eqs. (3.11), in which the fluid and the structural governing equations are solved only once per time step. Take the solution within time step t^n to t^{n+1} as an example. Given the solution at $t = t^n$ (i.e., W^n and P^n) as the initial condition, we first solve the fluid sub-system governed by a Laplace equation with a Robin boundary condition at the fluid-structure interface, i.e.

$$\begin{cases} \nabla^2 P^{n+1} = 0 & \text{in } \Omega_f, \quad (3.36a) \\ \alpha_f(x)\dfrac{\partial P^{n+1}}{\partial y} + P^{n+1}b = P^n b - \alpha_f(x)\rho_f \dfrac{\partial^2 W^n}{\partial t^2} & \text{on } \Sigma, \quad (3.36b) \\ \dfrac{\partial P^{n+1}}{\partial y}\Big|_{\Gamma_B} = 0,\ \dfrac{\partial P^{n+1}}{\partial y}\Big|_{\Gamma_L} = \dfrac{\partial P^{n+1}}{\partial y}\Big|_{\Gamma_R},\ P^{n+1}\Big|_{\Gamma_L} = P^{n+1}\Big|_{\Gamma_R}. & (3.36c) \end{cases}$$

Then, the resulting pressure load on Σ at $t = t^{n+1}$ (i.e., $P^{n+1}|_\Sigma$) is transferred to structural sub-system. Next, the structural solution is advanced from t^n to t^{n+1} by solving:

$$\begin{cases} EI\dfrac{\partial^4 W}{\partial x^4} + \rho_s bh\dfrac{\partial^2 W}{\partial t^2} = P^{n+1}|_\Sigma b \qquad \text{in } (t^n, t^{n+1}) \times \Omega_s, & (3.37a) \\ W(x, t^n) = W^n, & (3.37b) \\ \dfrac{\partial W(x,t^n)}{\partial t} = \dfrac{\partial W^n}{\partial t}, & (3.37c) \\ W\Big|_{\partial\Omega_s} = 0,\ \dfrac{\partial^2 W}{\partial x^2}\Big|_{\partial\Omega_s} = 0. & (3.37d) \end{cases}$$

More specifically, Eqs. (3.36) are solved using the conventional two-dimensional five-point finite difference scheme. Eqs. (3.37) are first semi-discretized using a standard Galerkin finite-element method. The resulting semi-discrete equation of motion can be written as

$$\mathbf{M}\ddot{W}_h + \mathbf{K}W_h = \mathbf{f}_{ext}, \tag{3.38}$$

where the subscript "h" denotes the semi-discrete solution, $\mathbf{M}$ is the mass matrix, $\mathbf{K}$ is the stiffness matrix and $\mathbf{f}_{ext}$ is the vector of external dynamic loads. Eq. (3.38) is integrated in time using the Hilber-Hughes-Taylor α (HHT-α) method, which yields a linear system for solution at $t = t^{n+1}$ (i.e., W_h^{n+1}):

$$\left[\bar{\mathbf{K}}\right] W_h^{n+1} = \left[\bar{\mathbf{F}}\right], \tag{3.39}$$

where

$$\left[\bar{\mathbf{K}}\right] = \frac{\mathbf{M}}{\beta\Delta t^2} + (1-\alpha)\mathbf{K}, \tag{3.40}$$

$$\left[\bar{\mathbf{F}}\right] = (1-\alpha)\mathbf{f}_{ext}^{n+1} + \alpha\mathbf{f}_{ext}^{n} + \left(\frac{\mathbf{M}}{\beta\Delta t^2} - \alpha\mathbf{K}\right) W_h^n + \frac{\mathbf{M}}{\beta\Delta t}\dot{W}_h^n + \mathbf{M}\left(\frac{1}{2\beta} - 1\right)\ddot{W}_h^n. \tag{3.41}$$

Then, the acceleration and velocity of the beam at $t = t^{n+1}$ are computed by

$$\ddot{W}_h^{n+1} = \frac{1}{\beta\Delta t^2}\left[W_h^{n+1} - W_h^n - \Delta t\dot{W}_h^n\right] - \left(\frac{1}{2\beta} - 1\right)\ddot{W}_h^n, \tag{3.42}$$

$$\dot{W}_h^{n+1} = \dot{W}_h^n + \Delta t\left[(1-\gamma)\ddot{W}_h^n + \gamma\ddot{W}_h^{n+1}\right]. \tag{3.43}$$

The values of α, β and γ in the equations above are set by

$$\begin{aligned} \alpha &= 1/3, \\ \beta &= (1+\alpha)^2/4, \\ \gamma &= 1/2+\alpha, \end{aligned}$$

which makes the scheme unconditionally stable.

Remark: We also solve the same model problem using a monolithic procedure, primarily as a way to verify the implementation of the above partitioned procedure. In the monolithic procedure, Eqs. (3.11a) and (3.11c) are discretized in space and time, yielding a system of linear equations that couples the beam displacement and fluid pressure. Specificially,

$$\begin{cases} EI\dfrac{W_{i-2}^{n+1}-4W_{i-1}^{n+1}+6W_i^{n+1}-4W_{i+1}^{n+1}+W_{i+2}^{n+1}}{\Delta x^4}+\rho_{s,i}bh\dfrac{W_i^{n+1}-2W_i^n+W_i^{n-1}}{\Delta t^2}=P_i^{n+1}b, & \text{(3.44a)} \\ P_{i+1,j}^{n+1}+P_{i-1,j}^{n+1}+P_{i,j+1}^{n+1}+P_{i,j-1}^{n+1}-4P_{i,j}^{n+1}=0. & \text{(3.44b)} \end{cases}$$

Figure 3.23 compares the solutions obtained using the partitioned and monolithic procedures for Case 1. The fluid and structural meshes and the time step size are kept the same. As expected, the two numerical solutions are in close agreement.

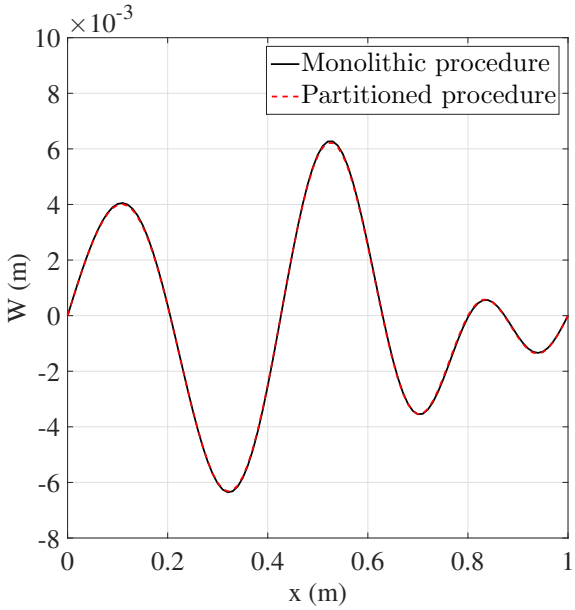

Figure 3.23: Comparison of the solutions of the partitioned and monolithic procedures for Case 1: Beam displacement at $t = 10^{-4}$ s.

Bibliography

[1] S. Piperno, C. Farhat, and B. Larrouturou, "Partitioned procedures for the transient solution of coupled aroelastic problems part i: Model problem, theory and two-dimensional application," *Computer methods in applied mechanics and engineering*, vol. 124, no. 1-2, pp. 79–112, 1995.

[2] C. A. Felippa, K. Park, and C. Farhat, "Partitioned analysis of coupled mechanical systems," *Computer methods in applied mechanics and engineering*, vol. 190, no. 24-25, pp. 3247–3270, 2001.

[3] G. Guidoboni, R. Glowinski, N. Cavallini, and S. Canic, "Stable loosely-coupled-type algorithm for fluid–structure interaction in blood flow," *Journal of Computational Physics*, vol. 228, no. 18, pp. 6916–6937, 2009.

[4] C. Farhat, A. Rallu, K. G. Wang, and T. Belytschko, "Robust and provably second-order explicit–explicit and implicit–explicit staggered time-integrators for highly non-linear compressible fluid–structure interaction problems," *International Journal for Numerical Methods in Engineering*, vol. 84, no. 1, pp. 73–107, 2010.

[5] F. Nobile, M. Pozzoli, and C. Vergara, "Time accurate partitioned algorithms for the solution of fluid–structure interaction problems in haemodynamics," *Computers & Fluids*, vol. 86, pp. 470–482, 2013.

[6] K. Stein, R. Benney, V. Kalro, T. E. Tezduyar, J. Leonard, and M. Accorsi, "Parachute fluid–structure interactions: 3-d computation," *Computer Methods in Applied Mechanics and Engineering*, vol. 190, no. 3-4, pp. 373–386, 2000.

[7] C. Farhat, K. G. Wang, A. Main, S. C. Kyriakides, L. Lee, K. Ravi-Chandar, and T. Belytschko, "Dynamic implosion of underwater cylindrical shells: experiments and computations," *International Journal of Solids and Structures*, vol. 50, no. 19, pp. 2943–2961, 2013.

[8] K. G. Wang, P. Lea, and C. Farhat, "A computational framework for the simulation of high-speed multi-material fluid–structure interaction problems with dynamic fracture,"

International Journal for Numerical Methods in Engineering, vol. 104, no. 7, pp. 585–623, 2015.

[9] H. Chung, S. Cao, M. Philen, P. S. Beran, and K. G. Wang, "Cfd-csd coupled analysis of underwater propulsion using a biomimetic fin-and-joint system," *Computers & Fluids*, 2018.

[10] S. Cao, Y. Zhang, D. Liao, P. Zhong, and K. G. Wang, "Shock-induced damage and dynamic fracture in cylindrical bodies submerged in liquid," *International Journal of Solids and Structures*, 2019.

[11] G. Liu, B. Geng, X. Zheng, Q. Xue, H. Dong, and G. V. Lauder, "An image-guided computational approach to inversely determine in vivo material properties and model flow-structure interactions of fish fins," *Journal of Computational Physics*, 2019.

[12] P. Causin, J.-F. Gerbeau, and F. Nobile, "Added-mass effect in the design of partitioned algorithms for fluid–structure problems," *Computer methods in applied mechanics and engineering*, vol. 194, no. 42, pp. 4506–4527, 2005.

[13] C. Förster, W. A. Wall, and E. Ramm, "Artificial added mass instabilities in sequential staggered coupling of nonlinear structures and incompressible viscous flows," *Computer methods in applied mechanics and engineering*, vol. 196, no. 7, pp. 1278–1293, 2007.

[14] J.-F. Gerbeau and M. Vidrascu, "A quasi-newton algorithm based on a reduced model for fluid-structure interaction problems in blood flows," *ESAIM: Mathematical Modelling and Numerical Analysis*, vol. 37, no. 4, pp. 631–647, 2003.

[15] S. Deparis, M. A. Fernández, and L. Formaggia, "Acceleration of a fixed point algorithm for fluid-structure interaction using transpiration conditions," *ESAIM: Mathematical Modelling and Numerical Analysis*, vol. 37, no. 4, pp. 601–616, 2003.

[16] S. Badia, A. Quaini, and A. Quarteroni, "Modular vs. non-modular preconditioners for fluid–structure systems with large added-mass effect," *Computer Methods in Applied Mechanics and Engineering*, vol. 197, no. 49-50, pp. 4216–4232, 2008.

[17] L. Radtke, A. Larena-Avellaneda, E. S. Debus, and A. Düster, "Convergence acceleration for partitioned simulations of the fluid-structure interaction in arteries," *Computational Mechanics*, vol. 57, no. 6, pp. 901–920, 2016.

[18] S. Badia, F. Nobile, and C. Vergara, "Fluid–structure partitioned procedures based on robin transmission conditions," *Journal of Computational Physics*, vol. 227, no. 14, pp. 7027–7051, 2008.

[19] F. Nobile and C. Vergara, "Partitioned algorithms for fluid-structure interaction problems in haemodynamics," *Milan journal of mathematics*, vol. 80, no. 2, pp. 443–467, 2012.

[20] F. Nobile, M. Pozzoli, and C. Vergara, "Inexact accurate partitioned algorithms for fluid–structure interaction problems with finite elasticity in haemodynamics," *Journal of Computational Physics*, vol. 273, pp. 598–617, 2014.

[21] M. A. Fernández, J. Mullaert, and M. Vidrascu, "Explicit robin–neumann schemes for

the coupling of incompressible fluids with thin-walled structures," *Computer Methods in Applied Mechanics and Engineering*, vol. 267, pp. 566–593, 2013.

[22] M. A. Fernández, M. Landajuela, and M. Vidrascu, "Fully decoupled time-marching schemes for incompressible fluid/thin-walled structure interaction," *Journal of Computational Physics*, vol. 297, pp. 156–181, 2015.

[23] S. Cao, A. Main, and K. G. Wang, "Robin-neumann transmission conditions for fluid-structure coupling: Embedded boundary implementation and parameter analysis," *International Journal for Numerical Methods in Engineering*, vol. 115, no. 5, pp. 578–603, 2018.

[24] L. Li, W. Henshaw, J. Banks, D. Schwendeman, and A. Main, "A stable partitioned fsi algorithm for incompressible flow and deforming beams," *Journal of Computational Physics*, vol. 312, pp. 272–306, 2016.

[25] S. Basting, A. Quaini, S. Čanić, and R. Glowinski, "Extended ale method for fluid–structure interaction problems with large structural displacements," *Journal of Computational Physics*, vol. 331, pp. 312–336, 2017.

[26] L. Gerardo-Giorda, F. Nobile, and C. Vergara, "Analysis and optimization of robin–robin partitioned procedures in fluid-structure interaction problems," *SIAM Journal on Numerical Analysis*, vol. 48, no. 6, pp. 2091–2116, 2010.

[27] S. Nie, Y. Cao, and Z. Wu, "Numerical simulation of parafoil inflation via a robin–neumann transmission-based approach," *Proceedings of the Institution of Mechanical*

Engineers, Part G: Journal of Aerospace Engineering, vol. 232, no. 4, pp. 797–810, 2018.

[28] M.-P. Errera and S. Chemin, "Optimal solutions of numerical interface conditions in fluid–structure thermal analysis," *Journal of Computational Physics*, vol. 245, pp. 431–455, 2013.

[29] Y. Yu, F. F. Bargos, H. You, M. L. Parks, M. L. Bittencourt, and G. E. Karniadakis, "A partitioned coupling framework for peridynamics and classical theory: Analysis and simulations," *Computer Methods in Applied Mechanics and Engineering*, vol. 340, pp. 905–931, 2018.

[30] J. W. Banks, W. D. Henshaw, and D. W. Schwendeman, "An analysis of a new stable partitioned algorithm for fsi problems. part ii: Incompressible flow and structural shells," *Journal of Computational Physics*, vol. 268, pp. 399–416, 2014.

[31] S. Turek and J. Hron, "Proposal for numerical benchmarking of fluid-structure interaction between an elastic object and laminar incompressible flow," in *Fluid-structure interaction*, pp. 371–385, Springer, 2006.

[32] B. E. Griffith and C. S. Peskin, "On the order of accuracy of the immersed boundary method: Higher order convergence rates for sufficiently smooth problems," *Journal of Computational Physics*, vol. 208, no. 1, pp. 75–105, 2005.

[33] Y.-H. Tseng and J. H. Ferziger, "A ghost-cell immersed boundary method for flow in complex geometry," *Journal of computational physics*, vol. 192, no. 2, pp. 593–623, 2003.

[34] Z. Jomaa and C. Macaskill, "Numerical solution of the 2d poisson equation on an irregular domain with robin boundary conditions," *ANZIAM Journal*, vol. 50, pp. 413–428, 2008.

[35] Z. Jomaa and C. Macaskill, "The shortley–weller embedded finite-difference method for the 3d poisson equation with mixed boundary conditions," *Journal of Computational Physics*, vol. 229, no. 10, pp. 3675–3690, 2010.

[36] T. Belytschko, W. K. Liu, B. Moran, and K. Elkhodary, *Nonlinear finite elements for continua and structures*. John wiley & sons, 2013.

[37] A. Main, "A study of fluid-structure interaction on overlapping grids with a focus on flexible beams," tech. rep., Technical Report LLNL-TR-643858, Lawrence Livermore National Laboratory, Livermore, CA (United States), 2013.

[38] C. H. Williamson, "Oblique and parallel modes of vortex shedding in the wake of a circular cylinder at low reynolds numbers," *Journal of Fluid Mechanics*, vol. 206, pp. 579–627, 1989.

Chapter 4

Shock-Induced Damage and Dynamic Fracture in Cylindrical Bodies Submerged in Liquid

(Published in *International Journal of Solids and Structures*, 169, 55-71, 2019)

Shunxiang Cao [a], Ying Zhang [b], Defei Liao [b], Pei Zhong [b], Kevin G. Wang [a]

[a] Department of Aerospace and Ocean Engineering, Virginia Polytechnic Institute and State University, Blacksburg, VA 24061, United States

[b] Department of Mechanical Engineering and Materials Science, Duke University, Durham, NC 90271, United States

Abstract

Understanding the response of solid materials to shock loading is important for mitigating shock-induced damages and failures, as well as advancing the beneficial use of shock waves for material modifications. In this paper, we consider a representative brittle material, Bego-Stone, in the form of cylindrical bodies and submerged in water. We present a computational study on the causal relationship between a single, prescribed shock load and the resulting elastic waves and damage in the solid material. A recently developed three-dimensional computational framework, FIVER, is employed, which couples a finite volume compressible fluid solver with a finite element structural dynamics solver through the construction and solution of local, one-dimensional fluid-solid Riemann problems. The material damage and fracture are modeled and simulated using a continuum damage mechanics model and an element erosion method. The computational model is validated in the context of shock wave lithotripsy and the results are compared with experimental data. We first show that after calibrating the growth rate of microscopic damage and the threshold for macroscopic fracture, the computational framework is capable of capturing the location and shape of the shock-induced fracture observed in a laboratory experiment. Next, we introduce a new phenomenological model of shock waveform, and present a numerical parametric study on the effects of a single shock load, in which the shock waveform, magnitude, and the size of the target material are varied. In particular, we vary the waveform gradually from one that features non-monotonic decay with a tensile phase to one that exhibits monotonic decay without a tensile phase. The result suggests that when the length of the shock pulse is comparable to that of the

target material, the former waveform may induce much more significant damage than the latter one, even if the two share the same magnitude, duration, and acoustic energy.

Keywords

Shock wave, Fluid-solid interaction, Damage and fracture, Lithotripsy

4.1 Introduction

The response of solid materials and structures to shock loading is a long-standing and active research area, motivated mainly by two categories of applications. The first category concerns the prevention and mitigation of shock-induced damages and failures, such as the design of protective structural materials, coatings, and devices [1, 2, 3, 4]. The second category aims to use carefully designed shock waves to achieve desired material modifications. Examples include, but are not limited to, shock wave lithotripsy, a first-line therapy of urinary stone disease [5, 6], "dynamic fracturing" for oil and natural gas extraction [7, 8], and the use of "acoustic sparkers" for biofouling control [9, 10]. A common feature in these applications is that the boundary between beneficial effects (e.g., fracture of a urinary stone) and detrimental effects (e.g., injury of urinary tissue) is often very narrow, which requires a clear understanding and predictive capability regarding the shock-material interaction and the resulting material damage and fracture.

The waveform, magnitude, and duration of a shock wave depend critically on the generation method, the parameters specified therein, and the surrounding medium. In particular, two distinct waveforms are often observed in practical applications: one that features a non-monotonic decay with a tensile phase (Figure 4.1a), and one that exhibits monotonic decay, without a tensile phase (Figure 4.1b). The former waveform can be generated, for example, by focusing a planar acoustic wave using a lens and through nonlinear wave propagation [11], while the latter can be obtained by inducing a rapid bubble expansion through detonation [12] or laser [13]. Previous studies have often focused on analyzing specific model problems in which the shock waveform — and in many cases, also the magnitude and duration — is fixed (e.g., [14, 15, 16, 17, 18, 19]). Nonetheless, comparing the impact of shock waves with different waveforms, magnitude, and duration to solid materials is intellectually valuable, and may provide new insights into applications that require "shock wave by design". To this end, we present in this paper a computational study, using a representative brittle material, namely BegoStone [20], in the form of a cylindrical body that is submerged in water. BegoStone is a commercial dental material, composed of primarily gypsum (99%), supplemented with iron and potassium oxides to increase its strength [21]. Its acoustic and mechanical properties can be tuned easily by varying the powder-to-water ratio [22]. It has been used as a model material for studying shock-induced damages and failures, mainly in the context of shock wave lithotripsy [23].

To simulate the shock-dominated fluid-solid interaction problem, we employ a recently developed three-dimensional computational framework, referred to as FIVER (a FInite Volume

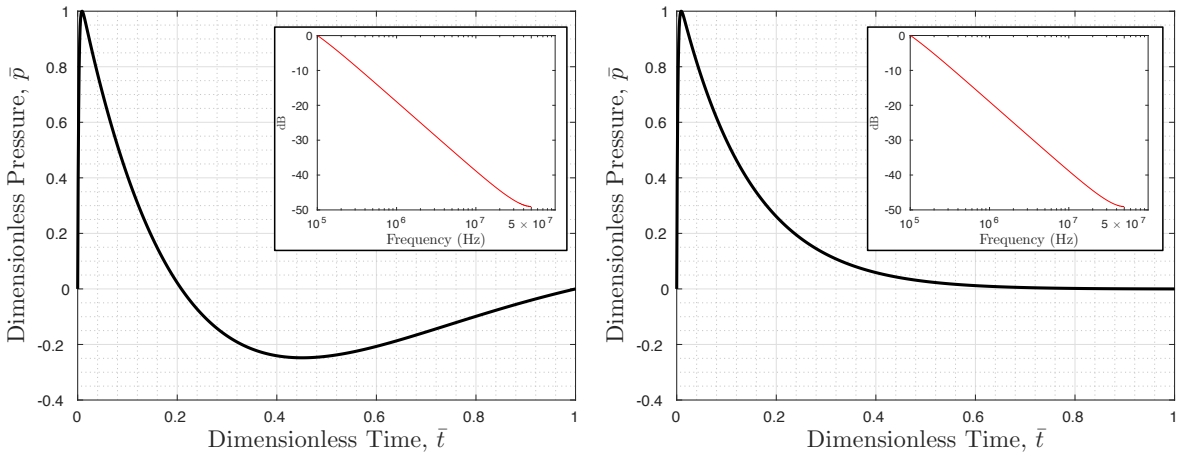

Figure 4.1: Two shock waves with the same magnitude (i.e., peak pressure), the same acoustic pulse energy, similar spectrum, approximately the same duration, yet clearly different waveforms: (a) with non-monotonic decay and a tensile phase; (b) with monotonic decay, without a tensile phase.

method with Exact fluid-solid Riemann solvers) [24, 25, 26, 27, 28]. FIVER couples a finite volume compressible fluid solver with a finite element structural dynamics solver using a second-order accurate partitioned procedure [24]. It enforces the continuity of velocity[1] and traction at the fluid-solid interface using an embedded boundary method, which features the construction and solution of one-dimensional fluid-solid Riemann problems [25, 26]. Because the embedded boundary method operates on non body-fitted CFD grids, it is particularly suitable for analyzing shock-induced dynamic fracture. In the past, FIVER has been verified and validated for several shock-dominated fluid-solid interaction problems including the collapse and rupture of thin-walled metal structures [29, 30, 31] and cavitation-induced material damage [32]. It has also been applied to a few other problems featuring large structural deformation and unsteady viscous flow [33, 34, 35].

[1] in the case of inviscid flow, normal velocity

In this work, we extend FIVER to model and simulate shock-induced damage and fracture in a brittle material, using a continuum damage mechanics model and an element erosion method. The basic idea is to use a scalar damage state variable, $D(\mathbf{X}, t)$, to represent small-scale damages (e.g., microcracks) that cannot be explicitly resolved by the computational grid. Accordingly, the material's elastic modulii are adjusted on the fly to reflect the local and gradual degradation caused by the damages. The growth of D in time is modeled using a truncated power-law function of maximum principal stress. Once D exceeds a critical value within an element, the element is deleted from the structural system [31]. Whereas the literature of continuum damage mechanics is rich, and offers more sophisticated models [36], the one employed in this work — sometimes referred to as the Tuler-Butcher model after [37] — has demonstrated the capability of reproducing experimentally observed fracture in plaster of Paris [18], glass [38], and BegoStone [39], when its parameters are calibrated using the same experiment. We first show that after calibration, the computational framework is capable of capturing the location and shape of the shock-induced fracture observed in our laboratory experiment. Based on the computational result, we discuss the causal relationship among the shock load, the elastic body and surface waves, and the resulting damage and fracture. Next, we present a new phenomenological model of shock waveform, which can model the two distinct waveforms mentioned above and allows the smooth transition in between. Using this model, we perform a series of parameter studies to examine the effects of shock waveform and magnitude, as well as the size of the target material.

It should be mentioned that many shock wave applications, including those mentioned above,

involve cavitation. The detailed effects of cavitation on material damage and fracture is still an active research topic (e.g., [40, 41]). In this work, we focus on investigating the interaction of a prescribed shock wave and a solid material. Cavitation is not included in the computational model. The validation experiment is also designed to suppress shock-induced cavitation.

The remainder of this paper is organized as follows. Section 4.2 summarizes the physical model and numerical methods, including the main features of the FIVER framework. Section 4.3 discusses the calibration and validation of the continuum damage mechanics model using a laboratory experiment. Section 4.4 presents the new model of shock waveform. Section 4.5 presents the aforementioned parameter study, and discusses the results. Finally, a summary and some concluding remarks are provided in Section 4.6.

4.2 Physical Model and Numerical Methods

4.2.1 Governing and constitutive equations

We consider the model problem illustrated in Figure 4.2. Ω_F and Ω_S denote the fluid and solid subdomains occupied by liquid water and BegoStone, respectively. Given that this is a shock-dominated problem, the fluid is assumed to be compressible and inviscid, governed by the following Euler equations which formulate the conservation of mass, momentum, and energy.

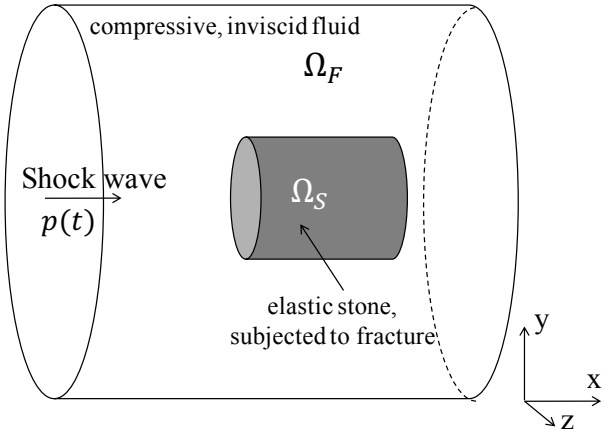

Figure 4.2: A model problem.

$$\frac{\partial W(\boldsymbol{x},t)}{\partial t} + \nabla \cdot \mathcal{F}(W) = 0, \quad \forall \boldsymbol{x} \in \Omega_F(t),\ t > 0, \tag{4.1}$$

where

$$W = \begin{bmatrix} \rho \\ \rho V \\ \rho e_t \end{bmatrix}$$

is the conservative state vector. t denotes time, ρ the fluid density, and $V = [u, v, w]^T$ the fluid velocity vector. $e_t = e + \frac{1}{2} V \cdot V$ denotes total energy per unit mass, in which e represents internal energy per unit mass.

$$\mathcal{F} = [\rho V, \rho V \otimes V + p\mathbf{I}, (\rho e_t + p)V]^T$$

is the flux vector, where $\mathbf{I}$ denotes the 3×3 identity matrix.

To close the above system of equations, we adopt the stiffened equation of state (EOS) [42], given by

$$p = (\gamma_L - 1)\rho e - \gamma_L p_L. \tag{4.2}$$

The model parameters γ_L and p_L are set to $\gamma_L = 6.12$, $p_L = 343$ MPa for liquid water, after [43] and [32].

The solid material is assumed to be in the form of a cylindrical body, subjected to a prescribed shock load along its axial direction (Figure 4.2). The governing equations of dynamic equilibrium are given by

$$\rho_s \ddot{\mathbf{u}}(\mathbf{X}, t) - \nabla \cdot \boldsymbol{\sigma}(\mathbf{u}, \dot{\mathbf{u}}) = \mathbf{b}, \quad \forall \mathbf{X} \in \Omega_S(0),\ t > 0, \tag{4.3}$$

where $\mathbf{u}$ denotes the displacement of the solid, ρ_s its density, and $\boldsymbol{\sigma}$ the Cauchy stress tensor. The body force, $\mathbf{b}$, is assumed to be zero in this work. The dot above a variable represents partial derivative with respect to time.

Previous studies have shown that fabricated BegoStone models can be considered as isotropic, and undergo brittle fracture under shock loading [22, 23]. Therefore, it is modeled here as a linear elastic and isotropic solid; and the constitutive equation is given by

$$\varepsilon_{ij} = \frac{1+\nu}{E}\sigma_{ij} - \frac{\nu}{E}\sigma_{kk}\delta_{ij}, \quad i, j = 1, 2, 3, \tag{4.4}$$

where

$$\varepsilon_{ij} = \frac{1}{2}\left(\frac{\partial u_i}{\partial x_j} + \frac{\partial u_j}{\partial x_i}\right), \qquad i,j = 1,2,3,$$

is the infinitesimal strain tensor. E and ν denote the material's Young's modulus and Poisson's ratio, respectively.

The fluid-solid interface, $\Gamma_{FS} = \partial\Omega_S \cap \partial\Omega_F$, is assumed to be impermeable, and governed by two interface conditions,

$$(V - \dot{\mathbf{u}}) \cdot \mathbf{n} = 0 \qquad \text{on } \Gamma_{FS} \tag{4.5}$$

and

$$-p\mathbf{n} = \boldsymbol{\sigma}(\mathbf{u}, \dot{\mathbf{u}}) \cdot \mathbf{n} \qquad \text{on } \Gamma_{FS}, \tag{4.6}$$

which enforce continuity of normal velocity and traction. $\mathbf{n}$ denotes the outward unit normal to Γ_{FS}.

The incident shock wave $p(t)$ can be applied either as a boundary condition or as an initial condition of the fluid governing equations [44]. The latter method is applied in this work. Specifically, $p(t)$ is converted into a pressure distribution in space by replacing t by $-x/c_0$, where x is the spatial coordinate in the direction of shock propagation (Figure 4.2), and c_0 is the speed of sound in water, calculated using the equation of state (Eq. (4.2)) and the

ambient fluid state. Then, the x-component of the initial fluid velocity is set by

$$u = \frac{p - p_0}{\rho c_0} \tag{4.7}$$

to enforce the incident shock wave, where p_0 denotes ambient fluid pressure.

4.2.2 A continuum damage mechanics model

We introduce a scalar damage state variable, $D(\mathbf{X}, t) \in [0, 1)$, to represent small-scale material damages that cannot be resolved by the computational solid dynamics mesh. The two limit values, 0 and 1, indicate the initial undamaged state and the final completely damaged state, respectively. In the current context of an isotropic, linear elastic material, the constitutive equation is modified by scaling Young's modulus linearly, i.e.

$$E(\mathbf{X}, t) = E_0\big(1 - D(\mathbf{X}, t)\big), \quad \forall \mathbf{X} \in \Omega_S(0), \tag{4.8}$$

where E_0 is the Young's modulus of the material without damage. The material's Poisson's ratio remains a constant. The growth of damage in time is modeled by a power-law function proposed by Tuler and Butcher[37], i.e.

$$D(\mathbf{X}, t) = \int_0^t \Big(\bar{\alpha} \max\big(\sigma_1(\mathbf{X}, t) - \sigma^*, 0\big)\Big)^s d\tau, \tag{4.9}$$

where σ_1 denotes the maximum principal stress. σ^*, s and $\bar{\alpha}$ are constant model parameters that are usually determined empirically[45, 46, 47, 48]. It is assumed that the material starts to fracture when D exceeds a critical value, D_c.

4.2.3 Numerical methods

In this work, a recently developed computational framework is extended to solve the above coupled problem, which couples a finite volume CFD solver with a finite element CSD solver using an embedded boundary method and a partitioned procedure. At the embedded fluid-solid interface, the kinematic interface condition (Eq. (4.5)) is enforced through the construction and solution of a one-dimensional fluid-solid Riemann problem [25], while the dynamic condition (Eq. (4.6)) is enforced by transferring distributed fluid-induced loads to the finite element model using the method presented in [49].

FIVER: A finite volume method based on exact Riemann solvers

We discretize the *augmented* fluid domain $\widetilde{\Omega}$, defined by $\widetilde{\Omega} = \Omega_F \cup \Omega_S \cup \Gamma_{FS}$, using a finite volume mesh, denoted by $\widetilde{\Omega}^h$ (Figure 4.3), where h designates the resolution of this discretization. $\widetilde{\Omega}^h$ is non-interface-conforming in the sense that it does not contain a native representation — comprised of element sides or control volume facets — of the solid material surface Γ_{FS}.

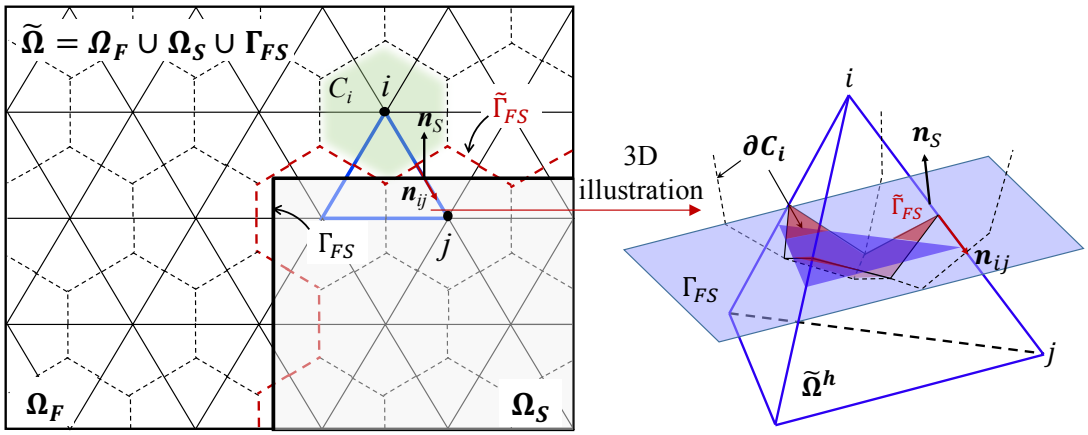

Figure 4.3: Illustration of the augmented fluid domain $\tilde{\Omega}$ and the non-interface-conforming finite volume mesh $\tilde{\Omega}^h$. In the left figure, the triangles with solid thin boundaries represent the elements in $\tilde{\Omega}^h$ and the hexagons with dashed boundaries represent the control volumes or cells. The tetrahedron on the right is the 3D illustration of the element.

Integrating Eq. (4.1) over a control volume, C_i, yields

$$\frac{\partial W_i}{\partial t} + \frac{1}{\|C_i\|} \sum_{j \in Nei(i)} \int_{\partial C_{ij}} \boldsymbol{F}(W) \cdot \boldsymbol{n}_{ij} dS = 0, \tag{4.10}$$

where W_i denotes the average of W in C_i, $\|C_i\|$ denotes the volume of C_i, $Nei(i)$ denotes the set of nodes connected to node i by an edge, $\partial C_{ij} = \partial C_i \cap \partial C_j$, and $\boldsymbol{n}_{ij}$ is the unit normal to ∂C_{ij}. Notably, when edge i-j intersects the embedded fluid-solid interface, the numerical approximation of the surface integral in Eq. (5.10) is based on the exact solution of a one-dimensional fluid-solid Riemann problem. Specifically, if node i belongs to the fluid subdomain, and j belongs to the solid subdomain (Figure 4.3), the following one-dimensional Euler equations with a constant initial condition and a moving wall boundary condition is

introduced.

$$\frac{\partial \boldsymbol{w}}{\partial \tau} + \frac{\partial \mathcal{F}(\boldsymbol{w})}{\partial \xi} = 0, \qquad \tau > 0,\ \xi < (\dot{\boldsymbol{u}}_0 \cdot \mathbf{n}_S)\tau, \tag{4.11}$$

$$\boldsymbol{w}(\xi, 0) = \boldsymbol{w}_i, \qquad \xi < 0, \tag{4.12}$$

$$v((\dot{\mathbf{u}}_0 \cdot \mathbf{n}_S)\tau, \tau) = \dot{\mathbf{u}}_0 \cdot \mathbf{n}_S, \qquad \tau > 0, \tag{4.13}$$

where $\mathbf{n}_S$ denotes the unit normal of Γ_{FS} at its intersection with edge i-j. ξ is the spatial coordinate along the one-dimensional axis aligned with $\mathbf{n}_S$ and centered at the midpoint between nodes i and j. The initial state $\boldsymbol{w}_i$ is the projection of W_i on $\mathbf{n}_S$, i.e.

$$\boldsymbol{w}_i = \begin{bmatrix} \rho_i \\ \rho_i (V_i \cdot \mathbf{n}_S) \\ \rho_i \left(e_i + \frac{1}{2} (V_i \cdot \mathbf{n}_S)^2 \right) \end{bmatrix}. \tag{4.14}$$

v is the velocity component of the 1D fluid state vector $\mathbf{w}$. $\dot{\mathbf{u}}_0$ denotes the velocity of the solid at $\tau = 0$. The exact solution of this Riemann problem can be derived analytically, and the state variable at the fluid-solid interface is plugged into the numerical flux function, thereby enforcing the first fluid-solid interface condition, Eq. (4.5). The resulting semidiscretization of Eq. (4.1) can be written in a compact form as

$$\frac{d\mathbf{W}^h}{dt} + \mathbf{V}^{-1}\mathbf{F}(\mathbf{W}^h) = 0, \tag{4.15}$$

where $\mathbf{W}^h$, $\mathbf{V}$, and $\mathbf{F}(\mathbf{W}^h)$ denote the vector of semidiscrete fluid state variable, the diagonal

matrix storing the volume of control volumes, and the vector of numerical flux, respectively.

A Finite Element CSD Solver

A standard Galerkin finite element method is applied to semi-discretize the weak form of Eq. (4.3), which yields

$$\mathbf{M}\frac{\partial^2 \mathbf{u}^h}{\partial t^2} + \mathbf{f}^{int}\left(\mathbf{u}^h, \frac{\partial \mathbf{u}^h}{\partial t}\right) = \mathbf{f}^{ext}, \tag{4.16}$$

where $\mathbf{M}$ denotes the mass matrix, $\mathbf{u}^h$ denotes the discrete displacement vector. $\mathbf{f}^{int}$ and $\mathbf{f}^{ext}$denote the discrete internal force and external force vector, respectively. The fluid-induced forces are computed based on the second fluid-solid interface condition, Eq. (4.6). Specifically, at the end of each time step, the nodal values of fluid pressure p are linearly extrapolated to the Gauss points of the discretized embedded interface, then integrated over each element of the surface. Figure 4.4 provides an illustration of this method, while additional details can be found in Section 3.8.3 of [49].

The initiation and propagation of dynamic fracture are simulated using an element erosion method. At any time instance, the scalar damage variable D is assumed to have a constant value within each element. When its value exceeds D_c, the stress in this element is set to zero and the element is deleted from the finite element model.

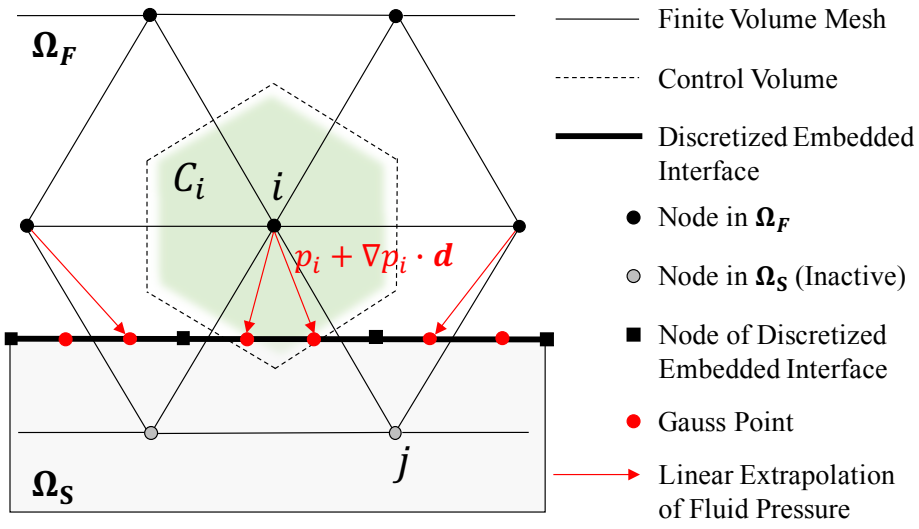

Figure 4.4: Schematic for the computation of fluid pressure force on the discretized embedded interface.

Staggered Time-Integration

The semidiscrete fluid and solid governing equations, Equations (4.15) and (5.16), are integrated using a staggered time-integrator presented in [24] (Figure 4.5). Specifically, the fluid equations are integrated using the explicit fourth-order accurate Runge-Kutta scheme, while the solid equations are integrated using the second-order accurate explicit central difference method. Notably, the fluid and solid time steps are offset by half a step. This feature is designed to allow the coupled time-integrator to achieve second-order accuracy, while maintaining numerical stability.

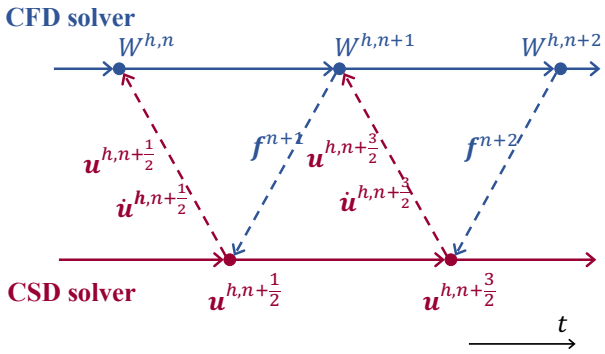

Figure 4.5: A staggered, second-order accurate fluid-solid time-integrator.

4.3 Numerical simulation of a shock wave lithotripsy experiment

We apply the computational framework described in Section 4.2 to simulate a dynamic fracture experiment featuring the use of shock waves generated by an electromagnetic (EM) lithotripter to break a cylindrical BegoStone submerged in water. The objective is twofold: to calibrate the parameters of the continuum damage mechanics model, and to explain, using numerical results, the causal relationship of the prescribed shock wave, the shock-induced elastic waves in the solid material, and the resulting damage and fracture.

4.3.1 Experiment

Figure 4.6 presents a schematic drawing of the experimental setup, with additional details provided in the Appendix. An electromagnetic acoustic transducer (EMAT) is used to generate pulsed planar waves. Each planar wave is then transformed into a shock wave with

maximum pressure $p_{max} = 52.0$ MPa, using a specially designed focusing lens. The target specimen is placed within the focal area of the lens, largely overlapping with the -6 dB focal zone, in which the peak pressure exceeds $p_{max}/2$. To suppress cavitation, the specimen holder is filled with 1,3-butanediol which has similar acoustic properties to water but higher viscosity [50].

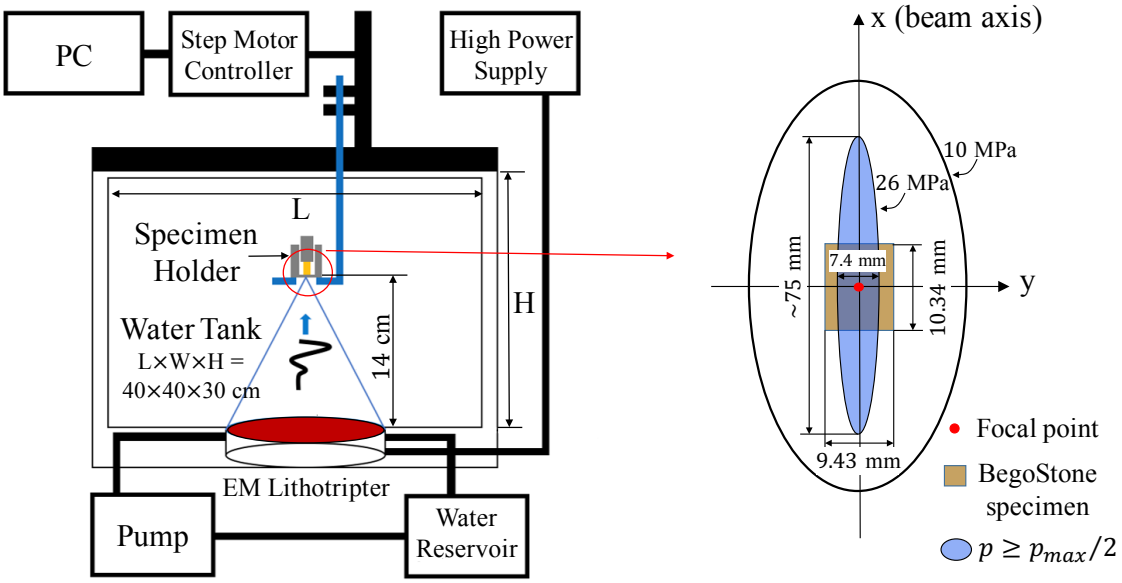

(a) (b)

Figure 4.6: Schematic drawing of experimental setup.

To characterize the shock waveform within the focal zone, we use a high-resolution fiber optic probe hydrophone to measure the pressure history at 41 locations distributed along y- and z-axes, shown in Figure 4.7. The result shows that the shock wave features a non-monotonic decay and a tensile phase, with a duration of approximately 10 μs. The peak pressure of the tensile phase is -11.0 MPa.

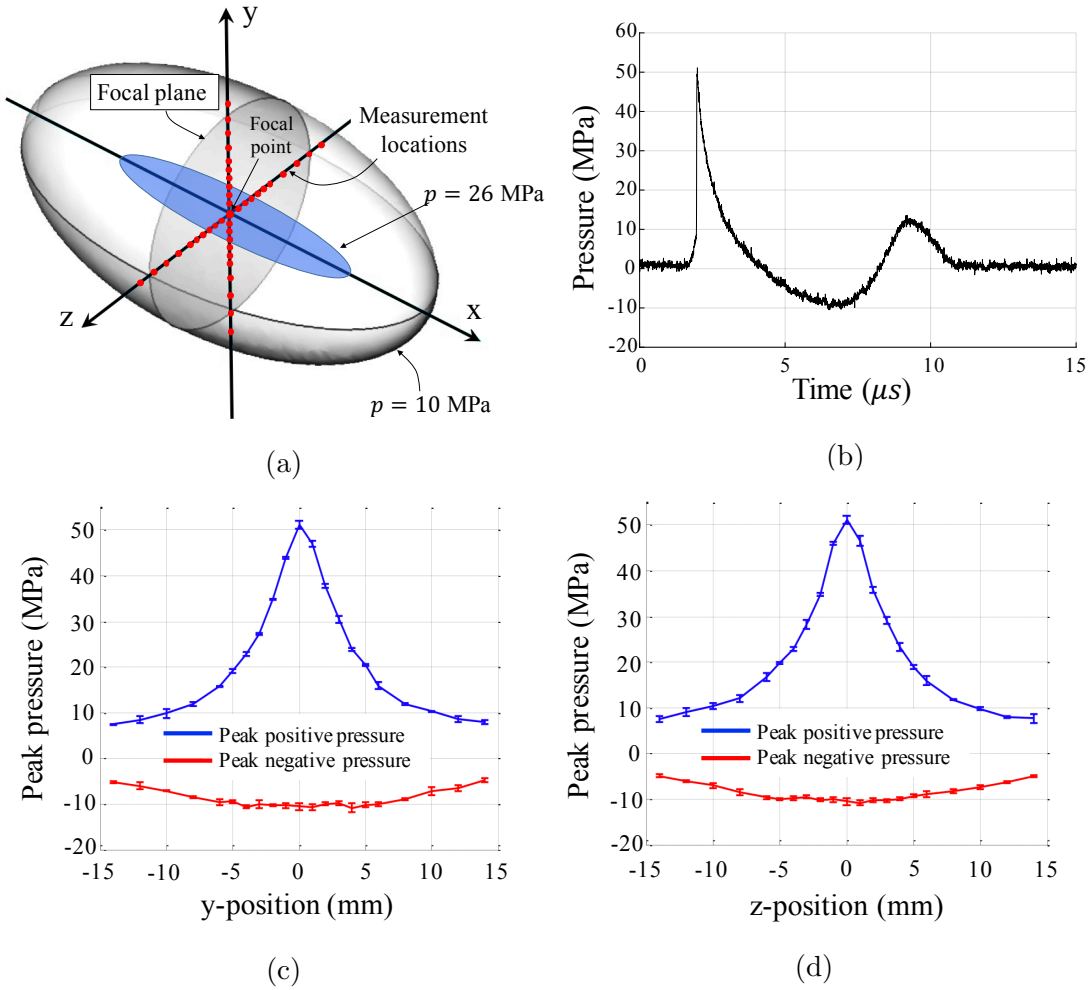

Figure 4.7: Characterization of shock waveform at focal plane perpendicular to the beam axis, using a fiber optic hydrophone (RP Acoustics FOPH 500): (a) A schematic drawing showing the distribution of 41 locations where pressure time-history is measured. (b) The pressure waveform measured at the focal point. (c) Variation of peak pressure along the y-axis, with error bars. (d) Variation of peak pressure along the z-axis, with error bars.

Eight (8) cylindrical BegoStone specimens are fabricated using an established procedure [22], with a powder-to-water mixing ratio of 5:1. One example is shown in Figure 4.8(a). For this mixing ratio, the previous study ([22]) has measured the material's elastic properties and tensile strength under static loading. These parameter values, and the dimensions of the

specimens, are shown in Table 4.1.

Material properties of BegoStone (powder-to-water ratio 5:1, dry) [22]						Dimensions	
C_L (m/s)	C_T (m/s)	ρ (kg/m^3)	E (GPa)	ν	Static Strength (MPa)	L (mm)	d (mm)
4159	2319	1995	27.4	0.27	16.3	10.34 (avg)	9.43 (avg)

C_L: longitudinal wave speed; C_T: transverse wave speed; ρ: density; E: Young's modulus; ν: Poisson's ratio; L: length; d: cross-section diameter.

Table 4.1: Material properties and dimensions of the cylindrical BegoStone specimens.

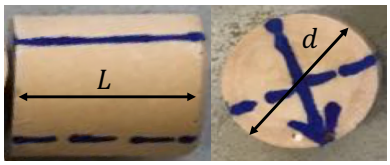

(a)

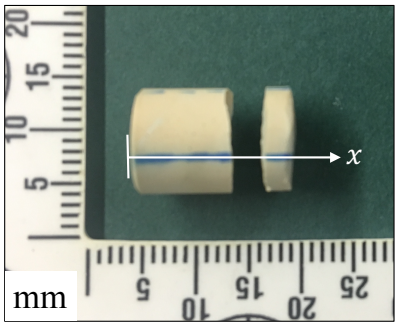

(b)

Figure 4.8: The BegoStone specimen. (a) A specimen before testing. (b) A specimen after first fracture.

The specimens are tested in a dry condition, that is, without being pre-soaked in water. In each test, shock waves of identical waveform are fired at a frequency of 0.5Hz until the first fracture, as showed in Figure 4.8b, is produced. The frequency is sufficiently low such that the successive shock loads do not affect each other. For the 8 samples, 5 ± 2 (mean $\pm$ std.

dev.) loads are required to produce the first fracture. For all of them, the initial fracture is found to be approximately planar, perpendicular to the stone axis, at $73 \pm 3\%$ of the stone length. Additional details are presented in the Appendix. Above all, the demonstrated capability of producing repeatable fracture location and shape in a brittle solid material through shock loading is remarkable.

4.3.2 Simulation setup

Figure 4.9a presents the setup of the numerical simulation, designed to simulate the above experiment. For the purposes of computational efficiency, a 90° slice of the cylindrical Bego-Stone is modeled, with symmetry boundary conditions applied to the two cut planes. Experimentally measured dimensions and material properties (Table 4.1) are applied. The model is discretized by a finite element CSD mesh with $1,033,202$ nodes and $6,027,564$ tetrahedron elements, with a characteristic element size (h) of 0.03 mm. The fluid computational domain, also a 90° slice of the actual 3D space, is discretized using a non-interface-conforming, unstructured CFD mesh with $3,139,728$ nodes and $16,246,504$ tetrahedron elements. In the most refined region — that is, near the solid — the characteristic element size is $h = 0.05$ mm. The far-field boundaries are set to be sufficiently far from the solid specimen such that wave reflections at the boundary do not affect the solid within the simulation time range.

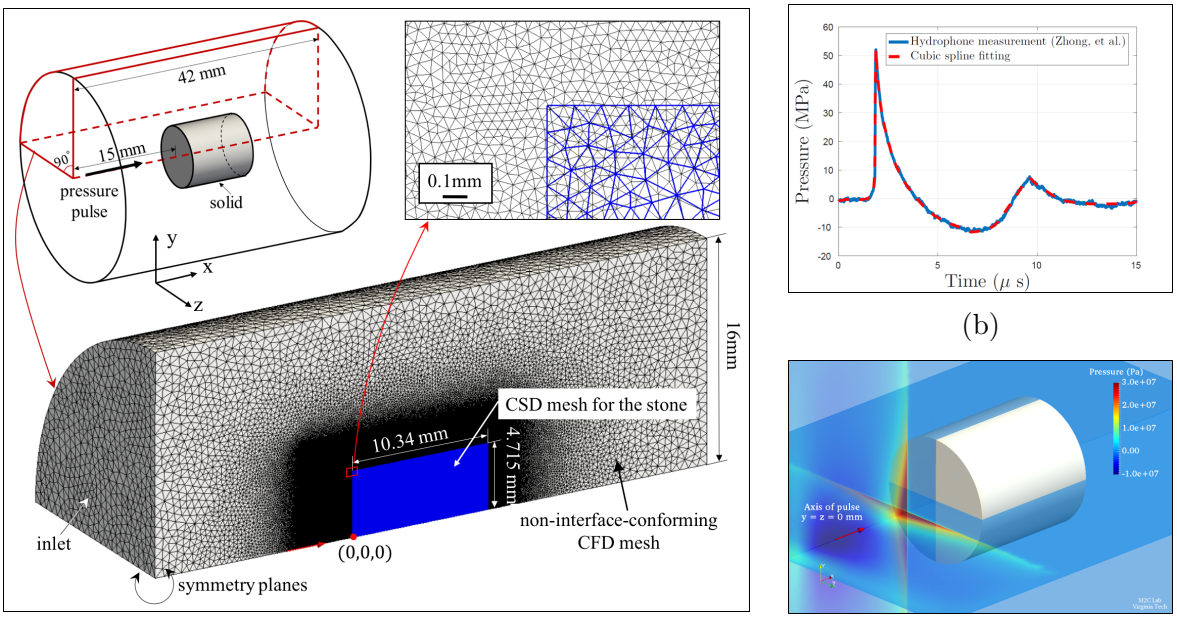

Figure 4.9: Simulation setup. (a) The computational domain and meshes (the computational fluid dynamics (CFD) and computational solid dynamics (CSD) meshes are shown in black and blue, respectively). (b) The cubic spline fitting of the shock waveform measured at the focal point. (c) The shock wave prescribed as an initial condition to the fluid governing equations.

The incident shock wave is considered axisymmetric, supported by the hydrophone measurements shown in Figures 4.7c and 4.7d. The waveform along the centerline (i.e. the x-axis) is prescribed to be the cubic spline fit of the experimental data (Figure 4.7b). The radial decay shown in Figures 4.7c and 4.7d are approximated using a fourth-order polynomial,

$$\frac{p(r)}{p(0)} = -5.0 \times 10^{-5} r^4 + 1.04 \times 10^{-3} r^3 + 1.65 \times 10^{-3} r^2 - 1.55 \times 10^{-1} r + 1.0 \qquad (4.17)$$

where r denotes the radial distance measured from the centerline, in millimeters. The shock wave is prescribed as the initial condition of the fluid governing equations, shown in Fig-

ure 4.9c.

Here, we simulate the response of Begostone specimen subjected to a single incident shock wave. Whereas the solver supports varying time-step sizes both in time and between the fluid and the solid, a constant time step size of 7.6×10^{-4} μs is used here. This value is chosen to ensure numerical stability of the explicit time-integrators in both sub-systems. The Cascades cluster [51] at Virginia Tech is used to performed the simulations presented in this paper. Each run consumed around 10,000 core-hours for achieving 10.0 μs simulation time.

4.3.3 Calibration of parameters in the continuum damage mechanics model

The continuum damage mechanics model introduced in Section 4.2.2 involves four parameters, σ^*, D_c, $\bar{\alpha}$, and s, which are usually determined empirically. We set σ^* to be the static tensile strength measured in a diametral compression test [22], i.e. $\sigma^* = 16.3$ MPa. For D_c, there is no directly relevant experimental data for BegoStone. We set $D_c = 0.5$, following Fovargue *et al.* [11].

Next, we calibrate s and $\bar{\alpha}$ to reproduce the experimental result. Specifically, we have varied s between 1.5 and 4.0, and $\bar{\alpha}$ between 10^{-6} and 10^{-5} $\text{Pa}^{-1}\text{sec}^{-s}$, with more than 20 samples. The optimal parameter values (among the tested samples) are determined by comparing the predicted fracture location with the experimental data. The predicted fracture location

is determined by averaging the locations of the first few elements in which $D > D_C$. In this way, we obtain $s = 3.5$ and $\bar{\alpha} = 4.05 \times 10^{-6}$ $\text{Pa}^{-1}\text{sec}^{-s}$, which predicts a fracture at $x = 6.85$ mm, that is, a 9% difference from the experimental result. For other sample values of s and $\bar{\alpha}$, we have observed variations in both the axial location of the initial fracture and the number of separated cracks (between 0 and 3).

The calibration study also shows that small variations (less than 10%) in s and $\bar{\alpha}$ do not abruptly change the resulting damage and fracture. However, with parameter values significantly different from the aforementioned optimal values, we have observed in several cases the formation of a wide, planar crack around the middle of the specimen (i.e. $x \approx L/2$), and the formation of a void (instead of a sharp crack) in the rear half of the specimen (i.e. $x > L/2$).

It should be mentioned that although in the experiment the first planar fracture (Figure 4.8b) is observed after an average of five (identical) shock loads, the current computational study focuses on the material damage and fracture induced by the first shock load. In particular, the calibration of the damage model exploits the assumption that small fracture initiates inside the solid during the first shock load, then propagates towards the boundary during subsequent loads. This also indicates that the calibrated parameter values may be specific not only to the experimental setup, but also to the computational approach adopted in this work.

4.3.4 Result and discussion

Figure 4.10 presents the numerical solution at five time instances, displaying the fluid pressure field, the maximum principal stress inside the solid and on its surface, and the cumulative damage D. Unless otherwise mentioned, the 2D solution snapshots presented in this paper visualize the plane $z = 0$. Overall, the result shows the interaction of the incident shock wave with the solid material, and the propagation and interference of the shock-induced stress waves. It also shows how microscopic damage evolves as the stress waves pass by, eventually leading to fracture.

Specifically, at $t = 4.21$ μs, the front of the incident shock wave has passed the front surface of the solid specimen by approximately 3 mm. The transmitted and reflected waves resulting from the interaction of the shock front with the front surface of the solid are clearly evident. The transmitted shock wave is in the form of a compressive longitudinal wave (denoted by P), propagating in the axial direction. The P wave appears forward of the incident shock wave in the fluid, because the speed of longitudinal waves in the solid, C_L, is greater than the speed of sound in the fluid. The interaction of the P wave with the side wall of the solid generates a shear wave, denoted by S, that converges towards the central axis. At the same time, the incident shock wave "squeezes" the side wall of the solid, as it is lagged behind the P wave in the solid. Because the speed of transverse waves in the solid, C_T, is also greater than the speed of sound in the fluid, the dynamic squeezing does not produce a clear wave front inside the solid. Instead, it generates tensile stress within a relatively broad region behind the S wave, marked by Π_1 in the figure. This is in contrast to previous findings for

"softer" materials with C_T lower than the speed of sound in the surrounding fluid (e.g., [17]). As the incident shock wave moves forward, Π_1 both expands and moves forward. This is again different from the behavior of softer materials in which the shear wave induced by squeezing converges towards a small region around the central axis.

Once the P wave reaches the distal surface of the solid, it reflects as a tensile longitudinal wave, denoted by P'. At the same time, as the squeezing-induced tensile stress (i.e. region Π_1) propagates from the side wall towards the central axis, it gradually builds up strength. Evident from the second row of Figure 4.10 (i.e. at $t = 6.45$ μs), when P' meets Π_1, the local tensile stress exceeds the damage threshold σ^*, leading to an area of damage centered at $x = 4.8$ mm, marked as region A in the figure. At this point of time, a fraction of the tensile phase of the shock wave (around 50% lengthwise) has passed through the front surface of the solid, and the resulting tensile stress also contributes to the damage in region A. The peak value of the maximum principal stress corresponding to this wave superposition is found to be 31 MPa. The maximum local damage within region A is found to be $D = 0.4$, below the fracture threshold D_c. The shear wave S also reflects at the distal surface, and the reflection is denoted by S'. The converging of S' results in a small region of high tensile stress around the axis of the solid, which moves in the $-x$ direction. This small region is marked by Π_2.

When Π_2 meets the squeezing-induced tensile stress, the local maximum principal stress again exceeds the damage threshold σ^*, with a peak value of 32 MPa achieved at $x = 7.87$ mm on the central axis. As shown in the third row of Figure 4.10 (i.e. at $t = 6.94$ μs), this wave superposition initiates another area of damage, marked as region B. Again, the tensile

phase of the shock wave, transmitted through the front surface of the solid, also contributes to the damage. At $t = 7.25$ μs, the cumulative damage D exceeds the threshold D_c at $x = 6.85$ mm on the central axis, leading to the initiation of a crack. This crack expands in the radial directions, at a speed of the order of 1 mm/μs. It is notable that the propagation speed of S' is of the same order of magnitude. In particular, within the plane of the crack (i.e. $\{x = 6.85 \text{ mm}\}$), it moves in the radial directions at approximately 2 mm/μs. Therefore, the propagation of the crack is likely driven by the combined effects of the propagation of S' and the stress concentration at the crack tip.

At $t = 7.78$ μs, Π_2 reaches region A and intensifies the damage therein. This leads to the initiation of another crack on the central axis, at $x = 5.1$ mm. This crack stops at a radius of 0.4 mm, much smaller than the first one in region B. After approximately $t = 9.5$ μs, the maximum principal stress drops below σ^* everywhere within the solid, and hence damage and fracture stop growing. The simulation is terminated at $t = 10.0$ μs.

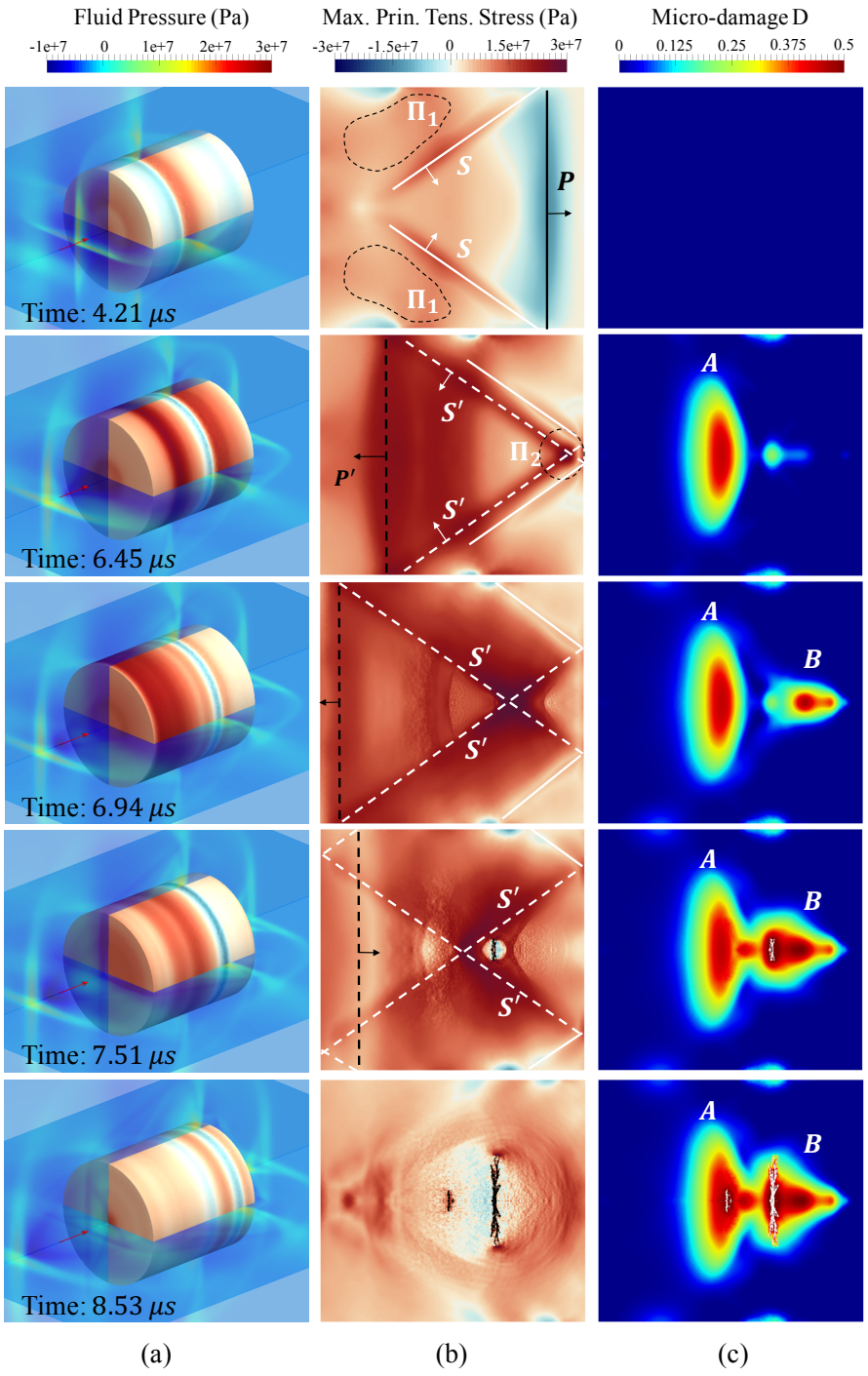

Figure 4.10: Snapshots of simulation result at five time instances. (a) The fluid pressure field and the maximum principal stress on the surface of solid material. (b) The maximum principal stress inside the solid, on plane $z = 0$. (c) The microscopic damage D inside the solid, on plane $z = 0$.

Remarks:

- We have examined the mesh sensitivity of the numerical result, particularly the predicted fracture, by varying the resolution of the CSD mesh between $h = 0.03$ mm and $h = 0.12$ mm, and for each fixed resolution, varying the specific unstructured mesh. Figure 4.11 presents the fracture predicted using a mesh with characteristic size $h = 0.03$ mm, i.e. the one used in the simulations described above, and two different meshes with $h = 0.06$ mm. The result shows that for all the three meshes, the location, shape, and size of the primary fracture are approximately the same.

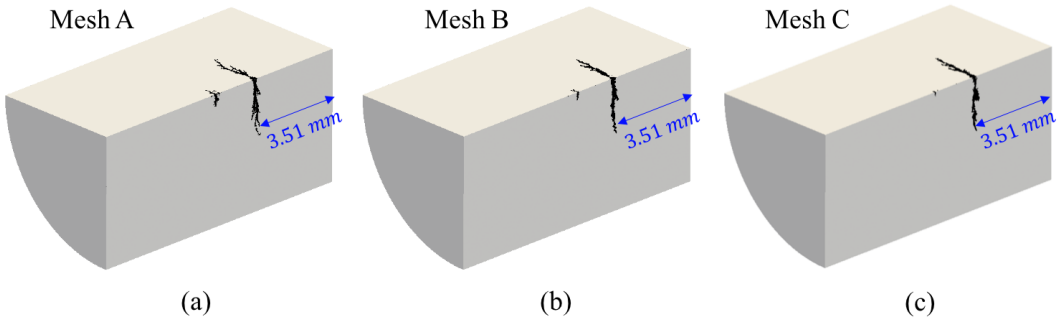

Figure 4.11: Predicted fracture at $t = 10$ μs, using three different unstructured tetrahedral CSD meshes. Mesh A: $h = 0.03$ mm, $\Delta t = 7.6 \times 10^{-4}$ μs. Mesh B and C: $h = 0.06$ mm, $\Delta t = 1.77 \times 10^{-3}$ μs.

- A rough estimation based on Griffith's theory of linear elastic fracture mechanics [52] indicates that for this model problem, the efficiency of fracture creation is likely on the order of 1%. Specifically, let E_{fr} and E_T denote, respectively, the new surface energy caused by fracture and the acoustic energy of the incident shock wave that is

transmitted into the specimen. By Griffith's theory,

$$E_{fr} = A_{fr}\gamma, \tag{4.18}$$

where A_{fr} is the fracture area, which is about 2.76×10^{-5} m^2 at the end of the simulation. γ is the fracture surface energy per unit area. We have not found measurement of γ for BegoStone in the literature. Therefore, we approximate it using that of gypsum (the main ingredient of BegoStone), i.e. $\gamma = 21.88$ Jm^{-2} [53]. The new surface energy is hence estimated as $E_{fr} = 6.04 \times 10^{-4}$ J. The acoustic energy of the transmitted shock wave E_T can be estimated by

$$E_T \approx E_p \left[1 - \left(\frac{Z_1 - Z_2}{Z_1 + Z_2}\right)^2\right], \tag{4.19}$$

where Z_1 and Z_2 are the acoustic impedance of water and BegoStone, respectively. E_p denotes the *effective* acoustic energy of the incident shock wave, defined by

$$E_p = \frac{1}{\rho_f c_0} \int_A \int_T p^2 dt d\boldsymbol{x}, \tag{4.20}$$

where ρ_f is the density of water, c_0 is the speed of sound in water, and A denotes the effective area of the shock loading, i.e., the cross-sectional area of the cylindrical specimen. In this case, $Z_1 = 1.45 \times 10^6$ kg/(m^{2}s), $Z_2 = 8.30 \times 10^6$ kg/(m^{2}s) and $E_p \approx 40.0$ mJ, which gives $E_T \approx 20.3$ mJ. Therefore, the energy efficiency mentioned

above can be estimated by

$$\eta = \frac{E_{fr}}{E_T} \approx 3\%. \tag{4.21}$$

In other words, the new surface energy caused by fracture formation is only a small fraction of the energy input from the incident shock wave.

- We have conducted a numerical experiment in which the tensile phase of the shock wave is removed. Figure 4.12 shows the resulting damage and fracture, in comparison with those produced by the original shock wave. It is clear that the tensile phase of the shock wave also contributes to damaging and breaking the solid material.

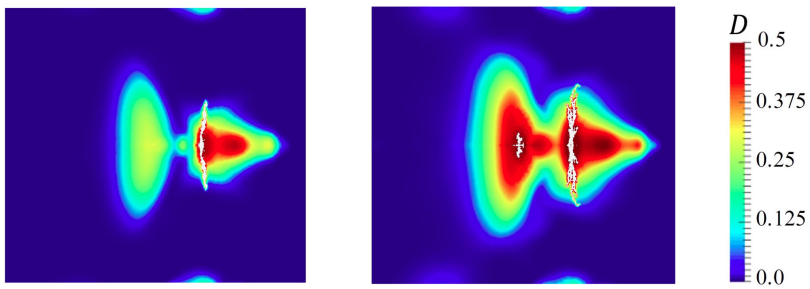

Figure 4.12: Damage and fracture produced by a modified shock wave in which the tensile phase is truncated (Subfigure (a)), in comparison with the result of the original shock wave (Subfigure (b)).

4.4 A novel phenomenological model of shock waveform

To facilitate the study of the impact of shock waves on solid materials, we design a new mathematical model that can be calibrated to fit different waveforms. In this regard, most, if not all, of the existing models have been designed to fit shock waves either with or without a tensile phase (e.g.,[54, 55, 56]). Therefore, a specific objective here is to be able to fit both types of shock waves. The proposed model function is

$$\bar{p}(\bar{t};\, \alpha, \beta, \bar{t}_1) = K \left(1 - \exp\left(-\frac{\bar{t}}{\bar{t}_1}\right)\right) \exp\left(-\alpha \bar{t}\right) \left((\beta - 1)\bar{t}^2 - \beta \bar{t} + 1\right), \tag{4.22}$$

where

$$K = \frac{1}{\max\limits_{0 \le \tau < 1} \left(1 - \exp(-\tau/\bar{t}_1)\right) \exp(-\alpha\tau) \left((\beta - 1)\tau^2 - \beta\tau + 1\right)}. \tag{4.23}$$

The dimensionless pressure $\bar{p}$ represents the pressure p normalized by the peak pressure $p_{\max}$, i.e. $\bar{p} = p/p_{\max}$. The dimensionless time $\bar{t}$ denotes the time t normalized by shock duration, i.e. $\bar{t} = t/T$. $\bar{t}_1$, α and β are dimensionless parameters controlling the shape of the waveform. Specifically, β controls the presence and magnitude of the tensile phase. When $\beta = 1$, the waveform exhibits monotonic decay, without a tensile phase. Figure 4.13a shows an example of fitting Eq. (4.22) to a waveform observed in underwater explosion [57], with the widely used Cole model [56] as reference. When $\beta > 1$, Eq. (4.22) generates a waveform with a

tensile phase. For example, Figure 4.13b shows the fitting of Eq. (4.22) to a typical shock wave generated by an electrohydraulic lithotripters [58].

When the rise time of the shock wave, $\bar{t}_r$, is small, it can be approximated by

$$\bar{t}_r = -\bar{t}_1 \ln\left(\frac{\bar{t}_1(\alpha+\beta)}{\bar{t}_1(\alpha+\beta)+1}\right), \tag{4.24}$$

after dropping higher order terms. In this case, substituting Eq. (4.24) into (4.23) gives a closed-form formula for parameter K.

The model function is C^∞ with respect to all the parameters, which allows smooth transitions between different waveforms.

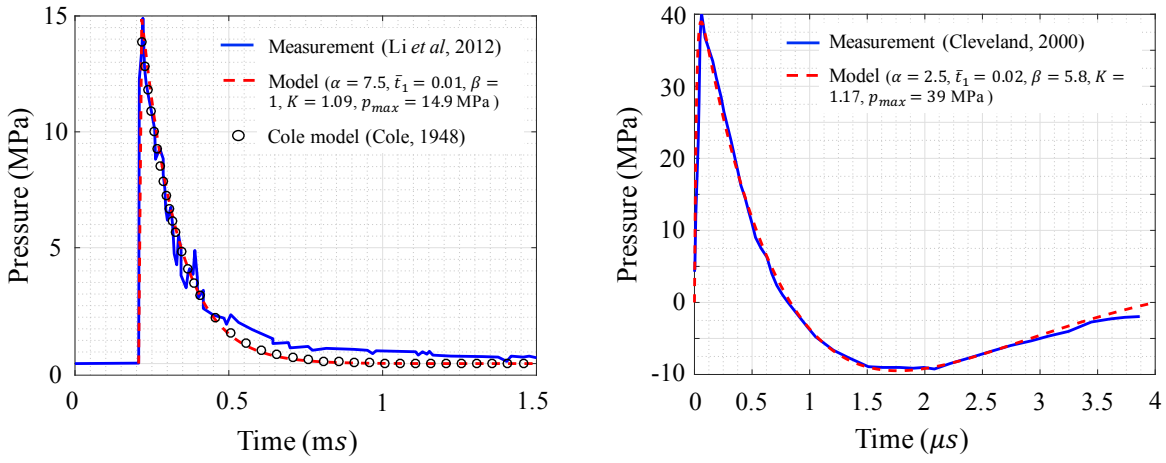

(a) (b)

Figure 4.13: Fitting of two types of shock waves. (a) A shock wave results from underwater explosion of 1.0 kg TNT (measured at a fixed point 3.0 m away from the explosion center) [57]. (b) Shock wave generated by an electrohydraulic lithotripter (Dornier HM3) [58].

4.5 Parametric studies

Using the waveform equation described above, we investigate the effects of shock waveform and magnitude on the elastic response and damage in BegoStone specimens. The same simulation model described in Section 4.3.2 is employed, except that the incident shock wave is prescribed using Eq. (4.22), and the radial decay function, Eq. (4.17), is not applied. In addition, we vary the size of the solid material to examine the size effects. For all the simulations presented in this section, the total simulation time is $t = 10.0$ μs.

In the study of the effect of shock waveform (Section 4.5.1) and specimen size (Section 4.5.2), we maintain the same *effective* acoustic energy, defined by Eq. (4.20). We also ensure that the shock wave rise time, defined by

$$t_r = T \arg\max_{0 \le \bar{t} \le 1} \bar{p}(\bar{t}), \tag{4.25}$$

is nearly the same.

The results obtained with different shock waves and specimen sizes are compared in terms of the maximum value of maximum principal stress, $\sigma_{\max}$, and the volume-averaged damage, D_{avg}, defined by

$$D_{\text{avg}} = \frac{1}{||\Omega_S||} \int_{\Omega_S} D(\boldsymbol{X}, t) d\boldsymbol{X}. \tag{4.26}$$

4.5.1 Effect of tensile phase

Five shock waves, denoted by SW-A1 through SW-A5 and plotted in Figure 4.14, are tested. This series represents a gradual transition from a shock wave that decays monotonically, without a tensile phase, i.e. SW-A1, to one that has a clear tensile phase, i.e. SW-A5. Characteristics of the five shock waves are given in Table 4.2.

Shock index	α	β	$\bar{t}_1$	K	$p_{\max}$ (MPa)	$p^-_{\max}$ (MPa)	T (μs)	t_r (ns)	E_p (mJ)
SW-A1	6.0	1.0	0.00217	1.09	20	0	10	94	15.3
SW-A2	2.25	4.0	0.00217	1.08	20	-1.83	10	91	15.3
SW-A3	2.0	4.8	0.00217	1.09	20	-3.59	10	91	15.3
SW-A4	2.3	5.8	0.00217	1.10	20	-4.96	10	88	15.3
SW-A5	3.0	7.4	0.00217	1.12	20	-6.34	10	86	15.3

α, β, $\bar{t}_1$ and K are model parameters in Eq. (4.22). $p^-_{\max}$, denotes the negative peak of tensile phase.

Table 4.2: Characteristics of five shock waves with different tensile phases.

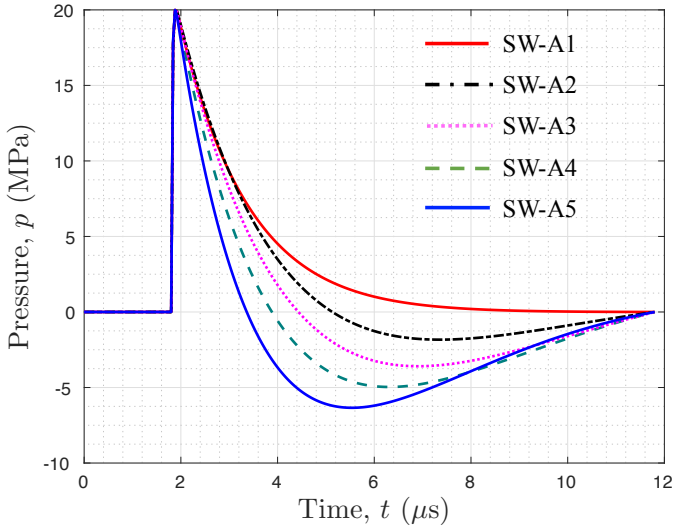

Figure 4.14: Five different shock waveforms with different tensile phase

Figures 4.15 and 4.16 compare the results of two representative cases, SW-A1 and SW-A4, at four time instances, which shows clear differences in both the elastic fields and the material damage.

Specifically, at $t = 4.38$ μs, the transient stress field (Figure 4.15, the left column) shows that SW-A1 induces a compressive stress region near the front surface of the solid, whereas SW-A4 produces tensile stress in this region. By comparing the pressure and stress along two lines, L_1 and L_2 (Figure 4.16, the first column, (a) and (b)), this region (marked by $\langle 1 \rangle$) corresponds to the interaction of the tail of the shock wave with the side wall of the solid, and the observed difference is due to the fact that SW-A4 has a tensile phase whereas SW-A1 does not.

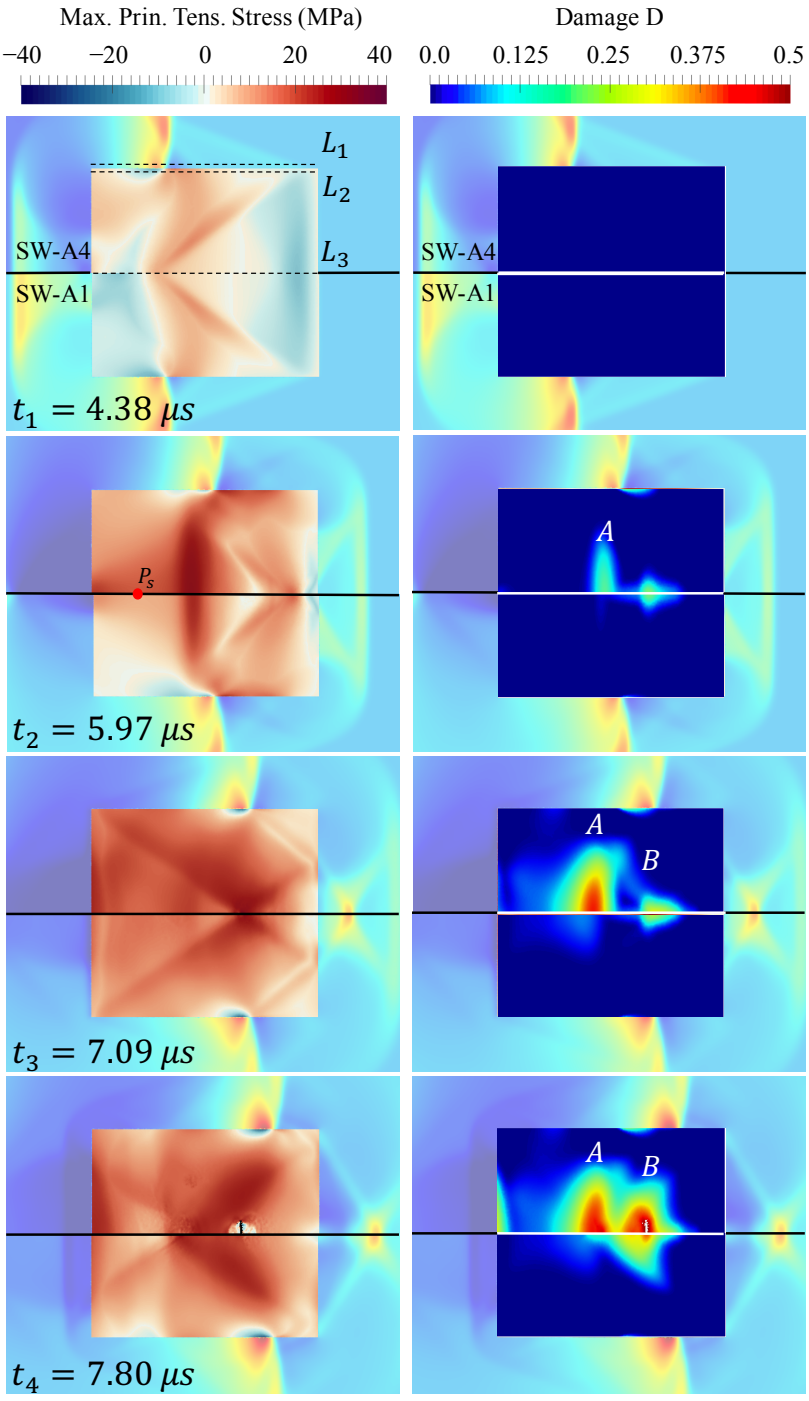

Figure 4.15: The evolution of transient stress field and cumulative damage D induced by SW-A4 and SW-A1 at four time instances. (For the ease of comparison, solutions from SW-A4 and SW-A1 are shown in the upper and lower halves of each image, respectively.)

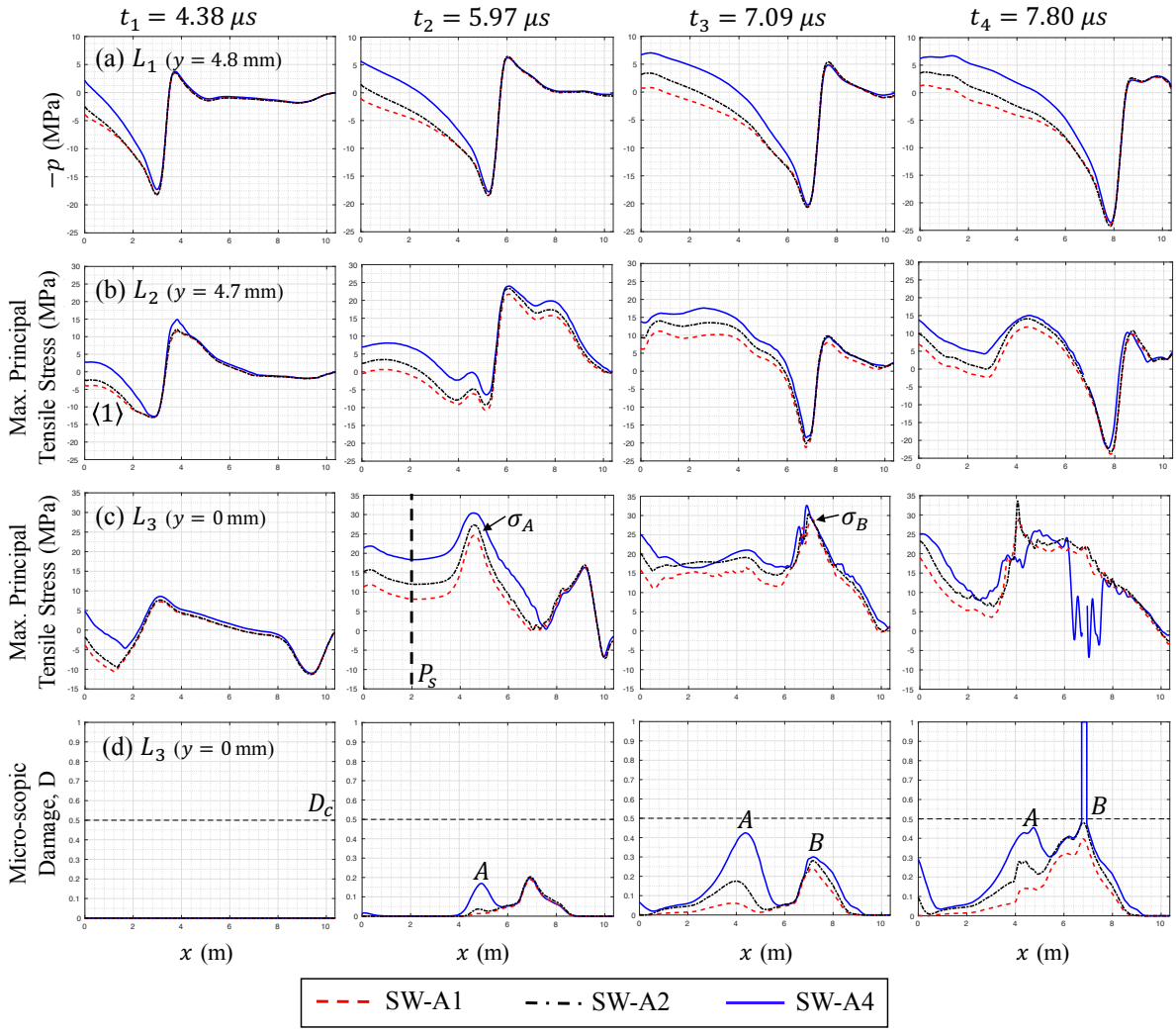

Figure 4.16: Comparison of transient solutions at four time instances. (a) Fluid pressure (inversed) along line L_1 ($y = 4.8$ mm, a line on plane $z = 0$ mm showed in Figure 4.15). (b) Maximum principal tensile stress along line L_2 ($y = 4.7$mm, $z = 0$ mm). (c) Maximum principal tensile stress along the cylinder's central axis L_3 ($y = 0$ mm, $z = 0$ mm). (d) Cumulative damage D along the cylinder's central axis L_3 ($y = 0$ mm, $z = 0$ mm).

In the case of SW-A1, as the compressive stress waves induced by the tail of shock wave propagate inwards, they counteract the squeezing effect described in Section 4.3.4. Specifically, at $t = 5.97$ μs, the magnitude of tensile stress at a sensor point along the stone axis,

P_s, shows a nearly 50% decrease for SW-A1 compared to SW-A4. Moreover, the peak tensile stress for SW-A1, which occurs within damage region A, is also lower compared to SW-A4, by approximately 17%. As shown in Figure 4.15, the local decrease of tensile stress results in dramatic decrease of damage within region A. For example, at $t = 7.09$ μs, the maximum damage induced by SW-A1 is 85% lower than that induced by SW-A4 (Figure 4.16 (d)).

A similar effect is observed for the peak tensile stress within region B, induced by the superposition of the converging shear wave S' and squeezing-induced tensile stress waves, as well as the resulting damage. Specifically, at $t = 7.09$ μs, SW-A1 produces a peak tensile stress of 28 MPa, 22% lower compared to SW-A4. Also, the damage caused by SW-A4 is large enough to initiate fracture, whereas the damage caused by SW-A1 is still below the fracture threshold.

Figure 4.17 compares the damage and fracture resulting from SW-A1 through SW-A4, obtained at the end of the simulation, i.e. $t = 10.0$ μs. The result suggests a trend toward larger shock-induced damage in both region A and B when the amplitude and duration of tensile phase of shock wave gradually increase. Despite the change in the amount of damage, fracture initiated at the same location in the cases of SW-A2 through SW-A4.

Figure 4.18 shows the effects of the tensile phase on D_{avg} and $\sigma_{\max}$. As the acoustic energy of the tensile phase increases from zero (SW-A1) to 4.3 mJ (SW-A4), the volume-averaged damage, D_{avg}, increases by 260%, from 0.0251 to 0.0914. In particular, SW-A2, with a very weak tensile phase that accounts for only 3.4% of the total acoustic energy, can induce twice as much damage as a shock wave without a tensile phase, SW-A1. The increase of

damage is nonlinear and the slope reduces as the tensile phase extends. When the acoustic energy of tensile phase exceeds approximately 1/3 of the total acoustic energy (i.e. SW-A4), the average damage stops growing. This is likely due to the reduced contribution from the compressive phase of the shock wave.

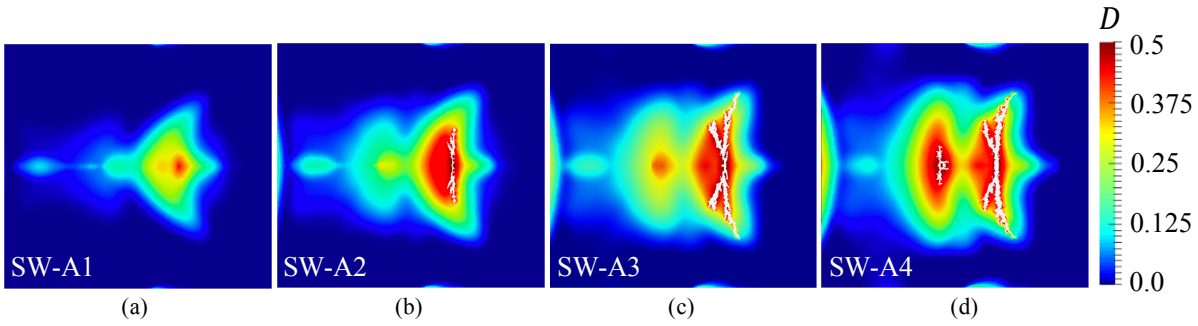

Figure 4.17: Comparison of the material damage and fracture induced by different shock waves (SW-A1 through SW-A4) at the end of simulation, i.e. $t = 10.0$ μs.

Figure 4.18 also presents the peak value of maximum principal stress, $\sigma_{\max}$, in the solid material. For all cases where fracture occurred (i.e., SW-A2 to SW-A5), the peak value appears at the tip of the crack, at approximately 40 MPa. For the case of SW-A1, where fracture did not occur, the peak stress appears on the centerline of the solid, at 31 MPa.

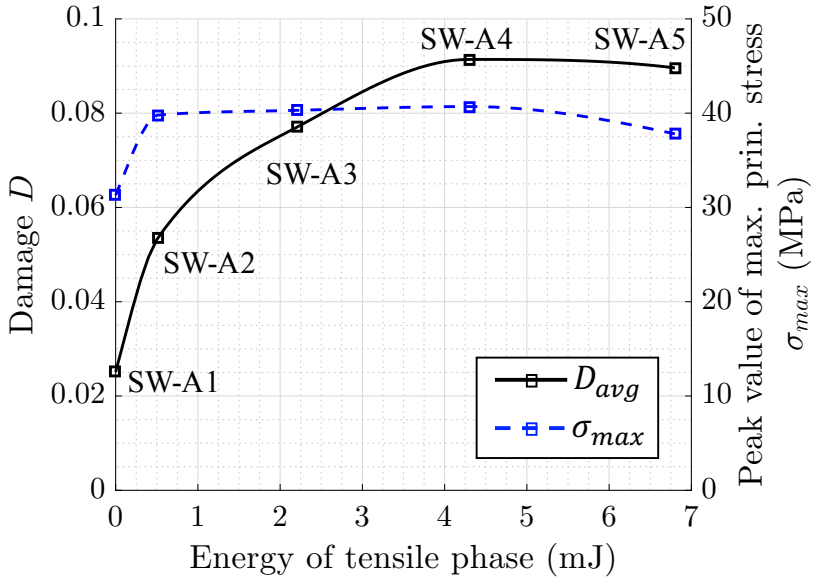

Figure 4.18: The peak value of the maximum principal stress $\sigma_{\max}$ and the average damage D_{avg}, as functions of the acoustic energy of tensile phase.

Remarks:

- The numerical results suggest that with the same magnitude, acoustic energy, and duration, a shock wave with a tensile phase can induce more significant damage and broader fracture to a target material than one without a tensile phase. For applications that use designed shock waves to modify or break solid materials, this indicates a possible approach to improve energy efficiency.

- Previous statistical models (e.g., [59, 60, 61]) tend to characterize a shock wave by its peak pressure, acoustic energy, duration, rise time, and some application-specific parameters. The above results suggest that in addition to these quantities, the energy

and magnitude of the tensile phase may also need to be considered.

4.5.2 Effect of target size

We consider six cylindrical specimens of different size, characterized in Table 4.3. The one denoted by S3 is the one used in the previous simulations. All the six specimens have the same length-to-diameter ratio. Their size, characterized by the ratio of the length of the specimen (L) to the length of the shock wave within water (L_{SW}), varies from 1.07 (S1) to 0.18 (S6). For each specimen, we apply both a shock wave with a tensile phase, SW-A4, and one without tensile phase, SW-A1.

Specimen index	Length, L (mm)	Diameter, d (mm)	L/L_{SW}
S1	15.51	14.15	1.07
S2	12.93	11.79	0.89
S3	10.34	9.43	0.71
S4	7.76	7.07	0.54
S5	5.17	4.72	0.36
S6	2.59	2.36	0.18

Table 4.3: Dimensions of six specimens for the study of size effect.

Figure 4.19 presents the change of volume-averaged damage, D_{avg}, with respect to the length ratio L/L_{SW}. For both shock waves, the size effect is significant. In both cases, the maximum value of D_{avg} is achieved in specimen S4, where $L/L_{SW} = 0.54$. When the size of the specimen is smaller, a significant decrease in D_{avg} is observed. Specifically, for specimen S6 ($L/L_{SW} = 0.18$), the value of D_{avg} is less than 10% of that in S4. This trend is consistent with the finding of Zhang *et al.* [23] that smaller specimens require more shock doses to

break, except that they tested specimens in clusters instead of individual ones. We have found that when the specimen becomes too small compared to the length of the incident shock wave, the trailing tensile phase can no longer work jointly with the leading compressive phase — through wave superpositions described in Section 4.3.4 — to increase damage. For example, Figure 4.20 presents the evolution of the stress field and the cumulative damage in S6 induced by SW-A4. At $t = 3.87$ μs, the front of shock wave in the fluid has just reached the distal end of the specimen, and the result shows that no more damage will accumulate inside the specimen beyond this time. The fluid pressure on line L_4 shows that, up to $t = 3.87$ μs, the specimen is mainly impacted by the compressive phase of the shock wave, while the tensile phase has barely reached the specimen.

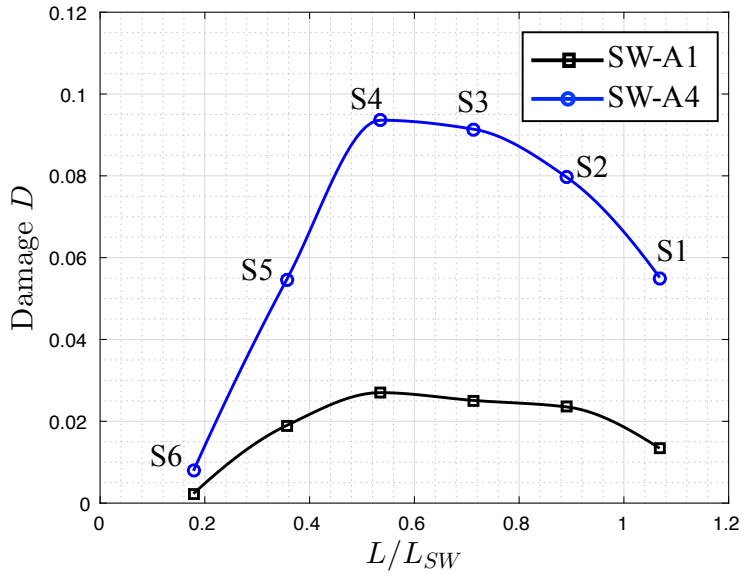

Figure 4.19: The volume-averaged damage D_{avg} induced by shock waves SW-A1 and SW-A4 in six specimens (S1 through S6) of different size.

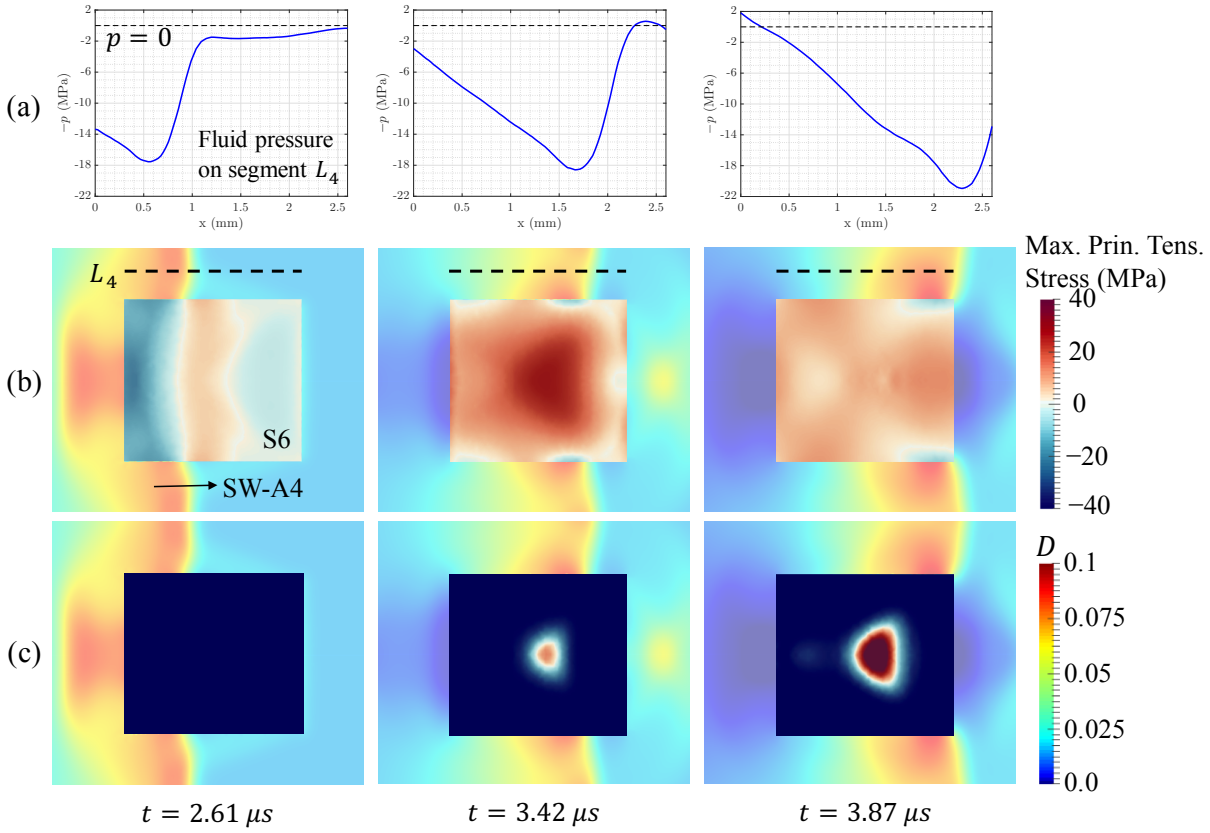

Figure 4.20: Impact of shock wave SW-A4 on a small target material, S6, with $L/L_{SW} = 0.18$.

For all the specimens, SW-A4 induces more significant damage than SW-A1. The difference in between varies from 187% (in the case of S5) to 264% (in the case of S4). Therefore, the main finding derived in Section 4.5.1 — that is, the presence of tensile phase can enhance material damage — may hold for a relatively wide range of specimen size, especially, when it is comparable to the length of the shock pulse.

4.5.3 Effect of shock magnitude

We consider two series of shock waves, generated by linearly scaling the pressure field of two representative waveforms with and without a tensile phase, that is, SW-A4 and SW-A1. For each waveform, four scaling factor values, 0.5, 0.75, 1.25, and 1.5, are considered. The generated shock waves are denoted by SW-B1 through SW-B8. Specifically, SW-B1 through SW-B4 are generated by scaling SW-A4, while SW-B5 through SW-B8 are generated by scaling SW-A1. All the ten shock waves involved are plotted and compared in Figure 4.21. For each pair with the same peak pressure (e.g., SW-B1 and SW-B5), the acoustic energy is nominally the same. The solid specimen used in this series of parameter study is the one denoted by S3 in Table 4.3.

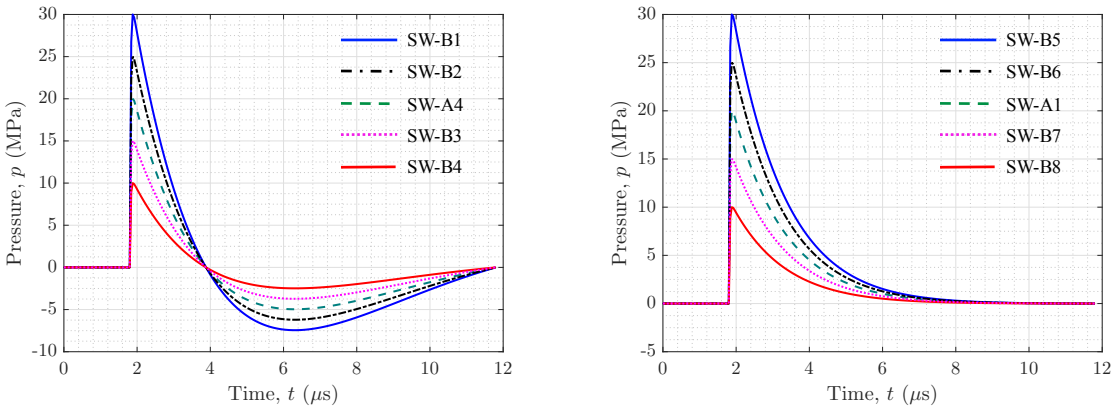

(a) (b)

Figure 4.21: Ten (10) shock waves with different magnitude and waveform.

Figure 4.22 presents the variation of D_{avg} with respect to the peak pressure of the shock wave. For both waveforms (with and without a tensile phase), D_{avg} is nonzero when $p_{\max} > 10$ MPa. As expected, D_{avg} increases as the shock magnitude increases.

Moreover, when $p_{\max}$ is greater than 10 MPa, a shock wave with a tensile phase always induces greater damage than its counterpart without a tensile phase. The difference varies between 460% (when $p_{\max} = 15$ MPa) and 45% (when $p_{\max} = 30$ MPa). The significant effect of the tensile phase can also be appreciated by comparing to the effect of shock magnitude and acoustic energy. For example, for the same target material, SW-B3 produces about the same damage (specifically, D_{avg}) as SW-A1 which has 33% higher peak pressure and 78% higher effective acoustic energy. Similarly, SW-A4 produces about the same damage as SW-B6 which has 25% higher peak pressure and 55% higher effective acoustic energy.

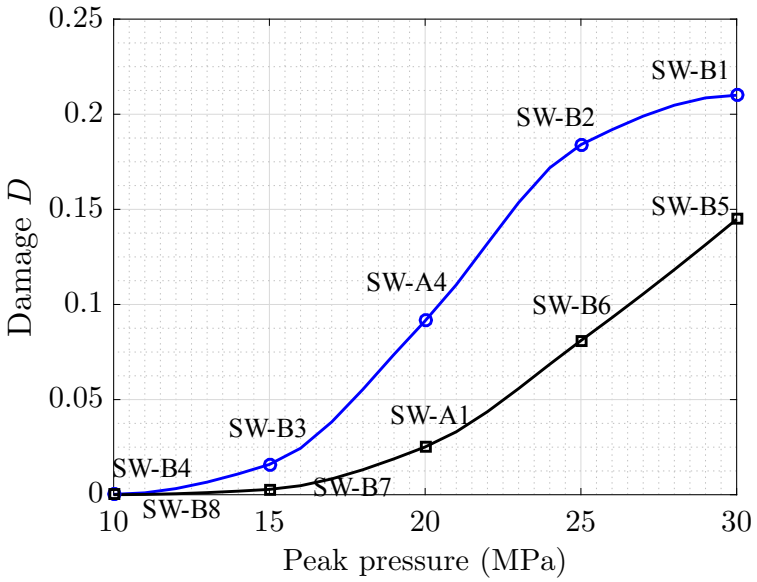

Figure 4.22: The volume-averaged damage D_{avg} induced by shock waves with different magnitude and waveform.

4.6 Conclusions

This paper presents a computational study of the response of solid materials to shock waves traveling in a surrounding liquid medium. In particular, we have focused on a model problem that features a brittle material, BegoStone, in the form of cylindrical bodies and submerged in water. For this problem, previous experiments have shown that shock waves with peak pressure between 10 MPa and 50 MPa can produce repeatable planar cracks at a nearly fixed location, which indicates the potential for designing shock waves to achieve desired material modifications. Nevertheless, the exact process of this deterministic fracture, the cause of it, and the effects of various parameters (e.g., shock waveform, magnitude, and specimen size) are still open questions.

We have employed a recently developed CFD-CSD coupled solver, FIVER, to solve this shock-dominated fluid-solid interaction problem. We begin by calibrating the continuum damage mechanics model employed in this solver using experimental data. After calibration, the solver can capture both the location of the fracture and its planar shape reasonably well. The numerical result shows that the superposition of traveling elastic waves, which depends on the geometry of the specimen, drives the process of damaging and breaking the specimen. For this specific specimen, the planar fracture is initiated jointly by the transmitted compressive shock front (specifically, its interaction with the specimen's side wall), the squeezing-induced tensile stress, and the transmitted tensile phase of the shock wave. Moreover, the tensile shear waves resulting from the interaction of the transmitted compres-

sive shock front with the side wall (i.e. S') facilitates the propagation of the initial crack in radial directions. Compared to previous studies in which maximum principal tensile stress and accumulated damage are used to predict the location of fracture, the modeling of damage and fracture in this work allows us to directly compare with experimental result. Also, simulating fracture allows us to capture additional information about crack propagation, as well as its relation with the propagation of stress waves.

We have also developed a novel waveform equation, which can model shock waves with and without a trailing tensile phase, and allows smooth transition in between. Using this equation, we have conducted a series of parametric studies in which the shock waveform, magnitude, and the size of the specimen are varied. The result shows that for relatively wide ranges of shock magnitude ($p_{\max} > 10$ MPa), and target size (relative to the length of the shock pulse, $0.18 < L/L_{SW} < 1.07$), a shock wave with a tensile phase can induce significantly greater damage to the target specimen than one without a tensile phase, even if the two have the same peak pressure, duration, and acoustic energy.

Finally, several limitations of the present study should be mentioned. First, although the computational model is generally applicable to various materials under high strain-rate loading conditions, the numerical analysis presented in this paper focuses on a representative brittle material, namely BegoStone, in a specific setting that is commonly used for lithotripsy research. Second, this work focuses on studying the material's response to a single shock load, whereas real-world applications often involve multiple (or many) shock loads. In this regard, the cumulative effects of multiple shock loads on the material damage and fracture,

as well as the effects of damage regions on the subsequent shock loads, are not considered in the calibration and the parametric studies. Third, the effects of cavitation are not considered in this study. In reality, the tensile phase of a shock wave may induce cavitation even in degassed water. The violent collapse of cavitation bubbles may cause damage to the specimen. The specific mechanisms and intensity of cavitation-induced damages in solid (and soft) materials are still open questions, which we also plan to investigate in the future.

Appendix

4.A Dynamic fracture experiment

Here we provide additional details about the dynamic fracture experiment presented in Section 4.3.1. The setup of this experiment is showed in Figure 4.6a. More specifically, an electromagnetic (EM) shock wave generator was mounted at the bottom of a Lucite tank ($40 \times 40 \times 30$ cm) filled with 0.2-μm-filtered and degassed water (< 3 mg/L concentration, 23°C) [50]. The shock wave generator is operated at 14.8 kV with a pulse repetition frequency (PRF) of 0.5 Hz. At the focus of the generator, where the intense shock wave is generated, a cylindrical BegoStone specimen (diameter $\times$ length = 9.43 mm $\times$10.34 mm) is held by a flat-base tube holder (inner diameter = 14 mm) made of silicon rubber. The axis of specimen and holder are aligned with the central axis of the generator using a 3D positioning system (VXM-2 step motors with BiSlide-M02 lead screws, Velmex, Bloomfield, NY). The stone

phantoms are fabricated by BegoStone Plus (BEGO USA, Smithfield, RI), with a powder-to-water mixing ratio of 5 : 1.

The stone specimen is subjected to multiple shock waves until the initial disintegration is observed. Figure 4.23 presents the photographs and statistics of initial fracture for 8 specimens. For all 8 specimens, planar fracture is clearly observed and the average location is at 73% of the stone length from the front surface.

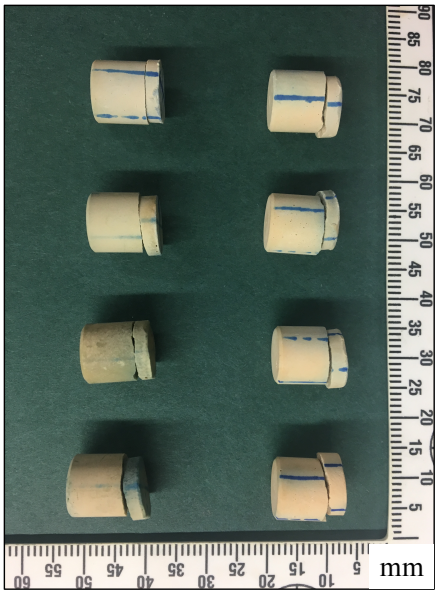

Test index	Distance from the front surface to fracture plane L_f (mm)	L_f/L
T_1	7.792	0.755
T_2	7.654	0.736
T_3	7.396	0.689
T_4	7.052	0.683
T_5	7.952	0.742
T_6	7.66	0.738
T_7	7.618	0.734
T_8	8.186	0.765
avg.	7.6	0.73
std.	0.34	0.027

Figure 4.23: Experimental result: photographs of fractured specimens and statistics.

Acknowledgements

S.C. and K.G.W. would like to acknowledge the support of the Office of Naval Research (ONR) under award N00014-17-1-2831, and the support of the National Science Foundation (NSF) under awards CBET-1751487 and CBET-1706003. Y.Z., D.L. and P.Z. would like to

acknowledge the support of the National Institutes of Health (NIH) on this work through grant R37-DK052985-21.

Bibliography

[1] M. Chen, J. W. McCauley, and K. J. Hemker, "Shock-induced localized amorphization in boron carbide," *Science*, vol. 299, no. 5612, pp. 1563–1566, 2003.

[2] R. G. S. Barsoum, *Elastomeric Polymers with High Rate Sensitivity: Applications in Blast, Shockwave, and Penetration Mechanics*. William Andrew, 2015.

[3] B. Ramirez and V. Gupta, "Evaluation of novel temperature-stable viscoelastic polyurea foams as helmet liner materials," *Materials & Design*, vol. 137, pp. 298–304, 2018.

[4] B. Li, A. Pandolfi, and M. Ortiz, "Material-point erosion simulation of dynamic fragmentation of metals," *Mechanics of Materials*, vol. 80, pp. 288–297, 2015.

[5] J. E. Lingeman, J. A. McAteer, E. Gnessin, and A. P. Evan, "Shock wave lithotripsy: advances in technology and technique," *Nature Reviews Urology*, vol. 6, no. 12, p. 660, 2009.

[6] P. Zhong, "Shock wave lithotripsy," in *Bubble dynamics and shock waves*, pp. 291–338, Springer, 2013.

[7] Z. P. Bažant and F. C. Caner, "Comminution of solids caused by kinetic energy of high shear strain rate, with implications for impact, shock, and shale fracturing," *Proceedings of the National Academy of Sciences*, vol. 110, no. 48, pp. 19291–19294, 2013.

[8] W. Chen, O. Maurel, T. Reess, A. S. De Ferron, C. La Borderie, G. Pijaudier-Cabot, F. Rey-Bethbeder, and A. Jacques, "Experimental study on an alternative oil stimulation technique for tight gas reservoirs based on dynamic shock waves generated by pulsed arc electrohydraulic discharges," *Journal of Petroleum Science and Engineering*, vol. 88, pp. 67–74, 2012.

[9] R. A. Brizzolara, D. J. Nordham, M. Walch, R. M. Lennen, R. Simmons, E. Burnett, and M. S. Mazzola, "Non-chemical biofouling control in heat exchangers and seawater piping systems using acoustic pulses generated by an electrical discharge," *Biofouling*, vol. 19, no. 1, pp. 19–35, 2003.

[10] R. Schaefer, R. Claudi, and M. Grapperhaus, "Control of zebra mussels using sparker pressure pulses," *American Water Works Association. Journal*, vol. 102, no. 4, p. 113, 2010.

[11] D. E. Fovargue, S. Mitran, N. B. Smith, G. N. Sankin, W. N. Simmons, and P. Zhong, "Experimentally validated multiphysics computational model of focusing and shock wave formation in an electromagnetic lithotripter," *The Journal of the Acoustical Society of America*, vol. 134, no. 2, pp. 1598–1609, 2013.

[12] R. H. Cole, *Underwater explosions*. Dover Publications, 1965.

[13] K. Niwa, K. Mizutari, T. Matsui, T. Kurioka, T. Matsunobu, S. Kawauchi, Y. Satoh, S. Sato, A. Shiotani, and Y. Kobayashi, "Pathophysiology of the inner ear after blast injury caused by laser-induced shock wave," *Scientific reports*, vol. 6, p. 31754, 2016.

[14] S. J. Mitchell, A. Pandolfi, and M. Ortiz, "Effect of brittle fracture in a metaconcrete slab under shock loading," *Journal of Engineering Mechanics*, vol. 142, no. 4, p. 04016010, 2016.

[15] L. E. Perotti, R. Deiterding, K. Inaba, J. Shepherd, and M. Ortiz, "Elastic response of water-filled fiber composite tubes under shock wave loading," *International Journal of Solids and Structures*, vol. 50, no. 3-4, pp. 473–486, 2013.

[16] Y. Zhou and P. Zhong, "The effect of reflector geometry on the acoustic field and bubble dynamics produced by an electrohydraulic shock wave lithotripter," *The Journal of the Acoustical Society of America*, vol. 119, no. 6, pp. 3625–3636, 2006.

[17] O. A. Sapozhnikov, A. D. Maxwell, B. MacConaghy, and M. R. Bailey, "A mechanistic analysis of stone fracture in lithotripsy," *The Journal of the Acoustical Society of America*, vol. 121, no. 2, pp. 1190–1202, 2007.

[18] M. Wijerathne, M. Hori, and H. Sakaguchi, "Simulation of dynamic crack growth in shockwave lithotripsy with PDS-FEM," *Journal of Applied Mechanics*, vol. 13, pp. 253–262, 2010.

[19] A. Neisius, N. B. Smith, G. Sankin, N. J. Kuntz, J. F. Madden, D. E. Fovargue, S. Mitran, M. E. Lipkin, W. N. Simmons, G. M. Preminger, *et al.*, "Improving the lens

design and performance of a contemporary electromagnetic shock wave lithotripter," *Proceedings of the National Academy of Sciences*, vol. 111, no. 13, pp. E1167–E1175, 2014.

[20] Y. Liu and P. Zhong, "Begostone: a new stone phantom for shock wave lithotripsy research (l)," *The Journal of the Acoustical Society of America*, vol. 112, no. 4, pp. 1265–1268, 2002.

[21] W. Simmons, F. Cocks, P. Zhong, and G. Preminger, "A composite kidney stone phantom with mechanical properties controllable over the range of human kidney stones," *Journal of the mechanical behavior of biomedical materials*, vol. 3, no. 1, pp. 130–133, 2010.

[22] E. Esch, W. N. Simmons, G. Sankin, H. F. Cocks, G. M. Preminger, and P. Zhong, "A simple method for fabricating artificial kidney stones of different physical properties," *Urological research*, vol. 38, no. 4, pp. 315–319, 2010.

[23] Y. Zhang, I. Nault, S. Mitran, E. S. Iversen, and P. Zhong, "Effects of stone size on the comminution process and efficiency in shock wave lithotripsy," *Ultrasound in Medicine and Biology*, vol. 42, no. 11, pp. 2662–2675, 2016.

[24] C. Farhat, A. Rallu, K. Wang, and T. Belytschko, "Robust and provably second-order explicit–explicit and implicit–explicit staggered time-integrators for highly non-linear compressible fluid–structure interaction problems," *International Journal for Numerical Methods in Engineering*, vol. 84, no. 1, pp. 73–107, 2010.

[25] K. Wang, A. Rallu, J.-F. Gerbeau, and C. Farhat, "Algorithms for interface treatment and load computation in embedded boundary methods for fluid and fluid–structure interaction problems," *International Journal for Numerical Methods in Fluids*, vol. 67, no. 9, pp. 1175–1206, 2011.

[26] K. Wang, J. Grétarsson, A. Main, and C. Farhat, "Computational algorithms for tracking dynamic fluid–structure interfaces in embedded boundary methods," *International Journal for Numerical Methods in Fluids*, vol. 70, no. 4, pp. 515–535, 2012.

[27] C. Farhat, J.-F. Gerbeau, and A. Rallu, "FIVER: A finite volume method based on exact two-phase Riemann problems and sparse grids for multi-material flows with large density jumps," *Journal of Computational Physics*, vol. 231, no. 19, pp. 6360–6379, 2012.

[28] A. Main, X. Zeng, P. Avery, and C. Farhat, "An enhanced fiver method for multi-material flow problems with second-order convergence rate," *Journal of Computational Physics*, vol. 329, pp. 141–172, 2017.

[29] C. Farhat, K. Wang, A. Main, S. Kyriakides, L.-H. Lee, K. Ravi-Chandar, and T. Belytschko, "Dynamic implosion of underwater cylindrical shells: experiments and computations," *International Journal of Solids and Structures*, vol. 50, no. 19, pp. 2943–2961, 2013.

[30] K. G. Wang, P. Lea, A. Main, O. McGarity, and C. Farhat, "Predictive simulation of underwater implosion: Coupling multi-material compressible fluids with cracking struc-

tures," in *ASME 2014 33rd International Conference on Ocean, Offshore and Arctic Engineering*, pp. V08AT06A028–V08AT06A028, American Society of Mechanical Engineers, 2014.

[31] K. Wang, P. Lea, and C. Farhat, "A computational framework for the simulation of high-speed multi-material fluid–structure interaction problems with dynamic fracture," *International Journal for Numerical Methods in Engineering*, vol. 104, no. 7, pp. 585–623, 2015.

[32] K. G. Wang, "Multiphase fluid-solid coupled analysis of shock-bubble-stone interaction in shockwave lithotripsy," *International journal for numerical methods in biomedical engineering*, vol. 33, no. 10, 2017.

[33] C. Farhat, A. Larat, A. Main, P. Avery, K. Wang, and C. Saint-Jalm, "An embedded boundary method for viscous fluid/structure interaction problems and application to flexible flapping wings," in *42nd AIAA Fluid Dynamics Conference and Exhibit*, p. 2688, 2012.

[34] Z. Huang, P. Avery, C. Farhat, J. Rabinovitch, A. Derkevorkian, and L. D. Peterson, "Simulation of parachute inflation dynamics using an Eulerian computational framework for fluid-structure interfaces evolving in high-speed turbulent flows," in *2018 AIAA Aerospace Sciences Meeting*, p. 1540, 2018.

[35] H. Chung, S. Cao, M. Philen, P. Beran, and K. Wang, "CFD-CSD coupled analysis of

underwater propulsion using a biomimetic fin-and-joint system," *Computers and Fluids*, (under review).

[36] S. Murakami, *Continuum damage mechanics: a continuum mechanics approach to the analysis of damage and fracture*, vol. 185. Springer Science & Business Media, 2012.

[37] F. R. Tuler and B. M. Butcher, "A criterion for the time dependence of dynamic fracture," *International Journal of Fracture Mechanics*, vol. 4, no. 4, pp. 431–437, 1968.

[38] A. Nyoungue, Z. Azari, M. Abbadi, S. Dominiak, and S. Hanim, "Glass damage by impact spallation," *Materials Science and Engineering: A*, vol. 407, no. 1-2, pp. 256–264, 2005.

[39] D. Fovargue, *Multiscale and multiphysics computational models of processes in shock wave lithotripsy*. PhD thesis, The University of North Carolina at Chapel Hill, 2013.

[40] G. L. Chahine, A. Gnanaskandan, A. Mansouri, C.-T. Hsiao, and R. Content, "Interaction of a cavitation bubble with a polymeric coating–scaling fluid and material dynamics," *International Journal of Multiphase Flow*, vol. 112, pp. 155–169, 2019.

[41] C.-T. Hsiao, A. Jayaprakash, A. Kapahi, J.-K. Choi, and G. L. Chahine, "Modelling of material pitting from cavitation bubble collapse," *Journal of Fluid Mechanics*, vol. 755, pp. 142–175, 2014.

[42] R. Saurel and R. Abgrall, "A simple method for compressible multifluid flows," *SIAM Journal on Scientific Computing*, vol. 21, no. 3, pp. 1115–1145, 1999.

[43] V. Coralic and T. Colonius, "Shock-induced collapse of a bubble inside a deformable vessel," *European Journal of Mechanics-B/Fluids*, vol. 40, pp. 64–74, 2013.

[44] R. O. Cleveland and O. A. Sapozhnikov, "Modeling elastic wave propagation in kidney stones with application to shock wave lithotripsy," *The Journal of the Acoustical Society of America*, vol. 118, no. 4, pp. 2667–2676, 2005.

[45] J. Jeong, H. Adib, and G. Pluvinage, "Proposal of new damage model for thermal shock based on dynamic fracture on the brittle materials," *Journal of Non-Crystalline Solids*, vol. 351, no. 24-26, pp. 2065–2075, 2005.

[46] Z. Zhang, F. Wu, W. Gao, J. Tan, Z. Wang, M. Stoica, J. Das, J. Eckert, B. Shen, and A. Inoue, "Wavy cleavage fracture of bulk metallic glass," *Applied physics letters*, vol. 89, no. 25, p. 251917, 2006.

[47] M. Wijerathne, M. Hori, H. Sakaguchi, and K. Oguni, "3D dynamic simulation of crack propagation in extracorporeal shock wave lithotripsy," in *IOP Conference Series: Materials Science and Engineering*, vol. 10, p. 012120, IOP Publishing, 2010.

[48] D. Fovargue, S. Mitran, G. Sankin, Y. Zhang, and P. Zhong, "An experimentally-calibrated damage mechanics model for stone fracture in shock wave lithotripsy," *International Journal of Fracture*, pp. 1–14, 2018.

[49] G. A. Main, *Implicit and Higher-order Discretization Methods for Compressible Multiphase Fluid and Fluid-structure Problems*. PhD thesis, Stanford University, 2014.

[50] N. Smith and P. Zhong, "Stone comminution correlates with the average peak pressure incident on a stone during shock wave lithotripsy," *Journal of biomechanics*, vol. 45, no. 15, pp. 2520–2525, 2012.

[51] V. T. Advanced Research Computing. `https://www.arc.vt.edu/`.

[52] A. A. Griffith, "Vi. the phenomena of rupture and flow in solids," *Philosophical transactions of the royal society of london. Series A, containing papers of a mathematical or physical character*, vol. 221, no. 582-593, pp. 163–198, 1921.

[53] A. Mota, J. Knap, and M. Ortiz, "Three-dimensional fracture and fragmentation of artificial kidney stones," in *Journal of Physics: Conference Series*, vol. 46, p. 299, IOP Publishing, 2006.

[54] C. C. Church, "A theoretical study of cavitation generated by an extracorporeal shock wave lithotripter," *The Journal of the Acoustical Society of America*, vol. 86, no. 1, pp. 215–227, 1989.

[55] L. Howle, D. G. Schaeffer, M. Shearer, and P. Zhong, "Lithotripsy: the treatment of kidney stones with shock waves," *SIAM review*, vol. 40, no. 2, pp. 356–371, 1998.

[56] R. H. Cole and R. Weller, "Underwater explosions," *Physics Today*, vol. 1, p. 35, 1948.

[57] J. Li and J.-l. Rong, "Experimental and numerical investigation of the dynamic response of structures subjected to underwater explosion," *European Journal of Mechanics-B/Fluids*, vol. 32, pp. 59–69, 2012.

[58] R. O. Cleveland, M. R. Bailey, N. Fineberg, B. Hartenbaum, M. Lokhandwalla, J. A. McAteer, and B. Sturtevant, "Design and characterization of a research electrohydraulic lithotripter patterned after the dornier HM3," *Review of Scientific Instruments*, vol. 71, no. 6, pp. 2514–2525, 2000.

[59] B. Granz and G. Köhler, "What makes a shock wave efficient in lithotripsy?," *The Journal of stone disease*, vol. 4, no. 2, pp. 123–128, 1992.

[60] S. Mishriki, N. Cohen, A. Baker, M. Wills, H. Whitfield, and R. Feneley, "Choosing a powerful lithotriptor," *BJU International*, vol. 71, no. 6, pp. 653–660, 1993.

[61] W. Eisenmenger, "The mechanisms of stone fragmentation in ESWL," *Ultrasound in medicine and biology*, vol. 27, no. 5, pp. 683–693, 2001.

Chapter 5

Shock-Induced Bubble Collapse Near Elastic and Viscoelastic Materials: Effects of Acoustic Impedance

(To be submitted to *Physical Review Fluids*)

S. Cao [a], G. Wang [a], O. Coutier-Delgosha [a], K. G. Wang [a]

[a] Department of Aerospace and Ocean Engineering, Virginia Polytechnic Institute and State University, Blacksburg, VA 24061, United States

Abstract

The fluid dynamics of a bubble collapsing near an elastic or viscoelastic material is coupled with the dynamics of the material. We apply a multiphase fluid-solid coupled computational model to simulate the collapse of an air bubble in water induced by an ultrasound shock wave, with different types of materials in its vicinity including metals (e.g., aluminum), polymers (e.g., polyurea), minerals (e.g., gypsum), and fat. We characterize the fluid-material interaction using fluid pressure, velocity, bubble volume, and the maximum tensile and shear stresses in the material. We show that the relative acoustic impedance of the material compared to that of the ambient fluid, namely Z/Z_0, plays a significant role, with $Z/Z_0 = 1$ being a critical point. When $Z/Z_0 < 1$, the material reflects the compressive shock front as a tensile wave. The reflected tensile wave impinges on the bubble and decelerates its collapse. As a result, the bubble collapse produces only a liquid jet, but not a shock wave. When $Z/Z_0 > 1$, the reflected wave is compressive. It accelerates the bubble collapse, thereby generating a shock wave with magnitude much higher than that of the incident shock. In return, this leads to significantly higher stresses inside the material.

Keywords

Cavitation, Fluid-solid interaction, Finite element method, Multiphase flow

5.1 Introduction

The collapse of a bubble near a material surface features a rapid, non-spherical compression of the internal gas, which may release mechanical and thermal energy in the forms of shock wave, liquid jet, and increased local temperature. This process is a fundamental event in many science and engineering applications that involve cavitation, either as a harmful byproduct leading to erosion, noise, and performance degradation, or as a useful mechanism for desired material modification and fabrication. Within the latter category, it has been demonstrated that the energy pulses released from bubble collapse may be used to remove contaminants or unwanted particles on a surface [1, 2], fabricate nanostructured solid materials [3], break agglomerates in a liquid metal [4], facilitate kidney stone destruction in shock wave lithotripsy [5], increase the permeability of human tissue or cell membrane for targeted drug/gene delivery [6, 7], and mediate cellular mechanotransduction [8] — just to name a few examples. A common issue in these applications is that the intensity, extent, and location of cavitation need to be controlled carefully, as the boundary between meritorious effects and deleterious effects can be narrow. For example, using cavitation to remove biofouling on ship hulls needs to avoid damage to hull coatings [2]. In lithotripsy, cavitation bubbles can contribute to stone fragmentation; yet they may also damage human tissue and scatter the focused ultrasound waves [9, 10]. Similarly, the use of cavitation to produce cell sonoporation produces therapeutic effects only when the detrimental side effects due to overdose do not occur [11]. In general, the need of controlled cavitation bubble collapse near various solid and soft materials calls for improved understanding of the two-way coupling between bubble

dynamics and a material's response.

In the past, the non-spherical collapse of a bubble near a rigid wall, including the resulting shock wave and microjet, has been studied using both experimental and computational methods (e.g., [12, 13, 14, 15, 16, 17]). The damage and fracture (e.g., pits, cracks, holes) in a nearby material after multiple cycles of bubble collapse have also been investigated (e.g., [18, 19]). Nonetheless, knowledge of the dynamic response of a solid or soft material to bubble collapse — such as the magnitude, profile, and propagation of surface and body elastic waves — is still limited. In this regard, a few teams (e.g., Freund *et al.* [20], Kobayashi *et al.* [21]) have applied Eulerian multiphase fluid dynamics solvers to simulate the interaction of collapsing bubbles with soft materials (e.g., tissues and fat), in which the soft materials are modeled as fluids. Turangan *et al.* [22] have applied a Lagrangian solver to simulate shock-induced bubble collapse near aluminum walls and foils. Chahine and Hsiao [23] have applied a fluid-solid coupled solver to simulate bubble collapse near metals and polymers, including the resulting permanent deformation (e.g., pitting). Wang [24] has applied a fluid-solid coupled solver to simulate shock-bubble-stone interaction in the context of shock wave lithotripsy. Moreover, although a few studies using high-speed photography and acoustic measurements have revealed significant impact of the Young's modulus of the material on bubble dynamics (e.g., [25, 26, 27]), the detailed reciprocal effects of the acoustic, elastic, and viscoelastic properties of the material on bubble dynamics are still largely unknown.

In this paper, we present a computational study of shock-induced bubble collapse near different solid and soft materials, focusing on describing the two-way fluid-material interaction

and investigating the effects of the material's acoustic impedance. Specifically, we consider an air bubble in liquid water next to a planar material boundary. We send an ultrasound shock wave with a sharp compressive front towards the bubble, which drives it to collapse. This setting is relevant to a number of ultrasound applications, and is possible to replicate in a laboratory environment. The acoustic impedance of a material is defined as $Z = \rho c$, where ρ and c denote mass density and acoustic (P-wave) velocity, respectively. Our interest in the effects of Z is motivated by two considerations. First, it is a fundamental material property that can often clearly distinguish different "hard" and "soft" materials in an application. Second, a few previous studies have indicated that the reflection of the shock wave against the material surface may have significant effects. For example, Calvisi *et al.* [13] highlighted that the reflected shock against a rigid wall intensifies the non-spherical bubble collapse. The results of Johnsen and Colonius [15] and Wang [24] also support this finding. Acoustic impedance is a key parameter in wave reflection and transmission; and a rigid wall can be considered as an extreme case with $Z = \infty$. Therefore, the finding mentioned above naturally suggests that it is valuable to investigate real materials with different (and finite) values of Z, including cases where its value is smaller than the acoustic impedance of the ambient fluid.

We employ a recently developed three-dimensional (3D), multiphase fluid-solid coupled computational framework in this study [28]. The important components of this framework relevant to the present work include: (a) an Eulerian finite volume, multiphase compressible Navier-Stokes equations solver, equipped with a level-set method for tracking the surface

of the bubble; (b) a Lagrangian finite element solid mechanics (elasticity and viscoelasticity) solver, including models of material damage and fracture; (c) an embedded boundary method for tracking the fluid-solid interface in an unstructured, non-body-conforming fluid mesh [29, 30]; (d) the FIVER ("FInite Volume Method with Exact multi-material Riemann solvers") method for enforcing the interface conditions at the liquid-gas and fluid-solid interfaces [31, 32, 33]; and (e) a second-order, numerically stable partitioned procedure for coupling the fluid and solid solvers [34]. This computational framework has been applied to simulate several fluid-structure interaction problems involving shock waves, large structural deformation, instability, and fracture (e.g., [35, 36, 37, 38]). It has also been verified and validated for a few two-phase flow problems involving a bubble collapsing near a rigid wall (e.g., [24, 33]). In this work, we simulate the collapse of a bubble near a broad range of materials including metals (e.g., aluminum), polymers (e.g., polyurea), minerals (e.g., gypsum), and fat. In each case, we characterize the two-way fluid-material interaction using fluid pressure, velocity, bubble volume, and the maximum tensile and shear stresses in the material. To the effect of Z on the dynamics of bubble collapse, we compare the bubble's collapse time, the minimum bubble volume, and the pressure load induced by the emitted shock wave on the material surface for different cases.

The remainder of this paper is organized as follows. Section 5.2 presents the physical model and numerical methods used in this study. Section 5.3 presents a verification of the computational framework using a three-dimensional benchmark problem featuring wave transmission and deflection at a fluid-solid interface. Next, Section 5.4 presents shock-induced bubble col-

lapse near three representative materials, focusing on describing the two-way interaction between the fluid dynamics and the response of the material. Furthermore, Section 5.5 presents an extended parametric study that considers different materials with acoustic impedance ranging from 0.063 MPa·s/m to 17.8 MPa·s/m and Young's modulus from 1.5 MPa to 71.1 GPa.

5.2 Physical model and numerical methods

5.2.1 Governing and constitutive equations

We consider a three-dimensional (3D) spatial domain comprised of multiple subdomains occupied by different materials. Figure 5.1 presents a schematic drawing of the problem setup. Let Ω_G, Ω_L and Ω_S denote the subdomains occupied by the bubble, the ambient liquid, and the solid (or soft) material, respectively. We model both the gas inside the bubble and the ambient liquid as compressible inviscid flows. Hence, in Ω_G and Ω_L, we solve the following Euler equations in the Eulerian frame.

$$\frac{\partial W(\mathbf{x},t)}{\partial t} + \nabla \cdot \mathcal{F}(W) = 0, \qquad \forall \mathbf{x} \in \Omega_L(t) \cup \Omega_G(t),\, t > 0, \tag{5.1}$$

with

$$W = \begin{bmatrix} \rho \\ \rho V \\ \rho e_t \end{bmatrix}, \qquad \mathcal{F} = \begin{bmatrix} \rho V^T \\ \rho V \otimes V + p\mathbf{I} \\ (\rho e_t + p)V^T \end{bmatrix},$$

where ρ, V, p and e_t denote the fluid density, velocity, pressure, and the total energy per unit mass, respectively. $\mathbf{I}$ is the 3×3 identity matrix. Equation (5.1) is closed by an equation of state (EOS) for each fluid material. We apply the perfect gas EOS to the gas inside the bubble, i.e.

$$p = (\gamma_G - 1)\,\rho e, \tag{5.2}$$

where γ_G is the heat capacity ratio, and e is the internal energy per unit mass. In this work we set $\gamma_G = 1.4$. We assume the ambient fluid is water, and apply the stiffened equation of state, i.e.

$$p = (\gamma_L - 1)\,\rho e - \gamma_L p_L, \tag{5.3}$$

where γ_L and p_L are model parameters, set by $\gamma_L = 6.59$ and $p_L = 410$ MPa.

Within the subdomain of the solid material, i.e. Ω_S, we adopt the Lagrangian frame and solve the following equation of motion that enforces the balance of linear momentum.

$$\rho_s \ddot{\mathbf{u}}(\mathbf{X}, t) - \nabla \cdot \sigma(\mathbf{u}, \dot{\mathbf{u}}) = \mathbf{b}, \qquad \forall \mathbf{X} \in \Omega_S(0),\, t > 0, \tag{5.4}$$

where $\mathbf{u}$ denotes displacement, ρ_s the material's mass density and σ the Cauchy stress tensor.

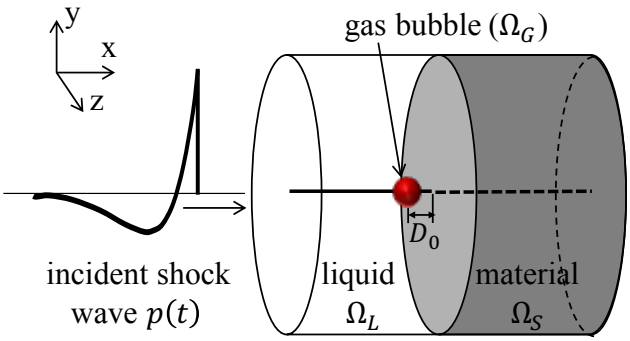

Figure 5.1: A 3D fluid-solid coupled model of shock-induced bubble collapse near a solid or soft material. (R_0 denotes the initial distance from the center of spherical bubble to the material surface.)

b denotes the body force acting in Ω_S, which is assume to be 0 in this study.

We adopt the generalized Maxwell model of viscoelasticity [39], which combines linear springs and linear dashpots. Assuming zero strain at $t = 0$, the stress at any time instance $t > 0$ can be written in the form of the hereditary integral,

$$\sigma(t) = \int_0^t G_R(t-s)\frac{d\epsilon(s)}{ds}ds, \tag{5.5}$$

where ϵ denotes strain tensor. $G_R(t)$ is the relaxation modulus, which can be expressed using a Prony series, i.e.

$$G_R(t) = G_0\left[1 - \sum_{i=1}^{N} g_i\left(1 - e^{-t/\tau_i}\right)\right], \tag{5.6}$$

where $G_0 = G_R(0)$ is the instantaneous modulus, g_i and τ_i are material-specific model parameters. Numerically, we compute $\sigma(t)$ using a recursive formula, as shown in Goh *et al.* [40].

For some of the materials investigated in this study (e.g., aluminum, steel), the viscoelastic effect of the material is negligible. These materials are modeled essentially by linear elasticity, with constitutive equation

$$\sigma = \frac{E\nu}{(1+\nu)(1-2\nu)} tr(\epsilon)\mathbf{I} + \frac{E}{1+\nu}\epsilon, \tag{5.7}$$

where E and ν denote the Young's modulus and Poisson's ratio of the material.

At the fluid-solid interface, $\Gamma_{FS} = \partial\Omega_S(t) \cap (\partial\Omega_L(t) \cup \partial\Omega_G(t))$, we enforce the continuity of normal velocity and surface traction, i.e.,

$$\begin{aligned} (V - \dot{\mathbf{u}}) \cdot \mathbf{n} &= 0, \\ -p\mathbf{n} &= \boldsymbol{\sigma}(\mathbf{u}, \dot{\mathbf{u}}) \cdot \mathbf{n}, \end{aligned} \qquad \text{on } \Gamma_{FS}, \tag{5.8}$$

where $\mathbf{n}$ denotes the outward unit normal to Γ_{FS}.

At the liquid-gas interface, $\Gamma_{FF}(t) = \partial\Omega_L(t) \cap \partial\Omega_G(t)$, we assume that the two fluid materials are immiscible. Also, surface tension is negligible compared to the pressure of the prescribed shock wave. Thus, the interface conditions are those describing a contact discontinuity, i.e.,

$$\begin{aligned} (V_L - V_G) \cdot \mathbf{n} &= 0, \\ p_L &= p_G, \end{aligned} \qquad \text{on } \Gamma_{FF}, \tag{5.9}$$

5.2.2 Fluid-solid coupled computational framework

We apply recently developed computational framework to solve the above model equations. The solver couples a finite volume, multiphase fluid dynamics solver with a finite element solid dynamics solver using an embedded boundary method and a second-order accurate partitioned procedure (Fig. 5.2).

As illustrated in Figure 5.2(a), the fluid governing equation is semi-discretized in an *augmented* fluid domain $\widetilde{\Omega}$, defined by $\widetilde{\Omega} = \Omega_L \cup \Omega_G \cup \Omega_S$, using an unstructured, node-centered, non interface-conforming finite volume mesh, denoted by $\widetilde{\Omega}^h$. Within an arbitrary control volume C_i, Eq. (5.1) becomes

$$\frac{\partial W_i}{\partial t} + \frac{1}{\|C_i\|} \sum_{j \in Nei(i)} \int_{\partial C_{ij}} \boldsymbol{F}(W) \cdot \boldsymbol{n}_{ij} dS = 0, \tag{5.10}$$

where W_i denotes the average of W in C_i, $\|C_i\|$ denotes the volume of C_i, $Nei(i)$ denotes the set of nodes connected to node i by an edge, $\partial C_{ij} = \partial C_i \cap \partial C_j$, and $\boldsymbol{n}_{ij}$ is the unit normal to ∂C_{ij}. Three scenarios arise in the numerical approximation of the surface integral on ∂C_{ij}:

1. If nodes i and j belong to the same fluid subdomain, the numerical flux across ∂C_{ij} is calculated using the well-known Monotonic Upwind Scheme Conservation Law (MUSCL) scheme and Roe's flux.

2. If nodes i and j belong to different fluid subdomains, a one-dimensional (1D) two-fluid

Riemann problem is constructed along edge i-j, i.e.

$$\frac{\partial \boldsymbol{w}}{\partial \tau} + \frac{\partial \mathcal{F}(\boldsymbol{w})}{\partial \xi} = 0, \qquad \text{with} \quad \boldsymbol{w}(\xi, 0) = \begin{cases} \boldsymbol{w}_i & \text{if } \xi \leq 0, \\ \boldsymbol{w}_j & \text{if } \xi > 0, \end{cases} \tag{5.11}$$

where τ denotes a fictitious time coordinate; ξ denotes the spatial coordinate along the 1D axis aligned with $\boldsymbol{n}_{ij}$ and centered at the midpoint between nodes i and j. The initial states $\boldsymbol{w}_i$ and $\boldsymbol{w}_j$ are derived from the reconstructed state variables on the two sides of ∂C_{ij}. Equations 5.9 are enforced at the moving interface for $\tau > 0$. The exact solution of this 1D Riemann problem is supplied to Roe's flux function to compute the flux across ∂C_{ij} [33, 32].

3. If node i belongs to a fluid subdomain, and j belongs to the solid subdomain, a 1D fluid-structure Riemann problem with a moving wall boundary is constructed and solved, i.e. [31]

$$\frac{\partial \boldsymbol{w}}{\partial \tau} + \frac{\partial \mathcal{F}(\boldsymbol{w})}{\partial \xi} = 0, \qquad \tau > 0,\ \xi < v_S \tau, \tag{5.12}$$

$$\boldsymbol{w}(\xi, 0) = \boldsymbol{w}_i, \qquad \xi < 0, \tag{5.13}$$

$$v(v_S \tau, \tau) = v_S, \qquad \tau > 0, \tag{5.14}$$

where ξ is the spatial coordinate along the normal direction of the fluid-solid interface and centered at the midpoint between nodes i and j. The initial state $\boldsymbol{w}_i$ is derived from the reconstructed fluid state at the interface. v denotes the fluid velocity at the

moving wall boundary, and v_S the normal velocity computed by the solid dynamics solver at the same location.

The above algorithm requires tracking the liquid-gas and fluid-solid interfaces in the unstructured, non interface-conforming mesh $\widetilde{\Omega}^h$. To this end, we track the evolution of the liquid-gas interface by solving the following level set equation,

$$\frac{\partial \phi(\boldsymbol{x}, t)}{\partial t} + V \cdot \nabla \phi = 0, \qquad \forall \boldsymbol{x} \in \Omega_L \cup \Omega_G \cup \Omega_S, \tag{5.15}$$

where $\phi(\boldsymbol{x}, t)$ represents the signed shortest distance from $\boldsymbol{x}$ to the interface. In this way, the large deformation and topological changes (e.g. interfacial splitting and merging) of the bubble surface are naturally accommodated. To track the fluid-solid interface, we apply a collision-based computational geometry algorithm as presented in [29, 28].

We apply a standard Galerkin finite element method to semi-discretize the weak form of Equation (5.4), which yields

$$\mathbf{M}\frac{\partial^2 \mathbf{u}^h}{\partial t^2} + \mathbf{f}^{int}\Big(\mathbf{u}^h, \frac{\partial \mathbf{u}^h}{\partial t}\Big) = \mathbf{f}^{ext}, \tag{5.16}$$

where $\mathbf{M}$ denotes the mass matrix, $\mathbf{u}^h$ denotes the discrete displacement vector. $\mathbf{f}^{int}$ and $\mathbf{f}^{ext}$denote the discrete internal force and external force vector, respectively.

We use a staggered fluid-solid time-integrator presented in [34] to advance the fluid and solid

subsystems. Specifically, the fluid subsystem is time-integrated using an explicit fourth-order Runge-Kutta scheme, while the solid subsystem is time-integrated using the second-order central difference scheme. Notably, the fluid and solid time steps are offset by half a step (Fig. 5.2(b)). This is a designed feature to achieve second-order coupling while maintaining numerical stability.

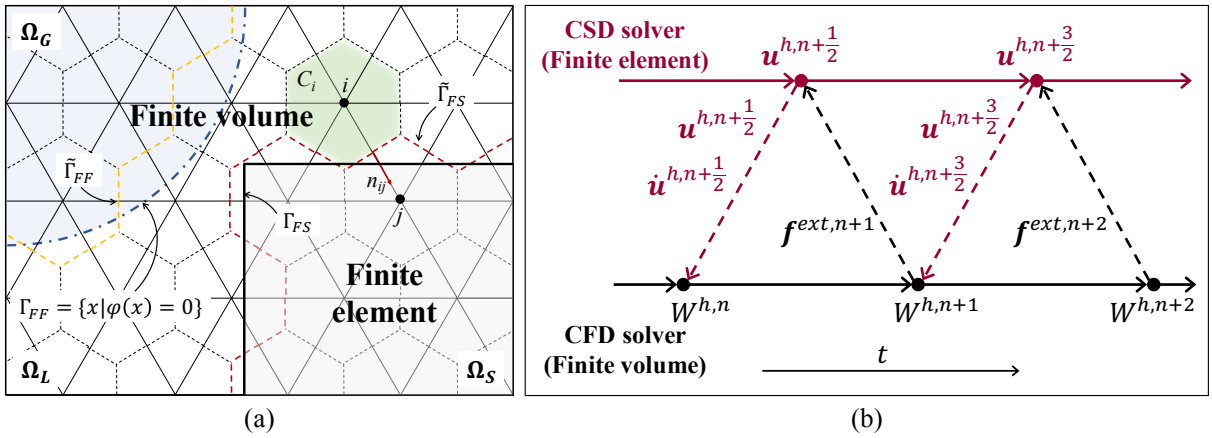

Figure 5.2: Illustration of the spatial (a) and temporal (b) discretization methods applied in the computational framework.

5.3 Verification

We first apply the computational framework described in Section 5.2.2 to solve a 3D model problem featuring the propagation of an impulsive pressure wave across a planar fluid-solid interface. The objective is to verify the computational framework for predicting wave transmission and deflection at a fluid-solid interface, which is an important feature of the bubble-material interaction problem under investigation. Fig. 5.3(a) presents the setup of the prob-

lem. We consider a cylindrical fluid-solid domain with a diameter of 12 mm and a height of 20 mm. In the fluid subdomain, a spherical pressure wave is generated from a monopole source located at a distance of $H = 2.4$ mm from the interface. We model the pressure wave using Ricker wavelet, which features a central peak and two side lobes. Table 5.1 summarizes the geometric and material properties involved in the simulation.

We prescribe the Ricker wavelet as the initial condition of the fluid. Specifically, the initial pressure at a distance r from the source is given by:

$$p(r) = p_0 + \frac{Q(-r/c_0)}{r}, \quad \text{with} \quad Q(s) = \left[1 - 2\pi^2 f_0^2 (s + s_1)^2\right] e^{-\pi^2 f_0^2 (s+s_1)^2}, \tag{5.17}$$

where p_0 denotes the hydrostatic pressure, c_0 the speed of sound in the fluid, f_0 the frequency of Ricker wavelet, and s_1 is a constant that controls the initial position of the wavelet. Table 5.1 summarizes the parameter values specified in the simulation. The initial pressure wave (Fig. 5.3(a)) has a peak magnitude of 913 Pa and a width of about 2 mm in the radial directions. Its central peak is located at about 1.31 mm above the interface.

The simulation is carried out using an unstructured, finite volume fluid mesh with 21,909,716 tetrahedral elements and a finite element solid mesh with 6,672,384 tetrahedral elements. In the most refined region, the characteristic element size is approximately 0.01 mm for the fluid and 0.04 mm for the solid. A constant time step size of 5.0×10^{-4} μs is used in both solvers.

Fig. 5.3(b) presents the numerical solution at four time instances, showing the fluid pressure

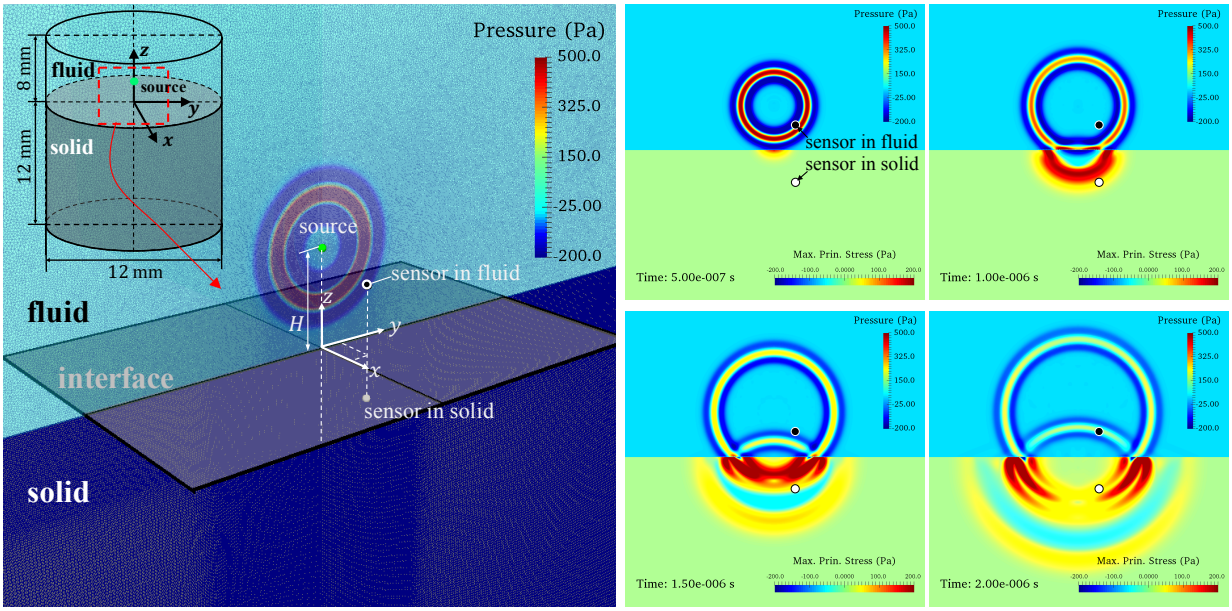

Figure 5.3: (a) Problem setup (The dynamic pressure of the fluid at $t = 0$ is visualized). (b) Snapshots of numerical solution at four different time instances, showing the dynamic pressure of the fluid and the maximum principal stress in the solid.

Ricker monopole source		**Fluid**		**Solid**	
H (mm)	2.4	ρ (kg/m^3)	1000	ρ_s (kg/m^3)	1995
f_0 (MHz)	1.43	c_0 (m/s)	1450	c_L (m/s)	4159
s_1 (μs)	0.76	p_0 (Pa)	1.01×10^5	c_T (m/s)	2319

c_L: longitudinal wave speed; c_T: transverse wave speed.

Table 5.1: Parameters of the problem.

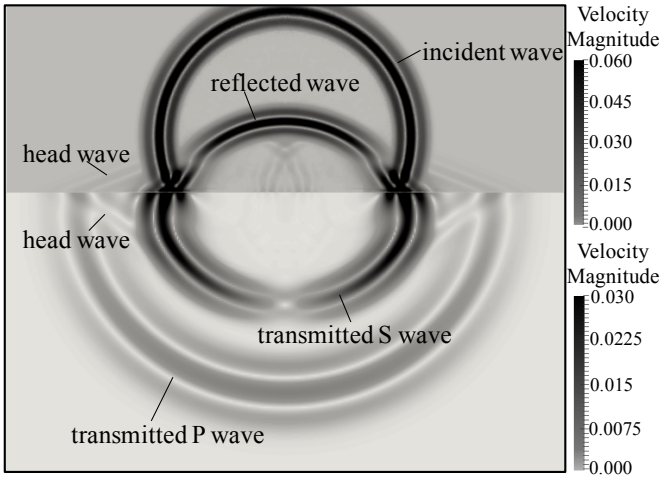

Figure 5.4: Snapshot of velocity magnitude at $t = 3$ μs (unit: mm/s, visualized in plane $x = 0$).

field and the maximum principal stress in the solid. The simulation captures the transient dynamics of wave propagation across the fluid-solid interface, including the reflection of the pressure wave and the elastodynamic response of the solid. More specifically, Fig. 5.4 shows different types of waves that occur at a specific time instance, including the incident and the reflected waves in the fluid, the longitudinal (or P) and transverse (or S) waves in the solid, and the head waves generated by the advancing of the transmitted P wave along the interface.

In this problem, the maximum dynamic pressure in the fluid is more than two orders of magnitude smaller than the hydrostatic pressure. Therefore, the incident wave can be considered as a small disturbance and modeled as an acoustic wave propagating in a homogeneous fluid medium. Given the assumption that the solid material is isotropic and linear elastic, this problem can thus be modeled adequately by coupling the linear acoustic wave equation with

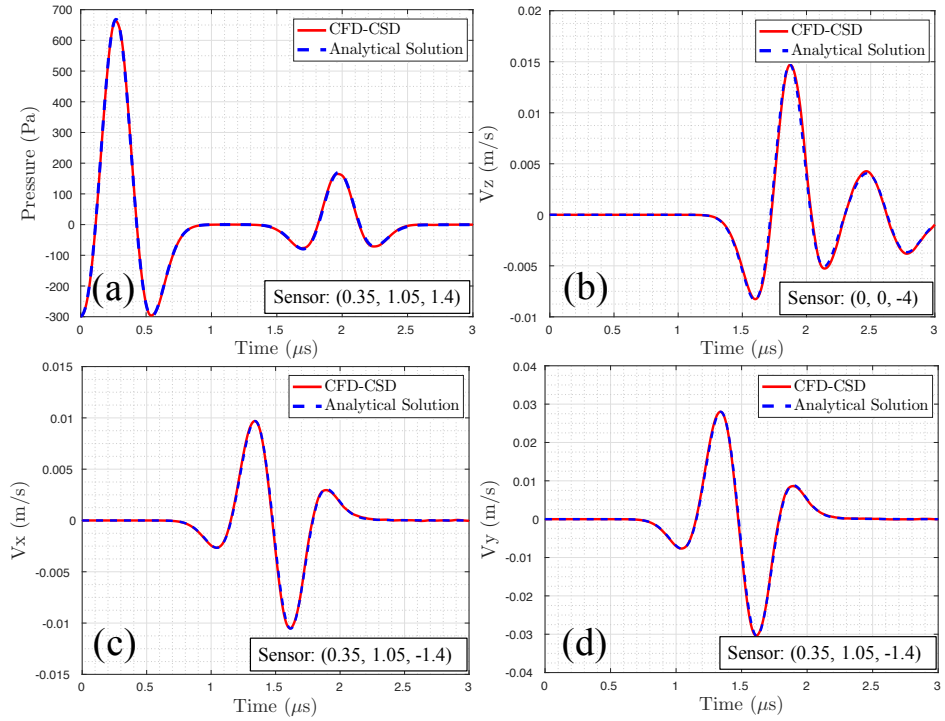

Figure 5.5: Comparison of the numerical solution (red line) with the analytical solution of the linear problem (blue dotted line). (a) Time history of pressure at sensor (0.35, 1.05, 1.4) mm in fluid. (b)-(d) Time history of z-velocity at sensor (0, 0, -4) mm and the x-,y-velocity at sensor (0.35, 1.05, -1.4) mm in solid.

the equation of motion for a linear elastic solid. The exact solution of this problem can be obtained using the Cagniard-de Hoop method [41], thereby providing a reliable reference for verifying our numerical solution. We use an open-source code, Gar6more3D [42], to compute the exact solution. Figs. 5.5(a)-(d) present a comparison of the numerical and analytical solutions at several sensors located in the fluid and solid subdomains. A close agreement is obtained. Specifically, the peak dynamic pressure recorded at sensor (0.35, 1.05, 1.4) mm between the two sets of solutions differ by only 0.66%.

5.4 Shock-induced bubble collapse near three representative materials

5.4.1 Setup of numerical experiment

In this section, we consider shock-induced bubble collapse near three representative materials, namely BegoStone (a strengthened gypsum plaster [43]), polyurea [44] and porcine subdermal fat [45]. Table 5.2 presents the important properties of these materials. In particular, their acoustic impedance vary significantly, from lower than that of the ambient water in the case of the fat, to 50.8 times higher in the case of BegoStone. Polyurea and the fat are both modeled as a viscoelastic material. For BegoStone, the viscoelastic effects are negligible under the simulated conditions, therefore it is modeled as an elastic material. As a reference, we also simulate the same bubble collapsing near a rigid wall, which can be seen as a material with infinite acoustic impedance.

Material	**Constitutive model**	**Density** ρ_s (kg/m^3)	**Young's Modulus** E_0 (GPa)	**Poisson's ratio** ν	$\mathbf{g}_1$	τ_1 (s)	Z (MPa·s/m)	**Ref.**
BegoStone	Linear elasticity	1995	27.4	0.27	–	–	8.3	[46]
Polyurea	Linear viscoelasticity	1100	0.235	0.485	0.478	6.41×10^{-5}	1.76	[23]
Fat	Linear viscoelasticity	920	1.6×10^{-3}	0.49	0.39	700	0.16	[45]

[a] For reference, the acoustic impedance of water is $Z_0 = 1.6$ MPa·s/m

Table 5.2: Material properties of three representative materials.

Fig. 5.6 shows the setup of the simulations. Initially, a spherical air bubble with a radius of $R_0 = 0.05$ mm is placed in water, at a distance of $D_0 = 2R_0$ from the material surface

(measured from the center of the bubble). The incident shock wave that induces the bubble's collapse has a compressive front with a positive peak of 35 MPa, followed by a tensile phase with a negative peak of 10.1 MPa [47]. This type of waveform can be generated in water through electrohydraulic or electromagnetic mechanisms (e.g., [48, 49]). We prescribe the incident shock wave as the initial condition of the fluid governing equation, following the method described in [38]. Away from the incident shock wave, the ambient flow velocity and hydrostatic pressure are set to 0 mm/s and $p_0 = 0.101$ MPa, respectively. For computational efficiency, we consider a 45° slice of the cylindrical domain with symmetry boundary conditions applied to the two cut planes. The computational domains for the solid and the fluid are discretized using 2,272,603 and 19,552,520 tetrahedron elements, respectively. Both meshes are refined within a region close to the bubble, where the characteristic element size is approximately 0.003 mm (for both meshes). A constant time step size of 5×10^{-5} μs is used in both solvers.

5.4.2 Result and discussion

Fig. 5.7 presents the simulation result of bubble collapse near BegoStone. Several key features are clearly captured. The impact of the incident shock wave at the proximal (left) side of the bubble causes the bubble's collapse. When the bubble reaches its minimum volume, a shock wave is generated. Also, during the non-spherical bubble collapse, a liquid-jet forms and penetrates the bubble. These features are consistent with the results of several previous studies (e.g. [47, 21, 24]). A remarkable feature of the current result is that it explicitly

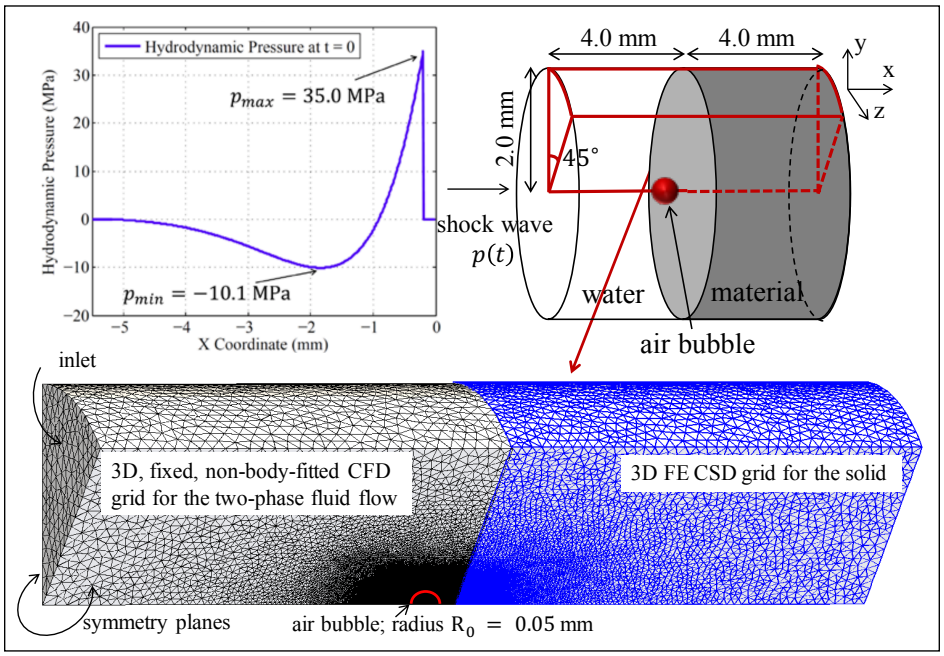

Figure 5.6: Simulation setup.

captures the propagation of the shock waves across the fluid-solid interface and that of the resulting elastic waves inside the material.

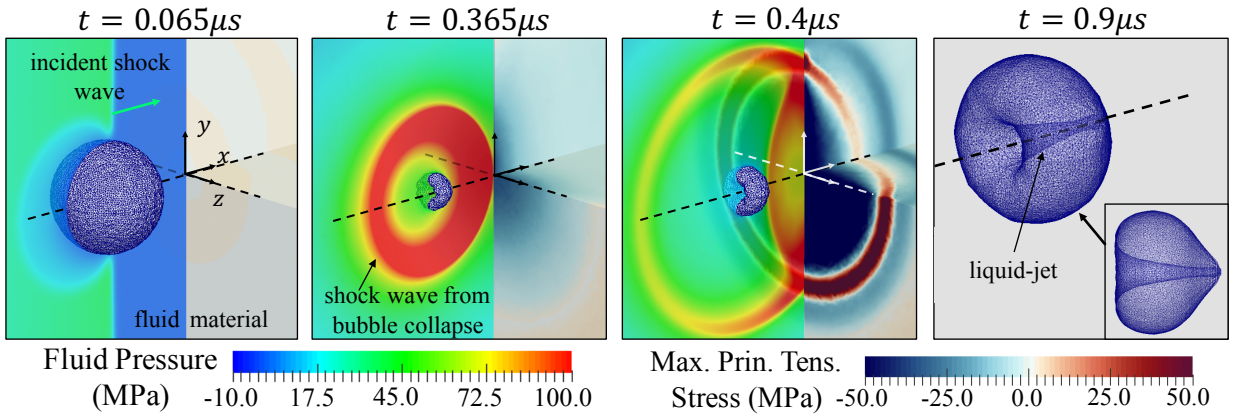

Figure 5.7: Simulation result for BegoStone at four time instants, displaying the transient fluid pressure, the maximum principal stress inside the material and on its surface, and the deformation of the bubble.

When the same bubble collapses near different materials, the speed of bubble collapse, the

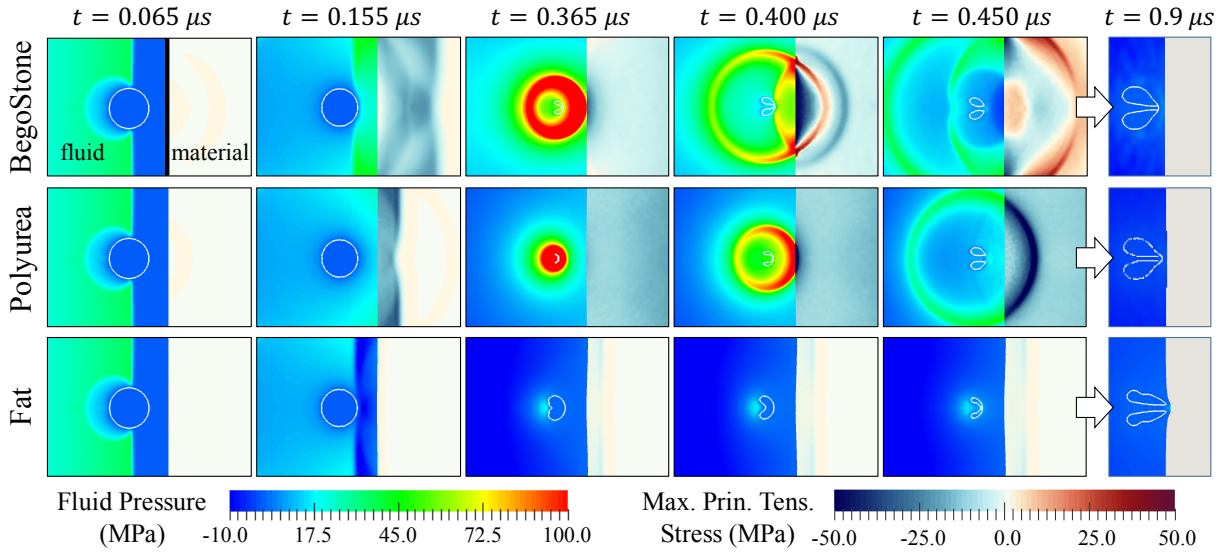

Figure 5.8: Shock-induced bubble collapse near three different materials: Numerical solutions at 6 time instances.

transient flow field, the pressure loads on the material's surface, and the transient stress in the material all vary. Fig. 5.8 compares the results of the three materials at six time instances. The first major difference lies in the reflection of the incident shock wave against the material's surface. This can be observed from the second row of images in Fig. 5.8, which are taken at $t = 0.155$ μs, when the reflection has just reached the distal (right) side of the bubble. In the case of BegoStone, the reflected wave is compressive. In the case of polyurea, the reflected wave is also compressive, yet its magnitude is much lower. By contrast, the reflection is a tensile wave in the case of the fat. At the same time, the transmitted wave inside the material also varies among the three cases. Both BegoStone and polyurea exhibit a compressive stress wave (P-wave), except that the magnitude and propagation speed of the wave are different.

The differences described above can be explained by the relative acoustic impedance of each material compared to that of the ambient fluid (i.e. Z/Z_0). Specifically, for an incident wave with a magnitude p_i which impinges normal to a plane surface , the magnitude of the reflected and transmitted waves are given by

$$p_r = p_i \frac{Z/Z_0 - 1}{Z/Z_0 + 1} \tag{5.18}$$

and

$$p_t = p_i \frac{2Z/Z_0}{Z/Z_0 + 1} \tag{5.19}$$

according to acoustic wave theory. For the three materials considered, Z/Z_0 is 5.18 for BegoStone, 1.1 for polyurea, and 0.1 for the fat. Substituting these values into the above equations, we obtain $p_r = 23.7$ MPa for BegoStone, $p_r = 1.67$ MPa for polyurea, and $p_r = -28.6$ MPa for the fat.

The reflected wave impinges on the distal (right) side of the bubble at a time it just started to collapse. In the case of BegoStone, the reflected wave is compressive, with a magnitude comparable to that of the incident shock. Therefore it accelerates the bubble collapse. By contrast, the reflected wave in the case of the fat creates a tensile stress field around the bubble, which slows down its collapse. The variation in the speed of collapse can be observed from the third row of images in Fig. 5.8, taken at $t = 0.365$ μs. By this time, the bubble near BegoStone has reached its minimum volume and is rebounding. The front of the shock wave emitted from its collapse has just arrived at the material surface. At the same time,

the bubble near polyurea has just reached its minimum volume. The collapse of the bubble near the fat is much slower. Its minimum volume is reached at $t = 0.53$ μs.

The variation in the speed of collapse has a clear impact on the emission of a shock wave and its magnitude, which can be observed from the images taken between $t = 0.365$ μs and $t = 0.450$ μs (i.e. the third, fourth, and fifth rows of Fig. 5.8). A striking difference is that the emission of shock wave is observed only in the cases of BegoStone and polyurea, but not in the case of the fat. Also, the magnitude of the emitted shock wave is higher in the case of BegoStone than in polyurea.

Furthermore, Fig. 5.8 also shows that in all the three cases, the bubble penetrates itself while rebounding from its minimum volume, thereby generating a liquid jet (also referred to as a "micro-jet") towards the material surface. In the case of the fat, this liquid jet creates a clear dimple on the material surface, as shown in the last row of Fig. 5.8). In the other two cases, the deformation is much smaller.

Next, we take a closer look at the fluid dynamics by examining the time history of bubble volume, the shock wave emitted at the end of the collapse, and the liquid jet formed during the bubble's rebound.

Fig. 5.9 compares the time history of bubble volume for all the simulated cases, including the degenerate case of the same bubble collapsing near a rigid wall. Initially, the bubble's volume is the same in all the cases, until approximately 0.15 μs, when the reflected wave arrives at the distal side of the bubble. Afterwards, the four curves start to diverge, indicating a clear

impact of the reflected wave. The bubble's collapse time, defined as the time between the arrival of the incident shock wave and the time the bubble reaches its minimum volume, is found to be 0.293 μs, 0.306 μs, 0.335 μs, and 0.493 μs in the case of the rigid wall, BegoStone, polyurea, and the fat, respectively. The bubble's minimum volume increases from 1.2×10^{-6} mm^3 in the case of the rigid wall to 2.4×10^{-5} mm^3 in the case of the fat. Given the causal relation between the material's acoustic impedance and the type (i.e. compressive vs. tensile) and magnitude of the reflected wave, the result shown in Fig. 5.9 suggests that a solid or soft material with low acoustic impedance may reduce both the energy released from bubble collapse and its peak power.

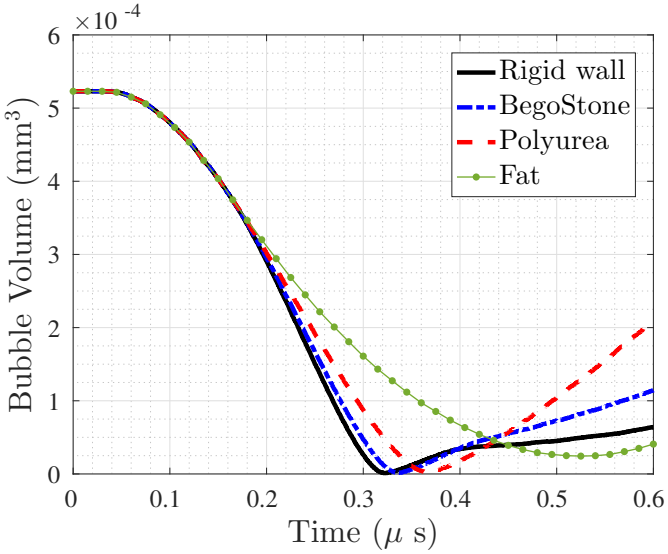

Figure 5.9: Time history of the bubble's volume.

This finding is also supported by fluid pressure and velocity data. Fig. 5.10 shows the time history of dynamic pressure at the center (i.e. on the x-axis) of the material surface. The peak pressure of the shock wave emitted from the bubble collapse is 303, 240 and 111 MPa

in the case of the rigid wall, BegoStone, and polyurea, respectively. Notably, these values are significantly higher than the peak pressure of the incident shock wave, which is 35 MPa. In the case of the fat, the bubble collapse is much slower, which does not generate a shock wave. Therefore, the time history of dynamic pressure is nearly a flat line.

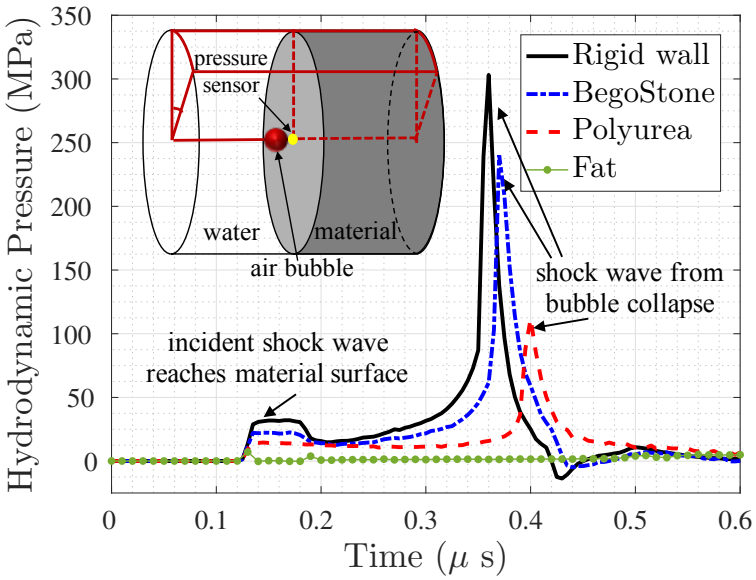

Figure 5.10: Time history of hydrodynamic pressure at a sensor on the material surface.

Furthermore, the fluid velocity field — particularly, the velocity of the liquid jet — also varies in the three simulated cases. Fig. 5.11 shows the velocity field around the bubble at different time instances. The first column of images are taken at 0.24 μs, right after the reflected wave passing the bubble. It can be observed that the magnitude of x-velocity at the distal (right) side of the bubble is higher in the case of BegoStone than that in the case of the fat. The second column of images are taken at the time when the bubble's surface velocity on the centerline reaches its maximum value in each case. The velocity magnitude decreases significantly from BegoStone to the fat. To clarify the difference, Fig. 5.12 compares the time

history of x-velocity at the proximal and distal sides of the bubble for the three materials. In the case of BegoStone, the net velocity between the proximal and distal sides of the bubble reaches 1600 m/s. This is 1.6 times as high as the maximum velocity observed in the case of polyurea, and more than 3 times higher than that for the fat. The third column of images in Fig. 5.11 present the snapshots taken at the time when the liquid jet reach in contact with the distal side of the bubble. It can be observed that the liquid jet becomes wider from BegoStone to the fat. Specifically, the width of the liquid jet in the case of the fat is more than twice as that in the case of BegoStone.

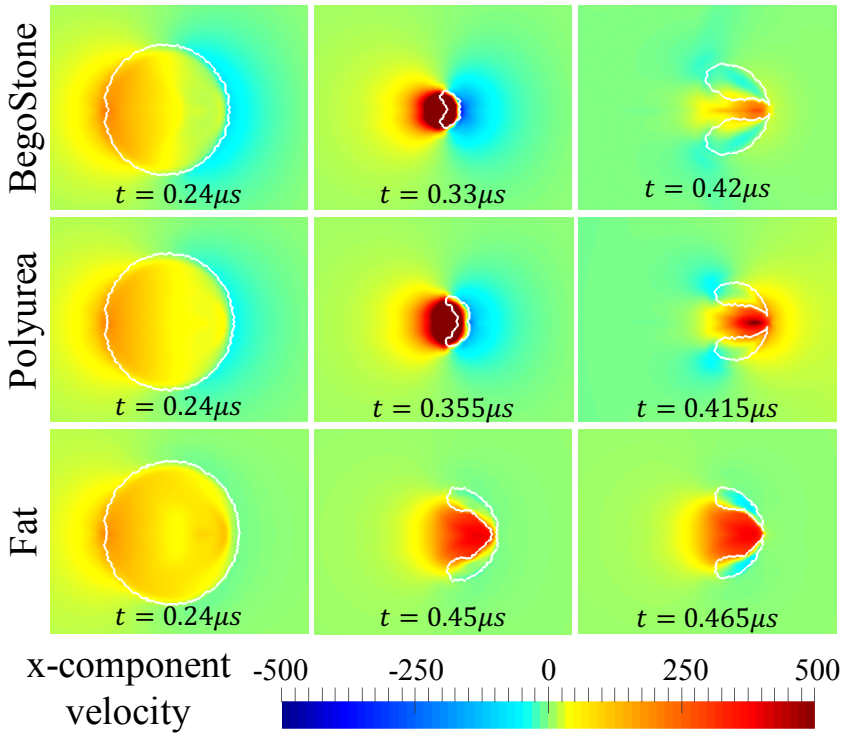

Figure 5.11: Snapshots of the fluid velocity field around the bubble.

The material's impact on the bubble dynamics leads to different hydrodynamic loading in return. Figs. 5.13(a) and 5.13(b) present two snapshots showing the response of BegoStone

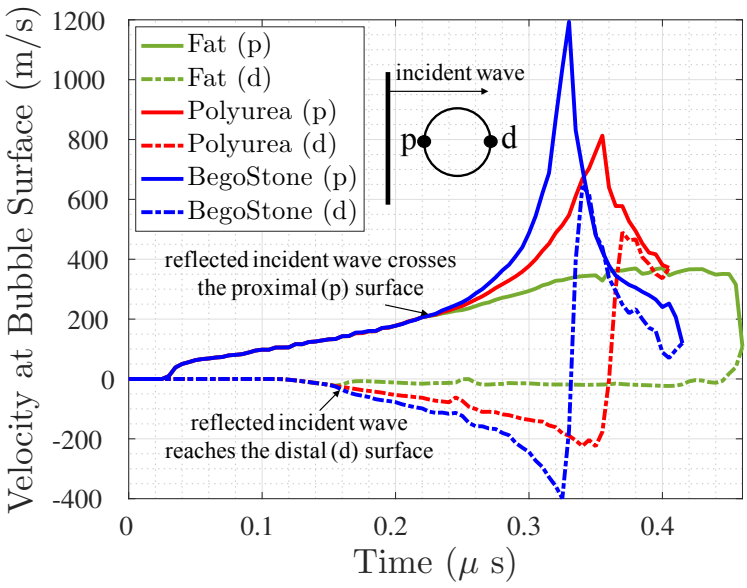

Figure 5.12: Time history of fluid velocity on the proximal and distal sides of the bubble surface.

and polyurea to the shock wave emitted from bubble collapse. For both materials, two types of elastic waves generated by the interaction of shock wave with the material surface can be clearly observed, that is, a longitudinal wave (P-wave) and a transverse wave (S-wave). Specifically, because the speeds of longitudinal and transverse waves in BegoStone are around 4159 m/s and 2319 m/s, greater than the speed of sound in water (c_0 = 1450 m/s), both waves propagate in a crescent shape and the P-wave is moving much forward of the shock wave in water. In polyurea, however, the longitudinal wave travels at a speed of 1600 m/s (closed to c_0), and hence the wavefront of P-wave appears aligned with the shock front at the interface. Also, the S-wave in polyurea appears as an almost straight line because the speed of transverse waves is around 300 m/s, much smaller than c_0.

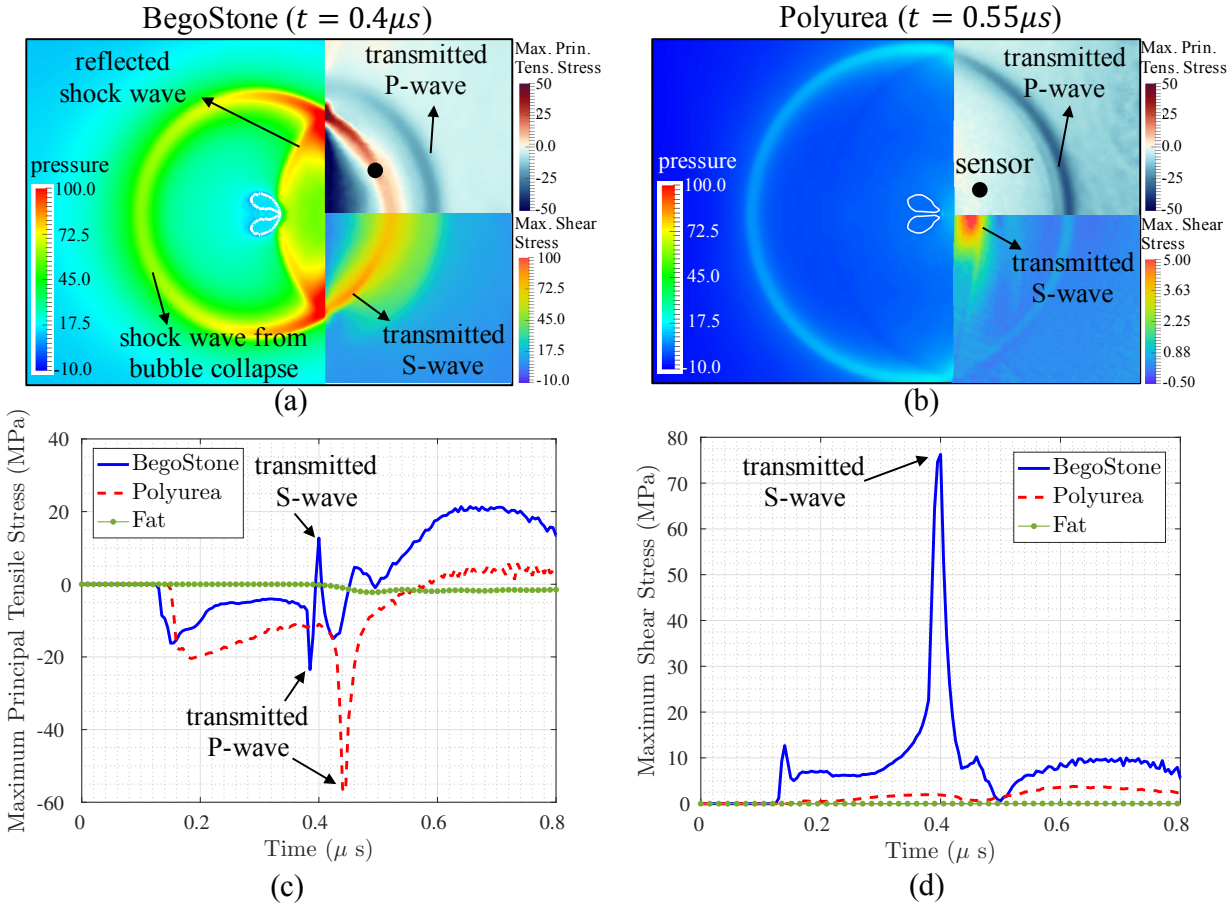

Figure 5.13: (a)-(b): Two snapshots showing different elastic waves propagating in BegoStone and the polyurea. (c)-(d): Time history of the maximum principal tensile stress and the maximum shear stress at a sensor located at (0.5,0.5,0.0) mm.

Remark:

1. Fig. 5.10 shows that even for a material with relatively large acoustic impedance such as BegoStone, modeling the material as a rigid wall boundary ($Z = Z_\infty$) of fluid domain leads to a 26% overestimate of the magnitude of the shock wave emitted from the bubble collapse. This suggests that taking into account the reciprocal effect of material's acoustic impedance is important in the study of this shock-induced bubble collapse problem.

2. We have performed another two simulations in which the polyurea and the fat are modeled as linear elastic materials (by setting $g_1 = 0$). Compared to the results presented above, neglecting the viscoelastic effect of the material only induces less than 1% difference in bubble collapse time for both cases. This is likely because, under this specific setting of the problem, the time scale of the bubble collapse is much smaller than the relaxation time in the viscoelastic model (i.e., τ_1).

5.5 An extended parametric study on the effects of acoustic impedance

In this section, we test five more materials with acoustic impedance varying in a relatively broad range (i.e. $0.063 \leq Z \leq 17.8$ MPa·s/m) to further characterize the effects of acoustic impedance on the dynamics of bubble collapse. Specifically, the materials are selected from

5 major material categories, including metals, concrete, polymers, elastomers, and foams (see Fig. 5.14(a)). Table 5.3 summarizes the elastic properties of these materials. Here, we model all the tested materials as linear elastic materials as the material's viscoelasticity is found to have a negligible impact on the bubble collapse under the current setting of the problem. The effects of Z on the bubble dynamics are characterized by comparing the bubble's collapse time, the minimum bubble volume, and the maximum hydrodynamic pressure on the material surface for different cases. For all the simulations presented in this section, the same simulation setup described in Section 5.4.1 is employed.

Material	**Density** ρ_s (kg/m^3)	**Young's Modulus** E_0 (GPa)	**Poisson's ratio** ν	**Acoustic impedance** Z (MPa·s/m)
Aluminum	2810	71.1	0.33	17.8
Stainless steel	7695	19.0	0.3	14.0
Ultracal-30 artificial stone [46]	1700	10.2	0.33	4.8
Silicone rubber	990	0.13	0.48	1.06
Polypropylene foam	150	0.027	0.01	0.063

Table 5.3: Elastic properties of the five materials with different acoustic impedance.

5.5.1 Effect on the bubble's collapse time

Fig. 5.14(b) presents the change of bubble's collapse time with the relative acoustic impedance of the material. For materials with $Z/Z_0 > 1$, the change of collapse time is relatively small. For example, when Z/Z_0 is reduced from 11.1 (i.e., aluminum) to 1.08 (i.e., polyurea), the collapse time increases only 10%. However, when $Z/Z_0 < 1$, the collapse time increases sig-

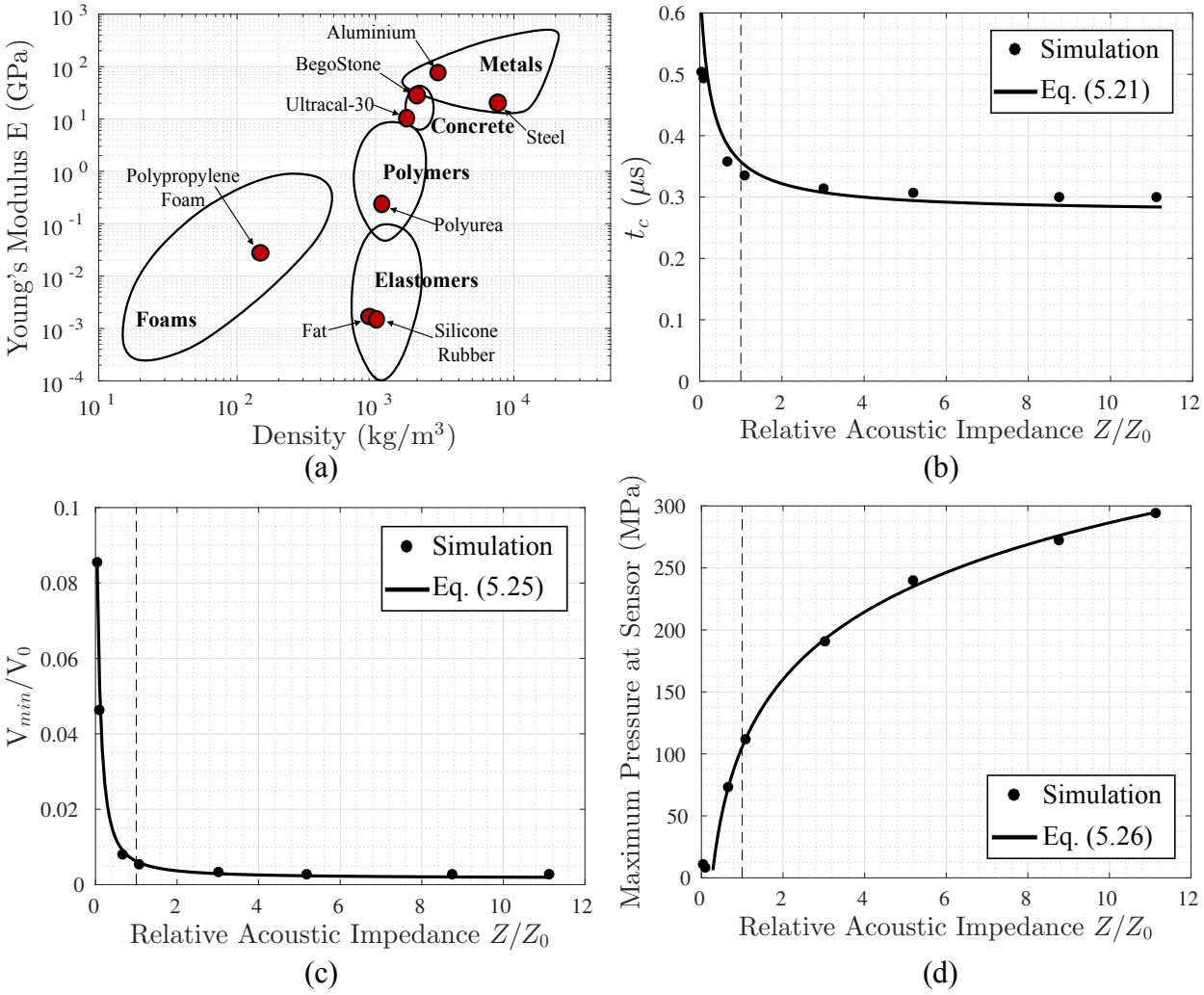

Figure 5.14: (a): Young's modulus-density plot for material selection. The red circular markers represent the tested materials, including the three listed in Table 5.2. (b)-(d): The change of the bubble collapse time, the minimum bubble volume, and the maximum hydrodynamic pressure on the material surface, with respect to the material's acoustic impedance. Dashed line: $Z/Z_0 = 1$.

nificantly with decreasing Z/Z_0. For example, t_c increases from 3.9 μs in the case of rubber ($Z/Z_0 = 0.66$) to 5.2 μs in the case of fat ($Z/Z_0 = 0.1$). To interpret this effect, we propose a closed-form formula to estimate the collapse time for shock-induced bubble collapse near materials with different acoustic impedance. For non-spherical Rayleigh collapse of an air bubble near a wall, Rattray [50] has proposed an estimation of the collapse time $t_c^{R,w}$:

$$t_c^{R,w} \approx t_c^R \left(1 + 0.205 \frac{R_0}{D_0}\right) \quad \text{with} \quad t_c^R \approx 0.915 \sqrt{\frac{\rho_l}{p_\infty - p_v}} R_0, \tag{5.20}$$

where, t_c^R is the time for the Rayleigh collapse of a spherical bubble in a free field [51]. p_∞ and p_v denote the pressure far from the bubble and the vapor pressure, respectively. Different from the Rayleigh collapse where the whole bubble is exposed simultaneously to constant pressure p_∞, the bubble under the current setting is first subjected to an incident shock wave featuring a specific waveform, and later, the reflected wave from the material surface. Thus, we modify Eq. (5.20) into the following form to estimate the time for shock-induced bubble collapse:

$$t_c = 0.915 \sqrt{\frac{\rho_l}{p_e \left(1 + C \frac{Z - Z_0}{Z + Z_0}\right) - p_0}} R_0 \left(1 + 0.205 \frac{R_0}{H_0}\right). \tag{5.21}$$

Specifically, we introduce an effective pressure p_e to model the impact of the incident shock wave. For the simulations presented in this work, $p_e = 20$ MPa (i.e., an average value of the peak pressure of the incident shock wave and 5 MPa) as the bubble is primarily interacting with the leading compressive phase of the shock wave within the collapse time. The constant C is introduced to account for the time lag of the reflected wave. Also, we assume $p_v = p_0$.

The solid line in Fig. 5.14(b) shows Eq. (5.21) with $C = 0.7$. The predicted collapse time is in good agreement with the simulation results and the effect of Z/Z_0 is explicitly characterized.

5.5.2 Effect on the minimum bubble volume

Fig. 5.14(c) presents the change of the minimum bubble volume (normalized by its initial volume, i.e., $V_{\min}/V_0$) with the relative acoustic impedance. Similar to the bubble's collapse time, the minimum bubble volume also increase significantly with decreasing acoustic impedance when $Z/Z_0 < 1$. Particularly, $V_{\min}/V_0$ for the case of polypropylene foam ($Z/Z_0 = 0.063$) is more than 9 times higher than that for the case of rubber ($Z/Z_0 = 0.66$). Notably, the simulation result can be well captured using a theoretical model modified from that for Rayleigh collapse. Specifically, for an adiabatic Rayleigh collapse of a spherical air bubble in a free field, the minimum bubble volume $V_{\min}^R$ can be calculated by [51]:

$$V_{\min}^R = \frac{4}{3}\pi \left(R_{\min}^R\right)^3, \tag{5.22}$$

where

$$R_{\min}^R = R_0 \left[\frac{p_0}{(\gamma - 1)\left(p_\infty - p_v\right)}\right]^{\frac{1}{3(\gamma-1)}}. \tag{5.23}$$

For the non-spherical bubble collapse, we define the minimum bubble radius as:

$$R_{\min} = \left(\frac{V_{\min}}{4\pi/3}\right)^{1/3}. \tag{5.24}$$

Similar to the modification shown in Eq. (5.21), we replace p_∞ in Eq. (5.23) to estimate $R_{\min}$ for the shock-induced bubble collapse, which gives:

$$R_{\min} = R_0 C_s \left[\frac{p_0}{(\gamma - 1)\left[p_e \left(1 + C \frac{Z - Z_0}{Z + Z_0} \right) - p_0 \right]} \right]^{\frac{1}{3(\gamma-1)}}. \tag{5.25}$$

The constant C_s also accounts for the difference between Rayleigh collapse and shock-induced collapse. The solid line in Fig. 5.14(c) shows the minimum bubble volume computed by Eq. (5.25) with $C = 0.7$ and $C_s = 7$, which matches well with the simulation results.

5.5.3 Effect on the maximum pressure on material surface

Fig. 5.14(d) presents the maximum hydrodynamic pressure $p_{\mathrm{w,max}}$ recorded at the sensor on the material surface for different cases. The result shows that as the material's acoustic impedance decreases, $p_{\mathrm{w,max}}$ becomes smaller. And the change of $p_{\mathrm{w,max}}$ is sharper when $Z/Z_0 < 1$. Particularly, in the cases of fat and polypropylene foam, the maximum pressure recorded after the bubble collapse are about 10 MPa, less than one third of the magnitude of the incident shock wave. This indicates that for materials with relatively small Z/Z_0, the shock wave emitted from the bubble collapse may not be the driving mechanism of material damage. Furthermore, we found that within the range of acoustic impedance tested (i.e., $Z/Z_0 \in [0.039, 11.1]$), $p_{\mathrm{w,max}}$ satisfies a linear relationship with $\log_{10}(Z/Z_0)$:

$$p_{\mathrm{w,max}} = \rho c_0^2 \left[0.0706 \log_{10} \left(\frac{Z}{Z_0} \right) + 0.0413 \right] \text{ Pa}. \tag{5.26}$$

It should be noticed that as Z/Z_0 increases beyond this region, $p_{\max}$ will gradually approach to an upper bound, that is, $p_{\mathrm{w,max}}$ in the case of rigid wall.

Remark:

1. For the materials presented above, the density and the Young's modulus also vary significantly, both of which affect the acoustic impedance. To separate the effects of Young's modulus and that of the acoustic impedance, we perform a numerical experiment using 5 materials that have different Young's modulus but the same acoustic impedance. The result shows that the change of bubble dynamics with the Young's modulus is relatively small compared to that with the acoustic impedance. Thus, the acoustic impedance is the key parameter that controls the reciprocal effects of material on the bubble dynamics. The details of the numerical experiment and discussion are present in the Appendix.

Appendix

5.A Effect of Young's modulus on the bubble collapse

Here, we present the numerical experiment for studying the effect of Young's modulus on the bubble collapse. We test five linear elastic materials with different Young's modulus

using the same simulation setup described in Section 5.4.1. Table 5.4 summarizes the elastic properties of these materials. Specifically, Material-2 is the aluminum tested in Section 5.5. The other four materials are artificial materials which has the same Poisson's ratio and acoustic impedance as the aluminum. Their Young's modulus varies from 142.6 to 21.4 GPa.

Material	**Density** ρ_s (kg/m^3)	**Young's Modulus** E_0 (GPa)	**Poisson's ratio** ν	**Acoustic impedance** Z (MPa·s/m)
Material-1	1500	142.6	0.33	17.8
Material-2 (Aluminum)	2810	71.1	0.33	17.8
Material-3	5000	42.8	0.33	17.8
Material-4	10000	21.4	0.33	17.8
Material-5	20000	10.7	0.33	17.8

Table 5.4: Elastic properties of the five materials for studying the effect of Young's modulus.

Table 5.5 compares the bubble's collapse time (t_c), the minimum bubble volume ($V_{\min}/V_0$) and the maximum pressure at the sensor on the material surface ($p_{\mathrm{w,max}}$) for five cases. The result shows that when the material's acoustic impedance is fixed, the change of bubble dynamics with the Young's modulus is relatively small. For example, the Young's modulus of Material-2 is almost 7 times of that of Material-5, but the differences in t_c, $V_{\min}/V_0$ and $p_{\mathrm{w,max}}$ between two cases are only 0.3%, 2.8% and 1.4%, respectively. For comparison, Table 5.5 also presents the result of Ultracal-30 artificial stone. Similar to Material-5, the Young's modulus of Ultracal-30 stone is around 1/7 of that of Material-2. However, the change of bubble dynamics is much more significant in this case. Specifically, the differences in t_c, $V_{\min}/V_0$ and $p_{\mathrm{w,max}}$ are 5%, 24% and 35%, respectively. Thus, the effect of acoustic

impedance is more significant than that of Young's modulus.

Material	**Bubble's collapse time** t_c (μs)	**Minimum bubble volume** $V_{\min}/V_0$	**Maximum surface pressure** $p_{\mathrm{w,max}}$ (MPa)
Material-1	0.300	0.00289	286
Material-2 (Aluminum)	0.299	0.00283	294
Material-3	0.298	0.00277	298
Material-4	0.298	0.00275	298
Material-5	0.298	0.00275	298
Ultracal-30 artificial stone	0.314	0.00350	190

Table 5.5: Comparison of bubble collapse time, the minimum bubble volume and the maximum hydrodynamic pressure on the material surface.

Acknowledgements

The authors gratefully acknowledge the support of the National Science Foundation (NSF) under Awards CBET-1751487 and CBET-1706003, and the support of the Office of Naval Research (ONR) under Award N00014-17-1-2831. The authors thank Dr. Ying Zhang and Dr. Qiwei Zhan for their advice and assistance on this study.

Bibliography

[1] S. Brems, M. Hauptmann, E. Camerotto, A. Pacco, T.-G. Kim, X. Xu, K. Wostyn, P. Mertens, and S. De Gendt, "Nanoparticle removal with megasonics: a review," *ECS Journal of Solid State Science and Technology*, vol. 3, no. 1, pp. N3010–N3015, 2014.

[2] S. Guo, B. C. Khoo, S. L. M. Teo, S. Zhong, C. T. Lim, and H. P. Lee, "Effect of ultrasound on cyprid footprint and juvenile barnacle adhesion on a fouling release material," *Colloids and Surfaces B: Biointerfaces*, vol. 115, pp. 118–124, 2014.

[3] H. Xu, B. W. Zeiger, and K. S. Suslick, "Sonochemical synthesis of nanomaterials," *Chemical Society Reviews*, vol. 42, no. 7, pp. 2555–2567, 2013.

[4] O. Kudryashova and S. Vorozhtsov, "On the mechanism of ultrasound-driven deagglomeration of nanoparticle agglomerates in aluminum melt," *Jom*, vol. 68, no. 5, pp. 1307–1311, 2016.

[5] P. Zhong, "Shock wave lithotripsy," in *Bubble dynamics and shock waves*, pp. 291–338, Springer, 2013.

[6] C. C. Coussios and R. A. Roy, "Applications of acoustics and cavitation to noninvasive therapy and drug delivery," *Annu. Rev. Fluid Mech.*, vol. 40, pp. 395–420, 2008.

[7] C. E. Brennen, "Cavitation in medicine," *Interface focus*, vol. 5, no. 5, p. 20150022, 2015.

[8] F. Li, C. Yang, F. Yuan, D. Liao, T. Li, F. Guilak, and P. Zhong, "Dynamics and mechanisms of intracellular calcium waves elicited by tandem bubble-induced jetting flow," *Proceedings of the National Academy of Sciences*, vol. 115, no. 3, pp. E353–E362, 2018.

[9] Y. A. Pishchalnikov, O. A. Sapozhnikov, M. R. Bailey, J. C. Williams Jr, R. O. Cleveland, T. Colonius, L. A. Crum, A. P. Evan, and J. A. McAteer, "Cavitation bubble cluster activity in the breakage of kidney stones by lithotripter shockwaves," *Journal of endourology*, vol. 17, no. 7, pp. 435–446, 2003.

[10] K. Maeda, A. D. Maxwell, T. Colonius, W. Kreider, and M. R. Bailey, "Energy shielding by cavitation bubble clouds in burst wave lithotripsy," *The Journal of the Acoustical Society of America*, vol. 144, no. 5, pp. 2952–2961, 2018.

[11] C.-D. Ohl, M. Arora, R. Ikink, N. De Jong, M. Versluis, M. Delius, and D. Lohse, "Sonoporation from jetting cavitation bubbles," *Biophysical journal*, vol. 91, no. 11, pp. 4285–4295, 2006.

[12] E. Brujan, G. Keen, A. Vogel, and J. Blake, "The final stage of the collapse of a cavitation bubble close to a rigid boundary," *Physics of fluids*, vol. 14, no. 1, pp. 85–92, 2002.

[13] M. Calvisi, J. Iloreta, and A. Szeri, "Dynamics of bubbles near a rigid surface subjected to a lithotripter shock wave. part 2. reflected shock intensifies non-spherical cavitation collapse," *Journal of Fluid Mechanics*, vol. 616, pp. 63–97, 2008.

[14] E.-A. Brujan and Y. Matsumoto, "Collapse of micrometer-sized cavitation bubbles near a rigid boundary," *Microfluidics and nanofluidics*, vol. 13, no. 6, pp. 957–966, 2012.

[15] E. Johnsen and T. Colonius, "Numerical simulations of non-spherical bubble collapse," *Journal of fluid mechanics*, vol. 629, pp. 231–262, 2009.

[16] S. Zhang, J. H. Duncan, and G. L. Chahine, "The final stage of the collapse of a cavitation bubble near a rigid wall," *Journal of Fluid Mechanics*, vol. 257, pp. 147–181, 1993.

[17] Q. Wang, "Multi-oscillations of a bubble in a compressible liquid near a rigid boundary," *Journal of Fluid Mechanics*, vol. 745, pp. 509–536, 2014.

[18] M. Dular, O. C. Delgosha, and M. Petkovšek, "Observations of cavitation erosion pit formation," *Ultrasonics sonochemistry*, vol. 20, no. 4, pp. 1113–1120, 2013.

[19] A. Philipp and W. Lauterborn, "Cavitation erosion by single laser-produced bubbles," *Journal of Fluid Mechanics*, vol. 361, pp. 75–116, 1998.

[20] J. Freund, R. Shukla, and A. Evan, "Shock-induced bubble jetting into a viscous fluid with application to tissue injury in shock-wave lithotripsy," *The Journal of the Acoustical Society of America*, vol. 126, no. 5, pp. 2746–2756, 2009.

[21] K. Kobayashi, T. Kodama, and H. Takahira, "Shock wave–bubble interaction near soft and rigid boundaries during lithotripsy: numerical analysis by the improved ghost fluid method," *Physics in Medicine & Biology*, vol. 56, no. 19, p. 6421, 2011.

[22] C. Turangan, G. Ball, A. Jamaluddin, and T. Leighton, "Numerical studies of cavitation erosion on an elastic–plastic material caused by shock-induced bubble collapse," *Proceedings of the Royal Society A: Mathematical, Physical and Engineering Sciences*, vol. 473, no. 2205, p. 20170315, 2017.

[23] G. L. Chahine and C.-T. Hsiao, "Modelling cavitation erosion using fluid–material interaction simulations," *Interface focus*, vol. 5, no. 5, p. 20150016, 2015.

[24] K. G. Wang, "Multiphase fluid-solid coupled analysis of shock-bubble-stone interaction in shockwave lithotripsy," *International journal for numerical methods in biomedical engineering*, vol. 33, no. 10, p. e2855, 2017.

[25] D. Gibson and J. R. Blake, "The growth and collapse of bubbles near deformable surfaces," *Applied Scientific Research*, vol. 38, no. 1, pp. 215–224, 1982.

[26] E.-A. Brujan, K. Nahen, P. Schmidt, and A. Vogel, "Dynamics of laser-induced cavitation bubbles near elastic boundaries: influence of the elastic modulus," *Journal of Fluid Mechanics*, vol. 433, pp. 283–314, 2001.

[27] G. Sankin and P. Zhong, "Interaction between shock wave and single inertial bubbles near an elastic boundary," *Physical Review E*, vol. 74, no. 4, p. 046304, 2006.

[28] K. Wang, P. Lea, and C. Farhat, "A computational framework for the simulation of high-speed multi-material fluid–structure interaction problems with dynamic fracture," *International Journal for Numerical Methods in Engineering*, vol. 104, no. 7, pp. 585–623, 2015.

[29] K. Wang, J. Grétarsson, A. Main, and C. Farhat, "Computational algorithms for tracking dynamic fluid–structure interfaces in embedded boundary methods," *International Journal for Numerical Methods in Fluids*, vol. 70, no. 4, pp. 515–535, 2012.

[30] D. Z. Huang, D. De Santis, and C. Farhat, "A family of position-and orientation-independent embedded boundary methods for viscous flow and fluid-structure interaction problems," *Journal of Computational Physics*, 2018.

[31] K. Wang, A. Rallu, J.-F. Gerbeau, and C. Farhat, "Algorithms for interface treatment and load computation in embedded boundary methods for fluid and fluid–structure interaction problems," *International Journal for Numerical Methods in Fluids*, vol. 67, no. 9, pp. 1175–1206, 2011.

[32] C. Farhat, J.-F. Gerbeau, and A. Rallu, "Fiver: A finite volume method based on exact two-phase riemann problems and sparse grids for multi-material flows with large density jumps," *Journal of Computational Physics*, vol. 231, no. 19, pp. 6360–6379, 2012.

[33] A. Main, X. Zeng, P. Avery, and C. Farhat, "An enhanced fiver method for multi-material flow problems with second-order convergence rate," *Journal of Computational Physics*, vol. 329, pp. 141–172, 2017.

[34] C. Farhat, A. Rallu, K. Wang, and T. Belytschko, "Robust and provably second-order explicit–explicit and implicit–explicit staggered time-integrators for highly non-linear compressible fluid–structure interaction problems," *International Journal for Numerical Methods in Engineering*, vol. 84, no. 1, pp. 73–107, 2010.

[35] C. Farhat, K. Wang, A. Main, S. Kyriakides, L.-H. Lee, K. Ravi-Chandar, and T. Belytschko, "Dynamic implosion of underwater cylindrical shells: experiments and computations," *International Journal of Solids and Structures*, vol. 50, no. 19, pp. 2943–2961, 2013.

[36] K. G. Wang, P. Lea, A. Main, O. McGarity, and C. Farhat, "Predictive simulation of underwater implosion: Coupling multi-material compressible fluids with cracking structures," in *ASME 2014 33rd International Conference on Ocean, Offshore and Arctic Engineering*, pp. V08AT06A028–V08AT06A028, American Society of Mechanical Engineers, 2014.

[37] H. Chung, S. Cao, M. Philen, P. S. Beran, and K. G. Wang, "Cfd-csd coupled analysis of underwater propulsion using a biomimetic fin-and-joint system," *Computers & Fluids*, vol. 172, pp. 54–66, 2018.

[38] S. Cao, Y. Zhang, D. Liao, P. Zhong, and K. G. Wang, "Shock-induced damage and dynamic fracture in cylindrical bodies submerged in liquid," *International Journal of Solids and Structures*, 2019.

[39] D. Cheneler, "Viscoelasticity of polymers: Theory and numerical algorithms," *APPLIED RHEOLOGY*, vol. 26, no. 4, pp. 10–52, 2016.

[40] S. Goh, M. Charalambides, and J. Williams, "Determination of the constitutive constants of non-linear viscoelastic materials," *Mechanics of Time-Dependent Materials*, vol. 8, no. 3, pp. 255–268, 2004.

[41] A. T. de Hoop and J. H. Van der Hijden, "Generation of acoustic waves by an impulsive point source in a fluid/solid configuration with a plane boundary," *The Journal of the Acoustical Society of America*, vol. 75, no. 6, pp. 1709–1715, 1984.

[42] Inria, "Gar6more3d." http://gar6more3d.gforge.inria.fr/, 2013.

[43] W. Simmons, F. Cocks, P. Zhong, and G. Preminger, "A composite kidney stone phantom with mechanical properties controllable over the range of human kidney stones," *Journal of the mechanical behavior of biomedical materials*, vol. 3, no. 1, pp. 130–133, 2010.

[44] A. Amirkhizi, J. Isaacs, J. McGee, and S. Nemat-Nasser, "An experimentally-based viscoelastic constitutive model for polyurea, including pressure and temperature effects," *Philosophical magazine*, vol. 86, no. 36, pp. 5847–5866, 2006.

[45] A. M. Sims, T. Stait-Gardner, L. Fong, J. W. Morley, W. S. Price, M. Hoffman, A. Simmons, and K. Schindhelm, "Elastic and viscoelastic properties of porcine subdermal fat using mri and inverse fea," *Biomechanics and modeling in mechanobiology*, vol. 9, no. 6, pp. 703–711, 2010.

[46] E. Esch, W. N. Simmons, G. Sankin, H. F. Cocks, G. M. Preminger, and P. Zhong, "A simple method for fabricating artificial kidney stones of different physical properties," *Urological research*, vol. 38, no. 4, pp. 315–319, 2010.

[47] E. Johnsen and T. Colonius, "Shock-induced collapse of a gas bubble in shockwave lithotripsy," *The Journal of the Acoustical Society of America*, vol. 124, no. 4, pp. 2011–2020, 2008.

[48] C. C. Church, "A theoretical study of cavitation generated by an extracorporeal shock wave lithotripter," *The Journal of the Acoustical Society of America*, vol. 86, no. 1, pp. 215–227, 1989.

[49] D. E. Fovargue, S. Mitran, N. B. Smith, G. N. Sankin, W. N. Simmons, and P. Zhong, "Experimentally validated multiphysics computational model of focusing and shock wave formation in an electromagnetic lithotripter," *The Journal of the Acoustical Society of America*, vol. 134, no. 2, pp. 1598–1609, 2013.

[50] M. Rattray, *Perturbation effects in cavitation bubble dynamics*. PhD thesis, California Institute of Technology, 1951.

[51] C. E. Brennen, *Cavitation and bubble dynamics*. Cambridge University Press, 2014.

Chapter 6

Conclusions and Perspectives for Future Work

6.1 Conclusions

This dissertation investigates the development of numerical algorithms for coupling computational fluid dynamics (CFD) and computational solid dynamics (CSD) solvers, and the use of these solvers for simulating fluid-solid interaction (FSI) problems involving large deformation, shock waves, and multiphase flow.

The first part of this dissertation focuses on a well-known issue associated with partitioned coupling procedures. It has been found that for FSI problems involving incompressible flow and strong added-mass effect, partitioned coupling procedures suffer from numerical insta-

bility. This work presents a fundamental study on the use of Robin interface condition to mitigate this instability issue. First, a novel CFD-CSD coupled computational framework is developed. It couples a projection-based incompressible flow solver and a finite element structural solver using a Robin-Neumann partitioned procedure. In particular, the framework features an embedded Robin boundary method which utilizes operating splitting and a modified ghost fluid method to enforce the Robin interface condition on non-body-conforming CFD grids, and thus, it can be advantageous in handling structures with complex geometries and large deformation. Numerical experiments using the Turek-Hron benchmark problem show that the Robin-Neumann partitioned procedure can outperform conventional Dirichlet-Neumann procedure in terms of both stability and accuracy, when the constant combination parameter α_f in Robin interface condition is carefully selected.

Next, two studies are carried out to characterize the effects of α_f on the numerical properties of the partitioned procedure. One is a numerical study using the Turek-Hron benchmark problem. The other one is an analytical study using a simplified 2-D model problem. Both studies reveal that smaller values of α_f tend to improve numerical stability, while larger values of α_f tend to have better accuracy. And the optimal α_f derived from the model 2-D model problem is found dependent on the material properties and geometry of the problem.

Therefore, to efficiently solve FSI problems involving non-uniform structures, the constant parameter α_f is then generalized into a spatially varying function, and two closed-form formulas are proposed to determine its local value based on the local material and geometric properties of the structure. Numerical experiments on several academic problems have

demonstrated that using this spatially varying Robin interface condition can significantly outperform the constant-parameter version recently discussed in the literature.

The second part of this dissertation focuses on extending a recently developed multiphase CFD-CSD coupled solver, FIVER, to study the FSI problems featuring shock waves, multiphase flow, and material damage and fracture. First, a three-dimensional (3D) fluid-solid coupled model is developed to simulate the shock-induced dynamic fracture in a brittle material in the context of shock wave lithotripsy. In particular, the material damage and fracture are modeled and simulated by applying a continuum damage mechanics model and an element erosion method. After calibration, the coupled model is capable of capturing the location and shape of the shock-induced fracture observed in a laboratory experiment. Most importantly, the simulation results explicitly elucidate the causal relationship between the prescribed shock wave, the propagation and superposition of different stress wave inside the material, and the resulting material damage and crack propagation. Based on this model, a series of parametric studies are carried out to investigate the effects of shock waveform, magnitude and target size on the material damage. The result shows that a shock wave with a tensile phase can induce significantly greater damage to the target material than one without a tensile phase, even if the two have the same peak pressure, duration, and acoustic energy. This finding holds for relatively wide ranges of shock magnitude ($p_{max} > 10$ MPa) and target size (relative to the length of the shock wave $0.18 < L/L_{SW} < 1.07$), indicating a possible approach to improve energy efficiency for applications that utilize shock wave for material modification.

Second, the 3D fluid-solid coupled model is applied to simulate the collapse of an air bubble in water induced by an ultrasound shock wave, with different types of materials in its vicinity. A level-set method, an embedded boundary method, and exact two-fluid and fluid-solid Riemann solvers are employed to explicitly capture the asymmetric bubble collapse, the resulting shock waves and liquid jet, and the material's response. The result shows that the relative acoustic impedance of the material compared to that of the ambient fluid, namely Z/Z_0, has a significant reciprocal impact on the collapsing dynamics of the bubble: when $Z/Z_0 > 1$, the process of bubble collapse is accelerated, resulting in stronger shock waves; when $Z/Z_0 < 1$, the collapse is decelerated, and the shock magnitude is reduced. The result also reveals that, even for hard ceramic material, modeling the solid material as a rigid wall boundary $Z/Z_0 = \infty$ of the fluid domain can lead to a 60% overestimate of the magnitude of the cavitation-induced shock wave. This finding suggests that taking into account the reciprocal effect of the material's acoustic impedance in the study of cavitation dynamics is important.

6.2 Perspectives for future work

First, for the new Robin-Neumann partitioned procedure proposed in this dissertation, future studies may consider exploring additional advantages of a spatially varying Robin interface condition (e.g., reducing the number of fluid-structure subiterations), developing new formulas for the spatially varying Robin parameter $\alpha_f(\mathbf{X})$, and applying the spatially varying

Robin interface condition to simulate more engineering applications (e.g., in the fields of underwater propulsion and hemodynamics). Also, the parameter α_f in the Robin interface condition can be generalized to temporally varying or solution-adaptive functions, which may be beneficial for certain types of problems.

Second, the study of shock-induced material damage presented in Chapter 4 considers a relatively ideal setup of the problem in which the material is subjected to a single shock wave that is well-aligned with it. However, real-world applications often involve multiple shock loads and misalignment with the target materials is also a common scenario. Therefore, it is highly desirable to study the cumulative effects of multiple shock loads on the material damage and fracture, as well as the effect of misalignment. This work is currently in progress.

Third, future development of the 3D multiphase fluid-solid coupled computational model presented in Chapter 5 will focus on incorporating the continuum damage mechanics model to simulate the material damage and fracture induced by the bubble collapse. This is conceptually straightforward, yet may require substantial effort on the model calibration and validation with laboratory experiments. After that, the extended model can be applied to investigate the effects of the bubble's stand-off distance, content, and size on the material damage and fracture, and separate the effects of the shock wave and microjet resulting from the collapse. Further extension of the model to study the collapse of tandem bubble or small bubble clusters near various materials will also be desirable because the theoretical foundation is still in its infancy.